VNIVERSITAT DE VALÈNCIA

FACULTAT DE FÍSICA

Institut de Física Corpuscular (IFIC, UV-CSIC)
i Departament de Física Atòmica, Molecular i Nuclear

DOCTORAT EN FÍSICA

Photon polarization in $B_s^0 \to \phi\gamma$ decays at the LHCb experiment

Ph.D. dissertation
Pablo Ruiz Valls

Supervisors
Arantza Oyanguren Campos
Fernando Martínez Vidal

Valencia, Spain
November, 2016

CERN-THESIS-2016-217
13/12/2016

Dra. María Aránzazu Oyanguren Campos,
Investigadora Ramón y Cajal y

Dr. Fernando Martínez Vidal,
Profesor titular de la UV

CERTIFICAN:

Que la presente memoria **Photon polarization in $B_s^0 \to \phi\gamma$ decays at the LHCb experiment** ha sido realizada bajo su dirección en el Departamento de Física Atómica, Molecular y Nuclear de la Universidad de Valencia por D. Pablo Ruiz Valls y constituye su trabajo de tesis doctoral para optar al grado de Doctor en Física.

Y para que así conste, firman el presente certificado.

Dra. María Aránzazu Oyanguren Campos

Dr. Fernando Martinez Vidal

El trabajo descrito en esta tesis se ha llevado a cabo en el **Instituto de Física Corpuscular** (IFIC) en Valencia, España.

El IFIC es un centro mixto del Consejo Superior de Investigaciones Científicas (CSIC) y de la Universitat de València. En Julio de 2015 recibió la acreditación **Severo Ochoa** (SEV-2014-0398) que le distingue como Centro de Excelencia. Dicha acreditación reconoce la excelencia y las contribuciones científicas que realizan los centros y unidades a nivel nacional e internacional, su impacto empresarial y social y su capacidad para atraer talento.

VNIVERSITAT DE VALÈNCIA

Perfer et obdura,
dolor hic tibi proderit olim.

OVID

So let us then try to climb the mountain,
not by stepping on what is below us,
but to pull us up at what is above us,
for my part at the stars;
amen.

MAURITS CORNELIS ESCHER

Acknowledgements

This achievement has been made possible thanks to the contribution of many people, they all deserve my gratitude.

Foremost, I would like to express my deep gratitude to my advisors, without whom this work would have never taken place and I'd be missing so many of the lessons I've learned in these years. Arantza Oyanguren Campos and Fernando Martínez Vidal have been by my side, guiding the way through hardships and showing an immense degree of patience when confronting my ignorance.

Besides my advisors, I would like to thank the rest of my thesis committee: Prof. Antonio Pich, Dr. Míriam Calvo and Dr. Thomas Blake, for their insightful comments.

My sincere thanks also go to Albert Puig and Cédric Potterat, my first tutors in LHCb, without whom I wouldn't be able to tell an analysis software package from a renaissance painter.

I'm also grateful to Vicente and Carlos, my partners in crime: I got extremely lucky in forging friendships with you, and I'm happy to see that you've also seen the end of your studentships. You deserve a medal. Ander, Fernando, Jonathan, Nacho, Victor, Damián, Rubén, Lluís, Luís, Carlos, Ane, Nuria, Javi, Rosa, Dani, and the rest of my brethren in science and life: thank you so much for dessert Mondays, and for enduring my whining and ramblings on absurd stuff like the stoichiometry of cheese. I've learned so much and become a better person through our friendship. Jabo, Miguel, Andrés, Chemita, Navo, Rodrigo, Alessandro, Catrin, Mónica and all of the rest up in the mountains and beyond the seas: thank you for your unending support and I want to apologize for being so busy all this time.

I want to thank Ramón, whose passion for physics and the writings of Lovecraft and Asimov were highly contagious. How I wish you were here!

I thank my family: my parents, my brother and sister, those who are far, and those who aren't here anymore. You gave me the most precious gift by patiently enduring all of the questions I could come up with, nurturing the

curiosity that made me what I am today. I wouldn't change a single iota of my upbringing. You've always been supportive, after all of my follies. I love all of you.

And to Clara, light of my heart, you were always there to conquer my fears. You opened my eyes and now I can see clearly. I love you most of all.

Contents

Summary **1**

Resumen **5**

1 Theoretical framework **9**
1.1 Spin, chirality and helicity 10
1.2 The Standard Model 12
1.3 Structure of the SM 13
1.3.1 Local gauge invariance 14
1.3.2 The Standard Model Lagrangian 15
1.3.3 Discrete symmetries 23
1.4 Radiative $B^0_{(S)}$ decays in the SM 24
1.4.1 Neutral meson oscillation 24
1.4.2 Photon polarization in the SM 33

2 The LHCb detector at the LHC **39**
2.1 LHCb at the Large Hadron Collider 39
2.2 Detector geometry and components 45
2.3 Tracking 48
2.3.1 The LHCb Magnet 48
2.3.2 Vertex Locator 49
2.3.3 Silicon Tracker 51
2.3.4 Outer Tracker 56
2.3.5 Tracking system performance 57
2.4 Particle identification 59
2.4.1 RICH 59
2.4.2 Calorimeters 61
2.4.3 Muon Detector 67
2.4.4 PID algorithms 70

2.5 Online system . . . 73
2.5.1 Data Acquisition System . . . 73
2.5.2 Timing and Fast Control . . . 73
2.5.3 Experiment Control System . . . 75
2.6 Trigger system . . . 75
2.6.1 Level-0 Trigger . . . 76
2.6.2 High Level Trigger . . . 77
2.7 Computing and data flow . . . 79
2.7.1 Data processing software in LHCb . . . 79

3 Stripping **81**
3.1 Stripping framework . . . 82
3.1.1 Stripping lines' format . . . 85
3.2 Radiative stripping . . . 88
3.2.1 Exclusive radiative stripping strategies . . . 89
3.2.2 Inclusive radiative stripping strategies . . . 91

4 Reconstruction of $B \to V\gamma$ decays **97**
4.1 Data samples and software versions . . . 98
4.2 Event selection . . . 98
4.2.1 Event reconstruction . . . 98
4.2.2 Trigger chain . . . 100
4.2.3 Stripping and Offline Selection . . . 101
4.2.4 Selected mass distributions . . . 106

5 B meson invariant mass fit **115**
5.1 Signal description . . . 115
5.2 Background species . . . 118
5.2.1 Backgrounds to $B_s^0 \to \phi\gamma$ . . . 120
5.2.2 Backgrounds to $B^0 \to K^{*0}(892)\gamma$ . . . 124
5.3 Data mass fit . . . 131
5.3.1 Mass fit to $B_s^0 \to \phi\gamma$ data . . . 132
5.3.2 Mass fit to $B^0 \to K^{*0}(892)\gamma$ data . . . 134
5.3.3 Validation of the fit . . . 136
5.3.4 Signal distributions . . . 136

6 Proper time description and reconstruction **145**
6.1 Proper time fit algorithm . . . 147
6.2 Proper time acceptance . . . 148
6.2.1 Contributions to the common acceptance . . . 149

6.2.2 Verification of the parametrization 151
6.3 Proper time resolution 153
6.3.1 Resolution control with $B^0 \to J/\psi K^{*0}(892)$ samples . . 157

7 Fit to the normalized proper time distribution 159
7.1 Fit strategy 159
7.1.1 Binning scheme 159
7.1.2 Fitting algorithm 161
7.1.3 Statistical sensitivity 164
7.2 Systematic uncertainties 168
7.2.1 External parameters 169
7.2.2 Proper time acceptance 169
7.2.3 Resolution 171
7.2.4 Signal and background modelling 173
7.2.5 Correlation between mass and proper time 175
7.2.6 Summary of systematic uncertainties 176
7.3 Results 178
7.3.1 Direct fit 178
7.3.2 Interpretation of the result 179

Conclusions 183

A The `PropertimeFitter` algorithm 185

Glossary 189

Summary

Results from high energy physics experiments generally agree with the predictions of the Standard Model (SM), which describes all known elementary particles and the strong and electroweak interactions between them. Notwithstanding, a broader model which encompasses other non-standard elements such as gravity, dark matter, dark energy and neutrino oscillations is needed. Several so-called Beyond Standard Model (BSM) theories introduce additional hypothetical processes and particles in the form of New Physics (NP) to explain the aforementioned phenomena in a framework consistent with the SM. Validation of these theories can be done via the study of electroweak loop processes, in which the new particles can mediate as virtual participants in lower collision energy thresholds than those of on-shell production. The study of B hadrons is specially interesting due to their quark content, as b quarks always undergo Cabbibo suppressed transitions in their decays, usually through flavour-changing charged currents, although some are only possible through loops, the so-called flavor-changing neutral currents (FCNC). Radiative B hadron decays with a photon in the final state are an excellent example of this type of phenomena.

In the scope of this work the focus is set on the $b \to s\gamma$ transition. It is a FCNC mediated by a single loop penguin transition, dominated by a virtual intermediate top quark coupling to a W boson. In the SM the photons emitted are polarized predominantly left-handed with a small right-handed component of order m_s/m_b, where m_s and m_b stand for the masses of the s and b quarks, respectively. Some BSM models predict alternative loop contributions which can alter the dynamics of the transition and affect the photon polarization in a measurable amount, thus a precise measurement of the photon polarization in $b \to s\gamma$ decays could test the predictions of several NP models, driving the motivation for this measurement. The $B_s^0 \to \phi\gamma$ time-dependent decay amplitude is sensitive to the photon polarization, and therefore it is chosen as the signal channel. Conversely, the

time-dependent amplitude of $B^0 \to K^{*0}(892)\gamma$ has almost no dependence on the photon polarization term, but being topologically and kinematically similar to $B_s^0 \to \phi\gamma$ it is adopted as a control channel. This work is organized as follows:

Chapter 1 introduces the theoretical background and demarcates a context for the strategy to extract an estimate of the photon polarization through an untagged lifetime measurement.

Because of the special characteristics of B meson decays and the precision requirements, dedicated detectors are designed and built with the purpose of studying this kind of particles. One of such detectors is LHCb, assembled on the LHC accelerator ring at the CERN facilities near Geneva. LHCb is a single-arm forward spectrometer that measures the decays of b-quark hadrons coming from pp collisions with high accuracy. Chapter 2 is dedicated to the detector description, as well as the treatment of the data taken therein.

One important stage of the data flow is the stripping, in which the bulky data filtered by the online trigger algorithms is reduced into manageable portions made available to the analysts to run their algorithms on. Part of the author's participation in LHCb concerned the coordination of the stripping lines in the rare decays working group as well as the maintenance of the radiative decays sub-working group lines, including the design and implementation of an inclusive selection strategy. A detailed description is contained in Chapter 3.

Using the data collected by LHCb between 2011 and 2012 at 7 TeV and 8 TeV centre-of-mass energy, respectively, a measurement of the photon-polarization-related observable in the $b \to s\gamma$ transition is obtained through the fit to the ratio of proper-time distributions of $B_s^0 \to \phi\gamma$ and $B^0 \to K^{*0}(892)\gamma$ decays. The driving motivation behind this choice is to cancel out systematic effects in the ratio. The similitude between the efficiencies of both channels is paramount, and the selection must be designed with this priority in mind, while also maximizing the signal purity for both channels. A total of 4072 ± 12 and 24808 ± 321 signal events are obtained of $B_s^0 \to \phi\gamma$ and $B^0 \to K^{*0}(892)\gamma$ decays, respectively. The former number stands as the largest sample obtained for $B_s^0 \to \phi\gamma$ so far. The selection strategy is presented in Chapter 4.

Once selected, a multicomponent mass fit including all the possible sources of background is applied to each channel sample separately Using knowledge of the mass signal shape, the background is subtracted and the signal proper-time distributions obtained. An estimator of the statisti-

cal uncertainty, related only to the number of events, is obtained from the signal yields of the fits. These procedures are explained in Chapter 5.

Due to the nature of the detector and the algorithms employed, the reconstruction of the proper time introduces two unavoidable effects: a time dependent efficiency, called acceptance, and a resolution. Knowledge of these effects is key to recover the correct physical value of the decay time of each event and, therefore, to make a correct assessment of the photon-polarization-related observable. Chapter 6 deals with the detailed description of these effects.

Only after having isolated and corrected the data that best represent the physical distributions of the decay time for both channels can the lifetime measurement be made. The distributions are binned and divided, and a least-squares minimization is performed to fit a binned "curve" to the data, leaving only the polarization parameter free. Several checks are performed to evaluate the magnitude of the systematic uncertainties from several sources. Chapter 7 closes the document with the results, and their uncertainties, for this measurement, along with its interpretation in the context of the SM and NP. This thesis represents the first measurement of a photon-polarization-related observable in a B_s^0 meson decay, and the analysis has been submitted for publication to Physical Review Letters [1].

The work presented here is the result of the joint effort of several people. Within said effort, the main contributions of the author concern the study of the variables with their relation to the proper time acceptance for the design of the selection; the development of the stripping, background subtraction, adaptive binning and proper time ratio fit algorithms; as well as tests for the description of the resolution.

Resumen

Los resultados de experimentos de física de altas energías concuerdan en general con las predicciones del Modelo Estándar (ME), el cual describe todas las partículas elementales que se conocen, así como las interacciones fuertes y electrodébiles entre ellas. Sin embargo, se requiere un modelo que incluya otros fenómenos físicos conocidos como son la gravedad, la materia oscura, la energía oscura o la oscilación de los sabores de neutrinos. Varios modelos teóricos de física más allá del modelo estándar (BSM[1]) introducen partículas o procesos hipotéticos adicionales que explican los fenómenos mentados en un marco compatible con el ME. Estas adiciones son denominadas Nueva Física (NF). Una forma de comprobar estas teorías es a través del estudio de los procesos de *loop* electrodébil, en los que las nuevas partículas pueden aparecer como miembros virtuales a escalas de energía menores a las de su umbral de producción. El estudio de los hadrones con contenido de quarks b es especialmente interesante, dado que los susodichos quarks siempre se desintegran a través de procesos con supresión de Cabibbo. Estas desintegraciones suelen suceder a través de corrientes cargadas con cambio de sabor, aunque algunas sólo son posibles a través de procesos de *loops*, las llamadas corrientes neutras con cambio de sabor (FCNC[2]). Las desintegraciones radiativas de hadrones B con un fotón en el estado final son un excelente ejemplo de esta clase de fenómeno.

Este trabajo centra en torno a la transición $b \to s\gamma$. Es una FCNC mediada a primer orden por una transición de *pingüino*, el cual está dominado por un quark top virtual acoplando a un bosón W. Según el ME, los fotones emitidos por esta transición lo hacen mayoritariamente con una polarización levógira, con una pequeña componente dextrógira del orden del cociente de las masas de los quarks s y b, m_s/m_b. Algunos modelos BSM

[1]Por las siglas de la voz inglesa *Beyond Standard Model*.

[2]Por las siglas de la voz inglesa *Flavour Changing Neutral Current*.

contienen participaciones adicionales en el *loop* que pueden alterar el proceso y producir un cambio mensurable en la polarización del fotón. Con ello, una medida precisa de la polarización del fotón en desintegraciones a través del proceso $b \to s\gamma$ puede proporcionar información adicional para comprobar las predicciones de los modelos mentados, motivando el trabajo de la presente obra. Por un lado, la amplitud de desintegración en función del tiempo de la desintegración $B_s^0 \to \phi\gamma$ es sensible a la polarización del fotón, y por tanto se elige como canal de señal. Por el otro, la amplitud correspondiente en la desintegración $B^0 \to K^{*0}(892)\gamma$ no tiene una sensibilidad al término de la polarización del fotón, pero debido a sus similitudes topológicas y cinemáticas con respecto a la desintegración $B_s^0 \to \phi\gamma$ se adopta como canal de control. Este trabajo está estructurado de la siguiente manera:

El capítulo 1 presenta una descripción de la base teórica y delinea un contexto estratégico para extraer información de la polarización del fotón a través de una medida del tiempo de desintegración de los mesones B sin distinguir conjugados de sabor.

Debido a la información que se puede extraer de la forma en que se desintegran los mesones B, se diseñan detectores con unas características específicas para poder medir con precisión las propiedades de los mismos. Un detector tal es LHCb, situado en el anillo acelerador del LHC en las instalaciones del CERN cerca de Ginebra. El detector LHCb es un espectrómetro frontal de un solo brazo que mide con alta precisión las desintegraciones de hadrones con contenido de quarks b producidos en colisiones pp. Una exposición detallada del detector figura en el capítulo 2.

Una etapa importante de la cadena de procesamiento de datos es el *stripping*, en la cual se filtran los datos de salida del detector hasta obtener unas partidas manejables para ser analizadas por los usuarios. Durante el desarrollo de su tesis y como parte de su participación en la colaboración LHCb, el autor realizo labores como coordinador de las líneas de *stripping* para el grupo de desintegraciónes raras de LHCb y de mantenimiento de las líneas del subgrupo de desintegraciones radiativas, incluyendo el diseño e implementación de una estrategia inclusiva de selección. Esta labor queda reflejado en el capítulo 3.

Con los datos obtenidos en LHCb durante 2011 y 2012 a energías de centro de masa de 7 y 8 TeV, respectivamente, se obtiene una medida de un observable relacionado con la polarización del fotón a través de un ajuste al cociente entre las distribuciones de tiempo de desintegración de los canales $B_s^0 \to \phi\gamma$ y $B^0 \to K^{*0}(892)\gamma$. El objetivo de realizar un cociente es

reducir las incertidumbres sistemáticas aprovechando las semejanzas entre los dos canales. La selección ha sido diseñada con la idea de preservar estas similitudes, a la vez que se intenta maximizar la pureza de eventos de señal en ambos canales. En total se obtienen 4072 ± 12 y 24808 ± 321 sucesos de señal de las desintegraciones $B_s^0 \to \phi\gamma$ y $B^0 \to K^{*0}(892)\gamma$, respectivamente. Ese número de eventos es, en el caso de la desintegración $B_s^0 \to \phi\gamma$, la mayor muestra obtenida hasta la fecha. El capítulo 4 describe la estrategia de selección.

Una vez han sido seleccionados los sucesos de interés, se realiza un ajuste a la distribución de masas de cada canal, incluyendo las posibles fuentes de fondo. Utilizando información de la distribución de masas de los eventos de señal y fondo, se sustraen las componentes de fondo con el fin de aislar las distribuciones de tiempo de desintegración de los eventos de señal. Asímismo, se estima la incertidumbre estadística, dependiente únicamente del tamaño muestral de señal, a partir de los resultados del ajuste. El capítulo 5 explica estos procedimientos.

Dada la naturaleza del detector y los algoritmos empleados, la reconstrucción del tiempo de desintegración introduce dos efectos experimentales inevitables: una eficiencia dependiente del tiempo, llamada aceptancia, y una resolución temporal. Un estudio exhaustivo de estos efectos es imprescindible para obtener una distribución correcta del tiempo de desintegración, y por tanto, para obtener un estimador preciso del observable de polarización. El capítulo 6 versa sobre estos efectos.

Sólo habiendo obtenido una muestra de datos aislada de los fondos y considerando todos los efectos se puede obtener un resultado del observable de polarización del fotón. Las distribuciones de ambos canales se agrupan en *bins* y se dividen, y se realiza un ajuste de mínimos cuadrados a la curva teórica, dejando únicamente el observable de polarización como parámetro de ajuste. Se realizan pruebas pormenorizadas para estimar la magnitud de las incertidumbres sistemáticas provenientes de distintas fuentes. El capítulo 7 cierra el documento con una exposición del ajuste, la evaluación de incertidumbres sistemáticas y los resultados finales, así como una interpretación del mismo en el contexto del ME y de NF.

Esta tesis es la primera medida de un observable relacionado con la polarización del fotón en la desintegración de un mesón B_s^0, y el análisis ha sido presentado para su publicación en la revista *Physical Review Letters* [1].

El trabajo descrito en esta memoria es el resultado del esfuerzo conjunto de diversas personas. En el marco de dicho esfuerzo, las contribuciones principales del autor consisten en el estudio de las variables y su efecto

sobre la aceptancia para el diseño de la selección; el desarrollo de los algoritmos de *stripping*, de sustracción de fondos, de *binning* adaptativo y de ajuste a la distribución del cociente de tiempos propios; así como pruebas para el estudio de la resolución temporal.

1 | Theoretical framework

The Standard Model (SM) is a quantum field theory describing all known interactions except for gravitation. A result of the combined effort of numerous theorists, its construction spans the second half of the 20^{th} century with many predictions confirmed by experimental results. Several Nobel prizes have been awarded to proponents of different pieces of the SM. Feynman, Schwinger and Tomonaga received the Nobel Prize in 1965 for the development of Quantum Electrodynamics (QED). The 1979 prize was given to Glashow, Salam and Weinberg for the unification of the electromagnetic and weak interactions, and the prediction of the W and Z bosons. The quantum formulation of the electroweak interaction made 't Hooft and Veltman worthy of the 1999 prize. The development of quantum chromodynamics (QCD) has awarded Nobel Prizes to Gell-Mann in 1969 and to Gross, Politzer and Wilczek in 2004. Kobayashi and Maskawa shared the 2008 prize for their work on the quark-flavour mixing mechanism of the SM and the prediction of the third quark family. The 2013 Nobel Prize was granted to Higgs and Englert for their description of the Spontaneous Symmetry Breaking (SSB) mechanism that explains how elementary particles acquire mass.

The SM has been tested exhaustively and its predictions have been found in the majority of cases accurate within experimental sensitivity and theoretical uncertainty. Nevertheless, the SM still does not completely describe all the observed phenomena and therefore is not a complete theory. For example, the model does not include a formulation for gravitational interaction, nor does it contain a description of possible components of dark matter. It also lacks mass terms for the neutrinos, needed to explain their observed flavour oscillation processes[1]. These so-called Beyond Standard Model (BSM) phenomena, among others, make necessary the construction of models that both comprise the tested structure of the SM and contem-

[1]Subject of another Nobel Prize in 2015, awarded to Kajita and McDonald.

plate these additional processes. Several of these models already exist, but lack of experimental evidence supporting them keeps from declaring any one the right paradigm.

Experimental results that definitely challenge the predictions of the SM are necessary to push the boundaries forward and test the predictions of the candidate models. This chapter deals with the description of the SM, focusing later on the phenomena of radiative decays of B mesons and the relevance of a measurement of the photon polarization in $b \to s\gamma$ transitions for both the SM and BSM theories, providing a motivation for the research presented in this dissertation.

1.1 Spin, chirality and helicity

One of the most interesting properties of quantum particles is spin. It is an intrinsic angular momentum associated to particles with no classical analogue and plays an essential role in the description of elementary particles and their interactions. Depending on their spin, the particles may behave differently. For example, the wave functions of identical particle systems are completely symmetric when interchanging the positions of any two if their spin is an integer and completely anti-symmetric if their spin is a half-integer. The former are called bosons while the latter are named fermions. This is what is called the spin-statistics theorem, and has important consequences in the macroscopic world. Since their wave functions transform anti-symmetrically, the amplitude of two fermions occupying the same state must vanish and thus it is forbidden, as stated by Pauli's exclusion principle. Bosons, on the other hand, don't follow this rule because of their spin.

This exclusion principle governs the ordering of electronic orbitals in atoms and determines the structure that lies beneath the periodic table, since electrons are fermions. The different orbitals correspond to increasingly complex angular momentum states for electrons, which have finite and discrete vacancies and occupancies, according to the possible quantum states therein. Because of this, elements can form molecules, electrons can interchange energy by migrating orbitals back and forth, and, in short, chemistry can take place.

In the context of particle physics, spin remains an essential piece of the theoretical framework. Eigenvalues of spin are measured as projections against a defined axis, experimentally generally defined by an electric or

magnetic field. To do away with the necessity of external parameters, one can use the momentum of the particle to define a direction against which spin can be measured. This gives rise to helicity, which is the projection of a particle's spin to its direction of movement. The corresponding operator for a spin $\frac{1}{2}$ particle,

$$\frac{1}{2}\frac{\mathbf{p}\cdot\vec{\sigma}}{p}, \tag{1.1}$$

where $\mathbf{p}$ is the particle's momentum and $\vec{\sigma}$ the spin operator given by the Pauli matrices. The possible eigenvalues for helicity are then $+\frac{1}{2}$ for particles with their spin in the same direction of motion and $-\frac{1}{2}$ when the directions are opposite. Unfortunately, helicity is not a well-defined intrinsic property of all particles. For massive particles, which necessarily travel at speeds lower than c, one can always boost through a Lorentz transformation to a reference frame in which the direction of movement is the opposite to the original frame. Therefore helicity is not Lorentz-invariant for massive particles, even if it is for massless ones.

A closely related quantity, chirality, is Lorentz invariant. The respective operator is the fifth Dirac matrix, γ_5, with eigenvalues $+1$ and -1 corresponding to the so-called right- and left-handed eigenstates, respectively. Chirality is an instrinic property of the Dirac four component bi-spinors, denoted by ψ, which describe the evolution of massive fermions and anti-fermions. One can recover the left- and right-handed chiral states by applying the respective chirality projectors, both denoted by a subindex with the initial of the handedness[2] as

$$\psi_L = P_L\psi = \frac{1}{2}(1-\gamma_5)\psi, \qquad \psi_R = P_R\psi = \frac{1}{2}(1+\gamma_5)\psi, \tag{1.2}$$

while the conjugated states transform similarly,

$$\bar{\psi}_L = \bar{\psi}P_R = \bar{\psi}\frac{1}{2}(1+\gamma_5), \qquad \bar{\psi}_R = \bar{\psi}P_L = \bar{\psi}\frac{1}{2}(1-\gamma_5). \tag{1.3}$$

Being projectors, the application of P_L over ψ_R returns the null state, $P_L\psi_R = 0$, with the same result switching the handedness of the state and the projector. Likewise, applying the same handedness projector repeatedly gives the same result as with the first application , $P_L\psi_L = P_LP_L\psi = \psi_L$ and viceversa.

Chirality is an important property to understand the Standard Model of particle physics, since several properties depend on it. Most notably, the

[2]I.e. L for left- and R for right-handed projectors and spinors.

charged weak interaction only affects left-handed chiral states. From this point forward, subindices R or L refer to the chirality (or handedness) of the states being discussed.

1.2 The Standard Model

The Standard Model (SM) is a gauge theory [2, 3] based on the symmetry group

$$SU(3)_C \otimes SU(2)_L \otimes U(1)_Y, \tag{1.4}$$

where $SU(3)_C$ describes the strong interaction via the exchange of eight massless gluons, g; and $SU(2)_L \otimes U(1)_Y$ include the weak interaction which proceeds with the exchange of three massive bosons, the $W^{\pm}$ and Z; and the electromagnetic interaction proceeding via photon, γ, exchange. C and Y represent the *colour* and *weak hypercharge* generators, respectively, whereas L denotes that weak interactions are left-handed.

The gauge symmetry is broken by the vacuum in what is called the Spontaneous Symmetry Breaking (SSB) mechanism, unifying the $SU(2)_L$ and $U(1)_Y$ groups into the electroweak group

$$SU(3)_C \otimes SU(2)_L \otimes U(1)_Y \xrightarrow{\text{SSB}} SU(3)_C \otimes U(1)_Q. \tag{1.5}$$

This mechanism gives rise to the masses of the weak gauge bosons and fermions and provokes the appearance of a scalar particle, the Higgs. In the SM, forces are mediated through the exchange of gauge bosons. The eight gluons carry the strong interaction, while the three weak bosons and the photon carry the electroweak interaction. The SM bosons are listed in Table 1.1

Fermions are spin-$\frac{1}{2}$ particles. They comprise the known leptons and quarks, organized in three distinct families:

$$\begin{bmatrix} \nu_e & u' \\ e^- & d \end{bmatrix}, \begin{bmatrix} \nu_\mu & c' \\ \mu^- & s \end{bmatrix}, \begin{bmatrix} \nu_\tau & t' \\ \tau^- & b \end{bmatrix}, \tag{1.6}$$

where

$$\begin{bmatrix} \nu_\ell & q_u \\ \ell^- & q_d \end{bmatrix} \equiv \begin{pmatrix} \nu_\ell \\ \ell^- \end{pmatrix}_L, \begin{pmatrix} q_u \\ q_d \end{pmatrix}_L, \ell^-_R, q_{uR}, q_{dR}, \tag{1.7}$$

plus the corresponding anti-fermions.

Table 1.1: SM bosons. Masses are taken from [4].

Boson	Symbol	Mass (GeV/c^2)	Force carried
Photon	γ	0	Electromagnetic interaction
Weak bosons	$W^{\pm}$	80.385 ± 0.015	Charged weak interaction
	Z	91.1876 ± 0.0021	Neutral weak interaction
Gluons	g	0	Strong interaction
Higgs	H	$125.09 \pm 0.21 \pm 0.11$	

Therefore, left-handed fields are $SU(2)_L$ doublets, while their right-handed partners are singlets of the same symmetry group. Worthy of note is the exclusion of right-handed neutrinos from the SM, causing them to be strictly massless. The three fermionic families behave identically under gauge interactions, but they have different masses and flavour quantum numbers. Quarks are distinguished as being *up*- or *down*-type regarding their positive or negative electrical charge, respectively. All of the SM fermions along with their properties are listed in Table 1.2.

Quarks are forbidden from appearing as isolated particles due to the colour confinement mechanism; and always observed to occur in quark triplets, called baryons, or quark anti-quark pairs, called mesons. Theoretically, states with four or five quarks called tetraquarks and pentaquarks are not forbidden. Absolute experimental confirmation of these states is lacking, but recent results indicate promising candidates [6, 7]. Known examples of baryons are the proton and neutron, with quark compositions uud and udd, respectively. Examples of mesons that will appear extensively throughout this text are the B_s^0 ($\bar{b}s$), B^0 ($\bar{b}d$), $\phi(1020)$ ($s\bar{s}$) and $K^{*0}(892)$ ($\bar{s}d$), with their quark composition indicated in parentheses.

1.3 Structure of the SM

The Lagrangian that describes the SM, this is, all the fundamental interactions except for gravity, can be summarized as

$$\mathcal{L}_{\mathrm{SM}} = \mathcal{L}_{\mathrm{EW}} + \mathcal{L}_{\mathrm{QCD}} + \mathcal{L}_{\mathrm{Higgs}} + \mathcal{L}_{\mathrm{Yukawa}}. \tag{1.8}$$

It arises as the combination of the Electroweak (EW) and Quantum Chromodynamics (QCD) Lagrangians that describe the fundamental inter-

Table 1.2: SM fermions, omitting their corresponding antiparticles for simplicity. All values are taken from [4]. The electron and muon masses have been measured with a precision better than 1 ppm. Anti-particles have the same mass but the opposite charge. Their electric charge, Q, is given in units of the positron charge $e = 1.60217 \times 10^{-19}$ C. Upper limits on the neutrino masses are given, as their masses are unknown. Cosmological evidence imposes $\sum m_\nu < 0.44$ eV (95% CL) [5]. I_3 is the third component of weak isospin, strictly conserved in weak interactions.

	Name	Symbol	$Q(e)$	Y	I_3	Mass (MeV/c^2)
Quarks	up	u	$+2/3$	$1/3$	$1/2$	$2.3^{+0.7}_{-0.5}$
	down	d	$-1/3$	$1/3$	$-1/2$	$4.8^{+0.7}_{-0.3}$
	charm	c	$+2/3$	$1/3$	$1/2$	1275 ± 25
	strange	s	$-1/3$	$1/3$	$-1/2$	95 ± 5
	top	t	$+2/3$	$1/3$	$1/2$	$(173.34 \pm 0.51 \pm 0.71) \times 10^3$
	bottom	b	$-1/3$	$1/3$	$-1/2$	4780 ± 60
Leptons	electron	e^-	-1	-1	$1/2$	0.511
	electron neutrino	ν_e	0	-1	$-1/2$	$< 2.05 \times 10^{-6}$ (95% CL)
	mu	μ^-	-1	-1	$1/2$	105.7
	muon neutrino	ν_μ	0	-1	$-1/2$	< 0.19 (90% CL)
	tau	τ^-	-1	-1	$1/2$	1776.86 ± 0.12
	tau neutrino	ν_τ	0	-1	$-1/2$	< 18.2 (95% CL)

actions, plus the terms for the Higgs potential and the fermion masses (Yukawa). It is built upon the foundation of relativistic Quantum Field Theory, which embeds the dynamical framework of quantum theory within the space-time structure of special relativity. The theory must follow the principle of local gauge invariance.

1.3.1 Local gauge invariance

Consider a free Dirac fermion field $\psi(x)$ governed by the Lagrangian

$$\mathcal{L}_0 = i\bar{\psi}\gamma^\mu \partial_\mu \psi - m\bar{\psi}\psi, \tag{1.9}$$

that can be transformed under $U(1)$ by

$$\psi \longrightarrow \psi' = e^{iT\alpha}\psi, \tag{1.10}$$

where T is the generator of a Lie algebra group and α a real-valued arbitrary phase associated to it. α might be constant, in which case the transformation is said to be *global*, or it may depend on the space-time coordinates, $\alpha = \alpha(x_\mu)$, in which case it is a *local* gauge transformation.

The transformation of $\mathcal{L}_0$ by Eq. (1.10) gives rise to a term that vanishes in the case of global transformations but not local ones, losing its invariance under the latter.

The introduction of an additional *gauge field* A_μ allows the definition of a *covariant derivative*, D_μ, to replace the partial derivative ∂_μ in Eq. (1.9) in order to preserve the invariance,

$$D_\mu \psi \equiv [\partial_\mu + igTA_\mu]\psi, \tag{1.11}$$

where g is a constant that determines the strength of the coupling. The new gauge fields transform as

$$A_\mu \longrightarrow (A_\mu)' \equiv A_\mu - \frac{1}{g}\partial_\mu \alpha, \tag{1.12}$$

cancelling the unwanted terms and thus preserving the invariance.

1.3.2 The Standard Model Lagrangian

Interactions in the SM can be divided in their different components, namely an Electroweak (EW) part and a Quantum Chromodynamics (QCD) part.

The EW theory is a non-abelian[3] theory based on the symmetry group $SU(2)_L \times U(1)_Y$ describing the electromagnetic and weak interactions between quarks and leptons. In addition to the three generators associated to $SU(2)$, which are $I_\pm$ and I_3, the weak hypercharge $Y \equiv 2(Q - I_3)$, where Q is the electric charge, is introduced to accommodate the difference between the electric charges for the left-handed doublets. The four generators, I_1, I_2, I_3 and Y are associated to four gauge fields, $\mathbf{W} = (W_\mu^1, W_\mu^2, W_\mu^3)$ and B_μ, respectively.

QCD is the theory that describes the strong interactions between quarks. It is based on the symmetry group $SU(3)_C$, where C makes reference to the colour quantum numbers it introduces. There are eight generators associated to $SU(3)_C$, $\lambda^a/2, a = 1, 2, \ldots, 8$, and therefore eight gauge fields, $G_\mu^a, a = 1, 2, \ldots, 8$, corresponding to the gluons.

[3] A group G is said to be non-abelian if at least one pair of elements of G do not commute.

Let the corresponding field strengths be defined as:

$$B_{\mu\nu} = \partial_\mu B_\nu - \partial_\nu B_\mu, \tag{1.13}$$

$$W^i_{\mu\nu} = \partial_\mu W^i_\nu - \partial_\nu W^i_\mu + g_{\mathrm{w}} \epsilon^{ijk} W^j_\mu W^k_\nu, \quad i = 1,2,3, \tag{1.14}$$

$$G^a_{\mu\nu} = \partial_\mu G^a_\nu - \partial_\nu G^a_\mu - g_s f^{abc} G^b_\mu G^c_\nu, \quad a = 1,2,\ldots,8, \tag{1.15}$$

where ϵ^{ijk} and f^{abc} are the $SU(2)_L$ and $SU(3)_C$ structure constants arising from the non-abelian nature of the groups, respectively; g_{w} and g_s are the coupling constants for their corresponding interactions. From these, the following Lagrangian can be written:

$$\mathcal{L} = -\frac{1}{4}\left[B_{\mu\nu}B^{\mu\nu} + W^i_{\mu\nu}W^{i\mu\nu} + G^a_{\mu\nu}G^{a\mu\nu}\right], \tag{1.16}$$

where again due to the non-abelian groups, self interaction terms for their corresponding fields V_μ (either G_μ or W_μ) appear:

$$\text{Triple gauge boson coupling} = ig\mathrm{Tr}\left\{(\partial_\nu V_\mu - \partial_\mu V_\nu)[V_\mu, V_\nu]\right\}, \tag{1.17}$$

$$\text{Quadruple gauge boson coupling} = \frac{g^2}{2}\mathrm{Tr}\left\{[V_\mu, V_\nu][V_\nu, V_\mu]\right\}. \tag{1.18}$$

The covariant derivatives must be introduced as defined in Eq. (1.11) to preserve invariance of the Lagrangian. The associated generators for each symmetry group are the hypercharge generator Y_q for $U(1)_Y$, the three, two-dimensional Pauli matrices σ_i for $SU(2)_L$, and the eight, three-dimensional Gell-Mann matrices λ_i for $SU(3)_C$. The covariant derivative is therefore

$$D_\mu\psi = \left(\partial_\mu - i\frac{g_s}{2}\lambda_a G^a_\mu - i\frac{g_{\mathrm{w}}}{2}\sigma_i W^i_\mu - i\frac{g}{2}Y_q B_\mu\right)\psi. \tag{1.19}$$

In the Lagrangian, the covariant derivative gives rise to fermion-gauge boson couplings in the form of $-g_i\bar{\psi}V_\mu\gamma^\mu\psi$. The two possible chiralities, right- and left-handedness, of the fermion fields interact differently with the gauge fields, as they sit in different representations of the group. Namely, left-handed fermions are weak isodoublets with $I_3 = +1/2$ and the right-handed fields are weak isosinglets with $I_3 = 0$, as shown in Eq. (1.7). Also, leptons are singlets in $SU(3)_C$, owing to the fact that they do not participate in the strong interaction.

The fermion kinetic energy terms can be written, ignoring the fermion masses for the time being, as

$$\mathcal{L}_{\mathrm{Kin}} = \bar{\mathbb{L}}_L i\not{D}\mathbb{L}_L + \bar{\mathbb{Q}}_L i\not{D}\mathbb{Q}_L + \bar{q}_{u_R} i\not{D} q_{u_R} + \bar{q}_{d_R} i\not{D} q_{d_R} + \bar{\ell}_R i\not{D}\ell_R, \tag{1.20}$$

where $\mathbb{L}_L$ and $\mathbb{Q}_L$ are the left-handed lepton and quark weak isodoublets, and the sum over all the fermion flavour families is implied. $\not{D}$ is the covariant derivative D_μ with zero couplings for the terms that don't affect the corresponding fields, for example leptons have no $\lambda_a G^a_\mu$ term, being singlets under $SU(3)_C$.

Spontaneous Symmetry Breaking (SSB)

So far, the EW part of the SM Lagrangian can be written explicitly as

$$\begin{aligned}\mathcal{L}_{\text{EW}} = &-\frac{1}{4}B_{\mu\nu}B^{\mu\nu} - \frac{1}{4}W^i_{\mu\nu}W^{i\mu\nu} \\ &+\bar{\mathbb{L}}_L\gamma^\mu\left(\partial_\mu - i\frac{g_{\text{w}}}{2}\sigma_i W^i_\mu - i\frac{g}{2}Y^L_\ell B_\mu\right)\mathbb{L}_L + \bar{\ell}_R\gamma^\mu\left(\partial_\mu - i\frac{g}{2}Y^R_\ell B_\mu\right)\ell_R \\ &+\bar{\mathbb{Q}}_L\gamma^\mu\left(\partial_\mu - i\frac{g_{\text{w}}}{2}\sigma_i W^i_\mu - i\frac{g}{2}Y^L_q B_\mu\right)\mathbb{Q}_L + \bar{q_u}_R\gamma^\mu\left(\partial_\mu - i\frac{g}{2}Y^R_u B_\mu\right)q_{u_R} \\ &+\bar{q_d}_R\gamma^\mu\left(\partial_\mu - i\frac{g}{2}Y^R_d B_\mu\right)q_{d_R},\end{aligned} \tag{1.21}$$

which describes a gauge theory of massless bosons and fermions and their interactions. The different hypercharges correspond to the particular generators for left and right-handed chiralities of leptons, $Y^{L,R}_l$; left-handed quarks, Y^L_q; and right-handed up- and down-type quarks, $Y^R_{u,d}$.

Introducing mass terms for the $W^\pm$ and Z bosons directly in the Lagrangian would violate the gauge symmetry so carefully built. The *Higgs mechanism*[4] solves this problem, allowing the creation of massive gauge bosons through the introduction of an additional scalar field, the Higgs field, which has a non-zero vacuum expectation value, meaning that it doesn't vanish at the lowest possible energy state [8–10]. This complex, colourless field, ϕ, is a doublet under $SU(2)_L$, with hypercharge $Y_\Phi = 1$:

$$\Phi = \begin{pmatrix}\phi^+ \\ \phi^0\end{pmatrix}. \tag{1.22}$$

In order to preserve invariance, it also follows the covariant derivative, thus

$$\mathcal{L}_{\text{Higgs}} = \left|\left(\partial_\mu - i\frac{g_{\text{w}}}{2}\sigma_i W^i_\mu - i\frac{g}{2}Y_\Phi B_\mu\right)\Phi\right|^2 - V(\Phi), \tag{1.23}$$

[4]Most known and shortest form of naming the Englert–Brout–Higgs–Guralnik–Hagen–Kibble mechanism.

where the Higgs potential $V(\Phi)$ has minimums at non-zero values of the field itself,

$$V(\Phi) = \mu^2(\Phi^\dagger\Phi) + h(\Phi^\dagger\Phi)^2, \tag{1.24}$$

where $\mu^2 < 0$ and $h > 0$. There is an infinite set of degenerate states with minimum energy satisfying

$$\langle 0|\, \phi^0 \,|0\rangle = \sqrt{-\frac{\mu^2}{2h}} \equiv \frac{v}{\sqrt{2}}, \tag{1.25}$$

where v is the desired non-zero vacuum expectation value of the neutral scalar. Since the electric charge is conserved, the vacuum expectation value of ϕ^+ must vanish.

Once a particular state belonging to the aforementioned set is chosen by the system, the $SU(2)_L \otimes U(1)_Y$ symmetry is spontaneously broken to the electromagnetic group $U(1)_Q$, which remains a true symmetry of the vacuum:

$$SU(2)_L \otimes U(1)_Y \xrightarrow{\text{SSB}} U(1)_{\text{Q}}. \tag{1.26}$$

The scalar doublet can then be parametrized as

$$\Phi = U(x)\frac{1}{\sqrt{2}}\begin{pmatrix} 0 \\ v + H(x) \end{pmatrix}, \tag{1.27}$$

where $U(x)$ is an arbitrary $SU(2)$ gauge transformation that allows to produce the most general complex-valued spinor field and $H(x)$ is the so-called Brout-Engler-Higgs boson field itself. It is a fluctuating real field with $\langle H(x)\rangle = 0$.

Expanding the derivative in Eq. (1.23) in terms of the Higgs doublet, the mass eigenstates that arise correspond to the electroweak boson fields $W^\pm_\mu$, Z_μ and A_μ:

$$W^\pm_\mu = \frac{1}{\sqrt{2}}(W^1_\mu \mp W^2_\mu), \qquad m_W = \frac{1}{2}v g_{\text{w}}, \tag{1.28}$$

$$Z_\mu = \frac{g_{\text{w}}W^3_\mu - gB_\mu}{\sqrt{g^2_{\text{w}} + g^2}}, \qquad m_Z = \frac{v}{2}\sqrt{g^2_{\text{w}} + g^2}, \tag{1.29}$$

$$A_\mu = \frac{g_{\text{w}}W^3_\mu + gB_\mu}{\sqrt{g^2_{\text{w}} + g^2}}, \qquad m_A = 0. \tag{1.30}$$

These fields correspond to the three massive weak bosons, $W^\pm$ and Z, and the massless photon, γ (A_μ).

Expanding the Higgs potential from Eq. (1.24) in terms of the parametrization from Eq. (1.27),

$$\mathcal{L}_{V(\Phi)} = -hv^2H^2 - hvH^3 - \frac{1}{4}hH^4, \tag{1.31}$$

the field itself acquires a mass of $m_H^2 = 2hv^2 = -2\mu^2$.

Simple fermion mass terms of the form $-m_l(\bar{\psi}_L\psi_R + \bar{\psi}_R\psi_L)$ are forbidden due to the different chiralities belonging to different $SU(2)$ representations and having different $U(1)$ charges. The introduction of these terms would therefore explicitly violate gauge invariance. Fortunately, the SSB mechanism can also solve this, introducing the Higgs field in terms of the form

$$\mathcal{L}_m = -\frac{1}{\sqrt{2}}\lambda_i\bar{\Psi}^i_L\Phi\psi^i_R + \text{h.c.}, \tag{1.32}$$

since the indices of the left-handed fermion doublet, Ψ_L, and the Higgs doublet are contracted, allowing mixed chirality terms. In the previous equation λ_i is a dimensionless coupling constant. Under the Higgs field parametrization from Eq. (1.27) and choosing the unitary gauge, $U(x) = \mathcal{I}$,

$$\mathcal{L}_m = -\frac{1}{\sqrt{2}}\lambda_i v\bar{\psi}^i_L\psi^i_R + \text{h.c.} + \ldots, \tag{1.33}$$

where each of the fermion fields ψ^i acquires a mass term of the form

$$m_i = \frac{\lambda_i v}{\sqrt{2}}. \tag{1.34}$$

This holds true for both leptons and quarks.

The CKM Matrix

The mass eigenstates obtained for the quarks in the previous section are not the same as the flavour eigenstates. The up- and down-type quarks in the flavour basis can be expressed as

$$u^i_L = (u_L, c_L, t_L), \quad d^i_L = (d_L, s_L, b_L), \tag{1.35}$$

and in the mass-diagonal basis with their primed counterparts as

$$u'^i_L = (u'_L, c'_L, t'_L), \quad d'^i_L = (d'_L, s'_L, b'_L). \tag{1.36}$$

The two bases are related by unitary transformations:

$$u_L^i = \mathbf{U}_u^{ij} u_L'^j, \quad d_L^i = \mathbf{U}_d^{ij} d_L'^j. \tag{1.37}$$

Then, the charged current can be expressed in terms of the mass eigenstates:

$$\frac{1}{\sqrt{2}} \bar{u}_L^i \gamma^\mu d_L^j W_\mu^+ = \frac{1}{\sqrt{2}} \bar{u'}_L^i \gamma^\mu \mathbf{U}_u^{ik\dagger} \mathbf{U}_d^{kj} d'^j_L W_\mu^+, \tag{1.38}$$

where the $\mathbf{U}_u^{ik\dagger}\mathbf{U}_d^{kj}$ term can be compacted into a $\mathbf{V}_{ij}$ matrix. This matrix is the Cabibbo-Kobayashi-Maskawa (CKM) matrix, $\mathbf{V}_{\text{CKM}}$ [11], and it allows charged currents to transition from flavours of different families, as it isn't diagonal in the mass eigenstate basis. Eq. (1.38) can be written explicitly in terms of this matrix as

$$\frac{1}{\sqrt{2}} \bar{u}_L^i \gamma^\mu d_L^j W_\mu^+ = \frac{1}{\sqrt{2}} \begin{pmatrix} \bar{u'}_L & \bar{c'}_L & \bar{t'}_L \end{pmatrix} \gamma^\mu \begin{pmatrix} V_{ud} & V_{us} & V_{ub} \\ V_{cd} & V_{cs} & V_{cb} \\ V_{td} & V_{ts} & V_{tb} \end{pmatrix} \begin{pmatrix} d'_L \\ s'_L \\ b'_L \end{pmatrix} W_\mu^+, \tag{1.39}$$

which is also valid in the case of W_μ^-. The matrix elements are complex and there are in general 18 parameters. Since the matrix is unitary, $\mathbf{V}_{\text{CKM}}\mathbf{V}_{\text{CKM}}^\dagger = 1$, conditions for the individual terms arise as

$$\sum_{k=1}^{3} V_{ki}^* V_{kj} = \delta_{ij}, \tag{1.40}$$

reducing the number of independent parameters to nine. Of these, phase terms can be absorbed by the six quark fields, but a global phase must be kept. This leaves four independent parameters, one of which is the aforementioned phase, δ, and the rest are rotation angles, called the quark-mixing angles θ_{ij}. In these terms, the matrix can be written as an Euler rotation around three axes [12], as

$$\mathbf{V}_{\text{CKM}} = \begin{pmatrix} c_{12}c_{23} & s_{12}c_{13} & s_{13}e^{-i\delta} \\ -s_{12}c_{23} - c_{12}s_{23}s_{13}e^{i\delta} & c_{12}c_{23} - s_{12}s_{23}s_{13}e^{i\delta} & s_{23}c_{13} \\ s_{12}s_{23} - c_{12}c_{23}s_{13}e^{i\delta} & -c_{12}s_{23} - s_{12}c_{23}s_{13}e^{i\delta} & c_{23}c_{13} \end{pmatrix}, \tag{1.41}$$

where c_{ij} and s_{ij} stand for $\cos\theta_{ij}$ and $\sin\theta_{ij}$, respectively. The terms in the CKM matrix scale the weak interactions[5] between quarks of different families. The interactions between members of a same family are quite more

[5] Which share a universal coupling constant, g_{W}.

favourable than the cross-family interactions. This is more evident under the Wolfenstein parametrization of the CKM matrix [13], where the terms are written as an expansion on $\sin\theta_{12}$. Defining the λ, A, ρ and η parameters as

$$\lambda = \sin\theta_{12}, \tag{1.42}$$

$$A = \frac{\sin\theta_{23}}{(\sin\theta_{12})^2}, \tag{1.43}$$

$$\rho = \frac{\sin\theta_{13}\cos\delta}{\sin\theta_{12}\sin\theta_{23}}, \tag{1.44}$$

$$\eta = \frac{\sin\theta_{13}\sin\delta}{\sin\theta_{12}\sin\theta_{23}}, \tag{1.45}$$

which are all real and $\sim \mathcal{O}(0.1)$, the matrix can be expanded in their terms up to $\mathcal{O}(\lambda^3)$,

$$\mathbf{V}_{\text{CKM}} = \begin{pmatrix} 1-\frac{\lambda^2}{2} & \lambda & A\lambda^3(\rho - i\eta) \\ -\lambda & 1-\frac{\lambda^2}{2} & A\lambda^2 \\ A\lambda^3(1-\rho-i\eta) & -A\lambda^2 & 1 \end{pmatrix} + \mathcal{O}(\lambda^4). \tag{1.46}$$

From the unitarity relations in Eq. (1.40), the so-called *unitarity triangles* can be built. For example, the relation

$$V_{ud}V_{ub}^* + V_{cd}V_{cb}^* + V_{td}V_{tb}^* = 0 \tag{1.47}$$

holds under unitarity. Since measurements of the V_{ij} elements are independent of this condition, these factors can be represented as a sum of complex-plane vectors, forming closed triangles if unitarity is held. The triangle corresponding to Eq. (1.47) is pictured in Figure 1.1, where the sides are divided by $V_{cd}^*V_{cb}$ and the inner angles are defined as

$$\alpha \equiv \arg\left(-\frac{V_{td}V_{tb}^*}{V_{cd}V_{cb}^*}\right), \tag{1.48}$$

$$\beta \equiv \arg\left(-\frac{V_{cd}V_{cb}^*}{V_{td}V_{tb}^*}\right), \tag{1.49}$$

$$\gamma \equiv \arg\left(-\frac{V_{ud}V_{ub}^*}{V_{cd}V_{cb}^*}\right). \tag{1.50}$$

The three vertices are therefore placed in the complex plane at $(0,0)$, $(1,0)$ and

$$\bar{\rho} + i\bar{\eta} = -\frac{V_{ud}V_{ub}^*}{V_{cd}V_{cb}^*}. \tag{1.51}$$

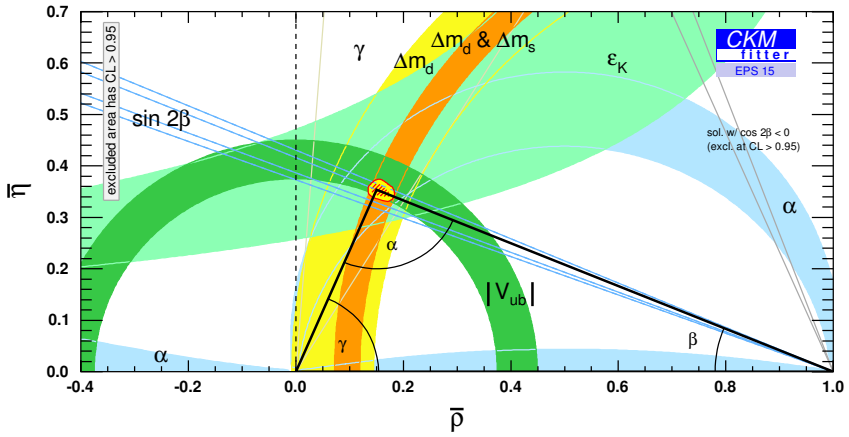

Figure 1.1: Current status of the unitarity triangle determination obtained through combination of available experimental data by the CKMFitter collaboration [14].

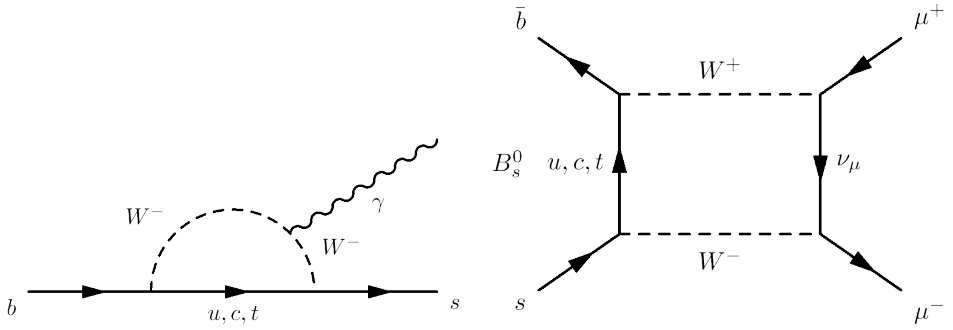

Figure 1.2: Effective flavour changing neutral current (FCNC) processes. The left one is the loop diagram that corresponds to the $b \to s\gamma$ transition, while the right one is a box diagram which describes the $B_s^0 \to \mu^+\mu^-$ decay.

It is important to note that the CKM matrix elements only come into play in weak charged currents, this is, with the $W^\pm$ bosons. The weak neutral interaction is described by the couplings of the quarks to the Z boson, and these are flavour-diagonal by definition, with terms of the form $\bar{q_{u_L}}\gamma^\mu q_{u_L} Z_\mu$. This implies that there are no *Flavour Changing Neutral Currents* (FCNC) at first order. Nevertheless, effective FCNC may arise as higher order processes. These are described in Feynman diagram notation with loop diagrams, as the ones pictured in Figure 1.2.

1.3.3 Discrete symmetries

The symmetry properties of a physical system are intimately related to the conservation laws characterizing that system. Noether's theorem [15] gives a precise description of this relation. The theorem states that each symmetry of a physical system implies that some physical property of that system is conserved. Conversely, each conserved quantity has a corresponding symmetry. Examples are the isometry of space giving rise to conservation of momentum, and the $U(1)$ gauge invariance relation to the conservation of electric charge, among others.

Discrete symmetries[6] describe non-continuous changes in a physical system. A few are of special interest in relation to the SM, namely Parity (P), Time reversal (T) and Charge conjugation (C). Consider a particle of momentum $\vec{p}$ and spin $\vec{s}$ represented by the state $|\vec{p}, h, \chi\rangle$ where $h = \vec{s} \cdot \vec{p}/|\vec{p}|$ is its helicity and χ accounts for its internal quantum numbers. The aforementioned discrete symmetries are defined as follows:

Parity
The spatial coordinates are simultaneously inverted, $P : (x, y, z) \to (-x, -y, -z)$, and the particle transforms as:

$$P|\vec{p}, h, \chi\rangle \to |-\vec{p}, -h, \chi\rangle. \tag{1.52}$$

Time Reversal
The time coordinate is reverted, $T : t \to -t$, and the particle transforms as:

$$T|\vec{p}, h, \chi\rangle \to |-\vec{p}, h, \chi\rangle^*. \tag{1.53}$$

Charge Conjugation
The particle's quantum numbers are inverted, effectively interchanging the particle for its antiparticle:

$$C|\vec{p}, h, \chi\rangle \to |\vec{p}, h, \bar{\chi}\rangle. \tag{1.54}$$

Since a second application of any same operator returns the original state up to an unobservable global phase, the eigenvalues of P and C can only be complex phases. A particle can be, but not necessarily, in an eigenstate of P if it is at rest. The corresponding eigenvalue is called intrinsic parity. Only completely neutral particles, namely with $\chi = 0$, can be eigenstates of

[6] As opposed to continuous symmetries.

C. In this case, the particle coincides with its antiparticle. Unlike P and C, there is no time reversal eigenvalue, because the T operator is antiunitary.

The product of all three symmetries, CPT, is known to be a fundamental symmetry of any Lorentz invariant local quantum field theory with a Hermitian Hamiltonian [16,17], such as the SM. It is, by definition, an exact symmetry of the theory.

The three symmetries, individually, are preserved by the strong and electromagnetic forces, but in charged-current weak interactions, the C- and P- symmetries are maximally violated, as confirmed by experimental data [18–20]. To preserve the symmetry of the system, it was proposed that the combined CP symmetry was exact for all the interactions [21], but later experimental results found that this was also violated [22]. The CKM matrix accounts for this through the δ complex phase. It is worthy noting that since CPT must be conserved, CP violation implies that T symmetry is also broken, a prediction corroborated by experiment [23].

1.4 Radiative $B^0_{(S)}$ decays in the SM

Neutral B decays are specially interesting subjects of study, since b quarks always decay through flavour changing currents involving the non-diagonal elements of the CKM matrix. Furthermore, they exhibit neutral meson oscillation, which allows access to studies of time-dependent CP-violating parameters among other observables. This makes them strong probes for BSM contributions as well as powerful tools for precise determination of SM parameters.

1.4.1 Neutral meson oscillation

Neutral meson mixing has been observed in the K^0, D^0, B^0, and B^0_s systems. The formalism described in this section applies generally to any of these cases [24]. These processes are represented by box diagrams at leading order, like the ones pictured in Figure 1.3 for the case of B^0_s mesons.

Considering any neutral self-conjugate pair of flavour meson eigenstates $\left|B^0\right\rangle$ and $\left|\bar{B}^0\right\rangle$, an arbitrary linear combination of the flavour eigenstates can be written as

$$a\left|B^0\right\rangle + b\left|\bar{B}^0\right\rangle, \tag{1.55}$$

with a and b two complex parameters. The time evolution of this combined

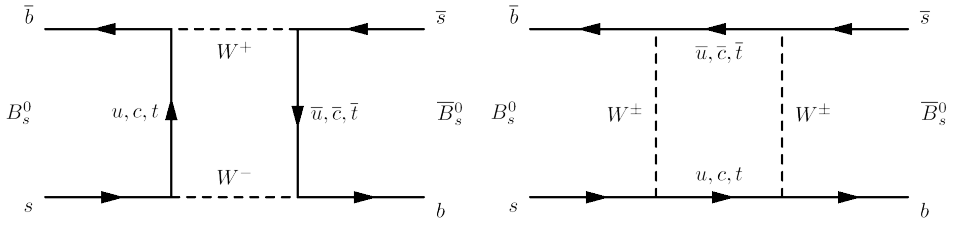

Figure 1.3: Leading order B^0_s meson mixing Feynman diagrams. The corresponding diagrams for the B^0 system are obtained by changing the s quark with a d quark.

state will follow the time-dependent Schrödinger equation

$$i\frac{\mathrm{d}}{\mathrm{dt}}\begin{pmatrix} a \\ b \end{pmatrix} = \mathcal{H}\begin{pmatrix} a \\ b \end{pmatrix} \equiv \left(\mathbf{M} - \frac{i}{2}\mathbf{\Gamma}\right)\begin{pmatrix} a \\ b \end{pmatrix}, \tag{1.56}$$

where $\mathbf{M}$ and $\mathbf{\Gamma}$ are two 2×2 hermitian matrices representing the masses and lifetimes of the states. CPT invariance ensures that the diagonal elements of these matrices are equal, hence the mass and lifetime of a particle are the same as its antiparticle's:

$$M_{11} = M_{22} \equiv m, \quad \Gamma_{11} = \Gamma_{22} \equiv \Gamma. \tag{1.57}$$

As discussed in Section 1.3.2, the mass eigenstates differ from the flavour eigenstates. The former are the eigenstates of $\mathcal{H}$ and can be written in terms of the latter,

$$\begin{aligned} |B_L\rangle &= p\left|B^0\right\rangle + q\left|\bar{B}^0\right\rangle, \\ |B_H\rangle &= p\left|B^0\right\rangle - q\left|\bar{B}^0\right\rangle, \end{aligned} \tag{1.58}$$

where the subindices L and H refer respectively to the light- and heavy-mass eigenstates. The complex parameters p and q are normalized through

$$|p|^2 + |q|^2 = 1. \tag{1.59}$$

The eigenvalues $E_{1,2}$ of $\mathcal{H}$ are found by solving the characteristic equation

$$\mathcal{H} - \mathbf{E}\mathbf{I}_{2\times 2} = 0, \tag{1.60}$$

and their values are

$$E_j = m - \frac{i}{2}\Gamma \pm \sqrt{\left(M_{12} - \tfrac{i}{2}\Gamma_{12}\right)\left(M^*_{12} - \tfrac{i}{2}\Gamma^*_{12}\right)} \equiv m_j - \frac{i}{2}\Gamma_j, \tag{1.61}$$

where the subscript $j = H, L$ for the positive and negative solutions, respectively. Since the eigenvectors take the forms $\begin{pmatrix} p \\ \pm q \end{pmatrix}$,

$$(\mathcal{H} - \mathbf{EI}_{2\times 2}) \begin{pmatrix} p \\ \pm q \end{pmatrix} = 0, \tag{1.62}$$

which leads to the relation

$$\frac{q}{p} = \sqrt{\frac{M_{12}^* - \frac{i}{2}\Gamma_{12}^*}{M_{12} - \frac{i}{2}\Gamma_{12}}}\,. \tag{1.63}$$

The time evolution of the $|B_L\rangle$ and $|B_H\rangle$ states is described by

$$\begin{aligned} |B_L(t)\rangle &= e^{-i\left(m_L - \frac{i}{2}\Gamma_L\right)t} |B_L\rangle\,, \\ |B_H(t)\rangle &= e^{-i\left(m_H - \frac{i}{2}\Gamma_H\right)t} |B_H\rangle\,, \end{aligned} \tag{1.64}$$

and recovering Eq. (1.58) the time evolution of the flavour eigenstates, $\left|B^0\right\rangle$ and $\left|\bar{B}^0\right\rangle$, can be expressed as

$$\begin{aligned} \left|B^0(t)\right\rangle =& \frac{1}{2}\left[\left(e^{-i\left(m_L - \frac{i}{2}\Gamma_L\right)t} + e^{-i\left(m_H - \frac{i}{2}\Gamma_H\right)t}\right)\left|B^0\right\rangle\right. \\ &\left. + \frac{q}{p}\left(e^{-i\left(m_L - \frac{i}{2}\Gamma_L\right)t} - e^{-i\left(m_H - \frac{i}{2}\Gamma_H\right)t}\right)\left|\bar{B}^0\right\rangle\right] \\ \equiv& h_+(t)\left|B^0\right\rangle + \frac{q}{p}h_-(t)\left|\bar{B}^0\right\rangle, \end{aligned} \tag{1.65}$$

$$\begin{aligned} \left|\bar{B}^0(t)\right\rangle =& \frac{1}{2}\left[\left(e^{-i\left(m_L - \frac{i}{2}\Gamma_L\right)t} + e^{-i\left(m_H - \frac{i}{2}\Gamma_H\right)t}\right)\left|\bar{B}^0\right\rangle\right] \\ &+ \frac{p}{q}\left(e^{-i\left(m_L - \frac{i}{2}\Gamma_L\right)t} - e^{-i\left(m_H - \frac{i}{2}\Gamma_H\right)t}\right)\left|B^0\right\rangle \\ \equiv& h_+(t)\left|\bar{B}^0\right\rangle + \frac{p}{q}h_-(t)\left|B^0\right\rangle, \end{aligned} \tag{1.66}$$

where $h_\pm(t)$ have been introduced to simplify notation. The time evolution of the probability of a state decaying as its original or opposite flavour is therefore

$$\left|\left\langle B^0\middle|B^0(t)\right\rangle\right|^2 = \left|\left\langle \bar{B}^0\middle|\bar{B}^0(t)\right\rangle\right|^2 = \frac{1}{4}\left(e^{-\Gamma_L t} + e^{-\Gamma_H t} + 2e^{-\bar{\Gamma}t}\cos\Delta m t\right), \tag{1.67}$$

$$\left|\frac{p}{q}\right|^2\left|\left\langle \bar{B}^0\middle|B^0(t)\right\rangle\right|^2 = \left|\frac{q}{p}\right|^2\left|\left\langle B^0\middle|\bar{B}^0(t)\right\rangle\right|^2 = \frac{1}{4}\left(e^{-\Gamma_L t} + e^{-\Gamma_H t} - 2e^{-\bar{\Gamma}t}\cos\Delta m t\right), \tag{1.68}$$

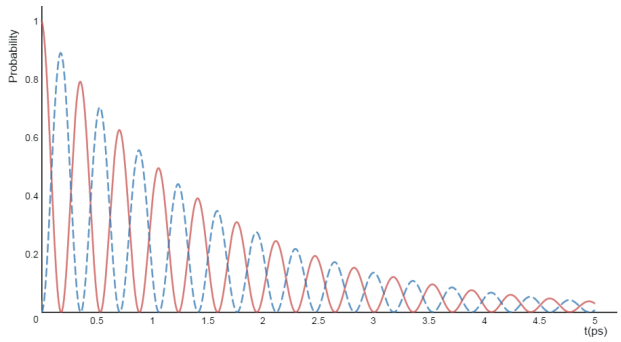

Figure 1.4: Probability of a neutral meson decaying into its original (solid red) or opposite (dashed blue) flavour. The input parameters correspond to the B^0_s meson form [25].

where $\bar{\Gamma} = (\Gamma_L + \Gamma_H)/2$ is the average decay width and $\Delta m = m_H - m_L$ is the difference between the masses of the mass eigenstates. Equations (1.67) and (1.68) imply that the states $\left|B^0\right\rangle$ and $\left|\bar{B}^0\right\rangle$ evolve from an initial pure flavour state into a changing superposition of both its original state and its conjugate, oscillating among them, as shown in Figure 1.4.

The time-dependent decay amplitudes of $\left|B^0\right\rangle$ and $\left|\bar{B}^0\right\rangle$ to a common final *CP* eigenstate[7] $|f\rangle$ can be derived from Eqs. (1.65) and (1.66). They can be expressed as

$$\begin{aligned}\Gamma_f(t) = \left|\left\langle f\middle|\mathcal{H}\middle|B^0(t)\right\rangle\right|^2 = |A_f|^2 \Bigg[&|h_+(t)|^2 + \left|\frac{q}{p}\frac{\bar{A}_f}{A_f}\right|^2 |h_-(t)|^2 \\ &+2\mathrm{Re}\left(h_+^*(t)h_-(t)\frac{q}{p}\frac{\bar{A}_f}{A_f}\right)\Bigg],\end{aligned} \tag{1.69}$$

$$\begin{aligned}\bar{\Gamma}_f(t) = \left|\left\langle f\middle|\mathcal{H}\middle|\bar{B}^0(t)\right\rangle\right|^2 = |A_f|^2 \Bigg[&\left|\frac{\bar{A}_f}{A_f}\right|^2 |h_+(t)|^2 + \left|\frac{p}{q}\right|^2 |h_-(t)|^2 \\ &+2\left|\frac{p}{q}\right|^2 \mathrm{Re}\left(h_+^*(t)h_-(t)\frac{q^*}{p^*}\frac{\bar{A}_f^*}{A_f^*}\right)\Bigg],\end{aligned} \tag{1.70}$$

where $A_f = \langle f|\mathcal{H}|B^0\rangle$ and $\bar{A}_f = \langle f|\mathcal{H}|\bar{B}^0\rangle$ are the instantaneous decay

[7] Meaning that $\bar{f} = f$.

amplitudes. Defining $\lambda_f \equiv \frac{q}{p}\frac{\bar{A}_f}{A_f}$, the previous amplitudes can be written as

$$\begin{aligned}\Gamma_f(t) =& \frac{\left|A_f\right|^2}{2} e^{-\bar{\Gamma}t}\left[\left(1+\left|\lambda_f\right|^2\right)\cosh\left(\frac{\Delta\Gamma}{2}t\right)+2\mathrm{Re}(\lambda_f)\sinh\left(\frac{\Delta\Gamma}{2}t\right)\right.\\ &\left.+\left(1-\left|\lambda_f\right|^2\right)\cos\left(\Delta m t\right)-2\mathrm{Im}(\lambda_f)\sin\left(\Delta m t\right)\right],\end{aligned} \tag{1.71}$$

$$\begin{aligned}\bar{\Gamma}_f(t) =& \frac{\left|A_f\right|^2}{2}\left|\frac{p}{q}\right|^2 e^{-\bar{\Gamma}t}\left[\left(1+\left|\lambda_f\right|^2\right)\cosh\left(\frac{\Delta\Gamma}{2}t\right)+2\mathrm{Re}(\lambda_f)\sinh\left(\frac{\Delta\Gamma}{2}t\right)\right.\\ &\left.-\left(1-\left|\lambda_f\right|^2\right)\cos\left(\Delta m t\right)+2\mathrm{Im}(\lambda_f)\sin\left(\Delta m t\right)\right].\end{aligned} \tag{1.72}$$

A further rewriting of Eqs. (1.71) and (1.72),

$$\begin{aligned}\Gamma_f(t) =& \frac{\left|A_f\right|^2}{2}\left(1+\left|\lambda_f\right|^2\right) e^{-\bar{\Gamma}t}\left[\cosh\left(\frac{\Delta\Gamma}{2}t\right)-\mathcal{A}^{\Delta}\sinh\left(\frac{\Delta\Gamma}{2}t\right)\right.,\\ &\left.+\mathcal{C}\cos\left(\Delta m t\right)-\mathcal{S}\sin\left(\Delta m t\right)\right]\end{aligned} \tag{1.73}$$

$$\begin{aligned}\bar{\Gamma}_f(t) =& \frac{\left|A_f\right|^2}{2}\left|\frac{p}{q}\right|^2\left(1+\left|\lambda_f\right|^2\right) e^{-\bar{\Gamma}t}\left[\cosh\left(\frac{\Delta\Gamma}{2}t\right)-\mathcal{A}^{\Delta}\sinh\left(\frac{\Delta\Gamma}{2}t\right)\right.,\\ &\left.-\mathcal{C}\cos\left(\Delta m t\right)+\mathcal{S}\sin\left(\Delta m t\right)\right]\end{aligned} \tag{1.74}$$

allows to introduce the $\mathcal{A}^{\Delta}$ (sometimes appearing as $\mathcal{H}$ in the literature), $\mathcal{C}$ and $\mathcal{S}$ parameters. These are defined in terms of λ_f as [26]:

$$\mathcal{C} = \frac{1-\left|\lambda_f\right|^2}{1+\left|\lambda_f\right|^2}, \quad \mathcal{S} = \frac{2\mathrm{Im}(\lambda_f)}{1+\left|\lambda_f\right|^2}, \quad \mathcal{A}^{\Delta} = -\frac{2\mathrm{Re}(\lambda_f)}{1+\left|\lambda_f\right|^2}. \tag{1.75}$$

CP violation (CPV) arises as a difference between $\Gamma_f(t)$ and $\bar{\Gamma}_f(t)$, and from the previous equations it can be attributed to different causes:

CPV in decay

The rate of particles decaying into f is different from the rate of the antiparticles decaying into the same state, $\left|\bar{A}_f/A_f\right|^2 \neq 1$.

CPV in mixing
The oscillations favour one of the flavours, $|p/q|^2 \neq 1$.

CPV in the interference
Even if both of the above don't apply, *CP* violation can appear from the interference in decay with and without mixing, if the term $\mathrm{Im}\left(\lambda_f\right) \neq 0$.

To relate the *CP*-violating parameters $\mathcal{C}$, $\mathcal{S}$ and $\mathcal{A}^\Delta$ to the photon polarization one should consider the left- and right-handed photon decay amplitudes, which are defined as

$$A_{L(R)} \equiv A(B \to f\gamma_{L(R)}), \quad \bar{A}_{L(R)} \equiv A(\bar{B} \to f\gamma_{L(R)}). \tag{1.76}$$

The amplitude of an initially pure B^0 state[8] to any of the final polarization states is therefore

$$\left\langle f\gamma_{L(R)} \middle| B^0(t) \right\rangle = A_{L(R)} h_+(t) + \frac{q}{p}\bar{A}_{L(R)} h_-(t), \tag{1.77}$$

and the unpolarized decay rate contains both contributing amplitudes

$$\Gamma_f(t) = \left|\left\langle f\gamma_L \middle| B^0(t) \right\rangle\right|^2 + \left|\left\langle f\gamma_R \middle| B^0(t) \right\rangle\right|^2, \tag{1.78}$$

which, when expanded using Eq. (1.77), yields

$$\begin{aligned}
\Gamma_f(t) &= \left(A_R h_+ + \frac{q}{p}\bar{A}_R h_-\right)\left(A_R^* h_+^* + \frac{q^*}{p^*}\bar{A}_R^* h_-^*\right) + \left(A_L h_+ + \frac{q}{p}\bar{A}_L h_-\right)\left(A_L^* h_+^* + \frac{q^*}{p^*}\bar{A}_L^* h_-^*\right) \\
&= |A_R|^2 |h_+|^2 + \left|\frac{q}{p}\right|^2 |\bar{A}_R|^2 |h_-|^2 + \frac{q^*}{p^*}\bar{A}_R^* A_R h_+ h_-^* + \frac{q}{p}\bar{A}_R A_R^* h_- h_+^* \\
&+ |A_L|^2 |h_+|^2 + \left|\frac{q}{p}\right|^2 |\bar{A}_L|^2 |h_-|^2 + \frac{q^*}{p^*}\bar{A}_L^* A_L h_+ h_-^* + \frac{q}{p}\bar{A}_L A_L^* h_- h_+^*.
\end{aligned} \tag{1.79}$$

Expanding $h_+(t)$ and $h_-(t)$ from Eqs. (1.65) and (1.66), the decay rate takes

[8] This is analogous for the case of a $\bar{B}^0$ meson with identical conclusions, omitted here for brevity.

the form

$$\begin{aligned}\Gamma_f(t) \propto \frac{1}{2}e^{-\Gamma t}\Bigg(&|A_R|^2\left[\cosh\left(\frac{\Delta\Gamma}{2}t\right)+\cos\left(\Delta m t\right)\right]+\left|\frac{q}{p}\right|^2|\bar{A}_R|^2\left[\cosh\left(\frac{\Delta\Gamma}{2}t\right)-\cos\left(\Delta m t\right)\right]\\&-\frac{q^*}{p^*}\bar{A}_R^*A_R\left[\sinh\left(\frac{\Delta\Gamma}{2}t\right)-i\sin\left(\Delta m t\right)\right]-\frac{q}{p}\bar{A}_RA_R^*\left[\sinh\left(\frac{\Delta\Gamma}{2}t\right)+i\sin\left(\Delta m t\right)\right]\\&+|A_L|^2\left[\cosh\left(\frac{\Delta\Gamma}{2}t\right)+\cos\left(\Delta m t\right)\right]+\left|\frac{q}{p}\right|^2|\bar{A}_L|^2\left[\cosh\left(\frac{\Delta\Gamma}{2}t\right)-\cos\left(\Delta m t\right)\right]\\&-\frac{q^*}{p^*}\bar{A}_L^*A_L\left[\sinh\left(\frac{\Delta\Gamma}{2}t\right)-i\sin\left(\Delta m t\right)\right]-\frac{q}{p}\bar{A}_LA_L^*\left[\sinh\left(\frac{\Delta\Gamma}{2}t\right)+i\sin\left(\Delta m t\right)\right]\Bigg).\end{aligned} \tag{1.80}$$

Grouping the trigonometric terms in the above equation, we recover the form of Eq. (1.73),

$$\begin{aligned}\Gamma_f(t) \propto \frac{1}{2}e^{-\Gamma t}\Bigg[&\cosh\left(\frac{\Delta\Gamma}{2}t\right)-\mathcal{A}^\Delta\sinh\left(\frac{\Delta\Gamma}{2}t\right)\\&+\mathcal{C}\cos\left(\Delta m t\right)-\mathcal{S}\sin\left(\Delta m t\right)\Bigg],\end{aligned} \tag{1.81}$$

and analogously for the conjugate

$$\begin{aligned}\bar{\Gamma}_f(t) \propto \frac{1}{2}e^{-\Gamma t}\Bigg[&\cosh\left(\frac{\Delta\Gamma}{2}t\right)-\mathcal{A}^\Delta\sinh\left(\frac{\Delta\Gamma}{2}t\right)\\&-\mathcal{C}\cos\left(\Delta m t\right)+\mathcal{S}\sin\left(\Delta m t\right)\Bigg],\end{aligned} \tag{1.82}$$

with the $\mathcal{A}^\Delta$, $\mathcal{C}$ and $\mathcal{S}$ parameters given in terms of the left- and right-handed photon polarization amplitudes, as

$$C = \frac{\left(|A_L|^2+|A_R|^2\right)-\left(|\bar{A}_L|^2+|\bar{A}_R|^2\right)}{|A_L|^2+|A_R|^2+|\bar{A}_L|^2+|\bar{A}_R|^2}, \tag{1.83}$$

$$S = \frac{2\mathrm{Im}\left[\frac{q}{p}\left(\bar{A}_LA_L^*+\bar{A}_RA_R^*\right)\right]}{|A_L|^2+|A_R|^2+|\bar{A}_L|^2+|\bar{A}_R|^2}, \tag{1.84}$$

$$\mathcal{A}^\Delta = \frac{2\mathrm{Re}\left[\frac{q}{p}\left(\bar{A}_LA_L^*+\bar{A}_RA_R^*\right)\right]}{|A_L|^2+|A_R|^2+|\bar{A}_L|^2+|\bar{A}_R|^2}, \tag{1.85}$$

where it has been assumed that $|p/q|^2 = 1$, as supported by experimental data for B^0 and B^0_s systems [25].

Assuming no direct *CP* violation [27], the different amplitudes can be written in terms of left- and right-handed phases $\phi_{L/R}$, for a self conjugate final state with *CP* eigenvalue $+1$, as

$$\begin{aligned} \bar{A}_L &= A\cos\psi e^{i\phi_L}, \\ \bar{A}_R &= A\sin\psi e^{i\phi_R}, \\ A_L &= A\sin\psi e^{-i\phi_R}, \\ A_R &= A\cos\psi e^{-i\phi_L}, \end{aligned} \tag{1.86}$$

where the angle ψ carries the information of the polarization fraction as

$$\tan\psi = \left|\frac{\bar{A}_R}{\bar{A}_L}\right| = \left|\frac{A_L}{A_R}\right|. \tag{1.87}$$

Under this assumption, $\mathcal{S}$ and $\mathcal{A}^\Delta$ can be expressed directly in terms of the polarization fraction as

$$\mathcal{S} = \sin(2\psi)\sin\phi, \quad \mathcal{A}^\Delta = \sin(2\psi)\cos\phi, \tag{1.88}$$

where ϕ is the sum of the left- and right-handed phases and the B mixing phase $\phi_M = \arg(p/q)$,

$$\phi = \phi_L + \phi_R + \phi_M. \tag{1.89}$$

If the amplitudes of the B and $\bar{B}$ decays to a common channel f are summed together the $\mathcal{S}$ and $\mathcal{C}$ terms cancel out, resulting in a decay rate given by

$$\Gamma_{f,\text{Untagged}}(t) = \Gamma_f(t) + \bar{\Gamma}_f(t) \propto |A_f|^2 e^{-\bar{\Gamma}t}\left[\cosh\left(\frac{\Delta\Gamma}{2}t\right) - \mathcal{A}^\Delta \sinh\left(\frac{\Delta\Gamma}{2}t\right)\right], \tag{1.90}$$

where it follows that without knowledge of the original flavour of the B meson a measurement of the decay lifetime to a common state is still sensitive to the photon polarization through the $\mathcal{A}^\Delta$ parameter. Since the phases of the hyperbolic functions depend on the difference between the decay widths, the B^0_s meson with $\Delta\Gamma_s = 0.083 \pm 0.006\,\text{ps}^{-1}$ is itself a specially suitable candidate to measure the photon-polarization parameter $\mathcal{A}^\Delta$.

For B mesons decaying into a final state, g, that is not an eigenstate of *CP*, such as $B^0 \to K^{*0}(892)\gamma$, the time dependent decay amplitude expressions

are different [28]. Following an analogous procedure as in the previous section, the time dependent decay amplitudes from a B^0 and a $\bar{B}^0$ to the original final state, $\Gamma_g(t) = \left|\langle g|\mathcal{H}|B^0(t)\rangle\right|^2$ and $\bar{\Gamma}_g(t) = \left|\langle g|\mathcal{H}|\bar{B}^0(t)\rangle\right|^2$, are

$$\begin{aligned}
\Gamma_g(t) &= \frac{\left|A_g\right|^2}{2} e^{-\bar{\Gamma}t}\left[\cosh\left(\frac{\Delta\Gamma}{2}t\right) + 2\mathrm{Re}(\lambda_g)\sinh\left(\frac{\Delta\Gamma}{2}t\right)\right. \\
&\quad \left. + \cos(\Delta m t) - \mathrm{Im}(\lambda_g)\sin(\Delta m t)\right], \\
\bar{\Gamma}_g(t) &= \frac{\left|A_g\right|^2}{2}\left|\frac{p}{q}\right|^2 e^{-\bar{\Gamma}t}\left[\cosh\left(\frac{\Delta\Gamma}{2}t\right) + 2\mathrm{Re}(\lambda_g)\sinh\left(\frac{\Delta\Gamma}{2}t\right)\right. \\
&\quad \left. - \cos(\Delta m t) + \mathrm{Im}(\lambda_g)\sin(\Delta m t)\right],
\end{aligned} \tag{1.91}$$

and the corresponding amplitudes to the conjugate final state, $\bar{\Gamma}_{\bar{g}}(t) = \left|\langle \bar{g}|\mathcal{H}|\bar{B}^0(t)\rangle\right|^2$ and $\Gamma_{\bar{g}}(t) = \left|\langle \bar{g}|\mathcal{H}|B^0(t)\rangle\right|^2$, are

$$\begin{aligned}
\bar{\Gamma}_{\bar{g}}(t) &= \frac{\left|\bar{A}_{\bar{g}}\right|^2}{2} e^{-\bar{\Gamma}t}\left[\cosh\left(\frac{\Delta\Gamma}{2}t\right) + 2\mathrm{Re}(\bar{\lambda}_{\bar{g}})\sinh\left(\frac{\Delta\Gamma}{2}t\right)\right. \\
&\quad \left. + \cos(\Delta m t) - \mathrm{Im}(\bar{\lambda}_{\bar{g}})\sin(\Delta m t)\right], \\
\Gamma_{\bar{g}}(t) &= \frac{\left|\bar{A}_{\bar{g}}\right|^2}{2}\left|\frac{q}{p}\right|^2 e^{-\bar{\Gamma}t}\left[\cosh\left(\frac{\Delta\Gamma}{2}t\right) + 2\mathrm{Re}(\bar{\lambda}_{\bar{g}})\sinh\left(\frac{\Delta\Gamma}{2}t\right)\right. \\
&\quad \left. - \cos(\Delta m t) + \mathrm{Im}(\bar{\lambda}_{\bar{g}})\sin(\Delta m t)\right],
\end{aligned} \tag{1.92}$$

where the diverse instantaneous amplitudes, A_g, $\bar{A}_g$ and λ_g are analogous to the previously introduced A_f, $\bar{A}_f$ and λ_f; and $\bar{A}_{\bar{g}} = \langle \bar{g}|\mathcal{H}|\bar{B}^0\rangle$, $A_{\bar{g}} = \langle \bar{g}|\mathcal{H}|B^0\rangle$ and $\bar{\lambda}_{\bar{g}} = \frac{p}{q}\frac{A_{\bar{g}}}{\bar{A}_{\bar{g}}}$. Since experimentally the decays are reconstructed through their final states, in the aforementioned case of $|p/q|^2 = 1$ both sums over common final states retain only the hyperbolic terms:

$$\begin{aligned}
\Gamma_g(t) + \bar{\Gamma}_g(t) &= \left|A_g\right|^2 e^{-\bar{\Gamma}t}\left[\cosh\left(\frac{\Delta\Gamma}{2}t\right) + 2\mathrm{Re}(\lambda_g)\sinh\left(\frac{\Delta\Gamma}{2}t\right)\right], \\
\Gamma_{\bar{g}}(t) + \bar{\Gamma}_{\bar{g}}(t) &= \left|\bar{A}_{\bar{g}}\right|^2 e^{-\bar{\Gamma}t}\left[\cosh\left(\frac{\Delta\Gamma}{2}t\right) + 2\mathrm{Re}(\bar{\lambda}_{\bar{g}})\sinh\left(\frac{\Delta\Gamma}{2}t\right)\right]
\end{aligned} \tag{1.93}$$

And since the decay width difference of the B^0 meson is quite small, $\Delta\Gamma_d/\Gamma_d = -0.002 \pm 0.010$ [25] the hyperbolic sine vanishes and the hyperbolic cosine equals 1. The sum over both final states is therefore

$$\Gamma_g(t) + \bar{\Gamma}_g(t) + \Gamma_{\bar{g}}(t) + \bar{\Gamma}_{\bar{g}}(t) = \left(\left|A_g\right|^2 + \left|\bar{A}_{\bar{g}}\right|^2\right) e^{-\Gamma_d t} \propto e^{-\Gamma_d t}. \tag{1.94}$$

This makes the B^0 system an excellent choice for a control channel, as it has no sensitivity to the sought $\mathcal{A}^\Delta$ parameter, and can serve to test experimental effects.

Knowing the original flavour of the B meson allows to build the time-dependend *CP* asymmetry, which is sensitive to both $\mathcal{A}^\Delta$ and $\mathcal{S}$. This technique is experimentally limited by the effective efficiency of the tagging algorithms, which in the case of the LHCb detector amounts to the order of 5% for B^0_s mesons combining different algorithms [29–31]. While not covered in this work, a tagged measurement of the photon polarization is planned with the additional statistics from the second data taking period of LHCb.

1.4.2 Photon polarization in the SM

To describe the radiative decays of B mesons, a useful framework is the low-energy effective Hamiltonian [32]. This is an effective field theory built using the Operator Product Expansion (OPE) formalism [33]. The transitions from an initial state, $|i\rangle$, to a final state, $|f\rangle$, related through the effective Hamiltonian transition matrix, $\mathcal{H}_{\text{eff}}$, can be expressed as a sum of transitions through partial operators

$$\langle f|\mathcal{H}_{\text{eff}}|i\rangle \propto \sum_k \mathcal{C}_k(\mu)\, \langle f|\mathcal{O}_k(\mu)|i\rangle\,, \tag{1.95}$$

where μ is the adequate renormalization energy scale, typically $m_b/2 < \mu < 2m_b$, $\mathcal{O}_k(\mu)$ are the local operators and $\mathcal{C}_k(\mu)$ are the so-called Wilson coefficients. The OPE formalism allows the separation between the long- and short-distance contributions in the decay amplitude. The former are due to non-perturbative strong interactions, and in Eq. (1.95) they are encoded in the hadronic matrix elements $\langle f|\mathcal{O}_k(\mu)|i\rangle$, whereas the latter can be computed perturbatively and are described by the Wilson coefficients. Since the perturbative part contains information about energy scales larger than μ, BSM effects appear as corrections to the coefficients.

In the case of the $b \to s\gamma$ transition, the chosen energy scale is of the order of the mass of the b quark, m_b, and the effective Hamiltonian is given by [34]

$$\mathcal{H}_{\text{eff}}(b \to s\gamma) = -\frac{G_F}{\sqrt{2}} V_{ts}^* V_{tb} \left[\sum_{i=1}^{6} \mathcal{C}_i(\mu)\mathcal{O}_i(\mu) + \mathcal{C}_{7\gamma}(\mu)\mathcal{O}_{7\gamma}(\mu) + \mathcal{C}_{8\text{G}}(\mu)\mathcal{O}_{8\text{G}}(\mu) \right], \tag{1.96}$$

where G_F denotes the Fermi constant. Since $|V_{us}^* V_{ub} / V_{ts}^* V_{tb}| < 0.02$, the terms proportional to $V_{us}^* V_{ub}$ are omitted. The explicit forms of the operators are:

$$\begin{aligned}
\mathcal{O}_1 &= \left[\bar{s}_i \gamma^\mu (1-\gamma_5) c_j\right] \left[\bar{c}_j \gamma^\mu (1-\gamma_5) b_i\right], \\
\mathcal{O}_2 &= \left[\bar{s}_i \gamma^\mu (1-\gamma_5) c_i\right] \left[\bar{c}_j \gamma^\mu (1-\gamma_5) b_j\right], \\
\mathcal{O}_3 &= \left[\bar{s}_i \gamma^\mu (1-\gamma_5) b_i\right] \left[\sum_q \bar{q}_j \gamma^\mu (1-\gamma_5) q_j\right], \\
\mathcal{O}_4 &= \left[\bar{s}_i \gamma^\mu (1-\gamma_5) b_j\right] \left[\sum_q \bar{q}_j \gamma^\mu (1-\gamma_5) q_i\right], \\
\mathcal{O}_5 &= \left[\bar{s}_i \gamma^\mu (1-\gamma_5) b_i\right] \left[\sum_q \bar{q}_j \gamma^\mu (1+\gamma_5) q_j\right], \\
\mathcal{O}_6 &= \left[\bar{s}_i \gamma^\mu (1-\gamma_5) b_j\right] \left[\sum_q \bar{q}_j \gamma^\mu (1+\gamma_5) q_i\right], \\
\mathcal{O}_{7\gamma} &= \frac{e}{8\pi^2} m_b \bar{s}_i \sigma^{\mu\nu} (1+\gamma_5) b_i F_{\mu\nu}, \\
\mathcal{O}_{8\text{G}} &= \frac{g}{8\pi^2} m_b \bar{s}_i \sigma^{\mu\nu} (1+\gamma_5) T^a_{ij} b_j G^a_{\mu\nu},
\end{aligned} \tag{1.97}$$

where i and j represent $SU(3)_C$ colour indices, sums over q involve all the quark flavours active at the m_b scale, concretely $q \in \{u, d, s, c\}$. $F_{\mu\nu}$ and $G^a_{\mu\nu}$ are the field strength tensors for the electromagnetic and strong interactions, respectively. $\mathcal{O}_1$ and $\mathcal{O}_2$ are the current-current operators, $\mathcal{O}_3$ through $\mathcal{O}_6$ represent the QCD penguins, $\mathcal{O}_{7\gamma}$ is the electromagnetic penguin and $\mathcal{O}_{8\text{G}}$ the chromomagnetic penguin.

In the $b \to s\gamma$ transition the most dominant operator is $\mathcal{O}_{7\gamma}$, the electromagnetic penguin operator. It is represented diagramatically in Figure 1.5. The form of the operator $\mathcal{O}_{7\gamma}$ in Eq. (1.97) is actually a simplified form of the full expression for the operator, given by

$$\hat{\mathcal{O}_{7\gamma}} = \frac{e}{8\pi^2} \bar{s}_i \sigma^{\mu\nu} \left[m_b (1+\gamma_5) + m_s (1-\gamma_5) \right] b_i F_{\mu\nu}, \tag{1.98}$$

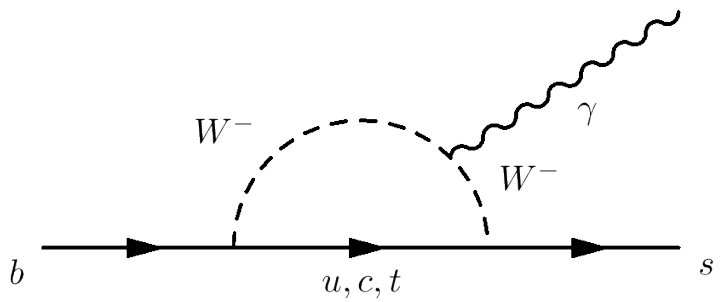

Figure 1.5: Feynman diagram of the electromagnetic penguin operator, $\mathcal{O}_{7\gamma}$, in the $b \to s\gamma$ transition.

where the $(1+\gamma_5)$ and $(1-\gamma_5)$ terms correspond to the emission of left- and right-handed photons, respectively, being the chirality projectors introduced in Section 1.1. The Wilson coefficients corresponding to the left- and right-handed emissions are $C_{7\gamma}$ and $C'_{7\gamma}$, respectively. Since the respective scales are the quark masses and $\frac{m_s}{m_b} \approx 0.022$, it is safe to neglect the right-handed term and deduce that in the SM almost all photons emitted in the $b \to s\gamma$ transition are left-handed[9]. This arises from the fact that the W boson couples only to left-handed fermions in the SM.

Including only $\mathcal{O}_{7\gamma}$, the right-handed "contamination" fraction $\frac{A_R}{A_L}$, is of the order of the aforementioned ratio of the quark masses, but the rest of the operators can contribute and the total contamination fraction can reach orders of up to 0.1 in the SM [35]. This translates to an $\mathcal{A}^\Delta$ value for the SM of $0.047 \pm 0.025 \pm 0.015_{\text{QCD}}$ [26]. In terms of the Wilson coefficients, $\mathcal{A}^\Delta$ can be approximated as

$$\mathcal{A}^\Delta \propto \frac{2\text{Re}\left[e^{-i\phi} C_{7\gamma} C'_{7\gamma}\right]}{\left|C_{7\gamma}\right|^2 + \left|C'_{7\gamma}\right|^2}. \tag{1.99}$$

A useful tool to quantify the photon polarization is the degree of photon

[9] It is implied hereafter that the antiparticle transition emits predominantly right-handed photons and its corresponding "wrong" polarization is left-handed. Since B ($\bar{B}$) mesons contain $\bar{b}$ (b) quarks, $\bar{B}$ (B) mesons emit mostly left-handed (right-handed) photons in their decays.

polarization, λ_γ, defined as

$$\lambda_\gamma \equiv \frac{\Gamma(b\to s\gamma_L)-\Gamma(b\to s\gamma_R)}{\Gamma(b\to s\gamma_L)+\Gamma(b\to s\gamma_R)} = \frac{\left|\mathcal{C}_{7\gamma}\right|^2-\left|\mathcal{C}'_{7\gamma}\right|^2}{\left|\mathcal{C}_{7\gamma}\right|^2+\left|\mathcal{C}'_{7\gamma}\right|^2}, \tag{1.100}$$

with possible values from -1 to 1 corresponding to maximum right- and left-handedness of the photon, respectively. In the SM the photon is predominantly left-handed and $\lambda_\gamma \simeq 1$, therefore any result that contradicts this is a clear indication of BSM physics, specially favouring models with right-handed couplings.

Photon polarization has been observed by LHCb in the $b\to s\gamma$ transition by studying the $B^+\to K^+\pi^-\pi^+\gamma$ decay [36]. Here the polarization appears as a significant (5.2σ) asymmetry between the directions of the photons with respect to a reference plane defined by the three final state hadron tracks [36–38]. Nevertheless, the handedness of the polarization or an actual value of λ_γ are difficult to extract because of the complex resonant structure present in the $K^\pm\pi^\mp\pi^\pm\gamma$ invariant mass spectrum. With better knowledge of the different resonances' contributions a full amplitude and angular analysis will reveal further information about the photon polarization.

Another measurement related to the photon polarization comes from the angular analysis of the $B^0\to K^{*0}(892)e^+e^-$ decay in the low-q^2 region [39]. Even though the decay has a lepton pair in the final state, at low-q^2 the electromagnetic penguin contribution dominates and the $\mathcal{C}_{7\gamma}$ and $\mathcal{C}'_{7\gamma}$ are accessible through the angular observables as

$$A_T^{(2)}\left(q^2\to 0\right) = \frac{2\mathrm{Re}\left(\mathcal{C}_{7\gamma}\mathcal{C}'^{*}_{7\gamma}\right)}{\left|\mathcal{C}_{7\gamma}\right|^2+\left|\mathcal{C}'_{7\gamma}\right|^2}, \quad A_T^{\mathrm{Im}}\left(q^2\to 0\right) = \frac{2\mathrm{Im}\left(\mathcal{C}_{7\gamma}\mathcal{C}'^{*}_{7\gamma}\right)}{\left|\mathcal{C}_{7\gamma}\right|^2+\left|\mathcal{C}'_{7\gamma}\right|^2}. \tag{1.101}$$

The results for $A_T^{(2)}$ and A_T^{Im} are found to be

$$A_T^{(2)} = -0.23\pm 0.23_{\text{stat.}}\pm 0.05_{\text{syst.}}, \tag{1.102}$$

$$A_T^{\mathrm{Im}} = \ \ 0.14\pm 0.22_{\text{stat.}}\pm 0.05_{\text{syst.}}, \tag{1.103}$$

consistent with the SM predictions. The expected data taken during Run II should reduce the now-dominant statistical sensitivity to about a third of its current value.

Both of these analyses represent breakthroughs in the measurement of the photon polarization and there is work in progress to improve upon their results.

Other measurements in radiative decays also provide constraints to the right-handed Wilson coefficient $\mathcal{C}'_{7\gamma}$. Namely, the measurement of the $\mathcal{S}$ parameter, defined in Eq.(1.88), in $B^0 \to K^{*0}(892)\gamma$ is equally sensitive to the photon polarization fraction, albeit with the sine of the phases instead of the cosine. The current average [25] for this parameter is

$$\mathcal{S}_{K^*\gamma} = -0.16 \pm 0.22,$$

consistent with the SM prediction of $\mathcal{S}_{K^*\gamma,\mathrm{SM}} = -0.023 \pm 0.015$.

The inclusive branching fraction, $\mathcal{B}(B \to X_s\gamma)$, can also suffer an enhancement proportional to $\mathcal{C}'_{7\gamma}$, but the world average [25] of

$$\mathcal{B}(B \to X_s\gamma) = (3.43 \pm 0.22) \times 10^{-4}$$

is also in good agreement with the SM prediction, $\mathcal{B}(B \to X_s\gamma)_{\mathrm{SM}} = (3.36 \pm 0.23) \times 10^{-4}$.

Photon polarization in BSM models

Models of BSM physics can further enhance this contamination fraction [27]. To quantify this, the right-handed counterpart of the $\mathcal{O}_{7\gamma}$ operator in Eq. (1.97) is expressed as

$$\mathcal{O}'_{7\gamma} = \frac{e}{8\pi^2} m_b \bar{s}_i \sigma^{\mu\nu} (1 - \gamma_5)\, b_j F_{\mu\nu}. \tag{1.104}$$

Note that this right-handed photon polarization operator is also scaled by m_b, so that the effective size of the contribution is given by the corresponding Wilson coefficient $\mathcal{C}'_{7\gamma}$. In these NP models, the $\mathcal{C}_{7\gamma}$ Wilson coefficient can be modified and, being perturbative calculations, be expressed as the sum of the SM prediction plus the NP contribution,

$$\mathcal{C}_{7\gamma} = \mathcal{C}^{\mathrm{SM}}_{7\gamma} + \mathcal{C}^{\mathrm{NP}}_{7\gamma}, \tag{1.105}$$

$$\mathcal{C}'_{7\gamma} = \mathcal{C}'^{\mathrm{NP}}_{7\gamma}, \tag{1.106}$$

since the right-handed operator does not exist in the SM.

Examples of models that can contribute to the photon polarization include the unconstrained minimal supersymmetry model (uMSSM) [40],

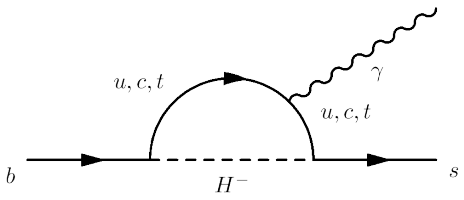

Figure 1.6: Possible Feynman diagram of a $b \to s\gamma$ decay with a charged Higgs in the LRSM.

where left-right squark mixing and gluino couplings can enhance the right-handed component greatly, dominated by a term scaled by the ratio of the gluino mass over the b mass, $\frac{m_{\tilde{g}}}{m_b}$. Since the parameter space is large, the associated predictions cover all the range of possible λ_γ values, from the SM case to a fully right-handed polarization scenario. The corresponding possible value range of $\mathcal{A}^\Delta$ is difficult to estimate, since by its definition in Eq (1.88) it depends on the B mixing phase, which in turn can be greatly affected by the NP model [41].

The Left-Right symmetric model (LSRM) [42] is based in the extended gauge group $SU(2)_L \otimes SU(2)_R \otimes U(1)_{\tilde{Y}}$, where L and R refer to left- and right-handedness and $\tilde{Y}$ is a modified hypercharge. The left-handed fermions are $SU(2)_L$ doublets and $SU(2)_R$ singlets as in the SM, and their right-handed counterparts are inversely so: $SU(2)_L$ singlets and $SU(2)_R$ doublets. The gauge symmetry is broken in two steps

$$SU(2)_L \otimes SU(2)_R \otimes U(1)_{\tilde{Y}} \to SU(2)_L \otimes U(1)_Y \to U(1)_{\mathrm{EM}}, \qquad (1.107)$$

introducing of a plethora of scalar fields. These include the SM bosons, as well as additional W-type charged bosons with right-handed couplings, charged Higgs, and neutral flavour changing Higgs fields. For example, the charged Higgs can replace the $W^\pm$ boson in the penguin loop as pictured in Figure 1.6. In this rich chirality structure, the potential for right-handed photon emission is considerable. Numerically, the contributions add up to a factor of $|\lambda_\gamma| = 0.33$ depending on several parameters and with no explicit information on the sign. This maximum value corresponds to $\mathcal{A}^\Delta = 0.67$ [27].

2 | The LHCb detector at the LHC

Building upon a prolific history of results in high energy physics experiments such as the B factories, BaBar and Belle, Tevatron, CDF, CLEO and D0, the LHCb detector was proposed in 1995 [43] to further explore the heavy flavour sector, taking advantage of the energy scale and high luminosity attainable at the Large Hadron Collider (LHC) . The goal of the LHCb collaboration is to look for evidences of new physics in *CP* violation and rare decays of beauty and charm hadrons. The baryonic asymmetry of the Universe cannot be explained solely with the *CP* violation of the CKM mechanism as described in the SM, supported so far by all experimental results [44]. A new source of *CP* violation beyond the Standard Model is needed to account for the baryon asymmetry of the Universe. Such a new source might be seen in heavy flavour physics, and many theoretical models produce contributions measurable in observables such as *CP* violating phases, rare decay branching fractions, and may generate decay modes forbidden in the SM. To survey such possibilities, *CP* violation and rare decays must be studied with unprecedented precision, using a larger dataset and a physics program that contemplates a wide array of different decay modes.

2.1 LHCb at the Large Hadron Collider

The Large Hadron Collider (LHC) is a two-ring superconducting hadron accelerator and collider installed in the 26.7 km tunnel constructed for the Large Electron-Positron Collider (LEP) underneath the surface of the franco-swiss border near the Geneva region, as pictured in Figure 2.1. The LHC both refers to the collider itself and the experimental collaborations encompassing the several experiments positioned along the ring, the main

of which are ATLAS, CMS, ALICE and LHCb. The aim of the LHC is to explore particle physics at unprecedented energy scales, with the hopes of finding evidence of physics beyond the SM, be it through indirect processes or direct searches. The former correspond to the creation of new states available at higher energies, while the latter also arises from the energy scale, which results in a production of an unexampled number of c, b, and t quarks that can serve to precisely test the SM. Another main objective for LHC, mainly concerning the ATLAS and CMS collaborations, was the direct search of the Higgs boson. Data from 2011 and 2012 was enough for a positive significant result, announced in early July 2012 [45, 46]. An example of an indirect constraint on NP comes from the LHCb measurement of the $B_s^0 \to \mu^+\mu^-$ decay [47], a highly suppressed decay in the SM but enhanced in several NP models. The measurement is consistent with the SM predictions and strongly constraints several models. To achieve its goals, the design centre-of-mass energy of the LHC is $\sqrt{s} = 14$ TeV, a goal that will be approached in increasing steps. The 2011 centre-of-mass energy was half of this, 7 TeV, increased to 8 TeV in 2012. In 2015, after the first operations long shutdown (LS1) in 2013–2014, operations were restarted and an energy of 13 TeV was achieved.

LHC is a pp collider, with two parallel proton beams accelerated in opposite directions which are crossed to attain collisions in designated points. The beams consist of sequences of stranded groups, called bunches. These are through the use of radiofrequency (RF) cavities and bends and focuses them with the use of diverse magnetic fields.

The bunches cannot be accelerated from a stationary state directly in the LHC ring, thus increasingly larger acceleration in different subsystems must be applied before injection into the main ring. This accelerator chain starts with a linear accelerator called Linac2, which injects the particles into the Proton Synchrotron Booster (PSB), in turn injecting into the Proton Synchrotron (PS) and this into the Super Proton Synchrotron (SPS), which then finally injects the bunches into the LHC ring. Protons are obtained by ionizing hydrogen gas and then accelerated in the Linac2 to 50 MeV. In the PSB they reach an energy of 1.4 GeV, then accelerated to 25 GeV in the PS and up to 450 GeV in the SPS. They are then injected into the LHC ring where they reach the final energy. Apart from protons, the accelerator can be operated with lead-ion beams, allowing three types of collisions: pp, p-Pb and Pb-Pb. The ALICE experiment is a dedicated experiment designed for the study of heavy-ion collisions.

The LHC ring consists of eight straight sections and eight bending arcs.

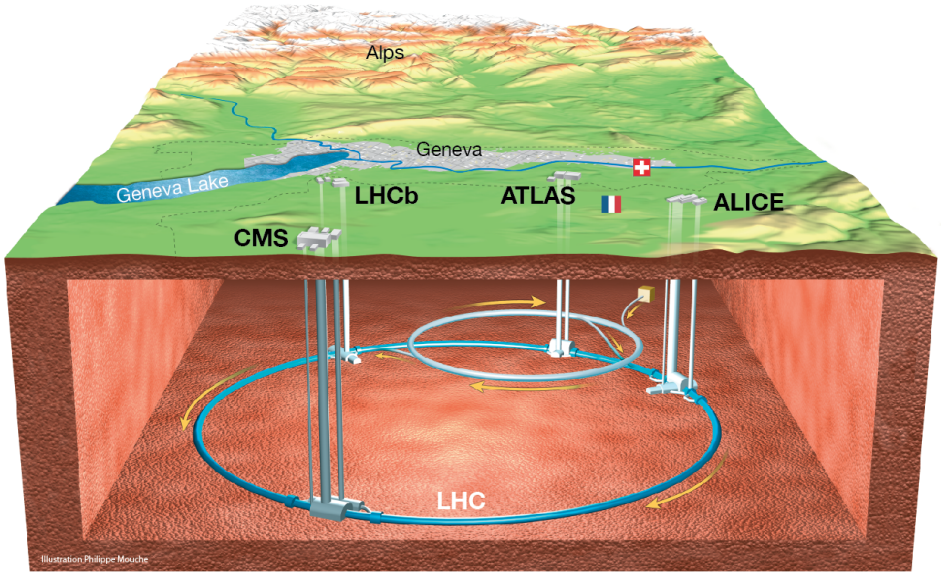

Figure 2.1: The LHC and its principal detectors.

Each straight section is approximately 528 m long and can serve as an experimental or utility insertion. The two high luminosity experimental insertions are located at opposite points: the ATLAS experiment is located at Point 1 and the CMS experiment at Point 5. Two more experimental insertions are located at Points 2 and 8, for ALICE and LHCb, respectively. These also include the injection systems for the beams.

The bending sections rely on superconducting magnets cooled to 1.9 K through the use of super-fluid helium, called cryodipoles, and operate at magnetic fields above 8 T. A schematic cross section of one of these is shown on Figure 2.2. A total of 1232 cryodipoles are employed by LHC, mostly in the arc sections. The end sections of the bending arcs contain the main quadrupoles used for beam focusing after bending.

For a particular process, p, the number of events, N, generated in a collider depends on its cross section, σ_p, and the machine luminosity, $\mathcal{L}$, by the simple relation $N = \mathcal{L}\sigma_p$. The luminosity depends only on the machine parameters and for a Gaussian beam distribution it is given by

$$\mathcal{L} = \frac{N_b^2 n_b f_{\text{rev}} \gamma_r}{4\pi\epsilon_n \beta^*} F,$$

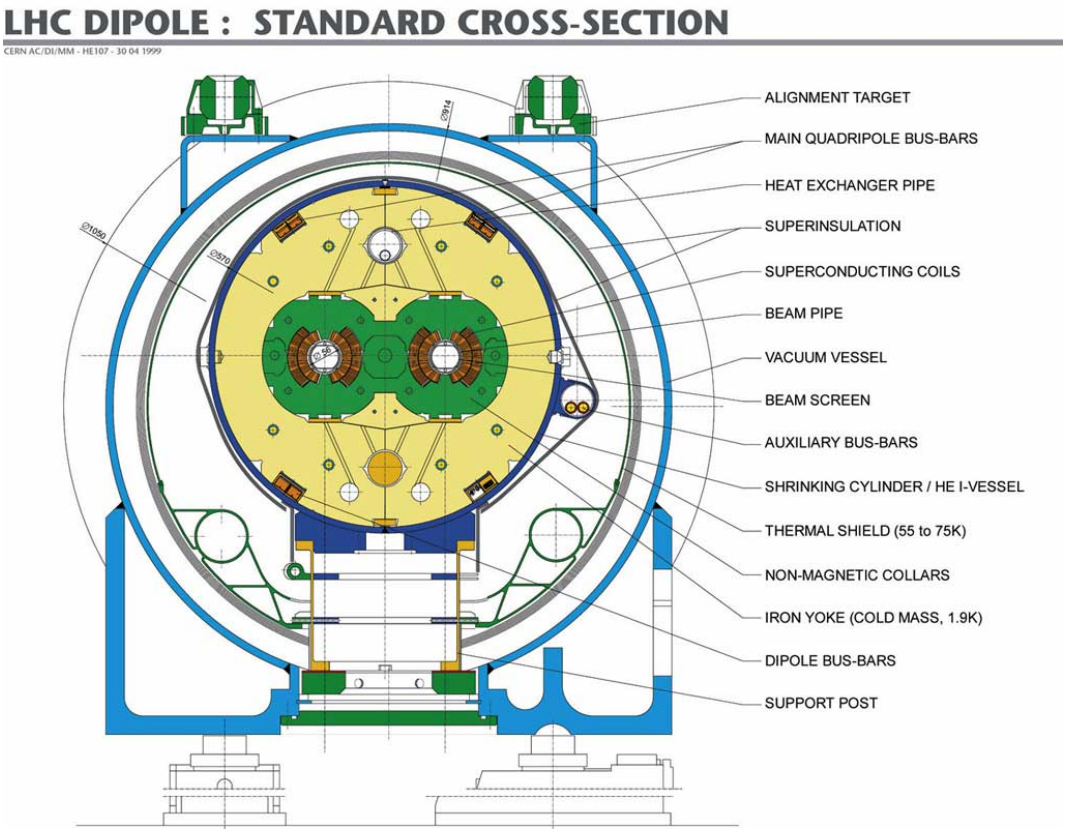

Figure 2.2: Cross-section of a LHC cryodipole.

where N_b is the number of particles per bunch, n_b the number of bunches per beam, f_{rev} the revolution frequency, γ_r the relativistic Lorentz factor, ϵ_n the normalized beam emittance, β^* the beam amplitude function at the interaction point and F the geometrical luminosity-reduction factor due to the crossing angle. This can be expressed, when assuming both beams are equal and perfectly round, as

$$F = \frac{1}{\sqrt{1 + \left(\frac{\theta_c \sigma_z}{2\sigma^*}\right)^2}},$$

where θ_c is the full crossing angle at the interaction point, σ_z is the root mean square (RMS) bunch length and σ^* the transverse RMS beam size at the interaction point.

With a $b\bar{b}$ production cross section of around 500 µb at an energy of 14 TeV, produced mainly through gluon fusion and flavour excitation, the

LHC is the most abundant source of b-mesons in the world, including $B^{0,\pm}$, B_s^0 and B_c^+. Also b-baryons such as Λ_b^0 are produced in large quantities. The corresponding fragmentation fractions are [25, 48]

$$f(B^0) = f(B^+) = 0.404 \pm 0.06,$$
$$f(B_s^0) = 0.104 \pm 0.005,$$
$$f(\Lambda_b) = 0.175 \pm 0.106.$$

The luminosity for the LHCb experiment can be adjusted by changing the beam focus at its interaction point independently of the rest of interaction points of the LHC circuit, and is kept lower than the LHC peak luminosity $\mathcal{L}_{\text{LHC}} = 10^{34} cm^{-2} s^{-1}$, as it provides some advantages. Firstly, events are dominated by a single pp interaction per bunch crossing, simplifying the analysis as events with multiple interactions increase the difficulty of discriminating the secondary vertices from b-hadron decays from primary vertices of additional pp interactions. Secondly, the occupancy of the detector is kept at a low level and finally the radiation damage to the detector material is reduced, extending the life of the subsystems. To achieve this, the beam directions at the LHCb collision point are slightly displaced to reduce the beam overlap and therefore the number of collisions. The LHC luminosity decreases with time because of beam-beam and beam-gas interactions. By adjusting the displacement at the LHCb point in real time the instant luminosity delivered to the experiment can be kept constant, as shown in Figure 2.3, in what is called the luminosity leveling.

A total of 3 fb^{-1} of integrated luminosity was collected at LHCb during Run I. At the time of writing, Run II is under way and the detector has already summed 1.31 fb^{-1}, as pictured in Figure 2.4. The plan is to surpass the 5 fb^{-1} mark before the start of the second long shutdown period (LS2), scheduled to start in July 2018. During that period detector upgrades are planned for all the major LHC experiments, including LHCb.

To profit from the extensive source of b hadrons that the LHC represents, the detector is designed to permit the correct identification and isolation of the relevant information in a high track multiplicity environment, inherent to hadronic colliders. This requires an efficient and versatile trigger, able to cope with the by-products of the collision without affecting the sensitivity to a wide spectrum of final states. Excellent vertex and momentum resolutions are mandatory for the study of the fast process of neutral meson oscillations, outlined in Chapter 1, take for instance the mean flight distance of a B_s^0 meson of 7 mm and its oscillation frequency of $17.757 \pm 0.021\,\text{ps}^{-1}$ [25],

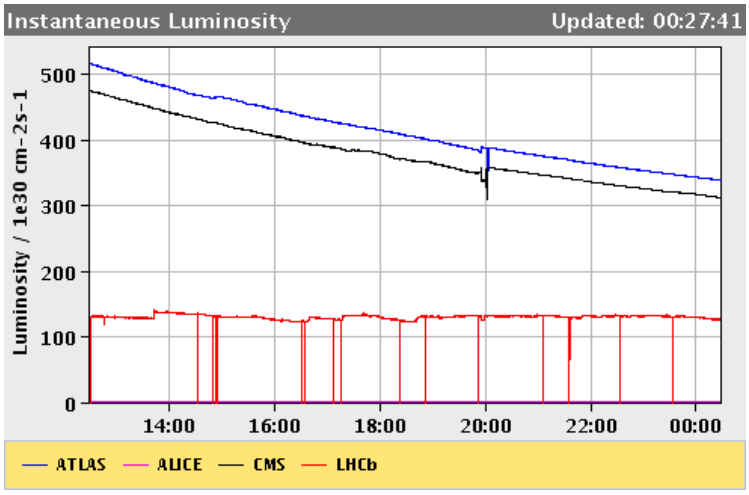

Figure 2.3: Instantaneous luminosity delivered to the LHC experiments. The luminosity leveling of LHCb is evident, compared with the luminosity losses in ATLAS and CMS. The red vertical lines correspond to the beam adjustment processes.

corresponding to an average wavelength of half a milimeter in the detector. The resolution is also needed for a good invariant mass resolution of b

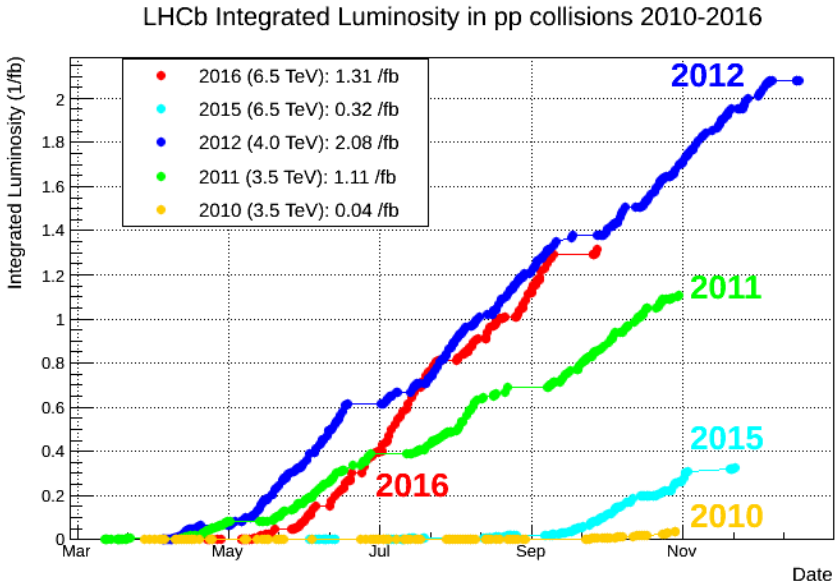

Figure 2.4: Integrated luminosity recorded by the LHCb experiment along time.

hadrons, essential to reduce combinatorial background. It is crucial to have a mechanism of identification of electrons, muons, protons, kaons and pions, as well as for the detection of neutral particles such as γ, π^0 and η, typical in the final states of key channels studied at LHCb. The data acquisition system must manage the flow of hundreds of gigabytes of data per second in an optimal and robust manner, requiring a high bandwidth and powerful online data processing capabilities. The aforementioned needs drive the design of the LHCb detector, described in this chapter.

2.2 Detector geometry and components

Housed in the Intersection Point 8 of the LHC, previously used by the DELPHI experiment during the LEP era, the LHCb detector is a single-arm forward spectrometer [43,49,50] with a coverage from approximately 10 mrad to 300(250) mrad in the bending (non-bending) plane, or in terms of pseudorapidity

$$\eta = -\ln\tan\left(\frac{\theta}{2}\right),$$

the acceptance of LHCb is $1.9 < \eta < 4.9$. The layout of the LHCb spectrometer is shown in Figure 2.5.

The right-handed coordinate system adopted has the z axis along the beam, and the y axis along the vertical. Therefore, the bending and non-bending planes previously mentioned are more accurately defined as the xz and yz planes, respectively. The polar angle is defined in cylindrical coordinates sharing the z axis from the aforementioned cartesian system. This geometry is chosen to profit on the spatial distribution of $b\bar{b}$ pairs produced, owing to the fact that the aforementioned quarks coming from pp collisions are boosted in the directions closest to the beams, seen in Figure 2.6 as the result of a PYTHIA simulation.

The hardware components that conform the LHCb detector are:

- the LHCb magnet,
- the VErtex LOcator (VELO),
- the Tracker Turicensis (TT),
- three tracking stations, or T-Stations—T1, T2, and T3—, each composed of a central Inner Tracker station (IT) surrounded by an Outer Tracker station (OT),

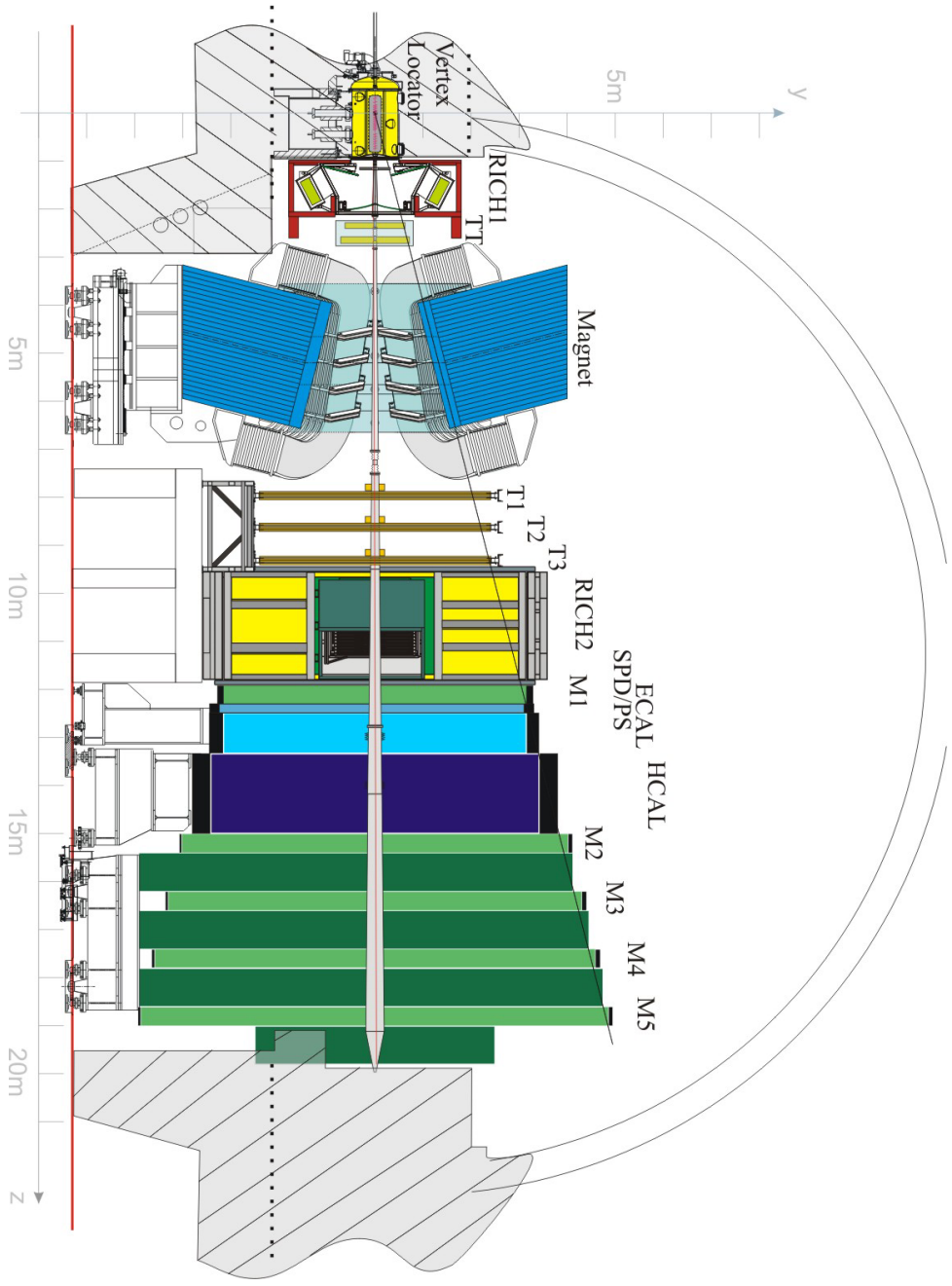

Figure 2.5: Transversal view of the LHCb detector.

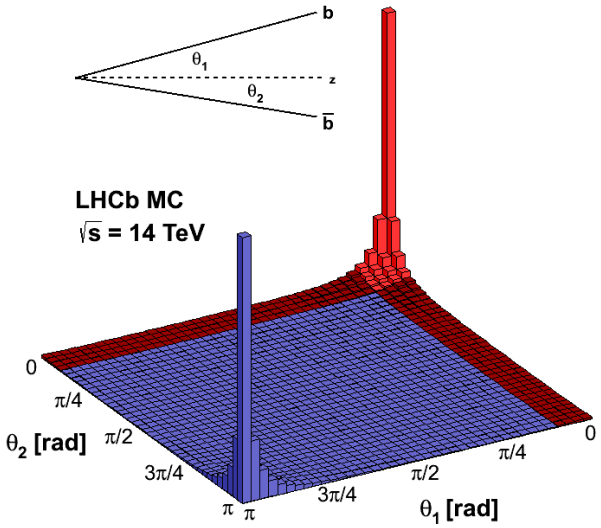

Figure 2.6: Simulated correlation of the polar angles of a b and a $\overline{b}$ from a $b\overline{b}$ pair produced at 14 TeV in LHC. The red region corresponds to the LHCb angular acceptance.

- two Ring Imaging CHerenkov detectors—RICH1 and RICH2,
- the Calorimeters, composed by the Scintillating Pad Detector (SPD), the Pre-Shower detector (PS), the Electromagnetic CALorimeter (ECAL) and the Hadronic CALorimeter (HCAL),
- and five muon stations—M1 through M5—which compose the Muon Detector.

These can be categorized in two major groups according to their purpose: the VELO, TT and tracking stations form the tracking system of the detector, along with the magnet; while the RICH, calorimeters and muon stations compose the particle identification system. Data taken at the LHCb detector must be triggered to reduce the rate in three tiers, starting with a hardware-based Level 0 (L0) trigger followed by the High Level Trigger (HLT), divided in two stages: the first one (HLT1) uses a partial reconstruction of the event to reduce the rate so that the second stage (HLT2) is able to perform a full event reconstruction and make more elaborate decisions.

After triggering, the data must be reliably and efficiently sent to storage for further analysis via the Online system.

2.3 Tracking

Heavy flavour physics studies require a precise knowledge of the lifetime of B mesons. Therefore, LHCb strictly requires the ability to accurately determine the flight distance of long lived mesons and their momentum. The required momentum resolution for several key measurements of the LHCb physics program [51] is $\delta p/p \approx 0.4\%$.

The tracking system is dedicated to the reconstruction of the trajectories of charged particles that pass through the LHCb detector. It consists of the VELO and four planar tracking stations: the TT upstream of the dipole magnet and T1–T3 downstream of the magnet. Silicon microstrip detectors are used in the VELO and TT, and only in the innermost regions of T1–T3, closer to the beam pipe, in what is denominated the IT. For the outer regions of T1–T3 straw drift tubes are employed, referred to as the OT. The TT and IT were developed in a common project called the Silicon Tracker (ST). Finally, while not being by itself an active detector, the role of the magnet is necessary for the tracking and it will be discussed along the tracking components.

2.3.1 The LHCb Magnet

A dipole magnet is used in the LHCb experiment to bend the charged tracks in order to measure their momenta and electric charge. In the original technical proposal [50] a superconducting magnet was included in the design, but it was later discarded in favor of a warm magnet due to budget and time constraints [52–54]. The design constraints for the magnet result in an integrated magnetic field of 4 Tm for tracks of 10 m length, accommodating the need of a field level inside both RICH detectors' envelope less than 2 Tm and a field as high as possible in the region between the VELO and the TT. A plot of the field intensity along the z axis, can be seen in Figure 2.7. The polarity of the magnet can be inverted to study detector related asymmetries.

Structurally, the magnet consists of two identical saddle-shaped coils in a window frame yoke with sloping poles, in order to cover a forward acceptance of ± 250 mrad vertically and ± 300 mrad horizontally. Each coil consists of five pancakes arranged in five triplets and produced of pure

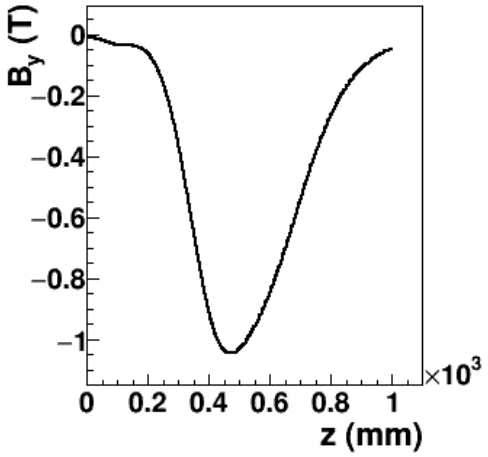

Figure 2.7: Magnetic field intensity as measured along the LHCb detector's z axis at transverse position $x = y = 0$ [55].

Al-99.7[1] hollow conductor in an annealed state. The yoke is also formed of identical halves, composed of 100 mm thick plates of laminated low carbon steel of a maximum weight of 25 tons each. Both components are assembled by placing each identical half mirror-symmetrically on top of each other, for a total weight of 1500 and 54 tons for the yoke and coils, respectively. A schematic of the full magnet structure is pictured in Figure 2.8.

2.3.2 Vertex Locator

The VErtex LOcator (VELO) provides measurements of track coordinates close to the interaction region, used to identify the displaced secondary vertices, a distinctive feature of long-lived particles such as b and c hadrons. It consists of a series of silicon microstrip modules arranged along the z-axis [56]. The VELO silicon sensors are single-sided 300 µm thick n-in-n type detectors with a half-circular shape covering a 182° angle, including a 2° overlap area with the opposite sensor. Figure 2.9 shows an r- and a ϕ-sensor adjacent to each other. They are centred around the beam-axis and their active area extends from a radius of 8.2 mm to 42.0 mm.

The strips in the r-sensor are concentric semi-circles segmented into four 45°-sectors. Each sector has 512 strips. The segmentation has beneficial effects on hit occupancy and strip capacitance. The strip pitch increases

[1] Aluminium with a certified purity of at least 99.7%.

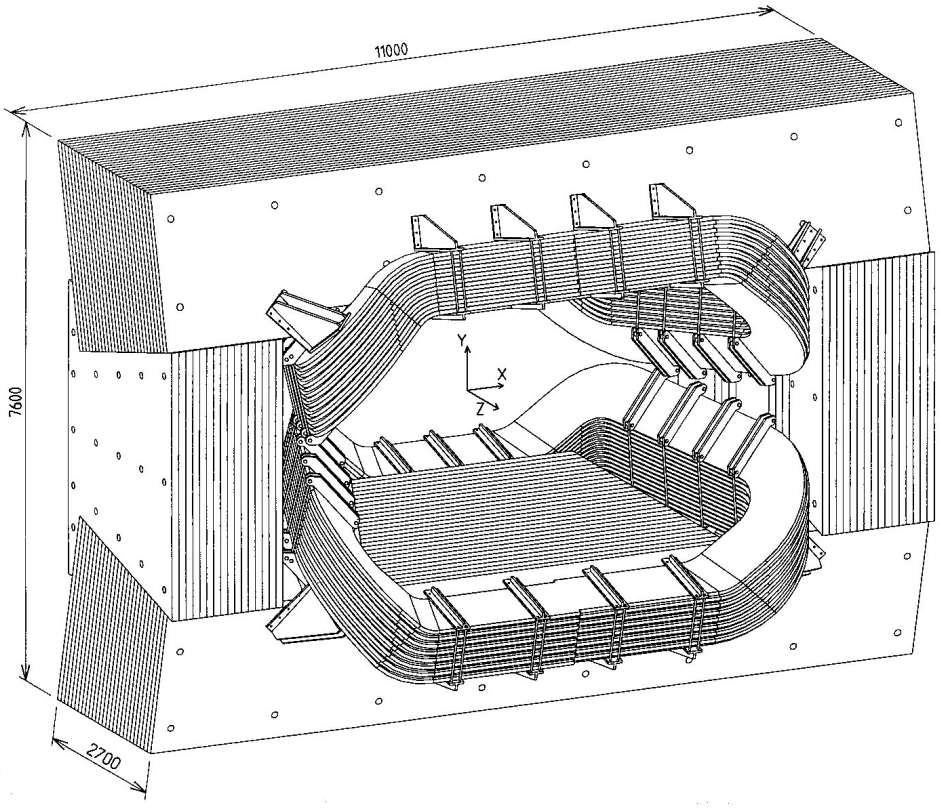

Figure 2.8: Schematic three-quarters view of the LHCb magnet along with the iron yoke.

linearly as a function of radius, from 38 μm at the inner edge to 101.6 μm at the outer edge. The strip orientation in the ϕ-sensor is semi-radial. The sensor is divided into an inner and an outer region in which the strips are skewed in opposite directions to form a dog-leg shape. At 8 mm the inner strips have an angle of 20° with respect to the radial, while the outer strips are at a 10° angle to the radial at 17 mm. By alternating the direction that the ϕ-sensors face, the strips in adjacent sensors have a stereo angle with respect to each other. This measure reduces the combinatoric background in the pattern recognition. Analogously to the r-sensor, the strip pitch of the ϕ-sensor increases linearly with radius. The pitch ranges from 38 μm – 78 μm in the inner region and 39 μm – 97 μm in the outer region.

Combining the measurements of each module with the position along the beam axis of the module the hits are located in a cylindrical coordinate system. Subsequent modules provide additional hits and the tracks are

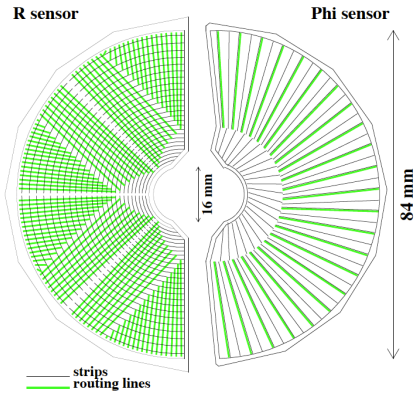

Figure 2.9: Schematics of the two variants of individual modules in the VELO for measurements of polar coordinates r (left) and ϕ (right). The black lines indicate the sensor strips which provide a coverage for either a single angular position or a single radial measurement. The combination of two such measurements determines a precise point in space.

interpolated with these hits. Four modules are located upstream of the interaction point, used for the *pile-up veto system* [57]. This system is used to discard events with a large number of primary vertices. The complete VELO layout is shown in Figure 2.10.

The VELO detector provides a spatial resolution of the Primary Vertex (PV) that depends on the number of tracks as shown in Figure 2.11. The average resolution is $\approx 42\,\mu m$ in the z axis and $\approx 10\,\mu m$ in the xy plane.

2.3.3 Silicon Tracker

The ST comprises two detectors: the Tracker Turicensis (TT) and the Inner Tracker (IT) [49, 58, 59]. The first one is located upstream of the bending magnet and covers the full LHCb angular acceptance, while the second one conforms the inner region of each of the tracking stations. Both of them are silicon microstrip detectors, with a strip pitch of about 200 µm. Each station is composed of four layers of strip modules with different orientations in what is called a stereo configuration indicated by (x-u-v-x), where the u and v planes are rotated slightly in opposite directions from the vertical axis, denoted by x.

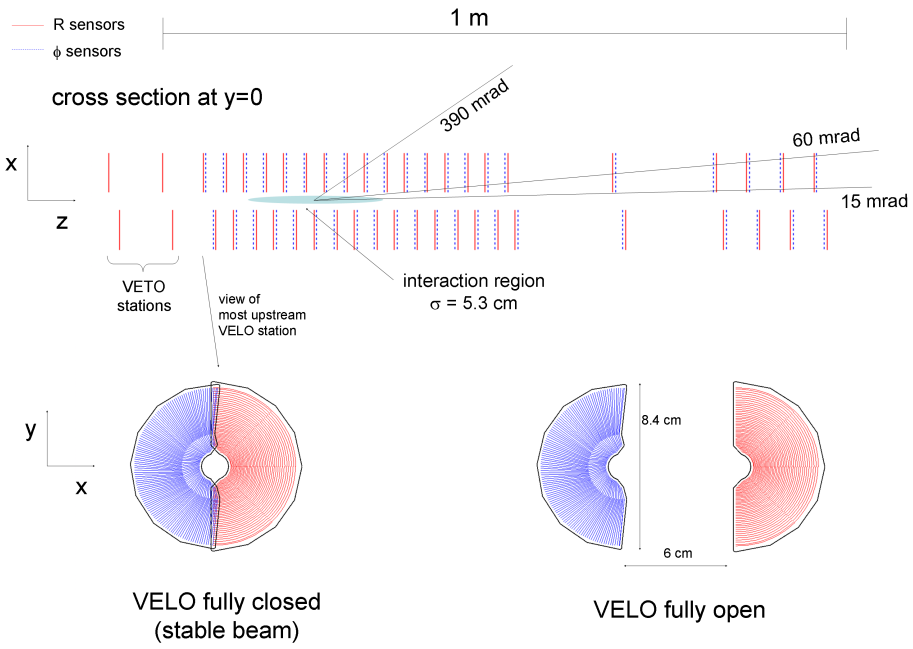

Figure 2.10: Layout of the VELO detector modules along the z axis (top) and the frontal configurations for stable beams (bottom left) and injection (bottom right).

Tracker Turicensis

The TT is a 150 cm high and 130 cm wide station with an active area of 8.4 mm^2. It is placed just before the magnet, and consists of one of the mentioned four layer modules. To aid reconstruction, the two pairs of layers, (x-u) and (v-x), are separated by 27 cm along the beam axis. Each layer is composed of half modules, conformed of 7 silicon sensors each. The layers of the first pair, (x-u), consist of 30 of these half modules divided in an upper and a lower half. The layers of the second pair, (v-x), have an additional sensor per quadrant, for a total of 34. These modules are staggered by about 1 cm in the beam axis and overlap in the transversal direction a few mm with adjacent modules to avoid acceptance gaps and aid the alignment of the modules.

A single silicon sensor is 9.64×9.44 cm, 500 µm thick, and carries 512 readout strips with a pitch of 183 µm. The 7 sensors in a half module are grouped in readout sectors depending on the proximity to the beam. For the 6 nearest half modules, the sensors are divided in groups of 4, 2 and 1

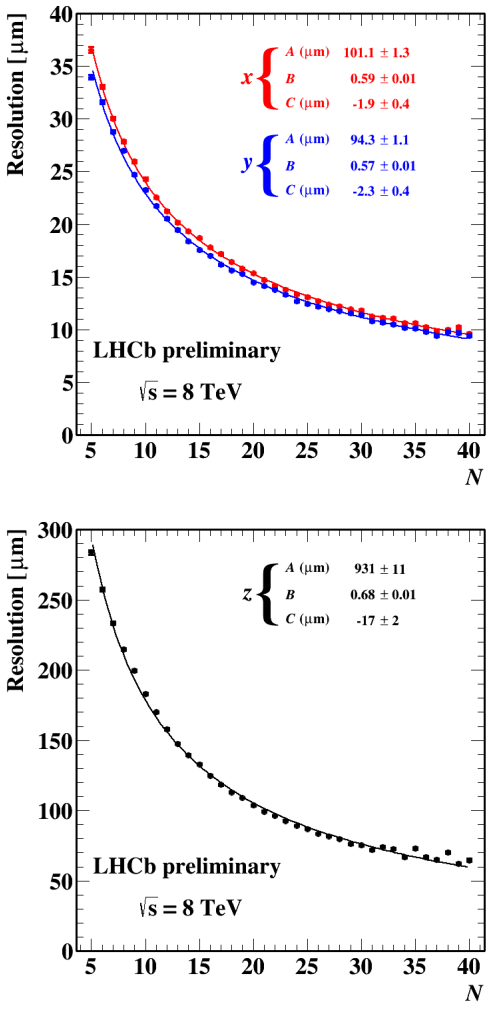

Figure 2.11: Spatial resolution of the Primary Vertex (PV) reconstruction as a function of the number of tracks N, measured with 2012 data. Red and blue squares in the top plot correspond to the x- and y-axes, respectively, while the bottom plot corresponds to the z-axis. The three distributions are fitted to a curve $\frac{A}{N^B} + C$, with the fitted parameters for each curve inlaid in the plots.

towards the beam, while for the rest the nearest 3 sensors are merged in a single group. A sketch of the third layer of the TT and a single 4-2-1 sensor are shown in Figure 2.12, illustrating all of this. The TT has a resolution of about 50 μm.

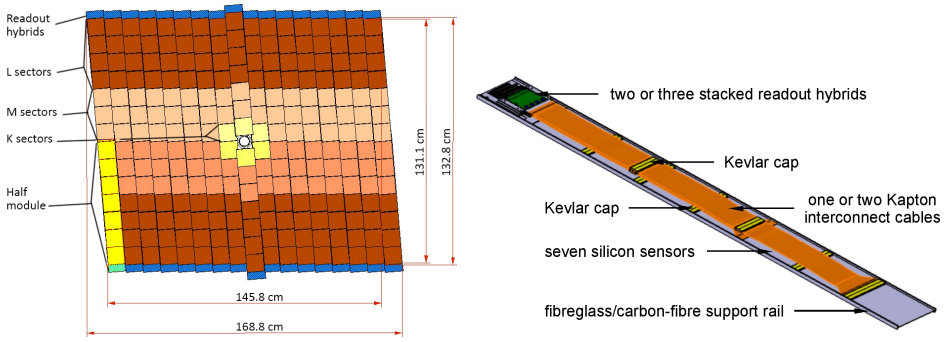

Figure 2.12: Layout of the third TT detection layer (left) and view of a 4-2-1 type TT half module (right).

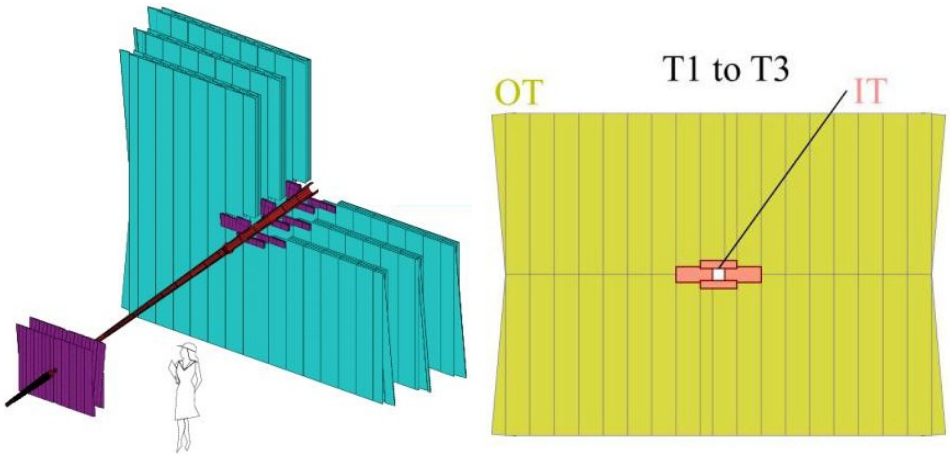

Figure 2.13: Relative scale and position of the TT and the tracking stations, with the ST shown in purple and the OT in blue (left). Single tracking Station division in their Inner and Outer tracker components (right).

Inner Tracker

The IT consist of microstrip modules placed in the innermost regions of the T1–T3 stations, as shown in Figure 2.13.

Cross shaped, the dimensions of each station reach 120 cm in width and 40 cm in height. Each IT station consists of four individual detector boxes arranged around the beam pipe. Each detector box contains four detection layers and each layer consists of seven detection modules. The layout of a layer in a station is shown in Figure 2.14. As seen in the image, single and double sensor modules are used for the different regions. These are identical, with the differences being the dimensions. The thickness of the

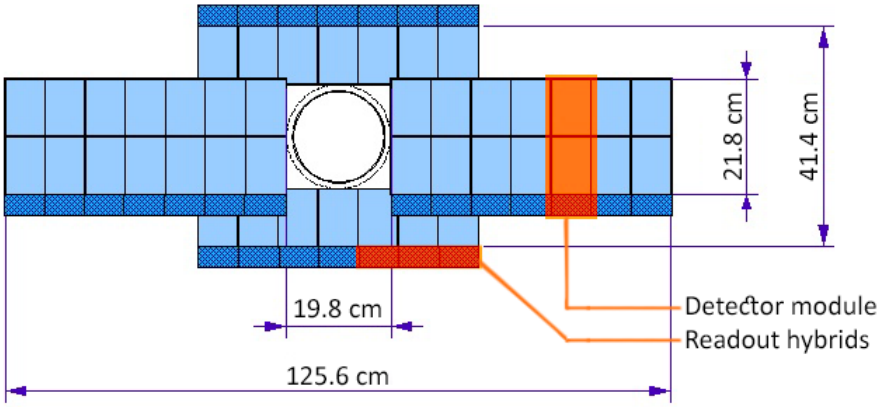

Figure 2.14: Layout of an x detection layer in the second IT station.

silicon sensor is 410 µm for the double sensor modules and 320 µm for the single ones, and each sensor is 7.6 cm wide and 11 cm long, carrying 384 readout strips with a pitch of 198 µm. The sensor modules are staggered by 4 mm in the beam axis and overlap 3 mm in the transversal axis to avoid acceptance gaps and aid the alignment of the modules. The IT has a spatial resolution of about 57 µm.

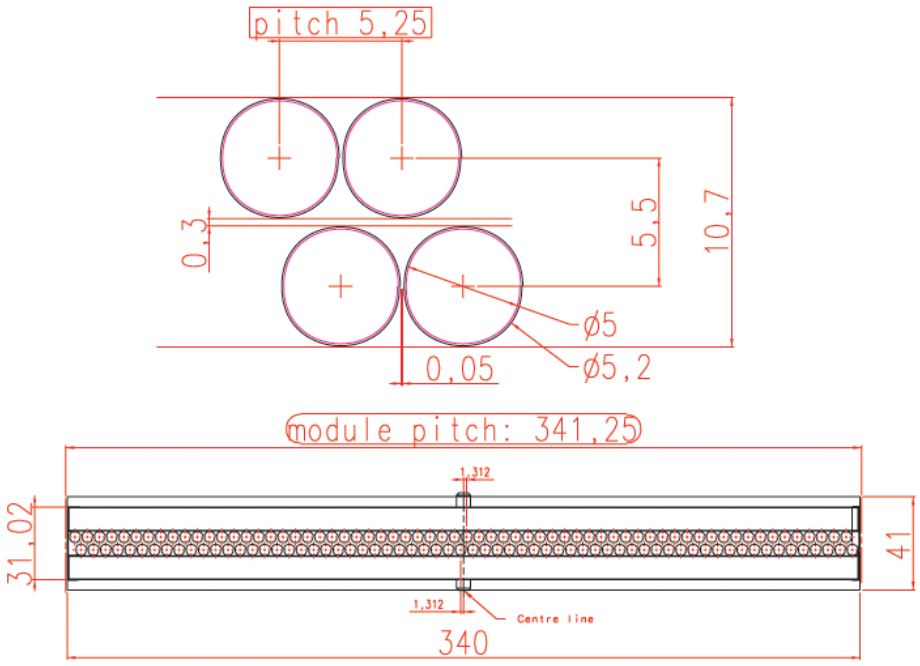

Figure 2.15: Cross section of the two drift tube layers in each of the OT modules. The dimensions quoted are in cm.

2.3.4 Outer Tracker

The Outer Tracker (OT) are drift-time detectors [49, 60, 61] that compose the outer region of the T-stations, as shown in Figure 2.13. Each module contains two staggered layers of 64 drift tubes each with inner diameters of 4.9 mm. A sketch of the cross section of one of these double layer modules is shown in Figure 2.15. Each station consists of four of these modules arranged in a *x*-*u*-*v*-*x* geometry. As with the TT, the x modules are oriented vertically while the u and v are tilted $+5$ deg and -5 deg with respect to the vertical, respectively. The counting gas inside the tubes is a mixture of Ar (70%) and CO_2 (30%), guaranteeing a drift time below 50 ns and a drift-coordinate resolution of 200 μm. The total active area of a station is $5971 \times 4850\,\text{mm}^2$, covering the LHCb acceptance, 300 mrad in the magnet bending plane (horizontal) and 250 mrad in the non-bending plane (vertical).

2.3.5 Tracking system performance

The reconstruction of tracks in LHCb consists in combining the hits in the different subsystems to form particle trajectories. The trajectories' curvature under the magnetic field allow the measurement of their momenta, and the extrapolation of the tracks through the particle identification systems permits the association of information obtained from both systems. Depending on the subdetectors they leave hits on, the tracks are classified differently. The different types of tracks are pictured in Figure 2.16 and defined as follows:

Long tracks cross the full tracking system, leaving hits in the VELO, the TT, and the T-stations. These kind of tracks have the best momentum resolution and consequently are the most commonly used for physics analyses.

Downstream tracks only produce hits in the TT and T-stations. These are relevant for the cases of neutral particles that decay into charged particles after the VELO, such as Λ and K^0_S.

Upstream tracks leave signal hits only in the VELO and TT. These are low momentum tracks bent out of acceptance when traversing the magnet, and usually have poor momentum resolution. They might leave signal in the RICH1 and in that case can be useful for background studies for the RICH algorithms.

Velo tracks only leave signal in the VELO. These are generally large angle backscattered tracks, used for vertex reconstruction.

T-tracks are those which leave hits only in the T-stations. Typically produced in secondary interactions, they are useful for pattern recognition in the RICH2 and help differentiate charged from neutral clusters in the ECAL.

The reconstruction of a track in LHCb starts with the so-called seeds, initial track candidates, sought in either the VELO or the T-stations, where the magnetic field is small. For a combination of hits to be considered a valid seed, they should be almost aligned. The track fitting algorithm uses a Kalman filter to refit the trajectory of the track seed, accounting for multiple scattering and energy losses. Then it tries to associate hits from the rest of the tracking system to the candidate, iteratively refitting and confirming

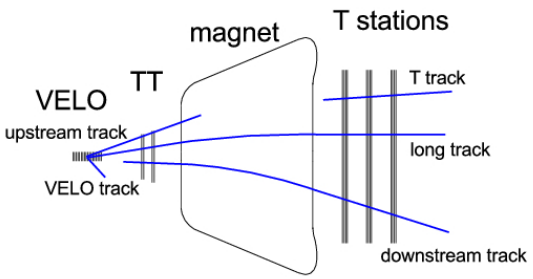

Figure 2.16: Schematic illustration of the different types of tracks in LHCb.

or discarding these additional hits depending on the change in χ^2 of the track fit and the pull distribution of the track parameters.

Using a Monte Carlo (MC) simulation sample of $B^0 \to J/\psi K^0_S$ events, the performance of the algorithm was evaluated [49] in terms of two quantities:

Reconstruction efficiency is the ratio of reconstructed tracks over possible reconstructible tracks. To be considered as reconstructed, a track must have at least 70% of its associated hits coming from the same simulated particle. To be considered reconstructible, tracks must have a minimum number of hits in the several tracking subsystems:

- **VELO** tracks require at least three r and three ϕ hits.
- **Upstream** tracks require the above and one hit in each of the TT stations.
- **T-tracks** tracks require one x and one stereo hit in each of the T-stations.
- **Long** tracks fulfil both the VELO and T-track criteria.

Ghost rate is the fraction of the reconstructed tracks with hits that do not correspond to a single particle.

The average efficiency for a long track produced by a particle with a momentum larger than 10 GeV/c is $\sim$94%, and its average ghost rate is $\sim$9%, with most ghost tracks having a low reconstructed p_T. The momentum resolution of the tracking system improves with a larger momentum of the tracks and varies from $\delta p/p = 0.35\%$ for low momentum to $\delta p/p = 0.55\%$ in the high end of the spectrum. The impact parameter (IP) resolution also

improves with momentum and can be parametrized as

$$\delta_{\mathrm{IP}} = 14\,\mu\mathrm{m} \oplus \frac{35\,\mu\mathrm{m}/(\,\mathrm{GeV}/c)}{p_{\mathrm{T}}}.$$

For upstream tracks with momentum larger than 1 GeV/c the average efficiency is ∼75% and the corresponding ghost rate is 15%. Because of the small value of the magnetic field integral in the track region, the momentum resolution is only $\delta p/p = 15\%$.

Downstream tracks present an average reconstruction efficiency of ∼80% for particles with momentum larger than 5 GeV/c, and the associated ghost rate is 15%. Their momentum resolution is $\delta p/p = 0.43\%$, owing to the fact that they traverse most of the magnetic field.

Further evaluations of the reconstruction efficiency with Run I $J/\psi \to \mu^+\mu^-$ data provide efficiencies of at least 95 % [62].

2.4 Particle identification

The Particle Identification (PID) system is essential to the experiment since it provides identification of the different particle types produced in b-hadron decays. It is composed of different subsystems, each providing unique information. The Ring Imaging Cherenkov detector (RICH) detectors are mainly used to distinguish charged pions from kaons. The two calorimeters offer separation between electromagnetic and hadronic particles, and can further discriminate particles internally. The final piece of the PID are the muon stations located at the downstream extreme of the experiment, able to detect the tracks of passing muons.

2.4.1 RICH

LHCb uses Ring Imaging Cherenkov detector (RICH) detectors [49, 63] to separate pions from kaons. As their name implies, they employ the Cherenkov effect to determine the type of particle detected. Charged particles crossing a medium with a speed v greater than the speed of light in that medium, c/n, where n is the refractive index of the medium, radiate energy in the form of photons. The angle of emission θ depends on the ratio of the light speed to the particle's speed in the medium, through the relation

$$\cos\theta = \frac{c}{nv} = \frac{1}{\beta n}.$$

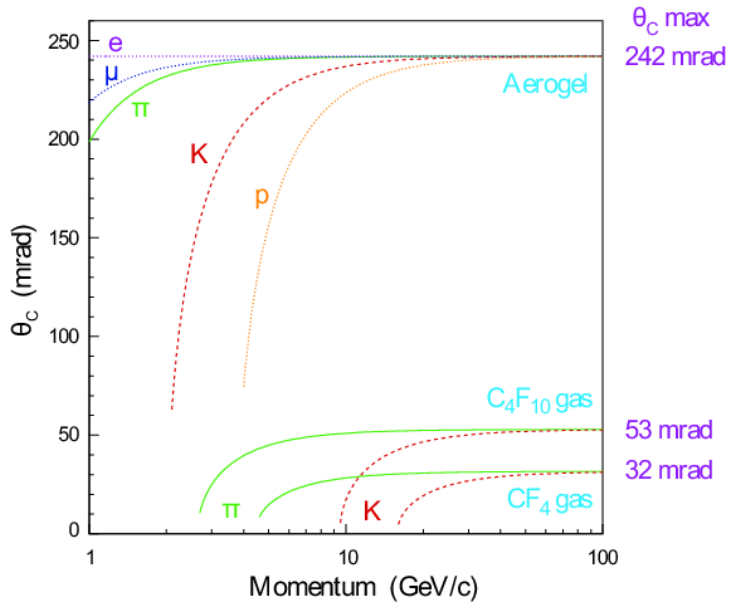

Figure 2.17: Cherenkov angle versus particle momentum for the RICH radiators.

For the same momentum, particles with different masses will have different speeds and therefore different Cherenkov angles, allowing their identification. The dependence with the refractive index of the chosen medium, called radiator, determines the range of momenta in which the detector can differentiate particles. Such behaviour can be observed in Figure 2.17.

Since the momentum spectrum of particles in LHCb can be correlated to the polar angle, two RICH detectors are included in the design in order to maximize the momentum coverage. The upstream detector, RICH1, covers the low momentum range ($\sim$1–60 GeV/c) using aerogel and decafluorobutane (C_4F_{10}) radiators, encompassing the full LHCb angular acceptance from $\pm$25 mrad to $\pm$300 mrad in the horizontal plane and $\pm$250 mrad in the vertical one. It is located upstream of the magnet to detect the low momentum particles, the trajectories of which can get bent outside of the acceptance. The second detector, RICH2, is located downstream and covers the high momentum range ($\sim$15 GeV/c to $\geq$100 GeV/c) through the use of a tetrafluoromethane (CF_4) radiator. While this detector does not comprise the full LHCb angular acceptance, ranging from $\pm$15 mrad to $\pm$120 mrad in the horizontal plane and $\pm$100 mrad in the vertical, it suffices to cover the region where high-momentum particles are produced.

The Cherenkov light emitted is measured by arrays of hybrid photon detectors (HPD) as circles of varying radii correlated to the emission an-

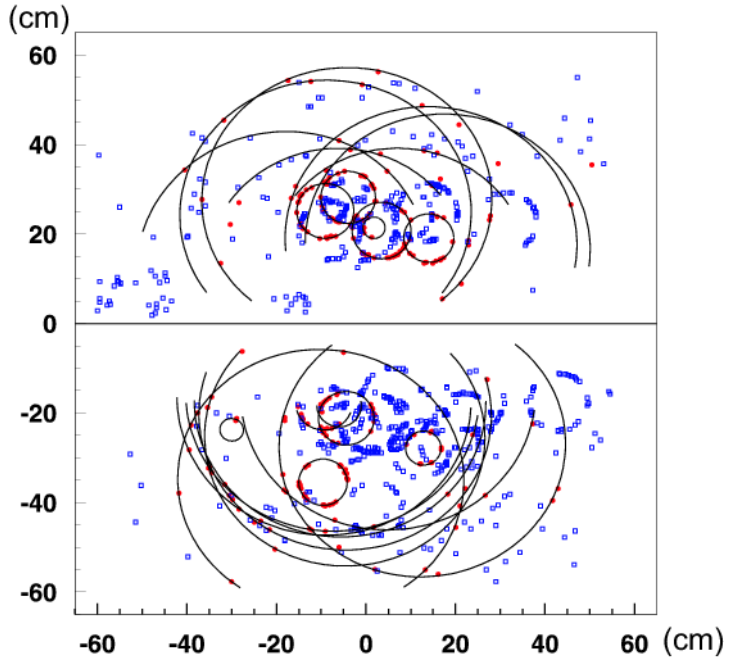

Figure 2.18: Cherenkov photon detector hits (rings overlaid in black lines) as detected by RICH1 as result of a typical LHCb simulated event. Red (blue) squares represent the hits accepted (rejected) by the reconstruction algorithm.

gle, as shown in Figure 2.18. These HPD arrays must be shielded from the strong magnetic field and placed out of the acceptance to reduce the material budget the particles must travel through. In order to achieve this and also reducing the length of the detector structure, the light cones produced by particles are reflected through the use of an optical system of mirrors to the HPD arrays. Schematic images of both RICH1 and RICH2 can be seen in Figure 2.19.

2.4.2 Calorimeters

LHCb employs a calorimeter system for several purposes [49, 64]. It provides identification of electrons, photons and hadrons as well as the measurement of their energies and positions. The previously described subsystems have the minimal material budget in order to reduce as much as possible the energy losses of the passing particles, permitting them to transit downstream of the detector. In the calorimeters the aim is the contrary, particles must deposit all their energy through subsequent decays within

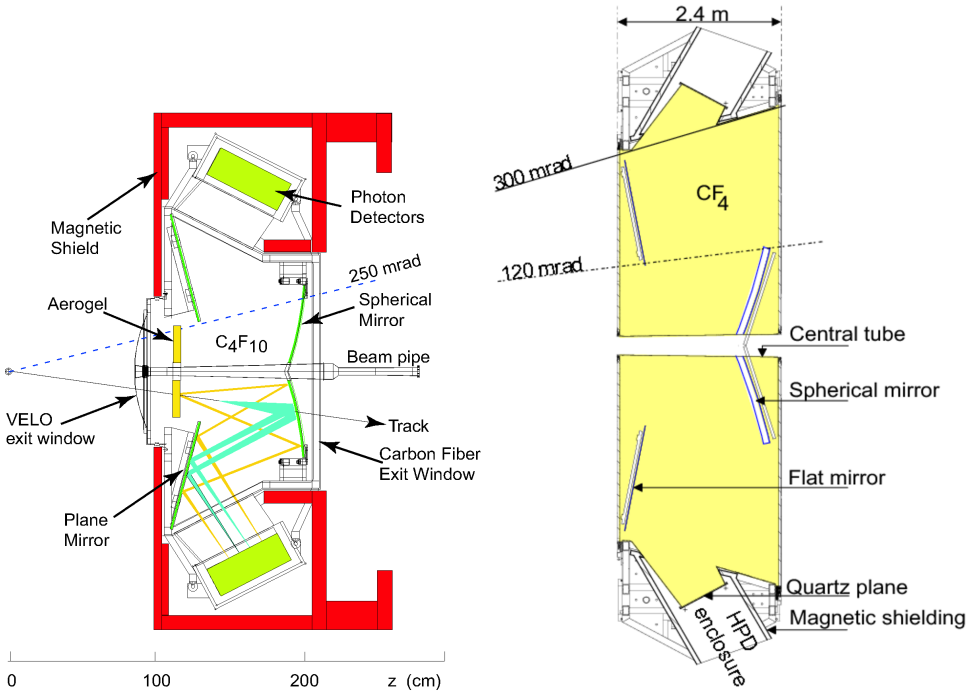

Figure 2.19: Transversal schematic views of the RICH1 (left) and RICH2 (right) detectors.

the confines of the detector material. This allows measurements of the particles' energies, even neutral ones that leave no tracks in the tracking and RICH detectors.

The calorimeter system in LHCb consists of an Electromagnetic Calorimeter (ECAL) followed by a Hadronic Calorimeter (HCAL). The ECAL includes the Scintillator Pad Detector (SPD) and the Preshower Detector (PS) subsystems which are necessary to reject charged and neutral pion background measurements. The SPD determines if the particles hitting the system are charged or neutral, while the PS indicates the electromagnetic character of the particle, e.g. whether it is an electron or pion. All these systems perform in the same way: the light emitted by the scintillating material that traps the particles is conducted via optical fiber to a photo-multiplier (PMT). All of these detectors adopt a variable lateral segmentation, shown in Figure 2.20, to compensate for the particle flux's inverse correlation with distance from the beam. The hit density varies by two orders of magnitude over the calorimeter surface. For the ECAL and SPD/PS the segmentation is made in three distinct regions, while for the

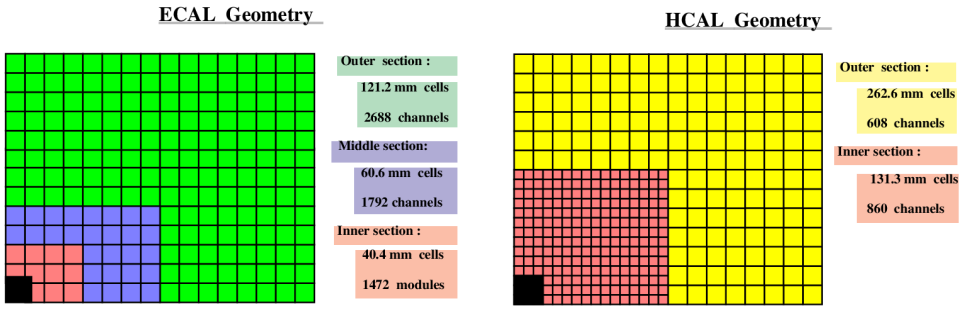

Figure 2.20: Transverse segmentation of the LHCb calorimeters. The SPD and PS detectors' segmentation follows the same configuration as the ECAL.

HCAL only two regions are employed, owing to the differences between the dimensions of electromagnetic and hadronic showers.

SPD/PS

The SPD/PS detector is a 15 mm thick lead converter sandwiched between planes of scintillating material segmented as shown in Figure 2.20. The total sensitive area is a rectangle 7.6 m wide and 6.2 m high, covering the full LHCb angular acceptance. This detector is segmented with its cells matching those of the ECAL, as shown in Figure 2.20. To provide the same angular projection, the dimensions of the SPD cells are smaller than those in the PS by a factor $\sim$0.45%.

The SPD is used to separate photons from electrons. Charged particles deposit energy in the scintillator material, while neutral particles pass undetected. Photons can be misidentified as charged if they convert into e^+e^- pairs in detector material before the SPD or if they produce charged particles inside the SPD material. Another source of misidentification is the backsplash, backwards moving charged particles produced in the lead converter between the SPD and the PS. Test beams showed that the probability of misidentification of photons with energies in the range 20 to 50 GeV is 0.8% when requiring a threshold of 0.7 Minimum Ionizing Particles (MIPs) for detection.

Separation of charged pions from electrons is done with the PS by measuring the shower dispersion after interaction with the lead plate. In test beams, with a threshold of 4 MIPs, charged pion rejection factors of 99.6%, 99.6% and 99.7% with electron retentions of 91%, 92% and 97% are

achieved for 10, 20 and 50 GeV/c momentum particles, respectively.

ECAL

The design for the LHCb Electromagnetic Calorimeter (ECAL) is based on the requirement of modest energy resolution coupled with fast time response and acceptable radiation resistance [65]. The *shashlik* technology has proven to be reliable in previous experiments [66, 67] and a sensible choice for LHCb. It consists of a sampling scintillator/lead structure read-out by plastic wavelength-shifting optical fibers. These fibers are perpendicular to the scintillator and transport the light to photomultiplier tubes (PMTs) for measurement. The energy resolution is, by design, given by

$$\frac{\sigma_E}{E} = \frac{10\%}{\sqrt{E}} \oplus 1\% \quad (E \text{ in GeV}),$$

where the first term comes from the statistical fluctuation of the shower and the second comes from the systematic uncertainties of the calibration.

The ECAL covers the angular acceptance from 25 mrad to 300 mrad in the bending (horizontal) and 250 mrad in the non-bending (vertical) planes. While the outer limits match the projection of the tracking system's angular acceptance, the inner acceptance is limited to reduce the radiation dose level to the detector. The segmentation of the calorimeter, pictured in Figure 2.20 (left), responds to the variation in hit density that ranges over two orders of magnitude from the nearest regions of the beam pipe towards the farthest regions. The ECAL is divided in three regions: inner, middle and outer, with square cell sizes of 40.4 mm, 60.6 mm and 121.2 mm sides, respectively. Each cell is built from 66 alternating layers of 2 mm thick lead plates, 120 μm thick white, reflecting TYVEK paper[2] and 4 mm thick scintillator tiles. The scintillating material is polystyrene doped with 2.5% PTP[3] and 0.01% POPOP[4]. The stack measures 42 cm in total and corresponds to 25 interaction lengths (X_0), enough to contain the full electromagnetic shower of high energy photons. Each of these stacks is wrapped in black paper to ensure light tightness in order to avoid cross-feed between cells. A final outer layer of 100 μm steel foil encloses the cell stack.

The performance of the ECAL was studied using test beams [71]. The response of the modules was found to be uniform within 8%. The results

[2] A brand of high-density polyethylene fiber.

[3] p-Terphenyl, a commonly used organic scintillator [68].

[4] 1,4-bis(5-phenyloxazol-2-yl) benzene, a well known secondary scintillator used to shift wavelengths towards longer values in order to improve energy resolution [69, 70].

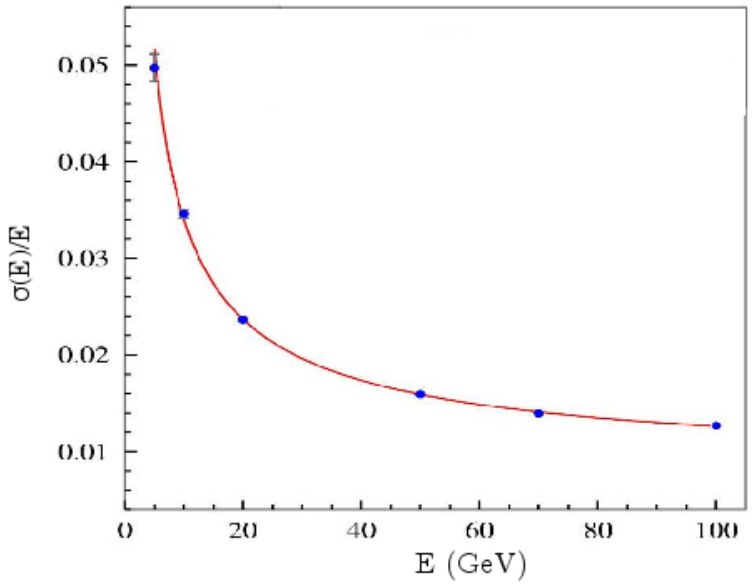

Figure 2.21: Energy resolution one of the outer ECAL region modules as measured in the test beam with electrons in a 30×60 mm surface.

for the energy resolution are shown in Figure 2.21. These points can be parametrized with a curve given by

$$\frac{\sigma_E}{E} = \frac{a}{\sqrt{E}} \oplus b \oplus \frac{c}{E},$$

where a, b and c stand for the stochastic, constant and noise terms, respectively. Depending on the module region and beam conditions the stochastic and constant terms were measured to be $8.5\% < a < 9.5\%$ and $b \approx 0.8\%$, in good agreement with the aforementioned design resolution.

The invariant mass resolution of radiative decays is dominated by the ECAL momentum resolution, and therefore worse than decays reconstructed through charged tracks. The B^0 mass resolution in $B^0 \to K^{*0}(892)\gamma$ is of 93 MeV/c^2, equivalent to a relative mass resolution of $\sigma_m/m = 1.76\%$, as opposed to the dimuon decays of J/ψ and Υ resonances, with a relative mass resolution of $\sigma_m/m = 0.5\%$ [51].

ECAL calibration

As the detector is exposed to the radiation flux, the scintillating material and optical fibers age and their performance deteriorates over time. This is an expected and unavoidable behaviour of radiation detectors. To account

for this, the gain of the detector must be scaled by a correction factor in order to ensure a precise performance. Since the aging process is stochastic in nature it is impossible to predict the correction factor in advance.

The main calibration strategy involves reconstructing π^0 mesons from two separate clusters in the ECAL and fitting the mass peak. The factor can be calculated by comparing the value of the peak mean to the nominal mass of the π^0.

Another strategy is comparing the energy deposited by an electron and to it's momentum calculated from its track. Since the electrons reaching the ECAL have small masses compared to their momentum, the distribution of the ratio $\frac{E}{p}$ should peak at 1.

HCAL

The LHCb Hadronic Calorimeter (HCAL) is similar to the ECAL in the design of the cells, utilizing alternating tiles of absorber and scintillating material. The main difference is that the orientation of the tiles run parallel to the beam axis, as shown in Figure 2.22. In the lateral direction the 3 mm tiles are interspersed with 1 cm iron absorber, whereas in the longitudinal direction the length of tiles and spacers correspond to the hadron interaction length in steel. The scintillator material is polystyrene mixed with 1.75% PTP and 0.05% POPOP. Each tile is wrapped in 120–150 μm thick TYVEK. The light is collected from the tiles' edges by WLS running along the detector towards the back side of the detector, where it is collected by PMTs.

As previously mentioned, the segmentation of the HCAL differs from the rest of the calorimetric system and only two regions are included in the design, as shown in Figure 2.20 (right). The inner region cells' surface is a 131.3 mm square, while the outer region has 262.6 mm sized squares.

The HCAL structure measures 8.4 m wide, 6.8 m high and 1.65 m long. The length is limited by space constraints in the cavern and with the configuration used, the material budget of the whole HCAL corresponds to only 5.6 X_0, insufficient to contain the full hadronic shower. Consequently, it gives an estimation of the hadron energy with a resolution, by design, of

$$\frac{\sigma_E}{E} = \frac{80\%}{\sqrt{E}} \oplus 10\% \quad (E \text{ in GeV}).$$

The performance of the HCAL was studied in a test-beam [71]. The response of the modules was found to be uniform within 3%. The resolution

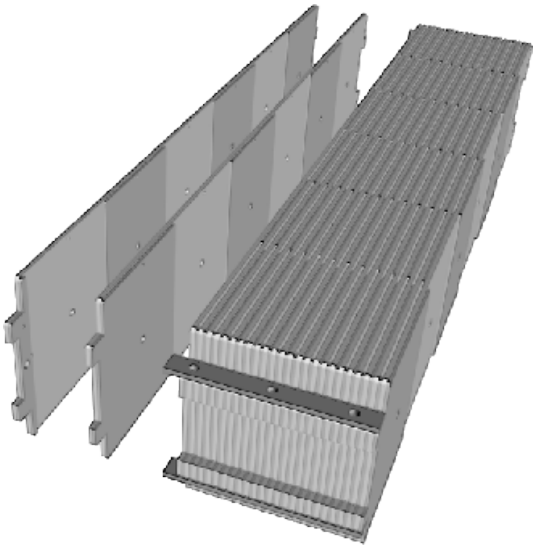

Figure 2.22: View of an HCAL module.

function fitted from data is

$$\frac{\sigma_E}{E} = \frac{(69 \pm 5)\%}{\sqrt{E}} \oplus (9 \pm 2)\% \quad (E \text{ in GeV}),$$

in good agreement with the design values.

2.4.3 Muon Detector

Muons have a long lifetime of $\tau_\mu \approx 2.2\,\mu s$, meaning a flight distance of $c\tau_\mu \approx 659\,m$. Along with a low interaction probability, this means that most muons fly through the whole detector. Muon detection systems must be designed with a large stopping power in mind to prevent the particles escaping unnoticed. Because of this, they are placed in the furthermost region from the interaction point, so that they only affect the most penetrating particles.

The LHCb muon system is composed of five rectangular stations, named M1–M5, placed along the beam axis [49, 72–74]. The full system is composed of 1380 chambers covering a total active area of 435 m^2. The angular acceptance of the muon system is 20–306 mrad in the bending (horizontal) plane and 16–258 mrad in the non-bending (vertical) plane. This corresponds to an acceptance of $\sim$20% for muons from inclusive b semileptonic decays.

Stations M2–M5 are placed downstream of the calorimeters and are interleaved with 80 cm thick iron absorbers to select penetrating muons.

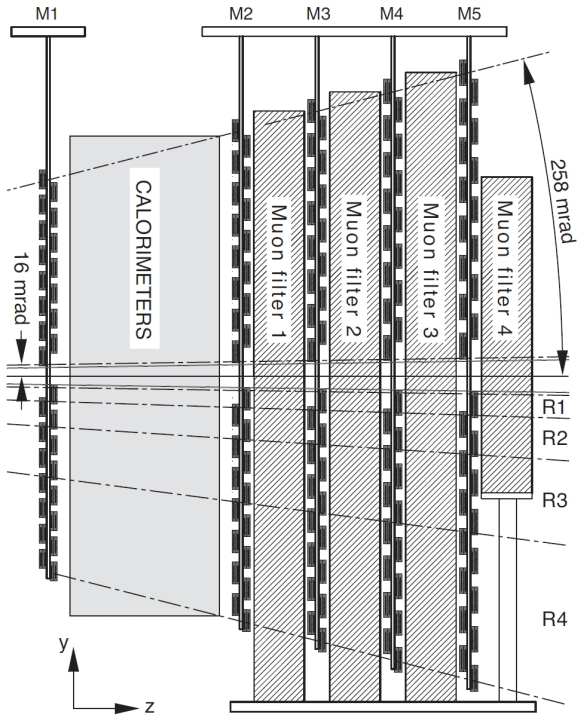

Figure 2.23: Schematic side view of the muon system.

Including the calorimeter system, this results in an absorber thickness of 20 X_0, requiring a minimum momentum of 6 GeV/c for a muon to cross all five stations. Station M1 is placed in front of the calorimeters and is used to improve fast response p_T measurements for the trigger decisions. Each subsequent station's transverse geometry is larger in scale than the previous counterpart with the aim to maintain the angular acceptance constant along the system. The layout of the muon system is pictured in Figure 2.23.

Each station is divided into four regions, labeled R1 to R4, with increasing distance from the beam axis. The linear dimensions of the regions and their segmentations scale in the ratio 1:2:4:8, as pictured in Figure 2.24. The particle flux and channel occupancy should be uniform over the four regions with this geometry. Stations M1–M3 have a high spatial resolution along the x coordinate (bending plane), since they are used to define the track direction and calculate the muon candidate p_T with a resolution of 20%. The remaining stations, M4 and M5, have limited spatial resolution,

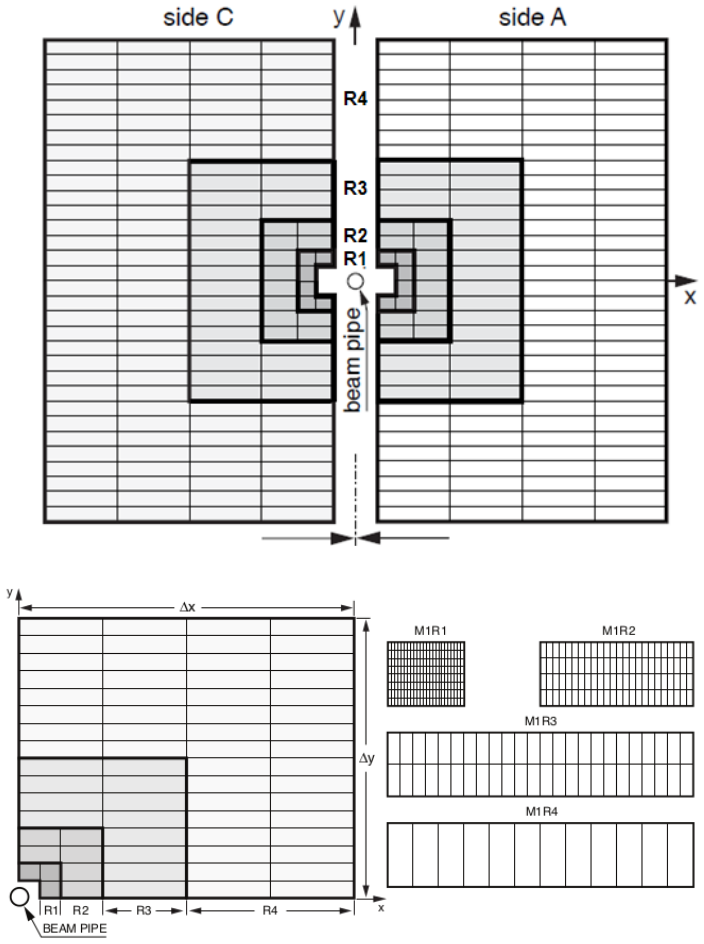

Figure 2.24: Top: layout of a complete muon station. Middle: a quadrant of M1 station. Each rectangle represents one chamber. Bottom: division into logical pads of four chambers belonging to the four regions of station M1. In stations M2, M3 (M4, M5) the number of pad columns per chamber is double (half) the number in the corresponding region of station M1, while the number of pad rows is the same.

as their main purpose is the identification of penetrating particles. The granularity of each station and region is pictured in Figure 2.24 (right)- The sizes of the logical pads scale accordingly to the region and the station and determine the x, y resolution.

The detector technology used in the muon system are multi-wire proportional chambers (MWPCs) for all regions, except for the innermost region of M1, M1R1, where triple gas electron multiplier (GEM) detectors are

used. The choice of triple-GEMs for this region stems from the expected particle rate in the M1R1 region, which exceeds safety limits for MWPC detector aging.

2.4.4 PID algorithms

The PID information obtained separately from the muon, RICH, and calorimeter systems is combined to provide a single set of more powerful variables. Two different approaches are used. In the first method (DLLx variables, where x is the particle hypothesis being tested) the likelihood information produced by each sub-system is simply added linearly, to form a set of combined likelihoods. These variables give a measure of how likely the mass hypothesis under consideration is, for any given track, relative to the pion hypothesis. The DLL for a particle of type a is then given by

$$\mathrm{DLL}_a = \Delta \ln \mathcal{L}_{a\pi} = \ln \mathcal{L}_a - \ln \mathcal{L}_\pi = \ln \left[\frac{\mathcal{L}_a}{\mathcal{L}_\pi} \right],$$

where $\mathcal{L}_a$ is the sum of the information of the subdetectors used for the identification. Using these variables one can define a DLL for any two particle types a and b as

$$\mathrm{DLL}_{ab} = \Delta \ln \mathcal{L}_{ab} = \ln \mathcal{L}_{a\pi} - \ln \mathcal{L}_{b\pi} = \ln \left[\frac{\mathcal{L}_a}{\mathcal{L}_b} \right] = \mathrm{DLL}_a - \mathrm{DLL}_b.$$

This has some limitations since it assumes the output of each subdetector can be presented as a log-likelihood, and therefore it needs rescaling the responses of some subsystems. It also omits detector information that cannot be linearized. A second approach (ProbNNx variables, where x refers to the particle hypothesis being tested) has been subsequently developed to improve upon the simple log-likelihood variables both by taking into account correlations between the detector systems and also by including additional information. This is carried out using non-linear multivariate techniques, combining PID information from each sub-system into a single probability value for each particle hypothesis.

A comparison of performances for both algorithms on simulated long pion and kaon tracks is pictured in Figure 2.25, where the performance improvement of ProbNN over DLL is evident.

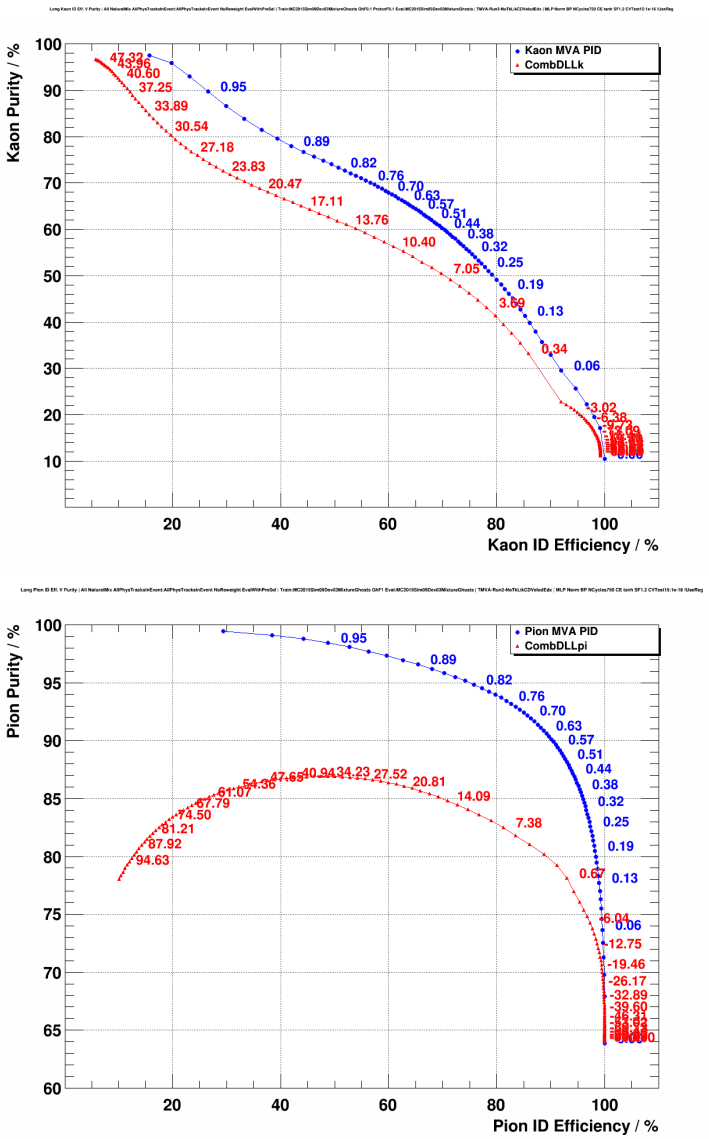

Figure 2.25: Performances of different cuts (values shown next to the curve) on the DLLx (red triangles) and ProbNN (blue circles) PID variables for long kaon (top) and pion (bottom) tracks, from simulation.

For electromagnetic objects two additional algorithms exist. One of these produces an estimator of the separation of photons from merged[5] π^0 with

[5]Meaning that the two photons from an energetic ($E_T > 2.5\,\text{GeV}$) π^0 decay are collimated and leave a single cluster signal.

a multivariate discriminator based on the shape of the clusters in the ECAL and PS. The second one distinguishes photons from charged tracks, mainly electrons, in the form of a "photon confidence level", defined as

$$\mathrm{CL} = \frac{\tanh(\Delta \ln \mathcal{L}) + 1}{2},$$

where the likelihood, $\mathcal{L}$, is obtained by combining the track-matching criteria with the information of the PS, SPD and ECAL detectors for the photon and non-photon hypotheses.

2.5 Online system

The purpose of the LHCb online system [49, 75, 76] is to ensure the data transfer from the front-end electronics (FEE) to the permanent storage. It can be described in terms of three subsystems: the Data Acquisition system (DAQ), the Timing and Fast Control system (TFC) and the Experiment Control System (ECS). A diagram showing the structure of the LHCb online system is pictured in Figure 2.26.

2.5.1 Data Acquisition System

The DAQ has the purpose of transporting the L0-accepted data in a given bunch crossing from the FEE to the permanent storage. Data arrive to the detector electronics and are buffered to LHCb-wide standarized readout boards (TELL1)[6] [77], placed outside the irradiated area via optical or analog links. These boards employ Field Programmable Gate Array (FPGA) technology and are designed to use simple protocols, a small number of components and are adaptable to changing system parameters. The boards have four pre-processing FPGAs where common-mode processing, zero-suppression or data compression is performed as needed by the different detectors. The resulting data packets are collected by a fifth FPGA (SyncLink) which formats it into a data packet able to be sent to the Event Builder computing farm, using Gigabit-Ethernet links. The Event Builder collates information from the subdetector for a single event and sends it to the HLT (see Section 2.6.2) for filtering and this in turn sends the data into permanent storage.

2.5.2 Timing and Fast Control

The TFC system drives all stages of the data readout of the LHCb detector between the FEE and the Event Filter Farm (EFF) by distributing the beam-synchronous clock, the L0 trigger, synchronous resets and fast control commands. The system is a combination of electronic components common to all LHC experiments and LHCb custom electronics and performs several tasks: the TFC optical distribution network transmits the beam-synchronous clock and features both a low-latency trigger channel

[6] The RICH detectors use a specific boards, UKL1, which are functionally identical to TELL1 from the data acquisition point of view.

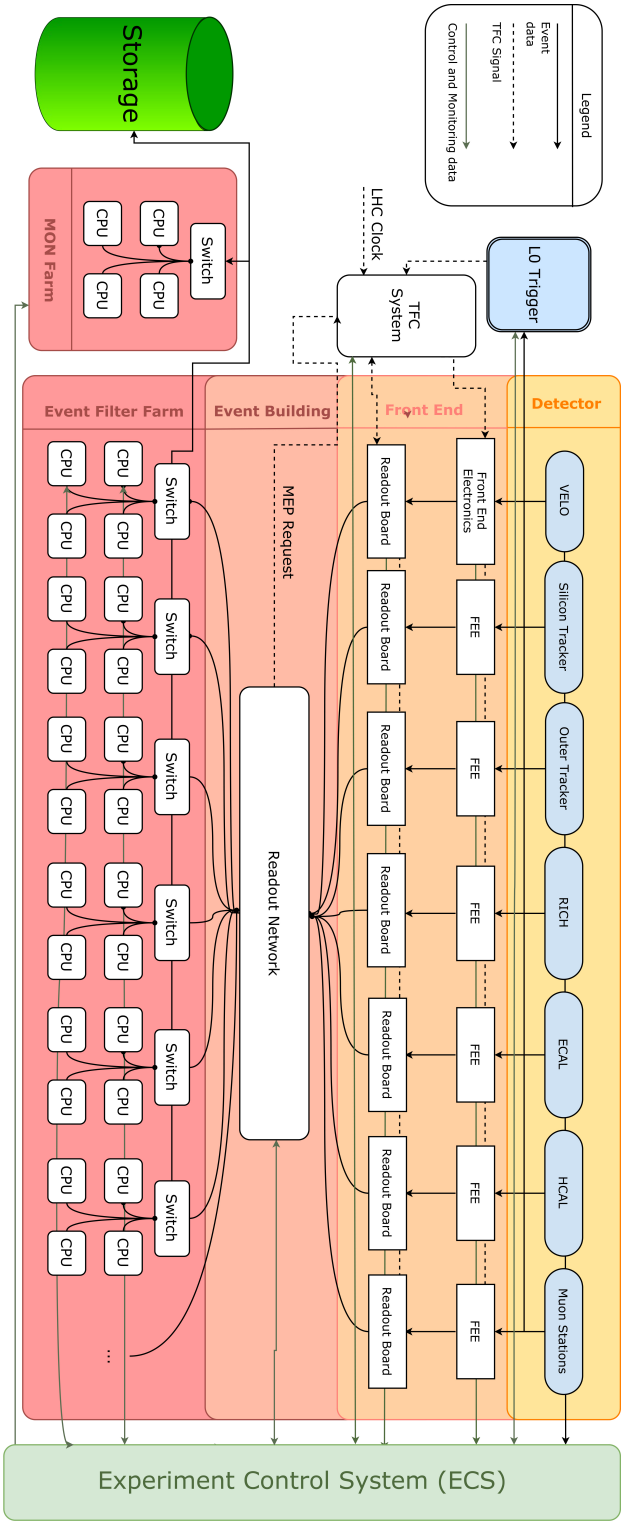

Figure 2.26: General architecture of the online system.

and a second channel used to encode control commands; the Readout Supervisor, the most important part of the system, implements the interface between the LHCb trigger and readout chain, synchronizing trigger decisions and beam-synchronous commands to the LHC clock and orbit signal supplied by the LHC; and the optical throttle network is used to transmit a trigger inhibit from the asynchronous parts of the readout system to the Readout Supervisor in case of congestion of the data pad. The Readout Supervisor can also perform load balancing among the nodes in the EFF by dynamically selecting the destination node for the incoming events, and can also produce a variety of auto-triggers for sub-detector calibration and tests.

2.5.3 Experiment Control System

The ECS oversees the whole LHCb detector and ensures the control and monitoring of its operational state. Apart from the traditional control domains, such as high and low voltages, temperatures, gas flows or pressures, it also encompasses the control and monitoring of the Trigger, TFC and DAQ systems. The LHCb system is hierarchical and distributed, meaning that the control of the whole detector happens at the top level and of dedicated subtrees at correspondingly lower levels. At any level a tree can be released from higher control and operated in standalone mode. Commands are propagated down the hierarchy, while states and alarms go upwards.

2.6 Trigger system

The trigger is a logical decision system that determines which events are to be saved depending on the information taken from the detector subsystems. In LHCb [49,78] it consists of two different stages, reducing the large initial interaction rate, $\sim$ 10 MHz, to a rate manageable by the offline and storage system, $\sim$ kHz. For Run I, the operational values are 40 MHz and 5 kHz respectively. These trigger stages are the Level-0 trigger (L0) and the High Level Trigger (HLT). The L0 is implemented in custom electronics and operates synchonously with the LHC bunch-crossing frequency of 40 MHz. It reduces the rate of visible pp collisions, 10–15 MHz, down to 1.1 MHz that can be readout by the electronics of the detectors. The HLT is executed by an asynchronous processor farm, and is divided on two consecutive stages named HLT1 and HLT2. In the first one, a partial event

reconstruction is executed and decisions are taken to select high p_T and IP candidates, effectively reducing the rate down to 50 kHz. At this rate the HLT2 can perform a full event reconstruction and make more specific and elaborate decisions, further reducing the rate to the final 5 kHz that will be saved to disk. A diagram of the Trigger structure can be seen in Figure 2.27.

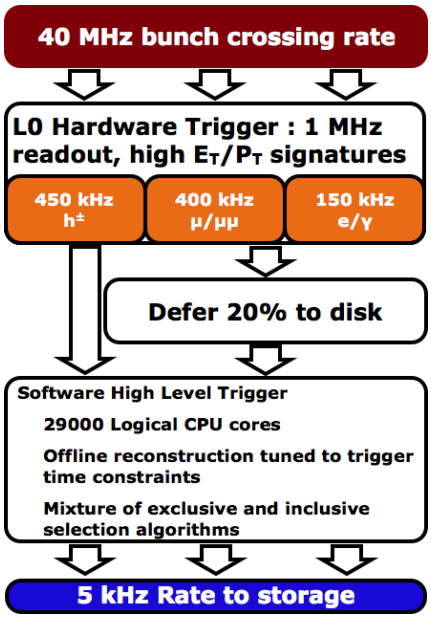

Figure 2.27: Diagram of the trigger structure during Run I.

2.6.1 Level-0 Trigger

The L0 is divided in three components: the pile-up system, the L0 calorimeter trigger and the L0 muon trigger. Each of these is connected to one detector and provides information to the L0 Decision Unit (DU), which then evaluates the final decision.

The pile-up system is part of the VELO detector (see Section 2.3.2) and aims to distinguish between crossing with single and multiple visible interactions. It provides the position of the PV candidates along the beam-line and a measure of the total backward charged track multiplicity.

The calorimeter trigger system looks for high E_T particles: electrons, γ, π^0 or hadrons. It builds 2×2 clusters adding their E_T and selects the cluster with the highest E_T sum. The clusters are identified based on the

responses from the SPD, PS, ECAL and HCAL. The total number of SPD hits is counted to provide a measurement of the charged-track multiplicity of the event. To veto events with a large number of primary vertices, only events with up to 600 hits in the SPD are accepted.

The muon trigger selects the two muons with the highest p_T for each quadrant of the muon detector. The standalone muon reconstruction allows a 20% resolution on the muons' p_T.

The L0 DU collects all this information and performs simple logic to combine these signatures into a single decision per crossing. The latency of the L0 trigger is the time elapsed between the collision and the arrival of the trigger decision to the front-end electronics (FEE). In LHCb it is fixed to 4 μs. Not counting for the time-of-flight of the particles and the delays in cable and FEE transmissions, this leaves 2 μs for the processing of the data to derive the decision.

2.6.2 High Level Trigger

The High Level Trigger (HLT) consists of a C++ application running on the Online Event Filter Farm (EFF). For Run I, the EFF contained ∼29,000 logical CPU cores, a number to increase in future upgrades [79]. Each application has access to the complete event data and uses this to reduce the input 1.1 MHz rate down to 3 kHz in two stages. First, the HLT1 uses a partial reconstruction of the event to make a decision based on several criteria and reduces the rate down to ∼50 kHz. Then the HLT2 completes the reconstruction and evaluates a more stringent set of conditions to achieve the 3 kHz rate. They are detailed in the following sections.

HLT1

The main purpose of HLT1 is to perform independently of the data taking running conditions, which are susceptible to variations. Different condition sets, called lines, exist for this trigger stage. One, for example, selects events with at least a single high-momentum, good quality track with a large IP with respect to all primary vertices in the event. Lifetime unbiased muon and electron lines also exist. Designed for lifetime studies, they select events containing electrons or muons based on the confirmation of L0 muon decisions or L0 clusters, respectively.

A HLT1 decision takes ∼15 ms. While the HLT1 must reject ∼95% of the L0 input events, the efficiency on signal events for all of the LHCb

benchmark channels has been found to be above ∼80% [80,81]. The events selected by the HLT1 are passed on to the HLT2 stage.

HLT2

The rate at this stage is small enough to fully reconstruct most events. To avoid heavy calculations, Global Event Cuts (GECs), such as a limit on the event's charged track multiplicity, are used to reject complex events before the reconstruction, as they can delay the functioning of the HLT2 stage. Once reconstructed, the events can be evaluated in terms of physical variables more akin to those used in offline selections and, therefore, with analyses in mind. Several lines are comprised in this stage, both inclusive and exclusive. The former refers to lines that search for generic features of B and D decays, such as displaced vertices or dilepton pairs, whereas the latter corresponds to lines that specifically select a decay chain, with conditions similar to an offline selection.

Changes for Run II

During the first planned maintenance shutdown, called Long Stop 1 (LS1), the software trigger system was redesigned for operations at the planned increased centre-of-mass energy, from 7–8 TeV in Run I to 13 TeV for Run II. The improved trigger scheme allows event selection at a higher rate and with better information than previously. In Run I, approximately 20% of events were deferred and processed by the HLT between fills. For Run II, all events that pass a HLT1 decision are deferred while calibration algorithms are run. The spatial alignments of the VELO and the tracking stations are evaluated at the start of each fill, since the VELO is closed around the beam at every restart and opened at the end of operations. These calibrations ensure that the performance of the trigger replicates that of the offline reconstruction, reducing systematic effects.

For Run II, the computing resources have been increased and now both stages of the software trigger benefit from an enhanced output rate, namely 150 kHz for HLT1 and 12.5 kHz for HLT2, to be compared to the values for Run I of 50 kHz and 3 kHz, respectively.

An additional introduction is the so-called "Turbo" stream [82], the lines in which run a tighter selection and discard all raw detector data to produce an immediately available sample for the user to analyze. This skips the stripping reprocessing step, which occurs at a delayed stage, saving a considerable amount of time and computing resources.

2.7 Computing and data flow

The LHCb computing model [49, 83] is based on a distributed multi-tier regional centre model with CERN as Tier-0, six additional Tier-1 nodes and more than a hundred of Tier-2 centres. The Tier-1 centres are CNAF (Italy), GRIDKA (Germany), IN2P3 (France), NIKHEF/SARA (The Netherlands), PIC (Spain) and RAL (United Kingdom). CERN also performs as a Tier-1 centre. Tier-1 centres are responsible for the production-processing tasks, while the Tier-2 nodes are mainly devoted to the production of simulated events.

There are several phases in the processing of event data. The various stages normally follow each other sequentially, but some may be repeated a number of times. Raw data from the detector is stored entirely in the CERN node and replicas distributed across the six Tier-1 centres. This raw detector information is reconstructed into tracks and particle information in the Tier-1 nodes, and saved into Stripping Data Summary Tape (SDST) files, which contain the necessary information for further event filtering on terms of physical variables of the event components.

The SDST files are filtered using the full reconstruction of the events and with looser time constraints than in the HLT stage This is what is known as Stripping, and is further described in Chapter 3. Stripping produces Data Summary Tape (DST) files, and these are made accessible to users to further process and produce tuples for their analyses. With improvement of the reconstruction, alignment and stripping software and algorithms, several of these steps are reapplied during centralized data reprocessing campaigns.

2.7.1 Data processing software in LHCb

The LHCb software is based on the GAUDI [84, 85] architecture, which provides an object oriented framework for all the applications used in the experiment [83]. Its flexibility allows use along the entire LHCb processing chain both from Monte Carlo simulation and real data samples. Data persistency is based on the ROOT software [86, 87], a set of object oriented frameworks designed for the analysis and handling of large amounts of data. The software applications in LHCb are the following:

GAUSS The simulation of physical events following pp collisions in the LHCb detector is handled by the GAUSS software [88–91]. The PYTHIA software [92–94] is used to simulate the collision event with

its products and the associated four-momentum vectors. The decays of these products are simulated using either PYTHIA or an EVTGEN package [95] with custom LHCb tuning in the case of B hadrons. The final state radiation is handled by PHOTOS [96, 97] and the interaction of particles with the detector is simulated using the GEANT4 package [98]. The detector geometry and material data are stored in a database.

BOOLE The BOOLE software package [99] simulates the digitization of the enery depositions in the LHCb detector and L0 trigger, taking into account the interfering leftover interactions from previous pp events, the spillover. After a BOOLE pass, the simulated and real data are both treated equally by the rest of the processing software.

MOORE The MOORE package [100] is used to run the HLT in the online system, either processing real data from the LHCb DAQ system or simulated data from BOOLE. It can also be used to rerun the trigger offline on stored data, both real and simulated.

BRUNEL The actual reconstruction of events from hits, calorimetric deposits and other raw information into tracks and, eventually, particles is done by the BRUNEL package [101]. The output data are saved in ROOT-based files which can be processed by analysis software

DAVINCI The analysis and selection tools are contained within the DAVINCI software package [102]. It includes particle identification algorithms as those described in Section 2.4.4 and functions for vertex fitting, as well as several frameworks for users to operate with and extract the information from the events and store it in ROOT tuple formats. These frameworks exist both in C++ and PYTHON languages.

Changes for Run II

With the addition of turbo streams for Run II comes the inclusion of the newly-developed TESLA software application. The turbo stream uses the HLT level reconstruction and therefore bypasses the BRUNEL step. The purpose of TESLA is the formatting of the trigger output for compatibility with user-level tools, the calculation of additional variables not available at the HLT stage and the dumping of the unnecessary raw banks to trim the file size.

3 | Stripping

Data bandwidth usage and file storage in the LHCb experiment are major concerns. The physical limitations of the data buses and memory units require the filtering of the data recorded by the detector. Furthermore, the analysts' access to the data should be an efficient process, only needing to deal with the most relevant events instead of a cumbersome and time consuming search through the integral dataset that would unnecessarily take up additional computing resources. As described in Chapter 2 the data must pass a selection chain for the systems to cope with the volume and for easy access for the end users, the analysts. This chain starts with the different trigger stages before being saved to disk and finally processed through the stripping algorithms to produce manageable datasets tailored to the physics program objectives.

Strictly speaking, the stripping project [103] is a series of offline selection algorithms run over data to produce user accessible copies of relevant selected data events. The stripping is divided in particular lines, these in turn grouped into streams. Each stripping line is designed with a particular analysis, group of analyses, or physics case in mind. During the design stage a compromise between bandwidth, usefulness and versatility must be found, as users have to determine the most relevant information required for their particular cases.

Members of the LHCb collaboration are expected to perform service tasks that benefit the whole collaboration, aiding the effort to keep it running smoothly. These tasks include software and hardware maintenance and operational shifts, among others. Some tasks related to the stripping, concretely the design and maintenance of the Radiative Decays Analysis Subworking Group stripping line code, and the coordination between the authors of the Rare Decays Working Group and the stripping coordinators, was done by the author as part of his Ph.D. studentship.

3.1 Stripping framework

Stripping campaigns

Stripping releases are planned regularly to process the data as it is recorded. The campaigns are scheduled by the LHCb Operations Planning Group (OPG), with considerable feedback from the Physics Planning Group (PPG). Generally a couple campaigns per year are expected, and from the line author's standpoint can be distinguished broadly in two classes:

Full strippings are those which run all lines over the data recorded during a designated period, generally this being one or several years.

Incremental restrippings are iterations over the full strippings. Only lines with bug fixes or new lines are run.

The naming scheme for a Stripping release is a string with the general format `SXrYpZ`, where `SX` corresponds to the full stripping release, `rY` to the data taking period and `pZ` to the incremental restripping step, if any. The convention for the data taking period is arbitrarily chosen as `r1` for 2011, `r0` for 2012 and `r2` for 2013. For example, `S20r1p1` corresponds to the first restripping of 2011 data adding to the release of `S20`. Some exceptions exist to this rule, such as the stripping of proton-heavy ion collisions recorded at the end of Run I in early 2013, for which the stripping version is `S20r3`.

Ending the first data taking run of the LHC, the first long shutdown (LS1) started in February 2013 and operations were restarted in June 2015, marking the beginning of Run II. For Run II the naming convention hasn't fully followed this convention. The data year isn't included and the different releases just follow the `SX` sequential numbering. For example, `S23` is the first stripping of data in 2015 performed in August 2015, running over data including the luminosity ramp-up, while `S23r1` was run the next month and added the lines that were not yet ready in August. This contradicts the Run I usage of the `rY` whereas `S26`, being the first stripping of 2016 data, does not include any reference to the data-taking year in its nomenclature. To better illustrate this, a relation of the stripping versions since `S20`, along with their purpose and approximate commissioning date, is listed in Table 3.1.

To maintain the operations in order, a hierarchy was devised so that the workload was evenly distributed. The most common case is that of the line

Table 3.1: Stripping versions since S20.

Stripping version	Commissioning	Purpose	Notes
S20<r1>	Winter 2013	Reprocessing of 2011 and 2012 data	
S20r<0,1>p1	Spring 2013	Incremental restripping over S20	
S20r2	Spring 2013	Restripping of 2013 data	
S20r3	June 2013	Stripping of 2013 Pb-p data	
S20r<0,1>p2	Autumn 2013	"	Stripping version used for the $B_s^0 \to \phi\gamma$ photon polarization analysis
S20r<0,1>p3	Winter 2014	"	Test inclusive algorithm for radiative lines
S21	December 2014	*Legacy Stripping* of Run I data	Last frequent reprocessing of Run I data, microDST enforced hereafter
S22	July 2015	Stripping of 2015 early data	First Run II stripping
S23	August 2015	Stripping of 2015 25ns data	
S23r1	September 2015	Second stripping of 2015 25ns data	
S22b	November 2015	Stripping of 2015 5 TeV data	
S24	February 2016	Restripping of 2015 data	
S25	February 2016	Stripping of November 2015	Heavy ion collision data
S21r<0,1>p1	March 2016	Incremental restripping of Run I data	
S26	April 2016	Online stripping of 2016 data	

authors, analysts in charge of writing and maintaining their own lines. No actual rules exist that enforce the number of authors in a group since the limits are set on the lines, as will be discussed shortly. Authors report to the stripping liaisons, who coordinate the lines of a single working group. Generally there is a single liaison per working group, but some working groups might maintain more if the number of lines is unmanageable. During a stripping campaign, the liaison is in charge of collecting all the lines from all the authors in his or her working group, testing them as a whole and reporting any irregularities back to the authors for adjustment. The liaisons then report to the coordinators, in charge of the package releases. At any time there are two stripping coordinators, who are in direct contact with the OPG and organize the campaigns. Before any release, they test all the stripping lines included in that particular campaign, and report back to the liaisons and users any issues.

A stripping line, in terms of code, consists of reconstruction and selection algorithms based on the DAVINCI package alongside a configuration dictionary with the values of the different parameters for the algorithm. The offline software automatically builds the code objects corresponding to the recorded tracks in a particular event, with associated properties such as mass, momenta, etc. These common particles can be used as input by the user to build the desired decay chain up to the mother. Along this chain the author can impose different selection requirements to the input particles. The values for the selection criteria are defined in a specific section of the code called the configuration dictionary.

When a particular physics case isn't covered by any of the existing lines, analysts request the addition of new lines to their Working Group (WG) conveners. After their approval, authors write the algorithms and report to their corresponding liaison for inclusion in the next campaign. During a campaign the liaison collects the configuration dictionaries of these new lines and any other that will run, and commits them all for their WG so that the configuration is fixed.

The total bandwidth allocated to a full stripping is currently 60 Mbyte/s, and this must be distributed along all the lines present in the experiment. The maximum bandwidth of incremental restrippings should be no more than 20% of the full stripping, e.g. 12 Mbyte/s. Each of the working groups has an assigned bandwidth as agreed in the PPG, and depends mostly on the type of analyses and previous performance of each group, in an effort to make an efficient and fair use of the computing resources. The contribution from each line to the bandwidth can be calculated as the product

of the rate of the line, which depends only on the selection efficiency of its algorithm, times the file size, which depends on the type of file chosen for that particular line.

3.1.1 Stripping lines' format

Currently, two file formats exist for the stripping outputs, Full Data Summary Tape (`FullDST`) and Micro Data Summary Tape (`microDST`). In the first one all the tracks of every candidate event are saved, thus having a larger file size, but allowing subsequent offline calculations involving those tracks. For example, one such calculation is the isolation information of the candidate, in which the candidate is refitted changing one or more of the original tracks with those in the vicinity and studying the χ^2 of the fit, as a measurement of certainty on the chosen tracks for the decay tree. In the `microDST` format only those tracks relevant to the decay tree are saved and any offline reprocessing that requires additional tracks is impossible. However, these types of calculations can be done online and the results saved with the candidates using the `RelatedInfoTools` package. In this framework users have developed several algorithms for producing track sensitive variables online such as adaptations of the isolation variable mentioned before or cone angle variables, which measure the spread of tracks within a solid angle measured from a particular point. In this way considerable amounts of memory can be saved by discarding the tracks once the calculations are completed, with the downside that further iterations are impossible on the `microDST`.

To address this, for lines going to `microDST` a copy of all the event tracks for the candidates may be requested to be stored in a common `FullDST` file called `MDST.DST`. If, after the stripping campaign, analysts require track sensitive information other than that requested originally, they may design a `RelatedInfoTools` algorithm that recovers whatever is needed. However, access to these copies is barred to end users and only in periodical centralized productions can they request any new or updated `RelatedInfoTools` algorithms to run. Differently from common stripping productions, in which all events are filtered, `MDST.DST` reprocessings only concern the calculations of the new algorithms on the tracks of the same candidates originally saved in the corresponding stripping.

Additionally to file formats, `RelatedInfoTools` and `MDST.DST` copies, line authors can request raw information, such as hits, calorimeter deposits, etc., from different detector subsystems to be saved for their

candidates individually by lines, in case such information is needed. The available raw banks correspond to the following subsystems:

- Trigger,
- Hadronic calorimeter,
- Muon stations,
- Electromagnetic Calorimeter (including information from the PS and SPD systems),
- RICH,
- VELO,
- Tracker.

From Stripping 21 onwards only the trigger banks are stored by default and any others must be explicitly requested when writing the line code.

Beginning in `S21`, lines should generally go to `microDST` except for extreme cases where `FullDST` is necessary. These cases generally concern analysis techniques which focus on studying the additional tracks and their correlations with the candidate events, in which periodical access to this information is insufficient. For a line to go into `FullDST`, the approval of the WG conveners and stripping coordinators is mandatory, after reviewing the justification proposed by the analysts. Such requests are declined if a suitable solution can be provided using a combination of the previously mentioned tools in combination with the `microDST` format.

The reconstruction of an event in a stripping algorithm starts from the final decay products and works by combining these into intermediate parent states and repeating as needed until the sought mother particle is reached, recreating the decay chain in reverse order. At every step some conditions can be demanded from the particles in order to accept or reject them as valid candidates. The basic tool for this task is LOKI's `CombineParticles`, which follows the general structure:

```
Algorithm = CombineParticles(
            'name',
            DecayDescriptor = 'A -> X Y Z',
            DaughtersCuts = {
                            'X' : 'X_cut',
                            'Y' : 'Y_cut',
                            },
            CombinationCut = 'PreVertexCuts',
            MotherCut = 'PostVertexCuts'
            )
```

Following PYTHON language conventions:

- the name is a string arbitrarily defined by the author to call the object within the code;
- the `DecayDescriptor` parses a string which describes the composition of the object being built. In the example it describes an object A decaying into three bodies, X, Y and Z. The decay descriptor admits all particle names listed in the official LHCb particle table[1]. Other operators can be included, for example to demand the charge conjugates or optional radiated photons from charged particles in the chain. While at first sight it might appear that only physically allowed processes can be written, this string only tells the algorithm how to interpret the input and how to call the output, and this can be exploited to build inclusive objects under certain conditions;
- the three selection criteria (`'cut'`) configurations correspond to different stages of the combination, but all in general work with a string of variable cuts using the LOKI variable namespace:
  - `DaughtersCuts` are applied to the states before any combination, and with a PYTHON dictionary can be specified (as in the example) for each daughter particle. Passing a string instead would apply the same cut indifferently to each particle X, Y and Z.
  - `CombinationCut` is applied to the array of daughter particles. In this stage the sums of the input particle variables can be cut, such as the sum of their masses.

[1]Omitted here for brevity, a copy is hosted in [104]. Name examples include `'gamma'` for photons, `B_s~0` for the $\bar{B}^0_s$ meson, among many others up to 930 unique particles.

- `MotherCut` is applied after a vertex has been built from the daughters. Any cut regarding the vertex information or the mother particle, A, can only be applied here, as it is not built previously.

As it can be seen, this tool is extremely versatile, as decay chains of any complexity can be built, with precise selection in every step. Once configured, the combination algorithm is appended to the reconstruction algorithm sequence with the corresponding input containers assigned. In the above example this corresponds to the locations of X, Y and Z objects. These objects can be the output of previous `CombineParticles` algorithms or `CommonParticles`, built automatically at the start of the offline processing and available for all users. The `CommonParticles` include all basic final state tracks such as $\pi^{\pm}$ or $K^{\pm}$ as well as other more complex, yet commonly used, combinations, such as `Jpsi2MuMu`. Any decay channel reconstruction must start from these basic building blocks.

3.2 Radiative stripping

As their name implies, radiative decays feature electromagnetic processes, generally with photons in their final states. The differentiating features for the stripping of radiative channels arise from this fact, mostly owing to the feature that neutral particles do not leave tracks in the tracking devices to build a vertex. Therefore, radiative stripping lines must deal with the rejection of calorimetric backgrounds imposing reasonable minimum requirements on the momentum of the photon, as well as differentiation from other neutral objects such as π^0 s.

Converted photons are another possible case of radiative processes, and correspond to those photons that decay as an e^+e^- pair. While charged particles should leave tracks in the detector, in the case of converted photons it depends greatly on the position of conversion. If the photon converts after the bending magnet, the e^+e^- pair will leave a single cluster in the ECAL. The SPD detector's corresponding cells should determine if the cluster corresponds to charged particles, resolving the degeneracy with a γ or a π^0. The charged pair can leave tracks in the T-Stations, depending on the point of conversion. On the contrary, if it converts before the bending magnet, the oppositely charged particles will leave separate tracks and energy deposits in the ECAL, but the energy resolution will be worse than downstream conversions due to bremsstrahlung losses and multiple scat-

tering. Converted photon lines follow similar criteria to their calorimetric counterparts with some additional adjustments to the photon selection regarding the dielectron pair vertex quality and mass constraints.

Until `S20rXp2`, all radiative lines followed an exclusive strategy. This means each and every one of the decay channels of interest had a dedicated line, and lines for new channels were added specifically when needs for them were found. Afterwards, from `S20rXp3` and until the time of writing, the main stripping for radiative decays was replaced by an inclusive strategy, with exclusive lines kept and developed only for those few cases not covered in the inclusive strategy and for calibration purposes. Both will be described in the following subsections.

3.2.1 Exclusive radiative stripping strategies

Dedicated lines for the $B_s^0 \to \phi\gamma$ and $B^0 \to K^{*0}(892)\gamma$ decays have been operational in LHCb since at least `S12`, corresponding to the earliest stripping campaign documented. Other decay channels were progressively added in different versions of the stripping, but the concept of the algorithm endured few changes since its inception until `S20r0p3`, when most of the lines, covered by the newly introduced inclusive algorithm, were removed. The peak number of lines was reached in `S20`, as the incremental restrippings `S20rXp<1,2>` included only lines which had their selections adjusted or bugs fixed. In `S20` the channels which had a specific line are listed in Table 3.2, along with the respective final states through which they were selected.

The respective charge conjugates, if any, are implied and selected along with their counterparts with no flavour discrimination. In the list, repetitions of decay channels have been omitted for brevity, e.g. $\phi(1020)$ mesons in all lines are selected through $\phi \to K^+K^-$.

All of these lines are built in the same way, using the `CombineParticles` tool as described above to select final state particles to build the intermediate hadrons and again to build the mother of the decay chain, the b hadrons. In the exclusive lines, final state particles are chosen with the specific Particle Identification (PID) variables[2] required to form the particular hadron of the decay. These lines have been successfully used to complete several analyses; the `S20` versions of `StrippingB2PhiGamma_B2VG_Line` and `StrippingB2KstGamma_B2VG_Line` are present in the measurement of

[2]Variables that discriminate between K, π, p, e^- and γ.

Table 3.2: Radiative decays lines in S20.

Line name	Decay channel
StrippingB2PhiGamma_B2VG_Line	$B_s^0 \to \phi\gamma$ through $\phi \to K^+K^-$
StrippingB2KstarGamma_B2VG_Line	$B^0 \to K^{*0}(892)\gamma$ through $K^{*0}(892) \to K^\pm\pi^\mp$
StrippingB2RhoGamma_B2VG_Line	$B^0 \to \rho\gamma$ through $\rho \to \pi^+\pi^-$ [a]
StrippingB2OmegaGammaHHH_B2VG_Line	$B^0 \to \omega\gamma$ through $\omega \to \pi^+\pi^-\pi^0$
StrippingB2KstarIsoGamma_B2VG_Line	$B^+ \to K^{*+}\gamma$ through $K^{*+} \to K_S^0\pi^+$
StrippingB2K1Gamma_B2VG_Line	$B^0 \to K_1(1270)^+\gamma$ through $K_1(1270)^+ \to K^+\pi^-\pi^+$
StrippingB2KstarPiGamma_B2VPG_Line	$B^+ \to K^{*0}(892)\pi^+\gamma$
StrippingLb2PPiGammaLb2PPiGammaLine	$\Lambda_b^0 \to \Lambda^0\gamma$ through $\Lambda^0 \to p\pi^-$
StrippingLb2PKGammaLb2PKGammaLine	$\Lambda_b^0 \to \Lambda(1520)^0\gamma$ through $\Lambda(1520)^0 \to pK^-$
StrippingB2PhiGammaConv_B2VG_Line	Version of the $B_s^0 \to \phi\gamma$ line with converted photons, $\gamma \to e^+e^-$
StrippingB2KstarGammaConv_B2VG_Line	$B^0 \to K^{*0}(892)\gamma$ analogue of the above
StrippingB2PhiPi0Gamma<Merged,Resolved>_B2VPG_Line	$B^0 \to \phi(1020)\pi^0\gamma$ with variants for merged[b] and resolved[c] π^0 s
StrippingB2KstarPi0Gamma<Merged,Resolved>_B2VPG_Line	$B^0 \to K^{*0}(892)\pi^0\gamma$ analogue of the above
StrippingB2PhiKSGamma_B2VPG_Line	$B^0 \to \phi(1020)K_S^0\gamma$
StrippingB2KstarKSGamma_B2VPG_Line	$B^0 \to K^{*0}(892)K_S^0\gamma$
StrippingB2RhoKSGamma_B2VPG_Line	$B^0 \to \rho K_S^0\gamma$
StrippingBs2KstarKstarGamma_B2VVG_Line	$B_s^0 \to K^{*0}(892)K^{*0}(892)\gamma$
StrippingBs2KstarPhiGamma_B2VVG_Line	$B_s^0 \to K^{*0}(892)\phi(1020)\gamma$
StrippingB2KstarPhiGamma_B2VVG_Line	$B^0 \to K^{*0}(892)\phi(1020)\gamma$
StrippingBs2PhiPhiGamma_B2VVG_Line	$B_s^0 \to \phi(1020)\phi(1020)\gamma$

[a] With a ρ (770) meson mass window wide enough to cover the channel $B^0 \to \omega\gamma$ through $\omega \to \pi^+\pi^-$.
[b] Neutral pion reconstructed from its decay into two photons, both found as a single deposit in the ECAL.
[c] Neutral pion reconstructed from its decay into two photons, found as separate deposits in the ECAL.

the ratio of branching fractions of $B_s^0 \to \phi\gamma$ and $B^0 \to K^{*0}(892)\gamma$ [105] and the measurement of the *CP* asymmetry in $B^0 \to K^{*0}(892)\gamma$ decays [106]. The `S20r0p1` version of `StrippingB2K1Gamma_B2VG_Line` is used in the measurement of photon polarization in $B^\pm \to K^\pm\pi^\mp\pi^\pm\gamma$ [36].

An example of exclusive line configuration dictionary and its evolution is the $B_s^0 \to \phi\gamma$ line, shown in Table 3.3. For $B^0 \to K^{*0}(892)\gamma$ the configuration is completely analogous, just requiring a different PID on the π daughters from $K^{*0}(892) \to K^\pm\pi^\mp$ and an adequate mass window (ΔM) around the $K^{*0}(892)$ resonance. As it can be seen, the configuration varied with the tightening of Ghost Probability (GhostProb)[3] cuts in `S20rXp1` and then the removal of DIRA[4] and Flight Distance (FD)[5] cuts in `S20rXp2`. Cutting on these variables generated differences between the $B_s^0 \to \phi\gamma$ and $B^0 \to K^{*0}(892)\gamma$ proper time distributions as described in Chapter 4, thus the change was strictly necessary for time-dependent measurements.

3.2.2 Inclusive radiative stripping strategies

`S21` was foreseen to be the legacy restripping of all Run I data, meaning that it would be the main source for data recorded in 2011 and 2012 after the end of LS1, since computing resources needed to be allocated for the processing of posterior runs. Only in circumstances of clear necessity should the Run I be restripped. With these constraints in mind, a strategy was devised in order to maximize the versatility of the stripped Run I data. Tested originally in `S20rXp3`, the inclusive strategy takes advantage over the small event size of the `microDST` format in order to allow the loosest selection possible. When originally designed, the retentions were tested in comparison to the `S20r0p2` exclusive lines, and adjustments were made to the selection and algorithms to ensure maximum coverage of the previously covered cases. At the time of writing, the latest tested version of the inclusive stripping is that committed to `S26`, the online stripping of 2016 data.

To illustrate the point, an overview of the general functioning of the inclusive strategy follows. The algorithm first imports `StdAllNoPIDsPions` from the `CommonParticles`. These are charged

[3] Variable that determines the probability that a track is formed by combining random hits.

[4] Angle subtended between the flight path of a long-lived particle and the direction of its momentum.

[5] Distance between the production and decay vertex of a long-lived particle.

Table 3.3: Evolution of the $B_s^0 \to \phi\gamma$ exclusive stripping line, `StrippingB2PhiGamma_B2VG_Line`, configuration through different stripping releases.

Stripping release		S20	S20rXp1	S20rXp2
$K^\pm$ track χ^2/ndf		< 3	< 3	< 3
$K^\pm$ track GhostProb		< 0.5	< 0.4	< 0.4
$K^\pm$ track χ^2_{IP}		> 16	> 16	> 16
(K^+,K^-) min p	MeV/c	> 3000	> 3000	> 3000
(K^+,K^-) min p_{T}	MeV/c	> 500	> 500	> 500
(K^+,K^-) $\sum p_{\text{T}}$	MeV/c	> 1500	> 1500	> 1500
(K^+,K^-,γ) $\sum p_{\text{T}}$	MeV/c	> 5000	> 5000	> 5000
$\phi(1020)$ χ^2_{vtx}		< 9	< 9	< 9
$\phi(1020)$ ΔM	MeV/c^2	< 15	< 15	< 15
γ E_{T}	MeV/c	> 2500	> 2500	> 2500
γ γ Confidence Level (gammaCL)		> 0.25	> 0.25	> 0.25
B_s^0 χ^2_{IP}		< 9	< 9	< 9
B_s^0 χ^2_{vtx}		< 9	< 9	< 9
B_s^0 DIRA	mrad	< 20	< 20	Removed
B_s^0 χ^2_{FD}		> 81	> 81	Removed
B_s^0 Mass	MeV/c^2	$[4000, 7000]$	$[4000, 7000]$	$[4000, 7000]$

tracks in the detector, with no PID requirements, meaning that even though the mass hypothesis is that of a pion, any charged particle can be present in the container, generally pions, kaons and protons. Using the `CombineParticles` algorithm as described previously, the charged tracks are used to reconstruct composite objects made up of either 2, 3 or 4 tracks, only allowing singled charged combinations for 3 track objects. Different tools were tested for building objects with 3 or more tracks, as the computation time of so many possible combinations grows dangerously with a loose selection. The most efficient algorithm, with no loss of coverage, was found to be the `NBodyDecay` tool for building multibody decays. This tool was later made mandatory for such decays, starting in `S21`. Regardless of the number of tracks used, the mass window is commonly defined for these objects to be in the range $[0.0, 7.9]\,\mathrm{GeV}/c^2$, wide enough to accommodate all desired resonances, even when changing the mass hypotheses of the tracks. This large mass window allows pretty much any track combination, so further cuts must be introduced to deal with high retention rates coming from random combinatorics. Therefore, the tracks must form a good vertex with χ^2_{vtx}[6] smaller than 10 and the sum of the transverse[7] momenta, p_{T}, of all the tracks exceeds $1.5\,\mathrm{GeV}/c$, while the p_{T} of the object itself can't be less than $150\,\mathrm{MeV}/c$.

Once these objects are built, photons in the event are requested from the `StdLooseAllPhotons` containers and matched to the aforementioned object to build a generic B meson. When building this meson, further constraints are imposed. The minimum mass is now 3.28, 2.90, and $2.56\,\mathrm{GeV}/c^2$ for intermediate objects made up of 2, 3, and 4 tracks, respectively. The differences account for the different possible configurations of mass hypotheses' changes, accumulating with the number of tracks. The vertex of the B meson is required to have a maximum impact parameter[8], χ^2_{IP}, of 9 and a further cut on the vertex quality $\chi^2_{\mathrm{vtx}} < 9$ is imposed. The p_{T} sum of the photon and the intermediate object must exceed $5\,\mathrm{GeV}/c$, and the reconstructed p_{T} of the B meson must be above $200\,\mathrm{MeV}/c$.

This configures the decay chain of the common stripping lines. To further extend the usefulness of the module, there are versions of some lines that use converted photons, replace the final tracks with neutral particles as π^0 and K^0_{S} or add an additional photon. Other additional lines use Λ

[6] An estimator of the quality of the vertex, literally the χ^2 of the vertex fit.

[7] The transverse plane in LHCb is defined with the beam axis as its normal.

[8] The minimum distance of a track or point from another given point, generally the associated primary vertex.

baryons as intermediate states, not covered by the general algorithms because of the detachment of the long-lived baryon's decay vertex. An inventory of lines is listed in Table 3.4 along with a description of the topology selected.They are categorized by number of bodies[9] in the final state.

All these decay chains are built into stripping lines within DAVINCI's framework, where the additional configuration is set. Here, all lines have `MDST.DST` support, all raw banks, and tagging information, enabled. Additionally, a trigger filter is applied to all lines, meaning that only events that are Trigger Independent of Signal (TIS) or Trigger On Signal (TOS) on a determined list of lines will be saved. The list of lines for the inclusive radiative stripping includes belong exclusively to the HLT2 stage and contain all of the radiative lines, all inclusive lines with a $\phi \to K^+K^-$ compatible final state and Boosted Decision Tree (BDT) based topological lines with final states of up to 4 bodies. The HLT is outlined in Section 2.6.2.

As mentioned before, after the introduction of the inclusive algorithm in `S20r0p3`, most lines were removed in favour of the inclusive format. However, some exclusive lines were kept as the inclusive algorithm didn't cover the concrete cases, and some new others were added. These lines persist at the moment of writing for `S24` and cover the cases listed in Table 3.5.

These lines provide coverage of a wide array of radiative decays, some allowing the realization of some key elements of the LHCb physics program and other opening windows for unplanned analyses and the search for new physics decay channels.

[9] Not counting the photon.

Table 3.4: Inclusive radiative stripping lines in `S21rXp1`, categorized by number of bodies, not counting the photon, in the final state.

Line name	Topology
Two body decays	
`StrippingBeauty2XGamma2pi_Line]`	2 charged tracks + γ
`StrippingBeauty2XGamma2pi_gammagamma_Line`	2 charged tracks + 2 γ's
`StrippingBeauty2XGamma2pi_wCNV<LL,DD>`[a]`_Line`	2 charged tracks + γ ($\rightarrow e^+e^-$)
`StrippingBeauty2XGammapi_Ks0_Line`	Charged track + K^0_S + γ
Three body decays	
`StrippingBeauty2XGamma3pi_Line`	3 charged tracks + γ
`StrippingBeauty2XGamma3pi_gammagamma_Line`	3 charged tracks + 2 γ's
`StrippingBeauty2XGamma3pi_wCNV<LL,DD>_Line`	3 charged tracks + γ ($\rightarrow e^+e^-$)
`StrippingBeauty2XGamma2pipi0<M,R>_Line`	2 charged tracks + π^0 + γ
`StrippingBeauty2XGammaphiOmega_2pipi0<M,R>_Line`	2 charged tracks + π^0 + γ[b]
`StrippingBeauty2XGamma2pi_Ks0_Line`	2 charged tracks + K^0_S + γ
Four body decays	
`StrippingBeauty2XGamma4pi_Line`	4 charged tracks + γ
`StrippingBeauty2XGamma3pi_Ks0_Line`	3 charged tracks + K^0_S + γ
`StrippingBeauty2XGamma3pipi0<M,R>_Line`	3 charged tracks + π^0 + γ
`StrippingBeauty2XGamma2pi_2Ks_Line`	2 charged tracks + 2 K^0_S's + γ
Decays including Λ as an intermediate state	
`StrippingBeauty2XGammapi_Lambda_Line`	Λ + charged track + γ
`StrippingBeauty2XGamma2pi_Lambda_Line`	Λ + 2 charged tracks + γ
`StrippingBeauty2XGamma3pi_Lambda_Line`	Λ + 3 charged tracks + γ

[a] Here `<x,y>` represents two variants of the same line, `<M,R>` for Merged and Resolved π^0's, respectively, and `<LL,DD>` for Long and Downstream dielectron tracks from a converted photon.

[b] Alternate version with a tighter mass window for the intermediate object and a relaxed p_T cut on the π^0 specifically made for studying the decays $\phi(1020) \rightarrow \pi^+\pi^-\pi^0$ and $\omega \rightarrow \pi^+\pi^-\pi^0$.

Table 3.5: Additional radiative stripping lines in `S21rXp1` for cases not covered by the inclusive strategy.

Line name	Details
`StrippingBeauty2XGammaExclusiveBs2PhiGammaLine`	Exclusive $B_s^0 \to \phi\gamma$ line with a tight selection based on `S20rXp2`, for track studies.
`StrippingBeauty2XGammaExclusiveBd2KstGammaLine`	Exclusive $B^0 \to K^{*0}(892)\gamma$ line based on its analogue from `S20rXp1`[a], with relaxed photon cuts, for the calibration of ECAL objects.
`StrippingBeauty2XGammaNoBiasBs2PhiGammaLine`	$B_s^0 \to \phi\gamma$ line with a very loose selection built around an exclusive proper time unbiased trigger line which drives the low retention rate, for time dependent analyses.
`StrippingBeauty2XGammaNoBiasBd2KstGammaLine`	The $B^0 \to K^{*0}(892)\gamma$ version of the above.
`StrippingLb2L0Gamma`	Lines for $\Lambda_b^0 \to \Lambda^0\gamma$, unreachable from the inclusive algorithm due to the non negligible lifetime of the trackless Λ baryon. A converted photon variant also exists.
`StrippingBs2GammaGamma_<*>Line`	Set of lines based on diverse combinations of photon conversions for $B_s^0 \to \gamma\gamma$, which has no hadron tracks and is therefore hidden from the inclusive algorithm.

[a] Including the DIRA and FD cuts.

4 | Reconstruction of $B \to V\gamma$ decays

This analysis focuses on obtaining a value of the $\mathcal{A}^{\Delta}$ parameter in $B_s^0 \to \phi\gamma$ through the study of its proper time distribution, related to the photon polarization fraction as described in Section 1.4. To achieve this goal, the first step involves obtaining a statistically significant sample of $B_s^0 \to \phi\gamma$ decays using an appropriate event selection sequence.

The signal channel is reconstructed matching a photon to a $\phi(1020)$ meson, reconstructed though the decay $\phi \to K^+K^-$, to then form the B_s^0 meson candidate. The flavour self-tagging decay $B^0 \to K^{*0}(892)\gamma$ with $K^{*0}(892) \to K^+\pi^-$, and similarly its *CP* conjugate $\bar{B}^0 \to \bar{K}^{*0}(892)\gamma$ with $\bar{K}^{*0}(892) \to K^-\pi^+$, is chosen as a control channel for its similarities to the signal one, with both being radiative decays to vector mesons, V with $V = \phi(1020), K^{*0}(892)$, these in turn reconstructed through opposite charged tracks. Hereafter, *CP* conjugate states are implied throughout the text unless otherwise specified. Some effects inherent to the detector itself or the reconstruction of displaced vertices are unavoidable and thus appear as time-dependent efficiencies, also known as the proper-time acceptance, as described in Section 6.2. With a selection such that the acceptance in $B^0 \to K^{*0}(892)\gamma$ is exactly the same as for $B_s^0 \to \phi\gamma$, computing the ratio of the reconstructed decay-time distributions of both channels eliminates the need of a complex parametrization, and reduces systematic uncertainties. The selection must then fulfill three objectives, chiefly, maximizing the yield of $B_s^0 \to \phi\gamma$ and $B^0 \to K^{*0}(892)\gamma$ events so as to reduce the statistical uncertainty, while at the same time reducing the combinatorial and physical background events to a minimum, and minimizing the differences between the acceptances of the aforementioned signal and control channels.

The current chapter first describes the data taking and simulation con-

ditions used for this purpose. Further on, the event selection and reconstruction strategies for the analysis are accounted for. Since the analysis deals with the same channels and conditions as a previous analysis measuring the ratio of $B_s^0 \to \phi\gamma$ and $B^0 \to K^{*0}(892)\gamma$ branching ratios [106], it is used as a starting point for the selection strategy. Some adjustments are needed for performing a time-dependent analysis, not in the scope of the aforementioned study.

4.1 Data samples and software versions

The data sample for this analysis was acquired during the first run of the LHC, spanning the years 2011 and 2012, and was taken at a centre-of-mass energy of $\sqrt{s} = 7\,\text{TeV}$ and $\sqrt{s} = 8\,\text{TeV}$, corresponding to a total integrated luminosity of $1\ \text{fb}^{-1}$ and $2\ \text{fb}^{-1}$, respectively. The 2011 data were stripped with stripping version `s20r1p2`, while the remaining $2\ \text{fb}^{-1}$ collected in 2012 were stripped with `s20r0p2`.

This analysis depends on several Monte Carlo (MC) simulation samples of the relevant channels, obtained from the centralized production at LHCb. The production aims to reproduce the running conditions and physical processes ongoing inside the detector, and are processed with the same software chain as real data, as discussed in Section 2.7.1. The channels and software versions for each simulated decay sample are listed in Table 4.1.

4.2 Event selection

4.2.1 Event reconstruction

As mentioned previously, the selection was tailored for both $B_s^0 \to \phi\gamma$ and $B^0 \to K^{*0}(892)\gamma$ events to maximize their yields, reducing the background contamination as much as possible, while minimizing the differences in proper-time reconstruction acceptance between both channels. With this in mind the selection is common for the signal and control channels, except for a few exceptions as detailed in this section.

The reconstruction chain of the events for both channels is analogous for both channels, barring flavor. The final state signature in the detector of a $B_s^0 \to \phi\gamma$ [$B^0 \to K^{*0}(892)\gamma$] decay appears as a pair of opposite charged hadronic tracks, corresponding to the K^+K^- [$K^\pm\pi^\mp$] pair; and an energy

Table 4.1: Summary of the main simultated samples used in this analysis.

Sample	GAUSS version	Statistics ($\times 10^6$)
Bd2KstGammaHighPt	sim08	9
Bs2PhiGammaHighPt	sim08	9
B2Rho0Gamma	sim06b	1
Bd2Rho0GammaHighPt	sim08a	3
Bd2OmegaGamma	sim06b	2
Bd_K+pi-pi0	sim08a	1.5
Lb2L1520Gamma	sim06b	1
Lb2L1670Gamma	sim06b	1
Bd2K1Gamma	sim06b	2
Bd2K1GammaHighPt	sim08a	1.5
Bu2K1410Gamma	sim06b	2
Bu2K1Gamma-mK1270	sim06b	2
Bu2K1Gamma-mK1400	sim06b	2
Bu2K1GammaHighPt-mK1270	sim08a	3
Bu2K1GammaHighPt-mK1400	sim08a	1
Bu2K2stGamma	sim06b	2
Bu2K2stGammaHighPt	sim08a	1
Bu_KstPigamma=HighPtGamma	sim08a	1.5
Bu2PhiKGamma	sim08a	1
Bu2PhiKGammaHighPt	sim08a	1.5
Bs2phiKsGamma	sim06b	1
Bs2PhiPi0Gamma	sim05	2
B2DmRhop	sim05	2
Bu_D0rho+_KSpipi	sim08a	1.5
Bu_D0rho+_Kpi	sim08a	1
Bu_D0rho+_Kpipi0	sim08a	1
Bu_D0rho+_Kpipipi	sim08a	1
Bu_K1eta_Kpipi=mK1270_gg	sim08a	2

deposit in the ECAL with no associated track, corresponding to the photon. The K^+K^- [$K^\pm\pi^\mp$] tracks come from the $\phi(1020)$ [$K^{*0}(892)$] vector meson as $\phi \to K^+K^-$ [$K^{*0}(892) \to K^\pm\pi^\mp$], and therefore both tracks must form a vertex in the detector. Since these decays follow from strong interactions, the proper time is extremely short, $\mathcal{O}(10^{-23})s$, and the meson decay vertex, called the Secondary Vertex (SV), essentially coincides with its pro-

duction point, the same point in which the mother B_s^0 [B^0] meson decays after a short flight in the detector, of approximately 1 cm in length, due to its non-negligible proper time, $\mathcal{O}(10^{-12})s$, and the boost with which it is produced. The momentum of the photon is added to the reconstructed vector meson to build the mother B meson at this point and the event is then fully built. The conditions for accepting or dismissing the many possible combinations are what conforms the selection of the events; starting with the trigger chain, on to the stripping requirements and finally via an offline selection.

4.2.2 Trigger chain

The trigger system is described thoroughly in Section 2.6, thus this section describes the specific trigger chain for this analysis. All trigger requirements are Trigger On Signal (TOS), meaning that the signal candidate objects are sufficient to trigger the event.

For radiative decays the first step is reducing combinatorics, requiring a high transversal energy, E_{T}, for the photon. This quantity is physically defined, for any calorimetric deposit, as

$$E_{\mathrm{T}} = \sqrt{m^2 + {p_{\mathrm{T}}}^2},$$

simplifying to $E_{\mathrm{T}} = p_{\mathrm{T}}$ in the case of the photon. This reduction is achieved in the L0 stage with a minimum requirement in the calorimeter unit for the E_{T} of the photon of 2.5, 2.72 and 2.96 GeV respectively for the data taking periods of 2011, early, and late 2012. The corresponding line is `L0Photon`, and the `L0Electron` line is added to accommodate converted photons. Alternatively, the events passing the high-p_{T} L0 lines of `L0PhotonHi` and `L0ElectronHi`, both with an E_{T} threshold of 4.2 GeV are accepted.

In the HLT1 stage the `Hlt1TrackAllL0` and `Hlt1TrackPhoton` lines are required to impose some requirements on the tracks. The former accepts events from the `L0Photon` and `L0Electron` lines, while the latter follows the high-p_{T} L0 lines. These select tracks with sufficient transverse momentum and impact parameter. For each line the specific requirements, including the corresponding L0 conditions, are detailed in Table 4.2.

Finally, in the HLT2 stage the exclusive lines for each channel are required, specifically `Hlt2Bs2PhiGamma` for $B_s^0 \to \phi\gamma$ and `Hlt2BdKstGamma` for $B^0 \to K^{*0}(892)\gamma$. In this stage the event is partially

reconstructed and mass and vertex requirements can be imposed, among others. The complete description of the cuts can be seen in Table 4.3.

A sketch of the possible trigger chains for the analysis is shown in Figure 4.1.

Table 4.2: Selection requirements applied in 2011 (2012) on the HLT1 lines relevant to radiative decays.

Line name		`Hlt1TrackAllL0`	`Hlt1TrackPhoton`
L0 channel		L0 physics	`L0PhotonHi` or `L0ElectronHi`
L0 photon requirements E_{T}	GeV	$> 2.5\,(2.72 - 2.96)$	> 4.2
VELO track hits		> 9	> 9
VELO missed hits		< 3	< 4
VELO track IP	µm	$--$ (> 100)	$--$ (> 100)
Track p	GeV/c	$> 10\,(3)$	$> 6\,(3)$
Track p_{T}	GeV/c	$> 1.7\,(1.6)$	> 1.2
Track χ^2		< 2	< 2
Track χ^2_{IP}		> 16	> 16

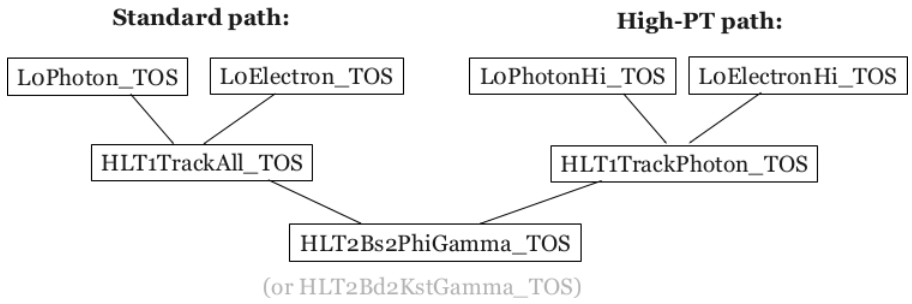

Figure 4.1: Schematic representation of the trigger path used to select $B^0_s \to \phi\gamma$ and $B^0 \to K^{*0}(892)\gamma$ decays.

4.2.3 Stripping and Offline Selection

As mentioned previously, $B^0_s \to \phi\gamma$ and $B^0 \to K^{*0}(892)\gamma$ events present themselves as a final signature of two tracks and an energy deposit in the ECAL. In terms of selection, for the reconstruction of signal events, some

Table 4.3: Selection of the HLT2 exclusive lines for the $B_s^0 \to \phi\gamma$ [$B^0 \to K^{*0}(892)\gamma$] channel.

Line name		`Hlt2Bs2PhiGamma` [`Hlt2Bd2KstGamma`]
L0 lines		`L0Photon` or `L0Electron`
HLT1		HLT1 Physics
Track p	MeV/c	> 3000
Track p_{T}	MeV/c	> 300
Track χ^2		< 5
Track χ^2_{IP}		> 20
V ΔM_{PDG}	MeV/c^2	< 20 [< 100]
V χ^2_{vtx}		< 25 [< 16]
Photon E_{T}	MeV	> 2600
B p_{T}	MeV/c	> 3000
B χ^2_{IP}		< 12
B DIRA	mrad	< 63 [< 45]
B ΔM_{PDG}	MeV/c^2	< 1000

guidelines are followed as listed below. The numbers indicate their correspondence in Table 4.4:

- The two tracks must:
  - **1** be of good quality, quantifiable via a small χ^2/ndof value of the track fit;
  - **2** come from a single particle and not be built from random hits in the detector from different sources;
  - **3** be separated from the primary vertex (PV), where the B meson is produced, meaning that their impact parameter (IP) — the distance of closest approach of the track to a given point — with respect to any PV in the event must be sufficiently large, evaluated through its χ^2;
  - **4–8** have high total and transverse momentum;
  - **9–11** be identified as a pair of oppositely charged kaons for the case of $B_s^0 \to \phi\gamma$ or a kaon and a pion for $B^0 \to K^{*0}(892)\gamma$;
  - **12** form a secondary vertex (SV), therefore having a small χ^2 value for the vertex fit;

13,14 have a reconstructed invariant mass compatible with that of the relevant vector meson.

- The photon must:

  15 have a high transverse energy deposit, E_T, in the ECAL;

  16 be discriminated from other particles using the CL variable (see Section 2.4.4);

  17 be sufficiently differentiated from neutral pions.

- The B meson must:

  18 have a large transverse momentum, p_T;

  19 come from a PV, meaning that it has a small reconstructed IP with respect to that point;

  20 have a good reconstructed vertex, evidenced as a small χ^2_{vtx} from the vertex fit;

  21 have a reconstructed invariant mass within a range compatible with the known B^0_s [B^0] mass value [4], but large enough to characterize the different background sources.

Both the stripping and the offline selections impose cuts (requirements) following these guidelines, with the main difference being that the former is a generic $B^0_s \to \phi\gamma$ [$B^0 \to K^{*0}(892)\gamma$] event filter arising as a necessity of the data storage system and the latter is a more stringent set defined specifically for further analysis. The stripping algorithms are described in Chapter 3, while what follows are the specific stripping requirements for the analysis. The versions used correspond to `S20rXp2` with `X` equal to 1 for 2011 data and equal to 2 for 2012 data. Selection configuration for both years is exactly the same.

Additional selection criteria to discriminate signal events from background, as cuts in the helicity angle (**22**) of the vector mesons or fiducial cuts related to the detection volume, are applied. These fiducial cuts consist of limiting the pseudorapidity range (**23**), setting a large but definite maximum momenta for the tracks (**24**), rejecting primary vertices far from the interaction point (**25**) and for events with more than one primary vertex, ensuring the B meson is sufficiently isolated (**26**).

The full selection requirements for both the stripping and the offline selections are listed in Table 4.4.

Table 4.4: Requirements for stripping and offline selections.

			Stripping `v20rXp2`	Offline selection
1	TRACK χ^2/ndf		< 3	–
2	TRACK GHOSTPROB		< 0.4	–
3	TRACK χ^2_{IP}		> 16	> 55
4	TRACKS MIN p	MeV/c	> 3000	–
5	TRACKS MIN p_{T}	MeV/c	> 500	–
6	TRACKS MAX p_{T}	MeV/c	–	> 1700 (> 1200 for Hlt1Photon)
7	TRACKS $\sum p_{\text{T}}$	MeV/c	> 1500	–
8	TRACKS AND γ $\sum p_{\text{T}}$	MeV/c	> 5000	–
9	$K^{\pm}$ PROBNNK		–	> 0.2
10	$\pi^{\pm}$ PROBNNPI		–	> 0.2
11	$\pi^{\pm}$ PROBNNK		–	< 0.2
12	V χ^2_{vtx}		< 9	–
13	$\phi(1020)$ ΔM	MeV/c^2	< 15	< 15
14	$K^{*0}(892)$ ΔM	MeV/c^2	< 150	< 100
15	γ E_{T}	MeV	> 2500	> 3000 (> 4200 for Hlt1Photon)
16	γ CL		> 0.25	–
17	γ/π^0 SEPARATION		–	> 0.6
18	B p_{T}	MeV/c	–	> 3000
19	B χ^2_{IP}		< 9	–
20	B χ^2_{vtx}		< 9	–
21	B MASS	MeV/c^2	$[4000, 7000]$	–
22	B HELICITY		–	< 0.8
23	TRACK η		–	$[2, 4.5]$
24	TRACK MAX p	GeV/c	–	< 100
25	PV z	mm	–	$[-100, 100]$
26	NPV > 1 && B $\chi^2_{\text{IP, NEXT BEST}}$		–	> 50
27	DIRA $B^0_s \to \phi\gamma$ [$B^0 \to K^{*0}(892)\gamma$]	mrad	–	< 60 (< 40)

The primary motivation of the selection values is optimizing the signal significance, defined as

$$\epsilon = \frac{S}{\sqrt{S+B}},$$

where S and B are the signal and combinatorial background yields, respectively. Monte Carlo (MC) simulations were used to extract the value for S, while the numbers for B were studied in the high-mass sideband of real data. The values for the cuts were optimized iteratively by studying each variable with the rest of the cuts kept at a fixed value until a maximum for ϵ was found. Figure 4.2 shows the optimization of the χ^2_{IP} of the tracks as an example.

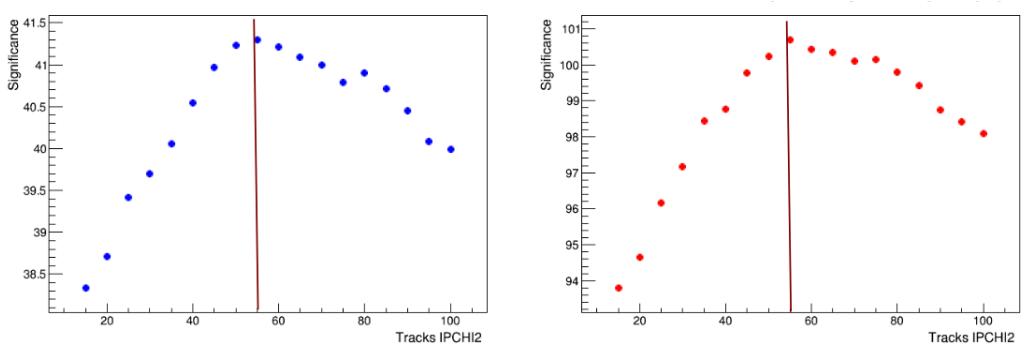

Figure 4.2: Optimization of the χ^2_{IP} (`IPCHI2` in the plot) requirement of the tracks. The requirement $\chi^2_{\text{IP}} >$ 55 maximizes the significance in both the $B^0_s \to \phi\gamma$ (left) and $B^0 \to K^{*0}(892)\gamma$ (right) samples.

To satisfy the other motivation of the selection, namely the minimization of differences in acceptance between both channels, the variables used in the selection were chosen from those well reproduced by the MC and those identified to inflict minimal effects in the relative acceptance ratio, as discussed in Section 6.2.

A notable exception exists, namely the direction angle (DIRA), defined as the angle between the line joining the PV to the SV and the direction of the reconstructed momentum of the B meson. This is a powerful variable to avoid background, as non-zero values could represent missing, wrongly reconstructed or combinatorial particles in the reconstruction. As neutral particles, photons do not precisely determine a direction in the detector to weigh the reconstructed momentum and while values populate the DIRA distribution around zero there is a significantly large width. Moreover, the DIRA distributions are quite distinct in the signal and control channel,

thus greatly affect the relative acceptance ratio, and should be avoided as much as possible. While the stripping patch of `S20rXp2` differs for the relevant lines in the removal of DIRA requirements in the selection with respect to previous versions, the exclusive trigger lines required for this study include cuts in this variable, as listed in Table 4.3. Since this requirement occurs at an intermediate state of the reconstruction an edge effect appears in the final reconstructed events, which must be dealt with. The offline values in Table 4.4 (**27**) then try to avoid this effect. As a consequence of these studies, for the Run-II[1] period of LHC proper-time-unbiased exclusive trigger lines for these channels were included.

Figures 4.3, 4.4, 4.5, 4.6, 4.7, and 4.8 show overlaid plots of MC samples and the background subtracted data[2] for different variables. There is general agreement between the variables, except for the fragmentation-related variables, namely the number of SPD hits and tracks. It is well known that the simulation does not reproduce perfectly these fragmentation variables, and derived variables may present some differences when comparing data and simulation, like the ghost probabilities or the χ^2 of the tracks included in the stripping selection. Nevertheless the selection is loose enough to not affect significantly the efficiency. In addition, these variables are very loosely correlated to the proper time variable.

4.2.4 Selected mass distributions

The reconstructed B mass distributions for $B^0 \to K^{*0}(892)\gamma$ and $B_s^0 \to \phi\gamma$ decays are shown in Figure 4.9. As the same ± 1 GeV/c^2 mass window is applied on B candidates in HLT2, stripping and offline selections, the different resolutions result in an acceptance bias in the vicinity of the corrected mass window borders. In order to reduce this acceptance effect, the fits to the reconstructed B mass distributions, explained in the following chapter, are limited to a mass range from 4600 to 6000 MeV/c^2.

[1] Starting in 2015.

[2] The procedure is detailed later, in Section 5.3.4.

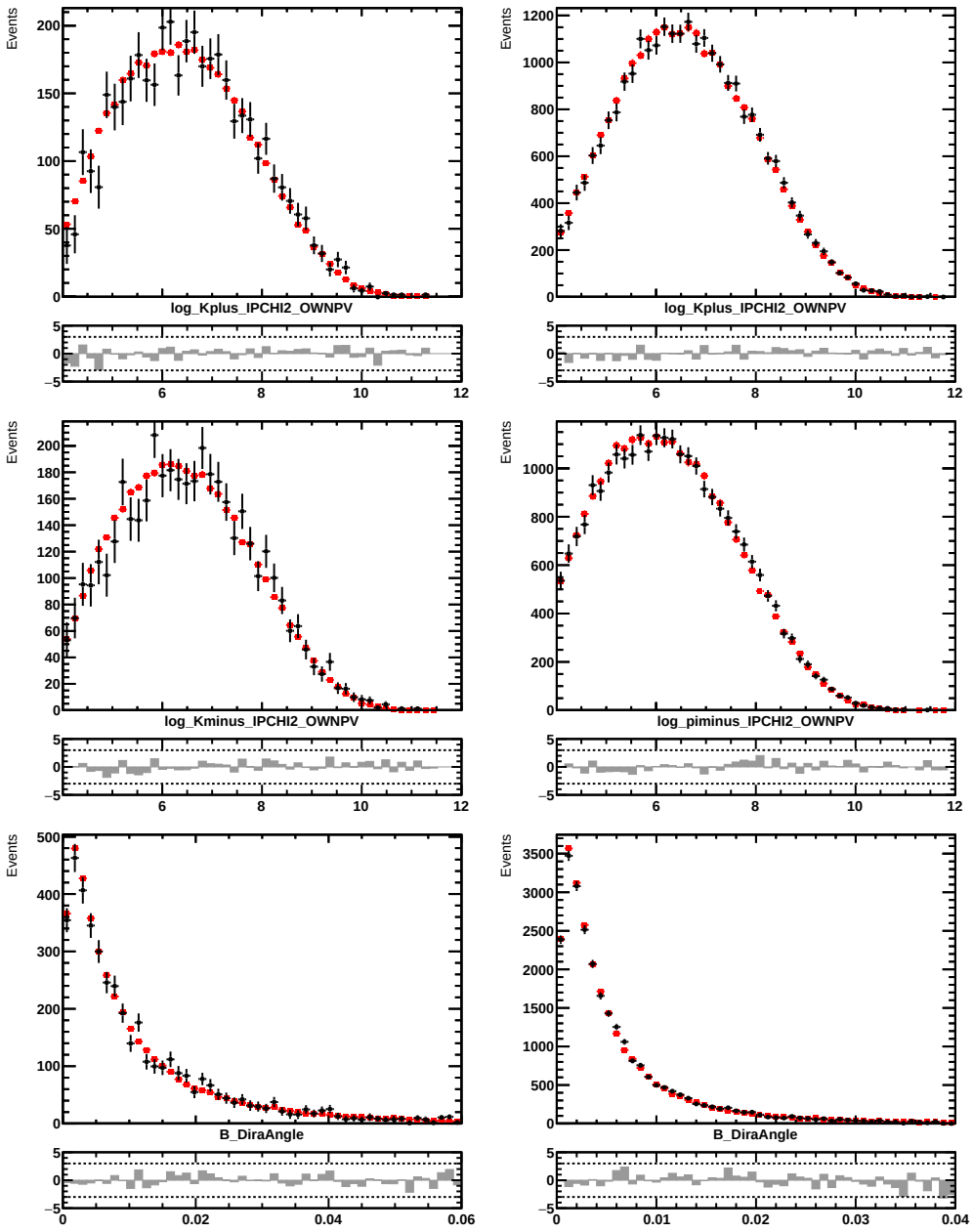

Figure 4.3: Comparison of the Monte Carlo (red squares) and data (black dots) distributions for $B_s^0 \to \phi\gamma$ (left) and $B^0 \to K^{*0}(892)\gamma$ (right). The full selection is applied to both samples, and the data is background subtracted. The distributions from Monte Carlo are normalised to the data statistics. In the plots, `log_x_IPCHI2_OWNPV` refers to the logarithm of the χ^2 value of the impact parameter with respect to the associated primary vertex of the particle `x`, be it a K^+ (`Kplus`), K^- (`Kminus`), π^+ (`piplus`), or π^- (`piminus`); and `B_DiraAngle` refers to the direction angle as defined in this section.

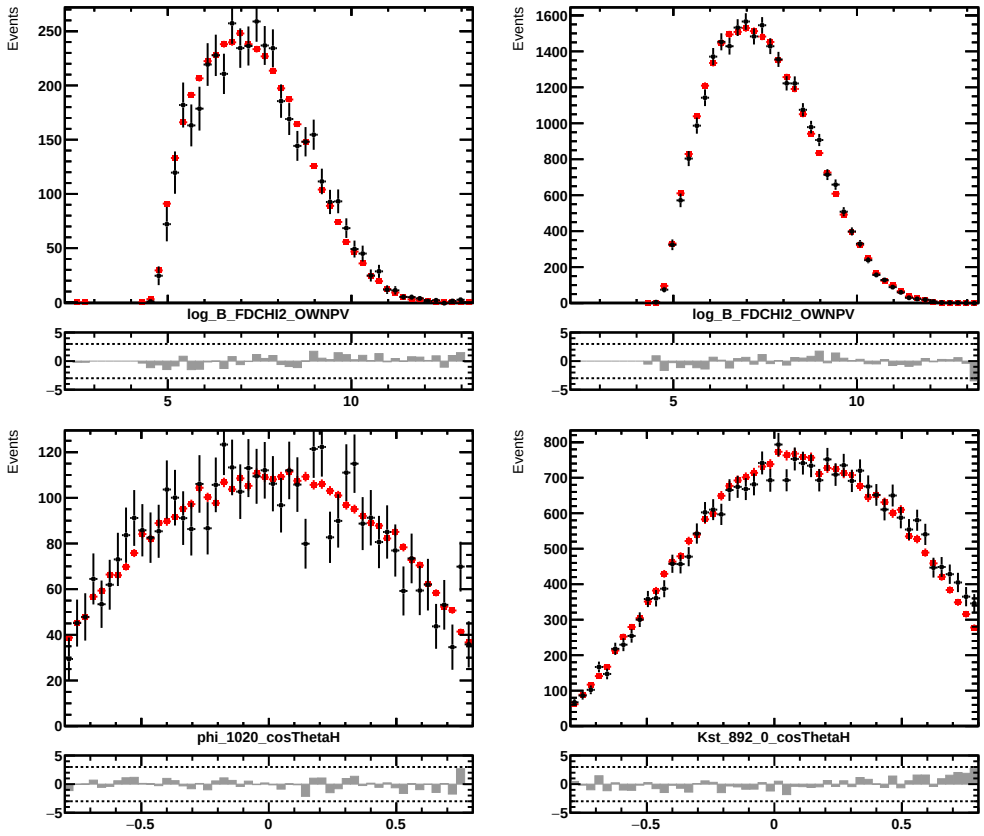

Figure 4.4: Comparison of the Monte Carlo (red squares) and data (black dots) distributions for $B_s^0 \to \phi\gamma$ (left) and $B^0 \to K^{*0}(892)\gamma$ (right). The full selection is applied to both samples, and the data is background subtracted as explained in the next chapter. The distributions from Monte Carlo are normalised to the data statistics. In the plots, `log_B_FDCHI2_OWNPV` refers to the logarithm of the χ^2 value of the flight distance with respect to the associated primary vertex of the B meson and `x_cosThetaH` refers to the cosine of the helicity angle of the daughters of the particle `x`, be it a $\phi(1020)$ (`phi_1020`) or a $K^{*0}(892)$ (`Kst_892_0`).

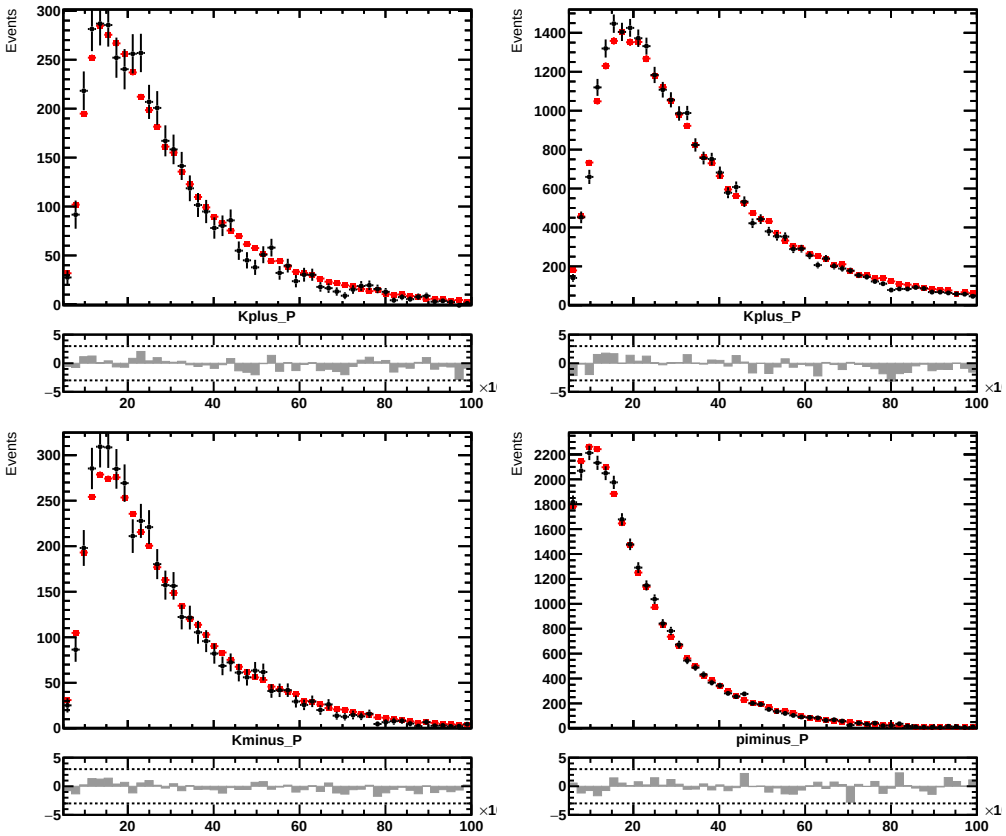

Figure 4.5: Comparison of the Monte Carlo (red squares) and data (black dots) distributions for $B_s^0 \to \phi\gamma$ (left) and $B^0 \to K^{*0}(892)\gamma$ (right). The full selection is applied to both samples, and the data is background subtracted as explained in the next chapter. The distributions from Monte Carlo are normalised to the data statistics. In the plots, `x_P` refers to the total momentum of the particle `x`, be it a K^+ (`Kplus`), K^- (`Kminus`), π^+ (`piplus`) or π^- (`piminus`).

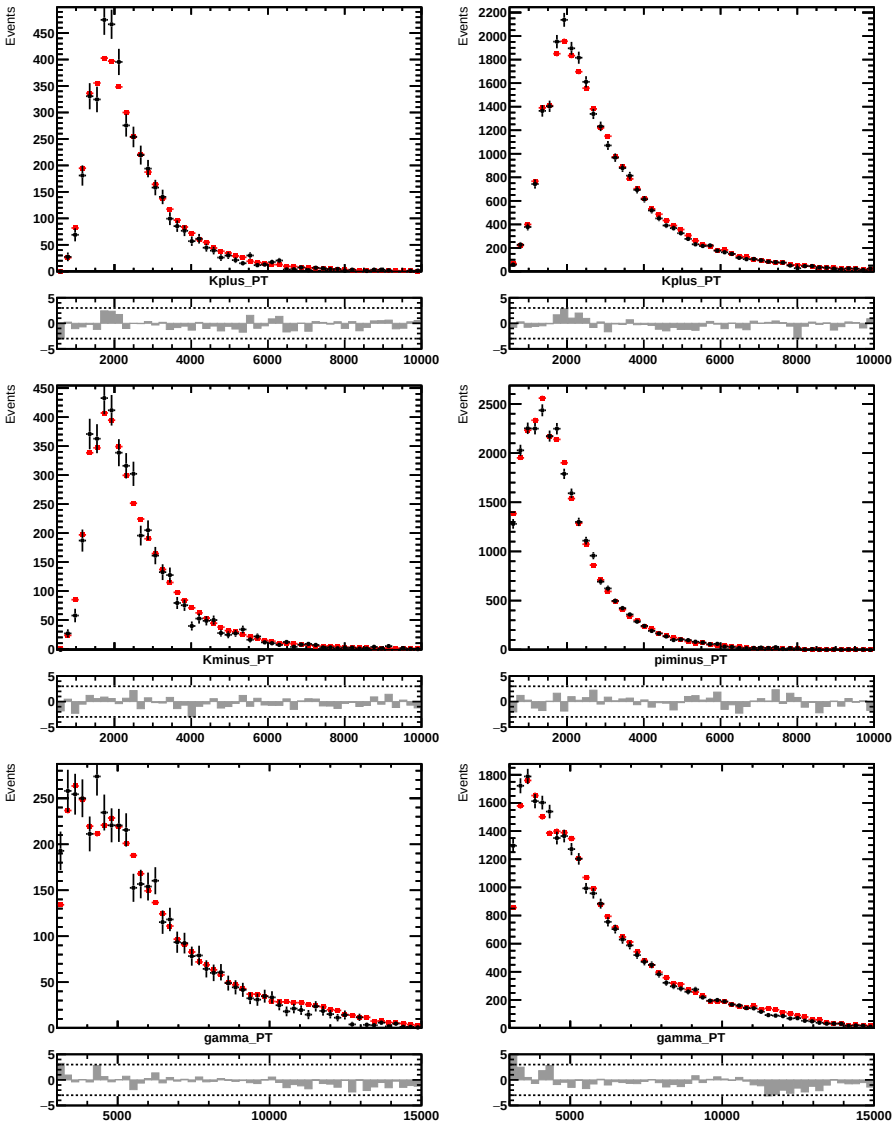

Figure 4.6: Comparison of the Monte Carlo (red squares) and data (black dots) distributions for $B_s^0 \to \phi\gamma$ (left) and $B^0 \to K^{*0}(892)\gamma$ (right). The full selection is applied to both samples, and the data is background subtracted as explained in the next chapter. The distributions from Monte Carlo are normalised to the data statistics. In the plots, `x_PT` refers to the transversal momentum of the particle `x`, be it a K^+ (`Kplus`), K^- (`Kminus`), π^+ (`piplus`), π^- (`piminus`) or a photon (`gamma`).

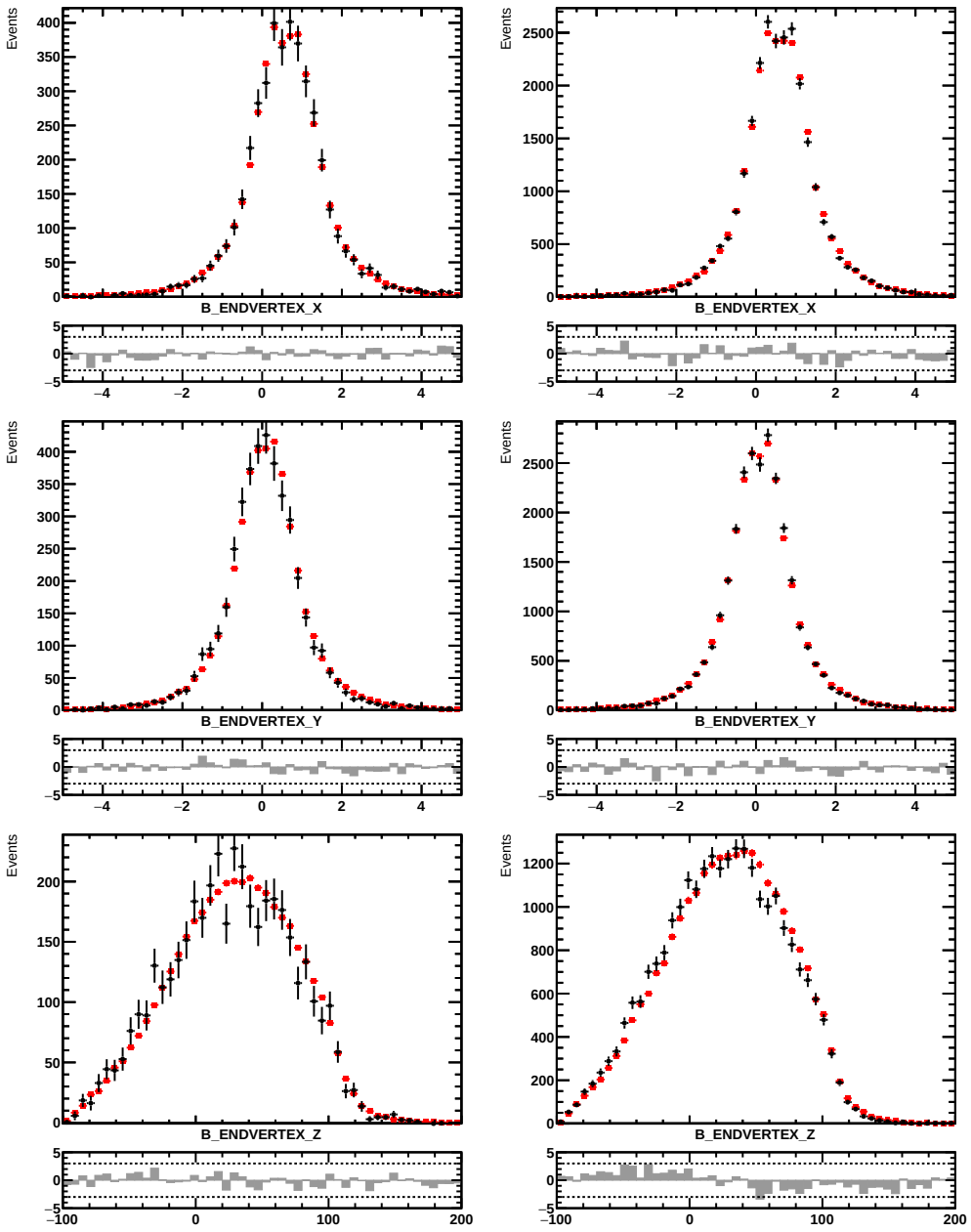

Figure 4.7: Comparison of the Monte Carlo (red squares) and data (black dots) distributions for $B_s^0 \to \phi\gamma$ (left) and $B^0 \to K^{*0}(892)\gamma$ (right). The full selection is applied to both samples, and the data is background subtracted as explained in the next chapter. The distributions from Monte Carlo are normalised to the data statistics. In the plots, `B_ENDVERTEX_a` refers to the spatial position in the detector reference frame of the B meson decay vertex for each axis `a`.

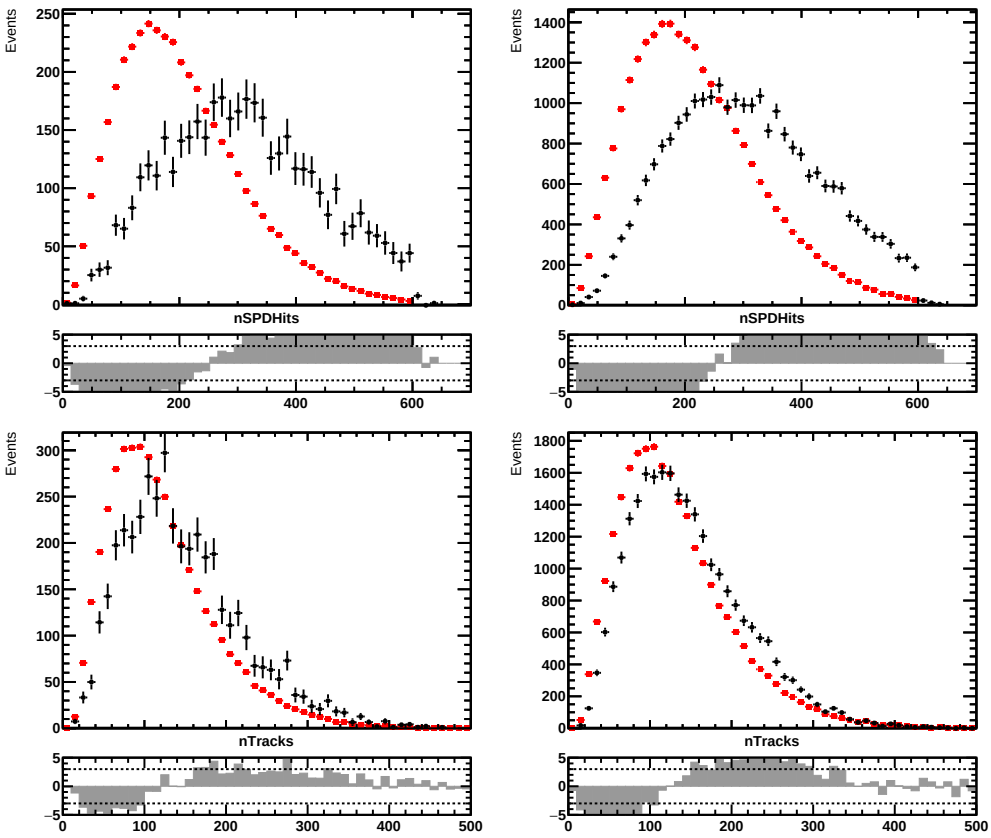

Figure 4.8: Comparison of the Monte Carlo (red squares) and data (black dots) distributions for $B_s^0 \to \phi\gamma$ (left) and $B^0 \to K^{*0}(892)\gamma$ (right). The full selection is applied to both samples, and the data is background subtracted as explained in the next chapter. The distributions from Monte Carlo are normalised to the data statistics. In the plots, `nSPDHits` and `nTracks` refer respectively to the number of hits in the SPD detector and the number of tracks in the whole event.

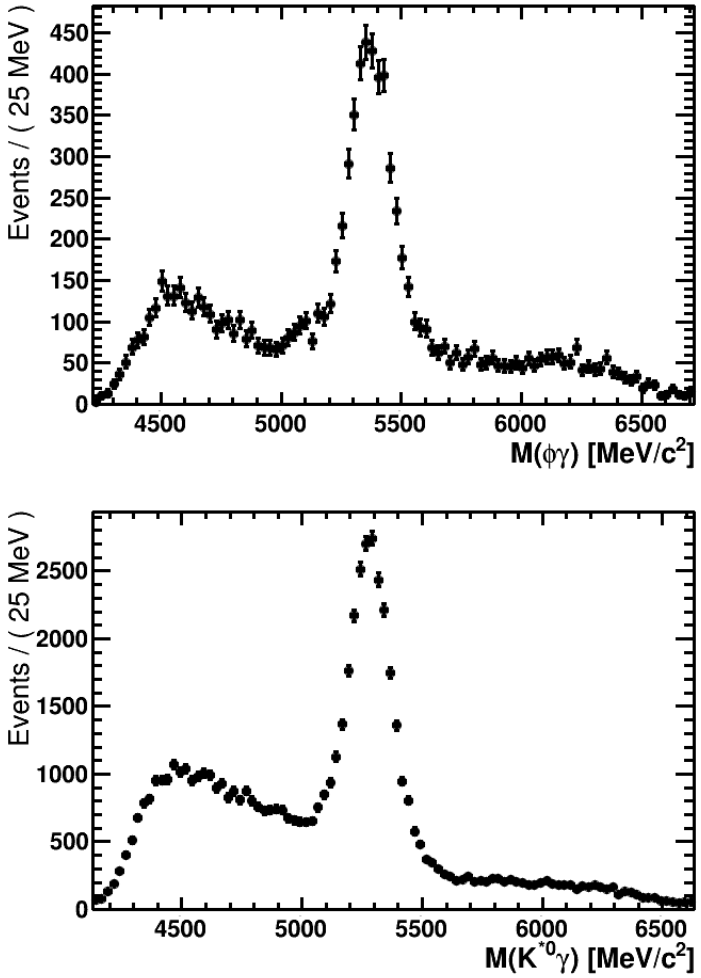

Figure 4.9: B mass distribution of the reconstructed $B_s^0 \to \phi\gamma$ (top) and $B^0 \to K^{*0}(892)\gamma$ (bottom) candidates in the $3\,\mathrm{fb}^{-1}$ data sample.

5 | B meson invariant mass fit

After the selection process some irreducible background remains in the sample. It is necessary to statistically isolate the signal from the background components in order to study the ratio of signal $B_s^0 \to \phi\gamma$ and $B^0 \to K^{*0}(892)\gamma$ events. This is done through a fit to the mass distributions taking into consideration all possible signal and background species present, their functional shapes under both channels' reconstruction hypotheses and the background expected yields. This section first describes the signal shapes and then the background species considered. A separate mass fit is done for $B_s^0 \to \phi\gamma$ and $B^0 \to K^{*0}(892)\gamma$ decays.

To avoid any confusion, during the description of the mass fit the term signal will refer to the signal component of both decays.

5.1 Signal description

The invariant mass distribution for the signal species of both $B_s^0 \to \phi\gamma$ and $B^0 \to K^{*0}(892)\gamma$ decays was studied using simulation samples. Of the hypotheses considered, the best fit was obtained using a double sided Crystal-Ball Probability Density Function (PDF), defined as

$$\mathrm{CB}(m;\mu,\sigma,\alpha_L,n_L,\alpha_R,n_R) = \begin{cases} A_L\left(B_L - \dfrac{m-\mu}{\sigma}\right)^{-n_L} & \text{for } \dfrac{m-\mu}{\sigma} \leq -\alpha_L, \\ \exp\left\{-\dfrac{(m-\mu)^2}{2\sigma^2}\right\} & \text{for } -\alpha_L < \dfrac{m-\mu}{\sigma} < \alpha_R, \\ A_R\left(B_R + \dfrac{m-\mu}{\sigma}\right)^{-n_R} & \text{for } \dfrac{m-\mu}{\sigma} \geq \alpha_R, \end{cases} \tag{5.1}$$

where $\alpha_{L(R)} > 0$ and

$$A_i = \left(\frac{n_i}{|\alpha_i|}\right)^{n_i} \exp\left\{-\frac{|\alpha_i|^2}{2}\right\}, \qquad B_i = \frac{n_i}{|\alpha_i|} - |\alpha_i|. \tag{5.2}$$

The tail parameters $n_{L(R)}$ and $\alpha_{L(R)}$ are fixed to the values obtained from a fit to the simulation, while the μ and σ are floated in the fit to the data. The results of the fits to MC signal for both channels are listed in Table 5.1, and their projections are shown in Figure 5.1 for $B_s^0 \to \phi\gamma$ and $B^0 \to K^{*0}(892)\gamma$.

Table 5.1: B mass fit results for $B_s^0 \to \phi\gamma$ and $B^0 \to K^{*0}(892)\gamma$ signal MC.

parameter	$B_s^0 \to \phi\gamma$	$B^0 \to K^{*0}(892)\gamma$
μ (MeV/c^2)	5369.74 $\pm$ 0.41	5283.82 $\pm$ 0.41
σ (MeV/c^2)	91.17 $\pm$ 0.40	90.26 $\pm$ 0.39
α_L	2.390 $\pm$ 0.029	2.397 $\pm$ 0.030
α_R	-1.508 ± 0.031	-1.479 ± 0.030
n_L	0.690 $\pm$ 0.050	0.778 $\pm$ 0.054
n_R	7.16 $\pm$ 0.64	7.71 $\pm$ 0.70

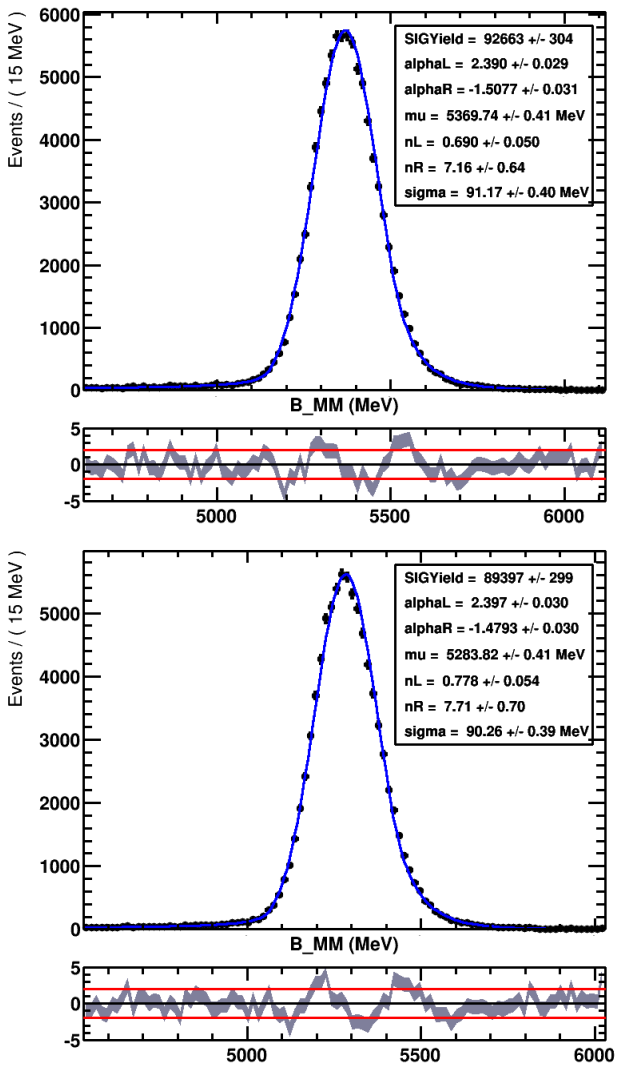

Figure 5.1: The $B_s^0 \to \phi\gamma$ (top) and $B^0 \to K^{*0}(892)\gamma$ (bottom) signal MC samples and their B mass (`B_MM` in the plot) fit projections using a double sided Crystal Ball function. Underneath each plot, the normalized residual distribution, calculated as the difference between the data points and the function curve, divided by the uncertainty of the data points, is shown.

5.2 Background species

As discussed previously, the selection does not suffice in removing non-signal components from the sample and these have to be studied carefully. From all of the by-products of the collision some combinations pass the selection criteria in the form of background. In this analysis, any decay with at least two tracks and a high-E_{T} neutral particle (γ or π^0) in the final state is a potential candidate to be reconstructed as signal. Depending on the sources, they can be categorized in two types:

- Combinatorial background, when a candidate is built from a random combination of tracks and energy deposits in the detector that pass the selection.
- Physical background, when the candidates are formed by mistaking decays of other particles in the detector for several reasons, such as misidentifying the components of the decay or missing additional tracks. These backgrounds have specific functional probability density functions that must be modelled into the fit, depending on their nature:
  - Misidentified $B \to h^+h^-\gamma$ and $B \to h^+h^-\pi^0$ decays form peaking contributions mostly under the signal region.
  - Partially reconstructed decays such as $B \to h^+h^-\gamma X$ and $B \to h^+h^-\pi^0 X$ produce peaked background at lower masses with a tail extending below the signal region.

A thorough study of similar channels provides a list of possible background sources. By studying simulation data reconstructed as signal candidates a functional form of their mass PDFs can be extracted and the level of contamination estimated. The contamination of any given background $H_b \to X$ to the signal is computed as a fraction of the signal yield, defined as

$$C^{\mathrm{signal}}_{H_b \to X} = \frac{N^{\mathrm{sel}}(H_b \to X)}{N^{\mathrm{sel}}(\mathrm{signal})} = \frac{\epsilon_{\mathrm{MC}}(H_b \to X)}{\epsilon_{\mathrm{MC}}(\mathrm{signal})} \times \frac{f_{H_b}}{f_{\mathrm{signal}}} \times \frac{\mathcal{B}(H_b \to X)}{\mathcal{B}(\mathrm{signal})}, \quad (5.3)$$

where $\mathcal{B}$ denotes branching ratios, f are the fragmentation fractions, ϵ_{MC} the efficiencies from simulation, and "signal" refers to either $B^0_s \to \phi\gamma$ or $B^0 \to K^{*0}(892)\gamma$. A summary of the relevant background contributions for $B^0 \to K^{*0}(892)\gamma$ and $B^0_s \to \phi\gamma$ is shown in Table 5.2.

Table 5.2: Summary of the background contributions for $B_s^0 \to \phi\gamma$ and $B^0 \to K^{*0}(892)\gamma$ channels. The effective branching fractions take into account the intermediate resonance decays to the relevant channels, with the numbers sourced from [4]. Uncertainties on these numbers range from 10 to 50% depending on the decay mode. Channels with contaminations below 0.01% are deemed negligible and not included in the mass fit model. Of the modelled species, most of their contamination fractions are left free in the final mass fit.

	Effective branching fraction ($\times 10^{-5}$)	Relative contamination to $B_s^0 \to \phi\gamma$	Relative contamination to $B^0 \to K^{*0}(892)\gamma$
$B^0 \to K_1(1270)^0\gamma$	4.1	$\mathcal{O}(0.2\%)$	$\mathcal{O}(7\%)$
$B^+ \to K_1(1270)^+\gamma$	2.6	$\mathcal{O}(0.1\%)$	$\mathcal{O}(12\%)$
$B^+ \to K_1(1400)^+\gamma$	0.98	$\mathcal{O}(0.01\%)$	$\mathcal{O}(5\%)$
$B^+ \to K_2^*(1430)^+\gamma$	0.35	$\mathcal{O}(0.01\%)$	$\mathcal{O}(2\%)$
$B^0 \to K^{*0}(892)\gamma$	2.9	0.1%	Signal
$B^0 \to \omega\gamma$	3.9×10^{-2}	–	0.01%
$B^0 \to \rho^0\gamma$	8.6×10^{-2}	–	0.15%
$B_s^0 \to \phi\gamma$	1.8	Signal	0.24%
Signal reflection[(1)]	2.9	–	0.16%
$B^0 \to K^{*0}(892)\pi^0$	0.22	–	2.05%
$B_s^0 \to \phi\pi^0$	see text	1.60%	–
$B^0 \to K^{*0}(892)\eta$	0.42	0.01%	2.04%
$B^+ \to D^0(K\pi\pi^0)\rho^+$	1.9×10^2	$\mathcal{O}(0.1\%)$	$\mathcal{O}(4\%)$
$B^+ \to D^0(K\pi\pi\pi)\rho^+$	1.1×10^2	–	$\mathcal{O}(0.4\%)$
$B^+ \to \rho^+\rho^0$	2.4	–	$\mathcal{O}(0.2\%)$
$B^+ \to \phi K^+\gamma$	0.13	1.2%	–
$\Lambda_b \to \Lambda(pK)\gamma$	0.42[(2)]	1.77%	1.38%

[(1)] Events in $B^0 \to K^{*0}(892)\gamma$ with both the pion from $K^{*0}(892) \to K^{\pm}\pi^{\mp}$ misidentified as a kaon and vice-versa.
[(2)] Production fraction $f_{\Lambda_b^0}/f_d$ included.

The contamination from $\Lambda_b \to \Lambda(pK)\gamma$ decays is computed using the value of its branching ratio times the ratio of production fractions [107]:

$$\mathcal{B}[\Lambda_b \to \Lambda(pK)\gamma]\frac{f_{\Lambda_b^0}}{f_d} = (4.2 \pm 0.7) \times 10^{-6}. \tag{5.4}$$

Since no simulated sample for $B_s^0 \to \phi\pi^0$ is available, it is assumed that the ratio of selection efficiencies of the photon and π^0 channel are the same for the B^0 and B_s^0 modes. This is a good assumption because the photon and π^0 have essentially the same kinematics in the B^0 and B_s^0 channels. Therefore the γ/π^0 separation cut will have the same efficiency and thus rejection rate in $B_s^0 \to \phi\gamma$ and $B_s^0 \to \phi\pi^0$ as it does in $B^0 \to K^{*0}(892)\gamma$ and $B^0 \to K^{*0}(892)\pi^0$. Since the performance of the γ/π^0 separation variable is not well reproduced by the simulation, the variable in $B^0 \to K^{*0}(892)\pi^0$ and $B^0 \to K^{*0}(892)\gamma$ simulated samples is weighted to reproduce its performance in data. This re-weighting is done using $B^0 \to K^{*0}(892)\gamma$ and $D^0 \to K^-\pi^+\pi^0$ data samples as a function of the neutral particle's transverse momentum and pseudo-rapidity.

In addition to the ratio of efficiencies, the ratio of branching ratios $\mathcal{B}(B_s^0 \to \phi\pi^0)/\mathcal{B}(B_s^0 \to \phi\gamma)$ is also needed in order to predict the contamination of $B_s^0 \to \phi\pi^0$ to $B_s^0 \to \phi\gamma$. The $B_s^0 \to \phi\pi^0$ decay has not yet been observed, but is predicted to be 1.6×10^{-7}which is $< 0.5\%$ of the $B_s^0 \to \phi\gamma$ rate. In contrast, the branching ratio of $B^0 \to K^{*0}(892)\pi^0$ has been measured to be $(3.3 \pm 0.6) \times 10^{-6}$ and is about 7.6% of the $B^0 \to K^{*0}(892)\gamma$ mode.

To compute the contamination fraction of $B_s^0 \to \phi\pi^0$ to $B_s^0 \to \phi\gamma$ it is safe to assume that the ratio of their branching fractions is the same as in the case of $B^0 \to K^{*0}(892)\pi^0$ to $B^0 \to K^{*0}(892)\gamma$. This initial estimate must be corrected for the fact that the helicity distributions, $\cos\theta_H$, of the $K^{*0}(892)\pi^0$ system are asymmetrical due to the mass difference between the kaon and the pion from the $K^{*0}(892)$ decay, as opposed to the corresponding distribution in the $\phi(1020)\pi^0$ system, which must be symmetrical since the $\phi(1020)$ decays to two charged kaons.

5.2.1 Backgrounds to $B_s^0 \to \phi\gamma$

The background categories considered for the $B_s^0 \to \phi\gamma$ case are:

- Partially reconstructed background from $B^+ \to \phi K^+\gamma$ and $B \to \phi\pi\gamma$ decays.
- Misidentification backgrounds from $B^0 \to K^+K^-\pi^0$, $\Lambda_b \to \Lambda\gamma$ and $B^0 \to K^{*0}(892)\gamma$ decays.

Missing the second same-charge kaon in $B^+ \to \phi K^+\gamma$ leads to background events. Its reconstruction as $B_s^0 \to \phi\gamma$ from a simulated sample

is shown in Figure 5.2, along with the corresponding fit to an ARGUS function convoluted with a Gaussian function. The probability density function of the ARGUS distribution is defined [108] as

$$f(x;\chi,c) = \frac{\chi^3}{\sqrt{2\pi}\,\Psi(\chi)} \cdot \frac{x}{c^2}\sqrt{1-\frac{x^2}{c^2}} \cdot \exp\left\{-\frac{1}{2}\chi^2\left(1-\frac{x^2}{c^2}\right)\right\},$$

for $0 \leq x < c$, where c is the cut-off parameter and χ the curvature parameter, and

$$\Psi(\chi) = \Phi(\chi) - \chi\phi(\chi) - \tfrac{1}{2},$$

with $\Phi(x)$ and $\phi(x)$ being the cumulative distribution and probability density functions of the standard normal distribution[1] respectively.

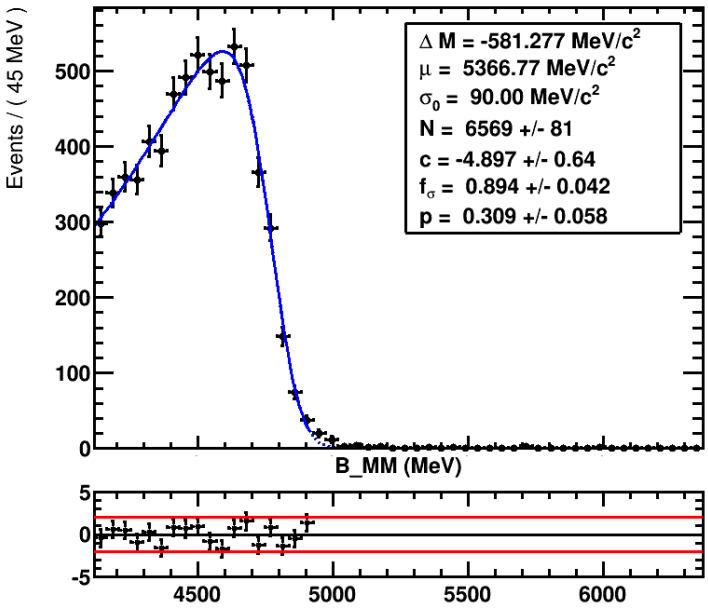

Figure 5.2: The $B_s^0 \to \phi\gamma$ invariant mass (`B_MM` in the plot) as reconstructed from a $B^+ \to \phi K^+\gamma$ simulated sample.

Likewise, the loss of a pion in the reconstruction of $B^0 \to \phi\pi^0\gamma$ decays could potentially appear as a background contribution. However, the branching ratio for $B_s^0 \to \phi\pi^0\gamma$ has not been measured yet, so the respective contribution is left free in the fit. Reconstructing a $B_s^0 \to \phi\pi^0\gamma$ simulated sample as $B_s^0 \to \phi\gamma$ produces the distribution shown in Figure 5.3,

[1] Normalized Gaussian with $\mu = 0$ and $\sigma = 1$.

which is modelled with the previously described ARGUS convoluted with a Gaussian.

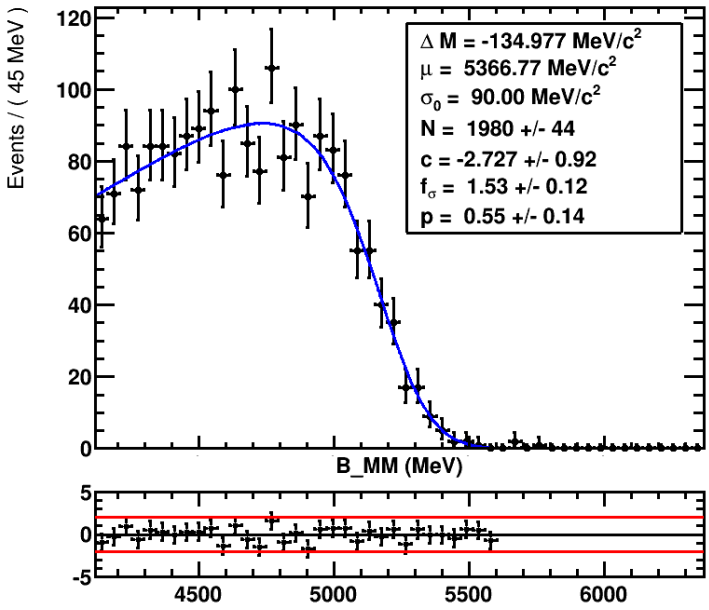

Figure 5.3: The $B_s^0 \to \phi\gamma$ invariant mass (`B_MM` in the plot) as reconstructed from a $B_s^0 \to \phi\pi^0\gamma$ simulated sample.

The decay $B_s^0 \to K^+K^-\pi^0$ has not yet been observed in either its resonant [via $\phi(1020)$] or non-resonant form, but is a possible component peaking in the signal mass region. The distribution of the reconstructed $B_s^0 \to \phi\gamma$ invariant mass distribution in the simulated sample is assumed to be the same as for the $B^0 \to K^{*0}\pi^0$ sample.

The invariant mass distribution of reconstructed $B_s^0 \to \phi\gamma$ candidates from $\Lambda_b \to \Lambda(pK)\gamma$ and $B^0 \to K^{*0}(892)\gamma$ samples are modelled with Crystal Ball shapes and are shown in Figure 5.4.

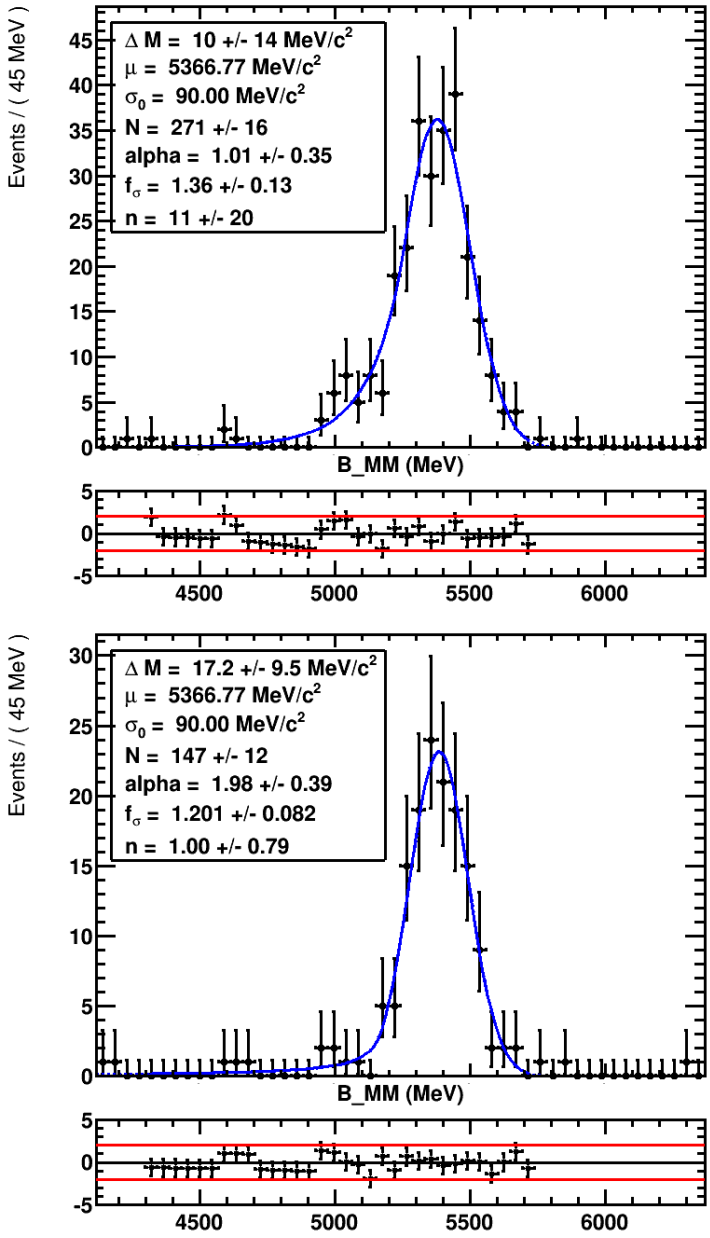

Figure 5.4: The $B_s^0 \to \phi\gamma$ invariant mass (B_MM in the plot) as reconstructed from $\Lambda_b \to \Lambda(pK)\gamma$ (top) and $B^0 \to K^{*0}(892)\gamma$ (bottom) simulated samples.

5.2.2 Backgrounds to $B^0 \to K^{*0}(892)\gamma$

Possible B backgrounds to the $B^0 \to K^{*0}(892)\gamma$ channel are studied in the same way as described for $B_s^0 \to \phi\gamma$. The descriptions for partially reconstructed and misidentification backgrounds apply here as well. In this case, however, the wider $K^{*0}(892)$ resonance and the kaon and pion in the final state (as compared to two kaons) increase the possible background sources.

Backgrounds to $B^0 \to K^{*0}(892)\gamma$ channel could be any b-hadron decay with a K, π and a neutral (γ or π^0) in the final state. Decays with a K^+K^- or $\pi^+\pi^-$ pair in the final state could also contribute but are suppressed due to PID cuts.

Partially reconstructed backgrounds

Most of these backgrounds come from higher order K^* resonances decaying to the signal vector meson such as $K_1(1270)^+ \to K^{*0}(892)\pi^+$, non-resonant decays of the mentioned higher resonances, decays through intermediate D mesons decaying to any of the final signatures, as for example $B^+ \to D^0(\to K^+K^-)\rho^+(\to \pi^+\pi^-)$, and decays with η in the final state. These backgrounds dominate in the low-mass region and after reconstruction as $B^0 \to K^{*0}(892)\gamma$ candidates can be grouped in the following categories, sharing common shape parameters in the final fit:

- $B \to K^*(892)^0\pi^0 X$ decays contribute via misidentification of the neutral pion as a photon and the loss of any X by-product in the final state.
- $B \to K^*(892)^0\pi\gamma$ with the loss of the additional pion.
- $B \to [K\pi]\,\pi\gamma$ with a non-resonant $K\pi$ pair, reconstructed with a lost pion as above.
- $B \to K^{*0}(892)\eta$ with the loss of one of the photons or pions from the η decay.

All these decays are well described by an ARGUS distribution convoluted with a Gaussian distribution.

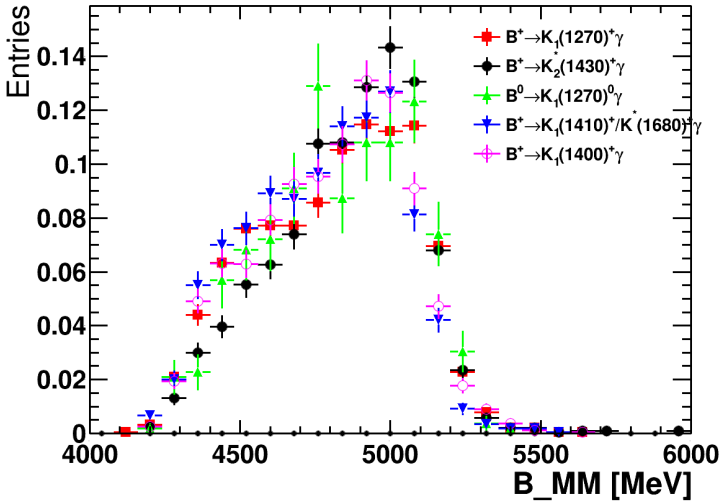

Figure 5.5: The reconstructed $B^0 \to K^{*0}(892)\gamma$ invariant mass (`B_MM` in the plot) in various $B \to K^*\gamma$ channels where the higher order K^* resonance decays via $K^*(892)\pi$.

Since most of the contaminations are floated in the fit, determining common shape parameters for the background categories aids in reducing the number of free parameters in the final mass fit for an easier convergence. It is easily justified by observing a comparison of the reconstructed shapes of the simulated species, such as those shown in Figure 5.5 for different K resonances.

Misidentification backgrounds

A strict application of particle identification cuts can suppress this kind of backgrounds, at some cost of signal efficiency. The optimal values described in Chapter 4 leave some remnants to be modelled in the mass fit. These kind of backgrounds have a peaking functional form generally around the reconstructed B^0 mass and each source has its own parametrization:

- $\Lambda_b \to \Lambda(pK)\gamma$, decays with a misidentification of the proton as a pion.
- $B \to K\pi\pi^0$, mistaking the neutral pion for a photon.

- $B_s^0 \to \phi\gamma$, with one of the daughter kaons identified as a pion.
- $B^0 \to \rho^0\gamma$, reconstructing one of the final state pions as a kaon.

The baryonic radiative decay $\Lambda_b \to \Lambda^*\gamma$ can appear via the intermediate $\Lambda(1520)$ and $\Lambda(1670)$ states decaying to pK, and their shapes, reconstructed as $B^0 \to K^{*0}(892)\gamma$, were studied separately over simulated samples. A Crystal-Ball function[2] is found to provide the best fit for the mass distribution. The corresponding fits are shown in Figure 5.6 for the $\Lambda(1520)$ on the top and the $\Lambda(1670)$ on the bottom.

To assess the shape of $B \to K\pi\pi^0$ backgrounds, $B^0 \to K^{*0}(892)\gamma$ candidates were built from a simulated sample of mixed sources of $B \to K\pi\pi^0$ channels. The generated proportions of the sample are shown in Table 5.3. Tracking the final candidates to its source it was found that 89.5% of the events came from the resonant $B^0 \to K^*(892)^0\pi^0$ decay. Figure 5.7 shows the $B^0 \to K^{*0}(892)\gamma$ invariant mass reconstructed in this mixed background sample, which has been fitted with a Crystal Ball function.

Decay channel	%
$B^0 \to K^*(892)^+\pi^-$	23.04%
$B^0 \to \rho^- K^+$	58.48%
$B^0 \to K^*(892)^0\pi^0$	6.67%
$B^0 \to K^+\pi^-\pi^0{}_{\text{non-resonant}}$	11.81%

Table 5.3: Generator level composition of the $B \to K\pi\pi^0$ simulated sample.

$B_s^0 \to \phi\gamma$ and $B^0 \to \rho^0\gamma$ contribute to $B^0 \to K^{*0}(892)\gamma$ due to $K \to \pi$ and $\pi \to K$ misidentification respectively. The left and right panels in Figure 5.8 show the $B^0 \to K^{*0}(892)\gamma$ invariant mass distributions as reconstructed in the simulated samples of $B_s^0 \to \phi\gamma$ and $B^0 \to \rho^0\gamma$ respectively. The overlaid fit is a double-tail Crystal-Ball function.

[2] See Eq. 5.1 in page 115.

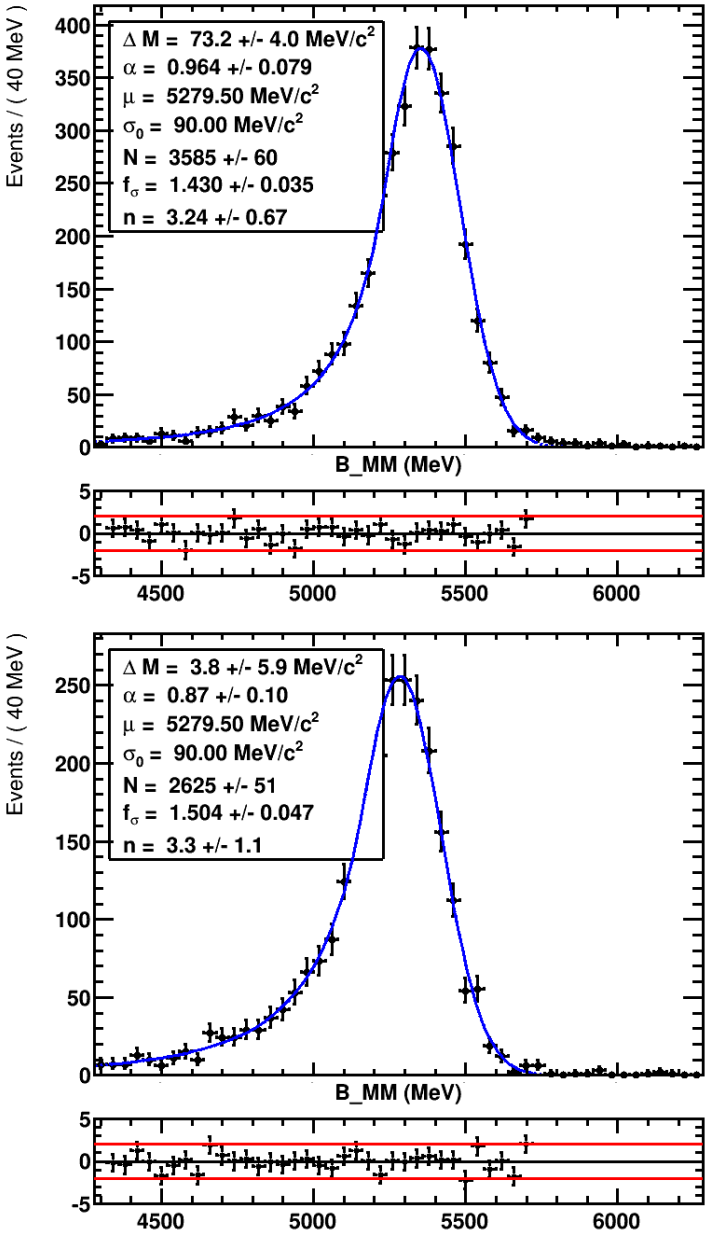

Figure 5.6: The $B^0 \to K^{*0}(892)\gamma$ invariant mass (B_MM in the plot) distributions reconstructed from $\Lambda_b \to \Lambda(pK)\gamma$ simulated data fitted with a Crystal Ball function. The top plot shows the distribution for $\Lambda_b^0 \to \Lambda(1520)(\to pK)\gamma$ while the bottom one shows the fit for $\Lambda_b^0 \to \Lambda(1670)(\to pK)\gamma$.

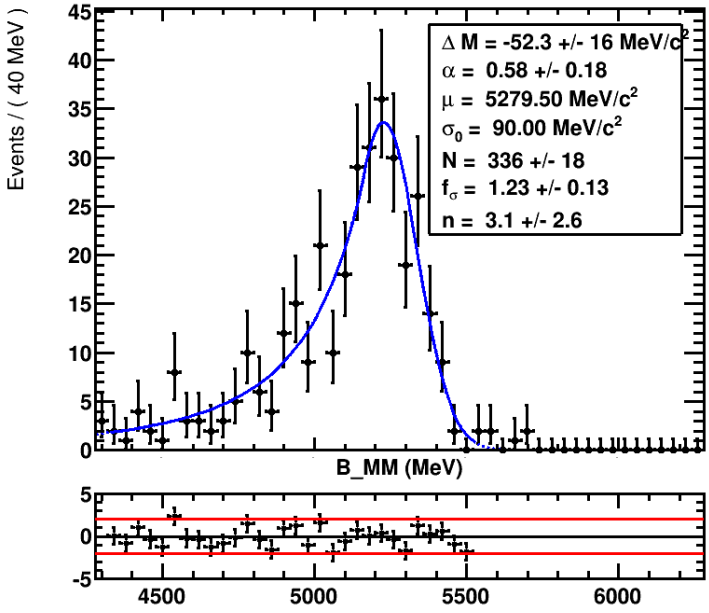

Figure 5.7: The $B^0 \to K^{*0}(892)\gamma$ invariant mass (`B_MM` in the plot) as reconstructed in $B \to K\pi\pi^0$ simulated data. The distribution has been fitted with a Crystal Ball functional form.

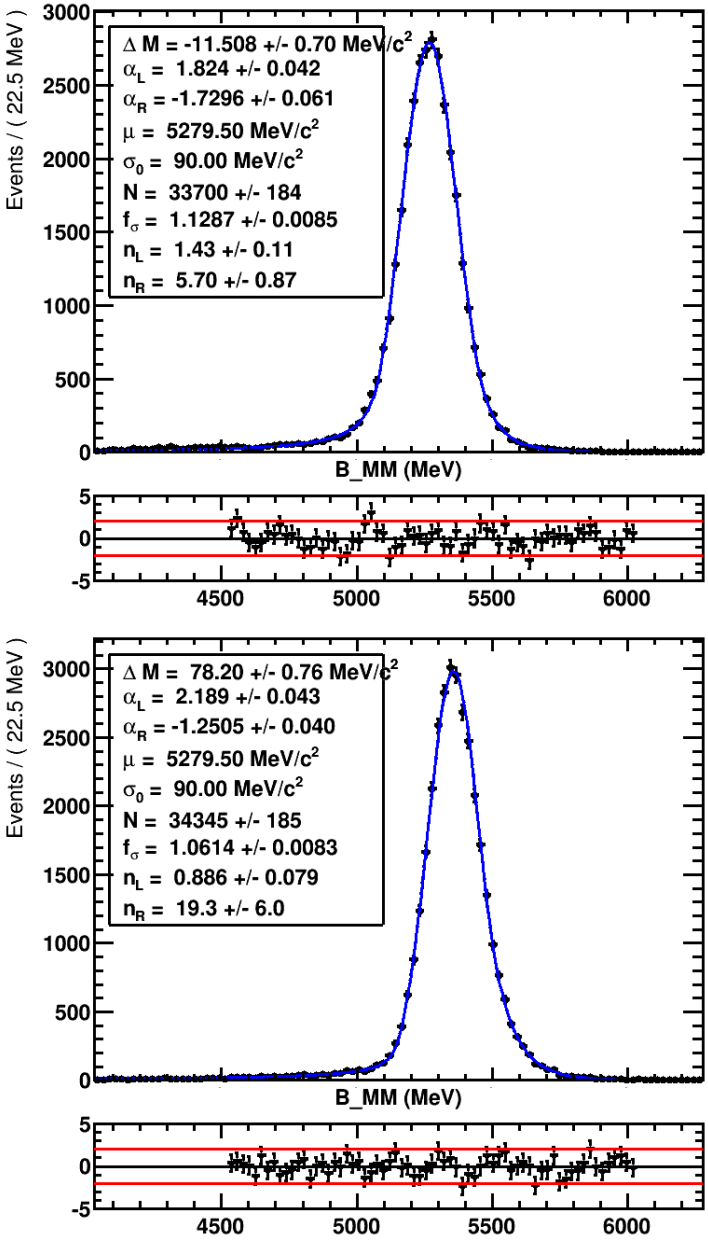

Figure 5.8: The $B^0 \to K^{*0}(892)\gamma$ invariant mass (`B_MM` in the plot) as reconstructed in $B_s^0 \to \phi\gamma$ (top) and $B^0 \to \rho\gamma$ (bottom) simulated samples. The distributions are fitted with a double-tail Crystal-Ball functional form.

5.3 Data mass fit

Having determined the shapes for each of the species present in the B mass distributions for both $B^0 \to K^{*0}(892)\gamma$ and $B_s^0 \to \phi\gamma$, the complete probability density function is built and tested. Note that in the final mass fit to the $B^0 \to K^{*0}(892)\gamma$ ($B_s^0 \to \phi\gamma$) signal, the normalization of all the components is left free within gaussian constraints to the values obtained in Table 5.2, with the exception of $\Lambda_b \to \Lambda(pK)\gamma$, $B^0 \to K^{*0}(892)\pi^0$ ($B_s^0 \to \phi\pi^0$) and signal cross-feed. The fit function to the invariant mass of B^0 (B_s^0) is built as a probability density function (PDF)

$$\mathrm{P}(m) = N_S S(m) + \sum_i N_i B_i(m), \tag{5.5}$$

where $S(m)$ is the signal PDF and $B_i(m)$ is the i-th background component PDF:

- The combinatorial background is modelled with a 1^{st} order polynomial function:
$$\mathrm{Comb}(m; p_0) = 1 + p_0 \cdot m. \tag{5.6}$$
- Partially reconstructed backgrounds are modelled with ARGUS functions convoluted with Gaussian resolutions, with the parameters fixed from simulation:
$$\mathrm{Partial}(m; c, p, \mu, \sigma) = \mathrm{ARGUS}(m; c, \mu - \mu_0, p) \otimes \mathrm{Gauss}(0, \sigma), \tag{5.7}$$
where $\mu_0 = m_\pi$ for missing pion background for $B^0 \to K^{*0}(892)\gamma$, $\mu_0 = m_K$ for missing kaon background for $B_s^0 \to \phi\gamma$, and μ_0 of $B \to K\pi\pi^0 X$ background for $B^0 \to K^{*0}(892)\gamma$ is fixed to $3m_\pi$, an empirical value obtained from MC sample studies.
- The background from $\Lambda_b \to \Lambda(pK)\gamma$ is modelled with a Crystal-Ball function, with parameters fixed from simulation.
- The background from $B^0 \to K\pi\pi^0$ is modelled with a Crystal-Ball function, with parameters fixed from simulation. The parameters for the $B_s^0 \to \phi\pi^0$ are assumed to be the same as for $B^0 \to K\pi\pi^0$ reconstructed as $B^0 \to K^{*0}(892)\gamma$, with the mean value shifted to accommodate the higher B_s^0 mass.
- Backgrounds from $B \to V\gamma$ (where V is ρ, ϕ or K^*) are modelled with a double-tail Crystal-Ball PDF.

5.3.1 Mass fit to $B_s^0 \to \phi\gamma$ data

The mass fit projection to the $B_s^0 \to \phi\gamma$ signal sample from the complete dataset of $3\,\text{fb}^{-1}$ taken during 2011 and 2012 is shown in Figure 5.9. Table 5.4 summarizes the corresponding fitted number of signal and different background components. After subtracting the peaking components, the signal yield is 4072 ± 82 events. The contamination from $B \to \phi\pi\gamma$ is found to be negligible and omitted in both the plots and the table, for clarity.

$\mathcal{N}(B_s^0 \to \phi\gamma)$	N events	4214 ± 90
	μ (GeV/c^2)	5371.88 ± 1.89
	σ (GeV/c^2)	86.31 ± 1.97
$B \to KK\pi^0$	C (%)	1.6
$\Lambda_b \to \Lambda(pK)\gamma$	C (%)	1.8
$B^0 \to K^{*0}(892)\gamma$	C (%)	0.1
Combinatorial	p_0 (MeV^{-1})	-0.27 ± 0.04
	N events	4004 ± 113
$B \to \phi K\gamma$	C (%)	6.95 ± 1.16

Table 5.4: Summary of the various parameters and yields obtained from the mass fit to the $B_s^0 \to \phi\gamma$ data sample. The N and C stand for the fitted number and contamination respectively, the p_0 is the exponent of the combinatorial mass shape, and the μ and σ are the fitted mean and width of the $B_s^0 \to \phi\gamma$ signal. The signal yield includes the peaking background numbers. Errors are statistical only. The contaminations without uncertainties are fixed from the simulation.

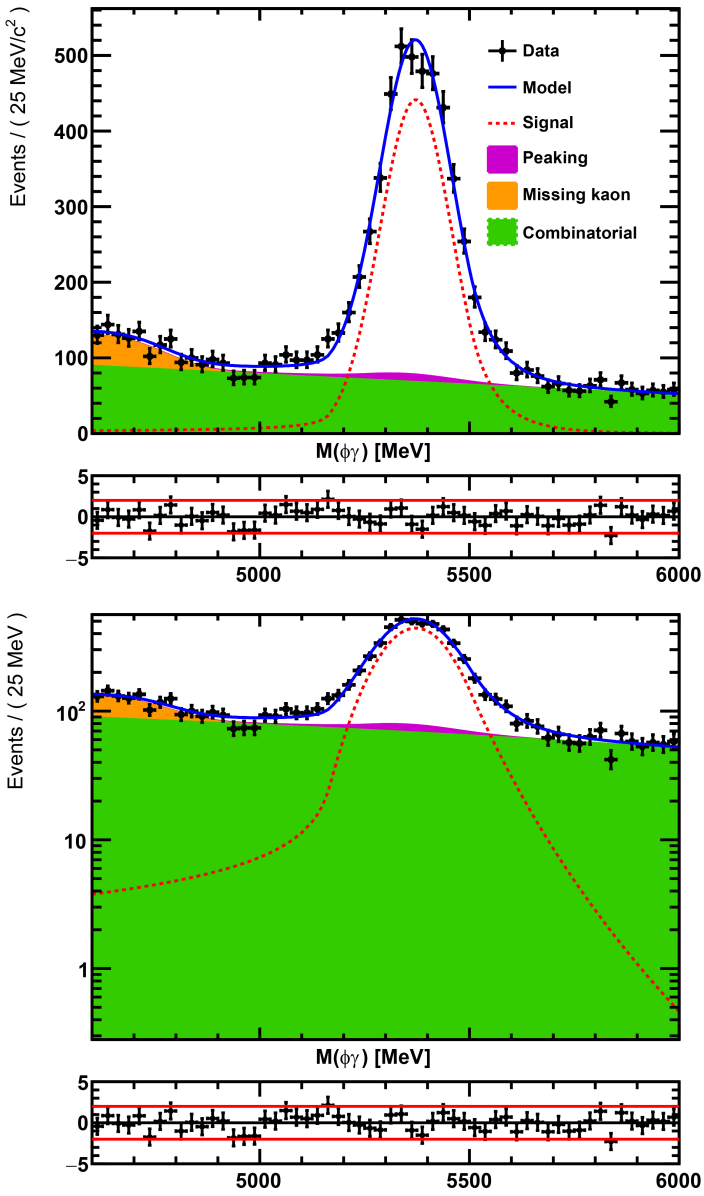

Figure 5.9: Projections of the fit to the $B_s^0 \to \phi\gamma$ candidates in the complete 3 fb^{-1} dataset in linear (top) and logarithmic (bottom) scales. The black points represent the data and the fit projection is represented as a solid blue line. The signal is shown as a dashed red line. The combinatorial background is shown in green shaded green. The background from $B \to \phi K\gamma$ is shown in orange shaded area. The peaking backgrounds are summed and shown in shaded purple area.

5.3.2 Mass fit to $B^0 \to K^{*0}(892)\gamma$ data

The projection of the mass fit to the $B^0 \to K^{*0}(892)\gamma$ data sample ($3\,\text{fb}^{-1}$, taken during 2011 and 2012) is shown in Figure 5.10. Table 5.5 summarizes the corresponding fitted number of signal and different background components. After subtracting the peaking components, the signal yield is 24808 ± 321 events. As discussed previously, the contaminations due to the $B^0 \to K^+\pi^-\pi^0$, $\Lambda_b \to \Lambda(pK)\gamma$, $B^0 \to \rho\gamma$, $B_s^0 \to \phi\gamma$ and $B^0 \to K^{*0}\eta$ decays are fixed from simulation.

	N events	$25\,760 \pm 301$
Signal	μ (MeV/c^2)	5284.07 ± 0.85
	σ (MeV/c^2)	87.83 ± 1.02
$B^0 \to K^*(892)^0\pi^0 X$	C (%)	19.17 ± 1.00
Missing pion	C (%)	25.46 ± 1.62
$B^0 \to K^{*0}\eta$	C (%)	2.04
Combinatorial	p_0 (MeV^{-1})	-0.16 ± 0.07
	N events	$14\,088 \pm 865$
$B^0 \to K^+\pi^-\pi^0$	C (%)	2.05
$\Lambda_b^0 \to \Lambda\gamma$	C (%)	1.4
$B^0 \to \rho\gamma$	C (%)	0.15
$B_s^0 \to \phi\gamma$	C (%)	0.24

Table 5.5: Summary of the various parameters and yields obtained from the mass fit to the $B^0 \to K^{*0}(892)\gamma$ data sample. N and C stand for the fitted yields and contaminations, respectively, the p_0 is the parameter of the combinatorial mass shape, and the μ and σ are the fitted mean and width of the $B^0 \to K^{*0}(892)\gamma$ signal. The signal yield includes the peaking background events. Errors are statistical only. The contaminations without uncertainties are fixed from the simulation.

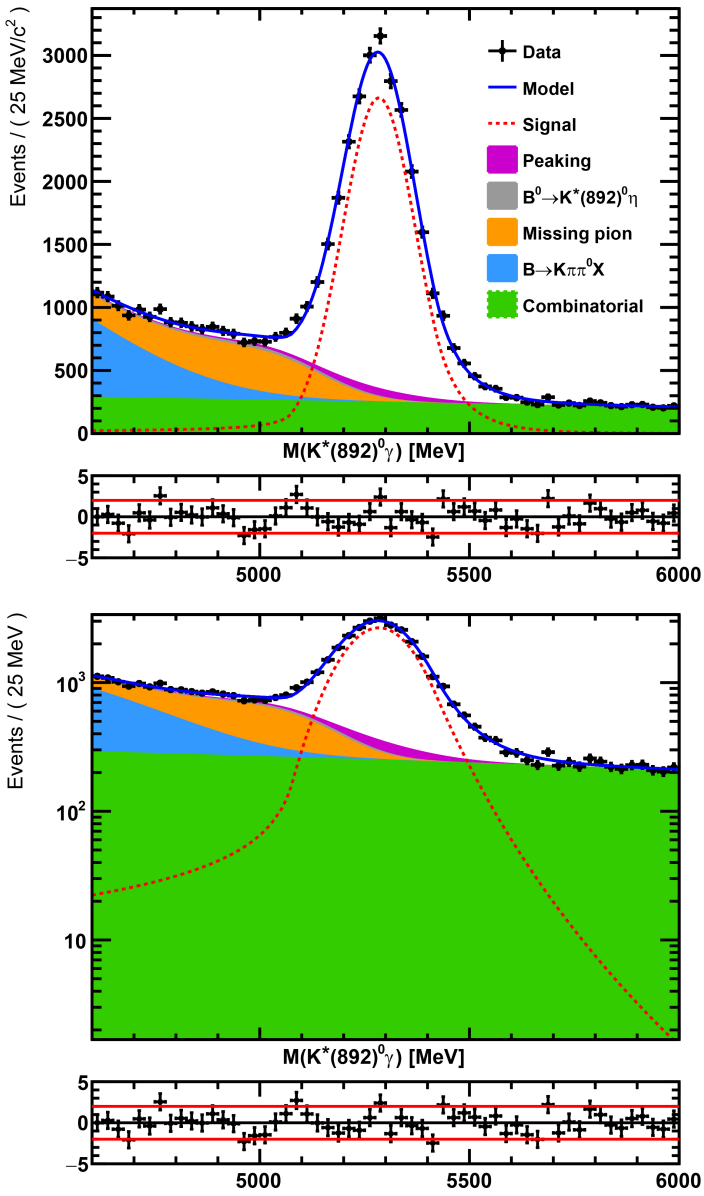

Figure 5.10: Projections of the fit to the $B^0 \to K^{*0}(892)\gamma$ candidates in the complete $3\,\text{fb}^{-1}$ dataset in linear (top) and logarithmic (bottom) scales. The black points represent the data and the fit projection is represented as a solid blue line. The signal is shown as a dashed red line. The combinatorial background is shown in green shaded green. The missing pion background is shown in orange shaded area, $B \to K\pi\pi^0 X$ in blue shaded area and $B^0 \to K^{*0}\eta$ in gray shaded area. The peaking backgrounds are summed and shown in shaded purple area.

5.3.3 Validation of the fit

In order to test the fitting procedure, Monte Carlo pseudo-experiment (AKA toy) samples have been produced using the central values obtained from the data fit (Tables 5.4 and 5.5) as generation values, then fitted upon with the complete PDF. For each toy experiment, the number of events for each signal and background component is varied according to a Poisson distribution. The "pull" distribution $\mathcal{P}(x)$ of a given parameter x is defined as

$$\mathcal{P}(x) = \frac{x_{\text{Fit}} - x_{\text{Gen}}}{\sigma_x}, \tag{5.8}$$

where the subscripts "Fit" and "Gen" refer to the fitted and generation value, and σ_x is the fitted uncertainty. The distribution of $\mathcal{P}(x)$ should follow a normal distribution with mean $\mu = 0$ and width $\sigma = 1$ in the case of well behaved fits. Results of $\mu \neq 0$ would indicate a systematic bias, while $\sigma < (>)1$ would reveal an overestimation (underestimation) of the statistical uncertainties. Asymmetrical skewness or non-zero kurtosis of the distribution could also point to more nuanced problems. Non-linear correlation of the fitted values and its respective statistical uncertainties could be a possible cause in such cases.

The pull distributions for the signal component parameters are shown in Figure 5.11 for the nominal mass fits, overlaid with the projection of their respective fits to Gaussian PDFs. The corresponding results of these fits are listed in Table 5.6. Here the number of signal events includes the yields of peaking backgrounds.

5.3.4 Signal distributions

The mass fit characterizes the species in the sample, but there is still one additional step left for isolating the candidates to obtain the sig-

	$B_s^0 \to \phi\gamma$		$B^0 \to K^{*0}(892)\gamma$	
	μ_{Pull}	σ_{Pull}	μ_{Pull}	σ_{Pull}
μ_{CB}	0.02 ± 0.03	0.98 ± 0.02	-0.07 ± 0.03	1.00 ± 0.02
σ_{CB}	-0.04 ± 0.03	0.99 ± 0.02	0.00 ± 0.03	0.97 ± 0.02
N_{Signal}	0.01 ± 0.03	1.02 ± 0.02	0.03 ± 0.03	1.02 ± 0.02

Table 5.6: Values of the parameters from Gaussian fits to pull distributions of the mass fit signal parameters.

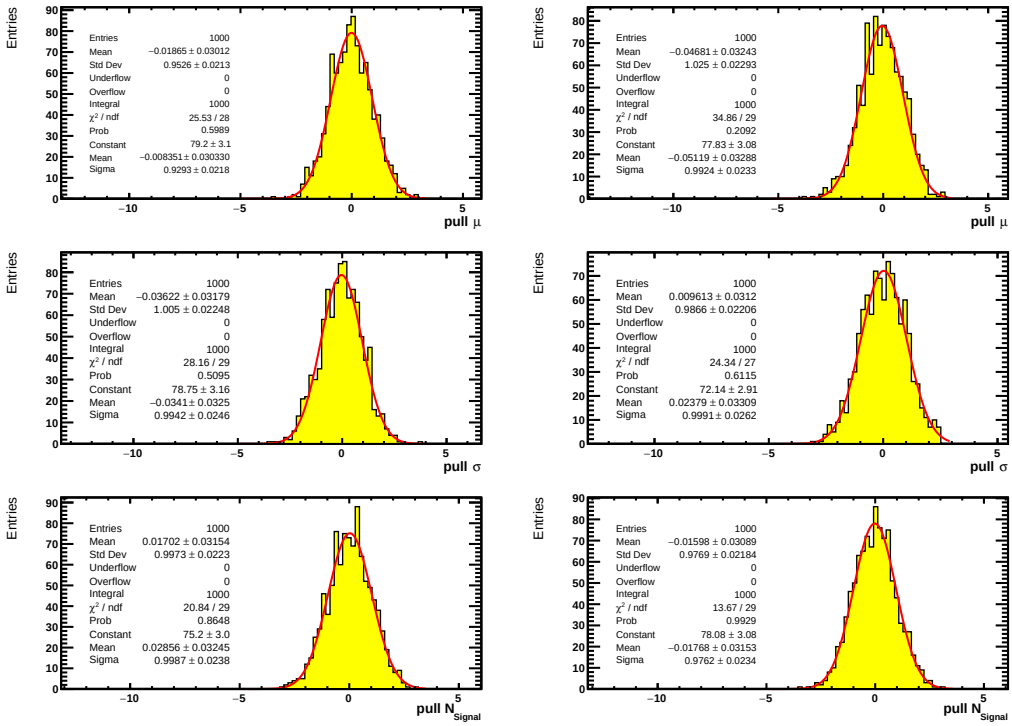

Figure 5.11: Pull distributions of the signal parameters mean (top), width (middle) and signal yields (bottom), from the $B_s^0 \to \phi\gamma$ (left) and $B^0 \to K^{*0}(892)\gamma$ (right) mass distribution fits. The projections of their respective fits to Gaussian distributions are overlaid on each plot.

nal component of the proper time distributions for both $B_s^0 \to \phi\gamma$ and $B^0 \to K^{*0}(892)\gamma$. Two techniques were deployed with this in mind, a weighting technique of the events based on their likelihoods as calculated from the mass fit, the so-called *sPlot* technique [109, 110]; and a method using the fitted yields for each background species and subtracting the corresponding number of events from their MC distributions, the background subtraction method.

sPlot formalism

The *sPlot* technique allows the reconstruction of *a priori* unknown distributions of a variable independently for each of the various species of events based on the behaviour of the distributions along a set of discriminating variables y. It is designed around maximum likelihood estimators as those

used in the aforementioned mass fits. Using the knowledge available for the discriminating variables the behaviour of the individual species of events with respect to the control variable can be inferred. This is true when two conditions are met:

1. The set of variables y must have a good discrimination power. That is, the different classes therein conform to sufficiently distinct models.

2. y must be uncorrelated with the target variable.

The *sWeight* for each event to be of the n-th species is calculated as

$$ {}_s\mathcal{P}_n(y_e) = \frac{\sum_{j=1}^{N_S} \mathbf{V}_{nj} \mathrm{f}_j(y_e)}{\sum_{k=1}^{N_S} N_k \mathrm{f}_k(y_e)}, $$

where $\mathrm{f}_i(y_e)$ is the value of the PDF of y for the i-th species for event e, N_S is the number of species in the sample, N_i is the average expected number of events for the i-th species and $\mathbf{V}_{ij}$ is the likelihood covariance matrix between species i and j, defined in terms of the likelihood, $\mathcal{L}$, as

$$ \mathbf{V}^{-1}_{ij} = \frac{\partial^2(-\mathcal{L})}{\partial N_i \partial N_j} = \sum_{e=1}^{N} \frac{\mathrm{f}_i(y_e)\mathrm{f}_j(y_e)}{\left(\sum_{k=1}^{N_S} N_k \mathrm{f}_k(y_e)\right)^2}, $$

where N is the total number of events in the sample.

In this analysis, the only discriminating variable used is the invariant mass of the B^0_s (B^0) candidates, so the likeness of each event to pertaining to any given class is calculated from the mass fit as described earlier in this chapter. The correlation between the invariant mass and the decay time distributions has been studied for the signal distributions and found to be negligible. The mass constrained proper-time is by definition uncorrelated to the mass (see Chapter 6 and Appendix A) and is therefore used afterwards.

After applying the *sPlot* weights to extract the signal distributions form data, these can be again compared to their MC counterparts. Agreement is general among all variables, except for the event fragmentation variables, as discussed in Section 4.2.3. I

Background subtraction method

A background subtraction strategy was developed as a complementary technique alongside the *sPlot* technique. As mentioned, the *sWeights* could be sensitive to correlations between the discrimination and the target variables. Since a direct background subtraction is indifferent to these correlations because they are included in the samples, this technique will allow to cross-check the *sWeighted* event weights.

All of the following is done separately for both $B_s^0 \to \phi\gamma$ and $B^0 \to K^{*0}(892)\gamma$. The contamination fractions of the various partially reconstructed backgrounds are extracted from the fit and the corresponding number of events is estimated in three regions of invariant mass. These regions depend on the fitted mean of the signal peak μ_{SIG} and are defined as follow:

Left Sideband (LSB) $[4600, \mu_{SIG} - 200)$ MeV/c^2,

Signal Region (SIG) $[\mu_{SIG} - 200, \mu_{SIG} + 200]$ MeV/c^2,

Right Sideband (RSB) $(\mu_{SIG} - 200, 6000]$ MeV/c^2.

To subtract the partially reconstructed background, their proper time distribution from fully reconstructed-as-signal MC samples is used, while data sidebands are used to subtract the combinatorial background distribution. In order to isolate the combinatorial component in the left sideband, partially reconstructed backgrounds are also subtracted from it.

To be precise, the expected number of background events are calculated as the product between the fitted contamination fraction and the integral of the PDF (normalized to the full mass range) of the species in the mass region times the fitted signal yield. These numbers are listed in Tables 5.7 and 5.8 for the $B_s^0 \to \phi\gamma$ and $B^0 \to K^{*0}(892)\gamma$ channels, respectively.

Background species	LSB	SIG	RSB	Total
$B_s^0 \to \phi\gamma$	168	3572	354	4094
Combinatorial	1478	833	743	3054
$B^+ \to \phi K^+\gamma$	359	0	0	359
$\Lambda_b \to \Lambda(pK)\gamma$	6	27	2	36
$B_s^0 \to \phi\pi^0$	13	22	0	35

Table 5.7: Number of events per background species in each mass band as calculated from a fit to the data, for the $B_s^0 \to \phi\gamma$ channel.

Background species	LSB	SIG	RSB	Total
$B^0 \to K^{*0}(892)\gamma$	935	24272	782	25988
Combinatorial	7976	5596	6095	19667
$B^0 \to K^+\pi^-\pi^0$	94	170	1	265
$B^0 \to K^*(892)^0\pi^0 X$	3519	32	0	3551
$B \to K^*(892)^0\pi\gamma$	3041	717	0	3758
$B \to (K\pi)\pi\gamma$	4925	552	0	5477
$\Lambda_b^0 \to \Lambda\gamma$	111	427	60	598
$B^0 \to \rho\gamma$	0	45	7	52
$B_s^0 \to \phi\gamma$	13	474	6	494

Table 5.8: Number of events per background species in each mass band as calculated from a fit to the data, for the $B^0 \to K^{*0}(892)\gamma$ channel.

As stated previously, the sidebands are extracted from data and the rest of the species are MC samples, both reconstructed as the signal channel, passing the whole selection chain. The reconstruction and selection efficiency in these samples is generally sub-optimal, and statistics are limited. In particular, very few events in the $B_s^0 \to \phi\pi^0$ (reconstructed as $B_s^0 \to \phi\gamma$) sample survived the selection cuts. For the $B^0 \to K^{*0}(892)\gamma$ channel, one of the background components is an inclusive mix of partially reconstructed decays mistaking a neutral pion with the photon ($B^+ \to K\pi\pi^0 X$). In the two cases the number of events in the MC was insufficient to construct the proper-time shape of this background. For these two backgrounds, a toy MC is generated with the mass PDF used in the fit and a proper time PDF

fitted to those few events. Tables 5.9 and 5.10 list the background sources used for the subtraction, for the $B_s^0 \to \phi\gamma$ and $B^0 \to K^{*0}(892)\gamma$ channels, respectively.

Background species	Remarks
Signal MC	
Combinatorial	Obtained from data sidebands
$B^+ \to \phi K^+ \gamma$	
$\Lambda_b \to \Lambda(pK)\gamma$	
$B_s^0 \to \phi\pi^0$	Generated based on a $B^+ \to K^+K^-\pi^+\pi^0$ MC sample

Table 5.9: Background sources for the $B_s^0 \to \phi\gamma$ channel. All samples are MC passing `S20r0p2`.

Background species	Remarks
Signal MC	
Combinatorial	Obtained from data sidebands
$B^0 \to K^+\pi^-\pi^0$	
$B^0 \to K^*(892)^0\pi^0 X$	
$B \to K^*(892)^0\pi\gamma$	Trigger selection removed to increase statistics
$B \to (K\pi)\pi\gamma$	
$\Lambda_b^0 \to \Lambda\gamma$	
$B^0 \to \rho\gamma$	
$B_s^0 \to \phi\gamma$	

Table 5.10: Background sources for the $B^0 \to K^{*0}(892)\gamma$ channel. All samples are MC passing `S20r0p2`.

Background subtraction was then performed to isolate the signal component. Example stack plots of the proper time distributions of the different components are shown in Figures 5.12 and 5.13. A comparison of both sidebands' distributions can be seen in Figure 5.14.

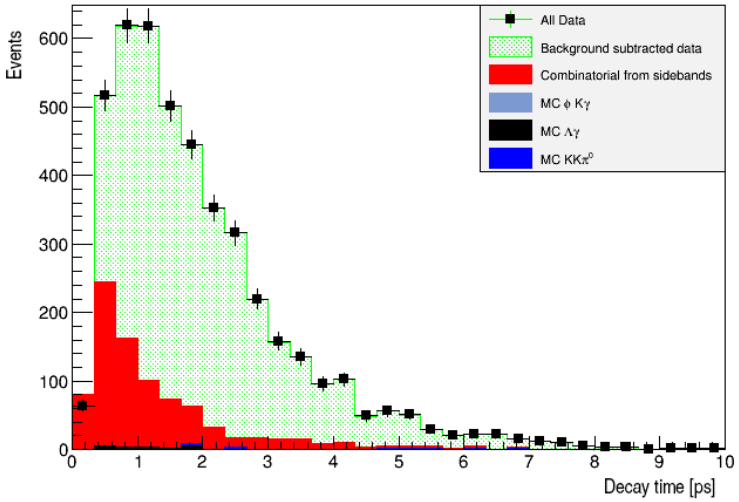

Figure 5.12: Proper time (stack) distributions for the background components of the $B_s^0 \to \phi\gamma$ candidates, where the combinatorial component has been taken from the right sideband.

To have a better representation, the combinatorial proper-time distribution is interpolated by summing events from both sidebands, with a proportion equal to the integrated PDF in each band normalized to the mass range. Using this mixed combinatorial background a more precise data subtracted distribution can be built, which is plotted for the $B^0 \to K^{*0}(892)\gamma$ channel in Figure 5.15 alongside the *sWeighted* distributionand the MC signal distribution. Good agreement between both techniques has been observed, reinforcing the decision to use the *sPlot* technique.

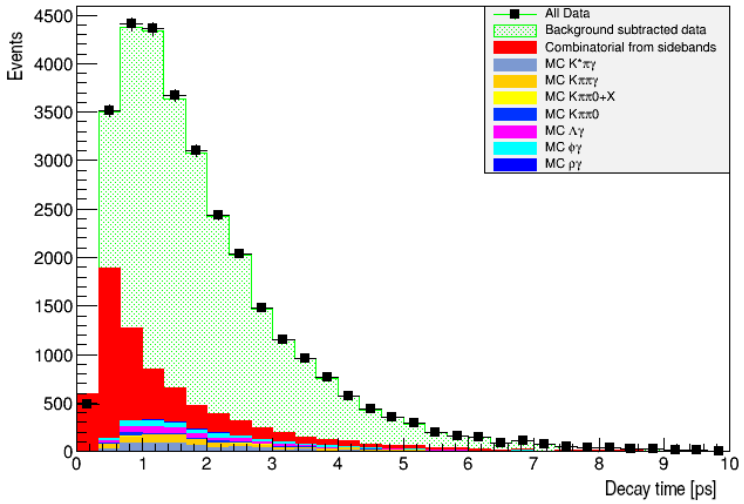

Figure 5.13: Proper time (stack) distributions for the background components of the $B^0 \to K^{*0}(892)\gamma$ candidates, where the combinatorial component has been taken from the right sideband.

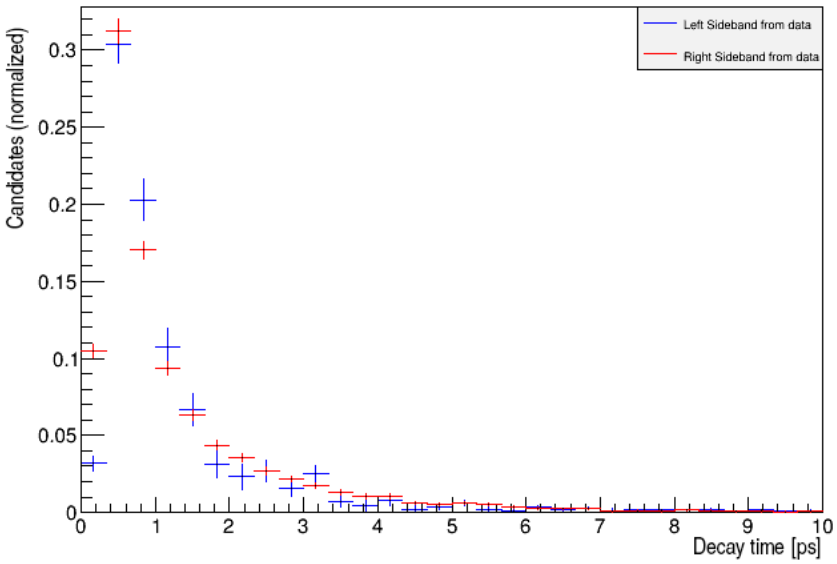

Figure 5.14: Comparison of the proper time distributions for the two sidebands after subtracting the peaking components, for the $B^0 \to K^{*0}(892)\gamma$ channel.

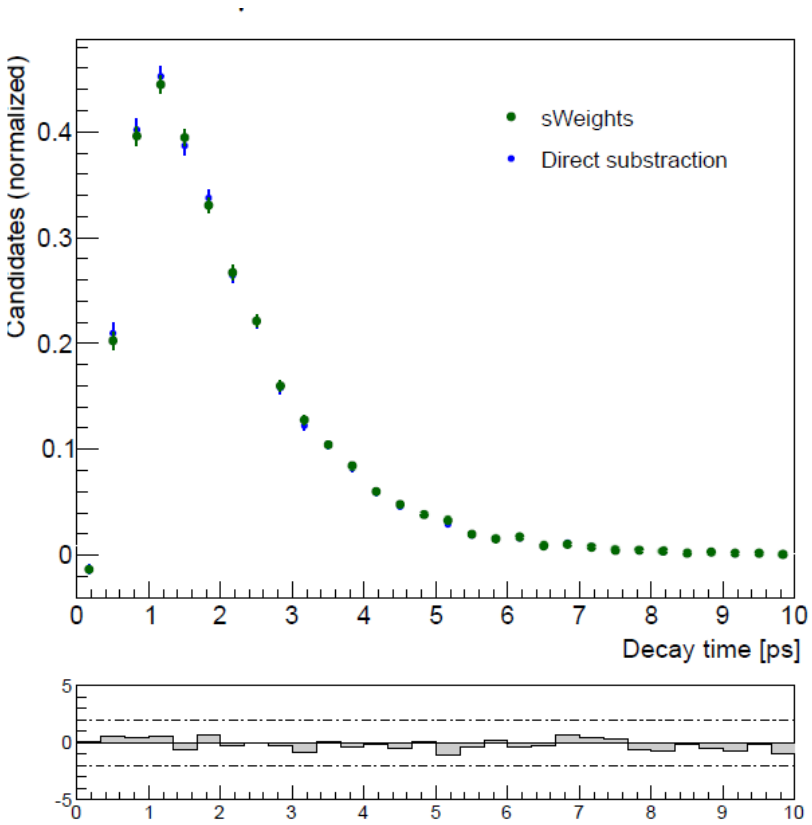

Figure 5.15: Background subtracted and *sWeighted* data proper time distributions. The residual plot is the difference between the first two distributions.

6 | Proper time description and reconstruction

This chapter includes the description of the proper time distributions of the decays and their characteristics. First, the algorithm used in LHCb to compute the proper time is explained. Afterwards, the functional form of the signal model is proposed, accounting for the reconstruction effects which affect the proper time, modelled as the acceptance function and the proper time resolution.

The decay time of a long lived particle is defined as

$$ct = \frac{L}{\beta\gamma} = \frac{m_B}{|\vec{p}_B|}L, \tag{6.1}$$

where L, the flight distance, is measured as the distance between the primary and secondary reconstructed vertices, and m_B and $\vec{p}_B$ are respectively the mass and momentum of the B meson candidate.

It has been shown in Section 1.4 that the untagged time-dependent decay rate of $B_s^0 \to \phi\gamma$ decays takes the form

$$\Gamma_{B_s^0 \to \phi\gamma}(t; \mathcal{A}^\Delta, \Gamma_s, \Delta\Gamma_s) = e^{-\Gamma_s t}\left[\cosh\left(\frac{\Delta\Gamma_s t}{2}\right) - \mathcal{A}^\Delta \sinh\left(\frac{\Delta\Gamma_s t}{2}\right)\right], \tag{6.2}$$

where the sensitivity to the photon polarization is contained in the $\mathcal{A}^\Delta$ parameter. The case of the self-tagging $B^0 \to K^{*0}(892)\gamma$ decay simplifies to

$$\Gamma_{B^0 \to K^{*0}(892)\gamma}(t; \Gamma_d) = e^{-\Gamma_d t}, \tag{6.3}$$

due to the negligible decay width difference between the B^0 mass eigenstates, $\Delta\Gamma_d = 0.0013 \pm 0.0066\ \text{ps}^{-1}$, sixty times smaller than that of B_s^0, $\Delta\Gamma_s = 0.083 \pm 0.006\ \text{ps}^{-1}$ [25]. Since the lifetimes of the B_s^0 and B^0 meson are very similar $\tau_{B_s^0} = 1.505 \pm 0.004\,\text{ps}$ and $\tau_{B^0} = 1.520 \pm 0.004\,\text{ps}$ [25],

respectively, the ratio of their untagged time-dependent decay rates, $\Gamma_{B_s^0 \to \phi\gamma}(t)/\Gamma_{B^0 \to K^{*0}(892)\gamma}(t)$, is dominated by the hyperbolic components in Eq. (6.2). This reveals the contribution of the $\mathcal{A}^\Delta$ parameter to the distribution of the ratio of proper times, as illustrated in Figure 6.1.

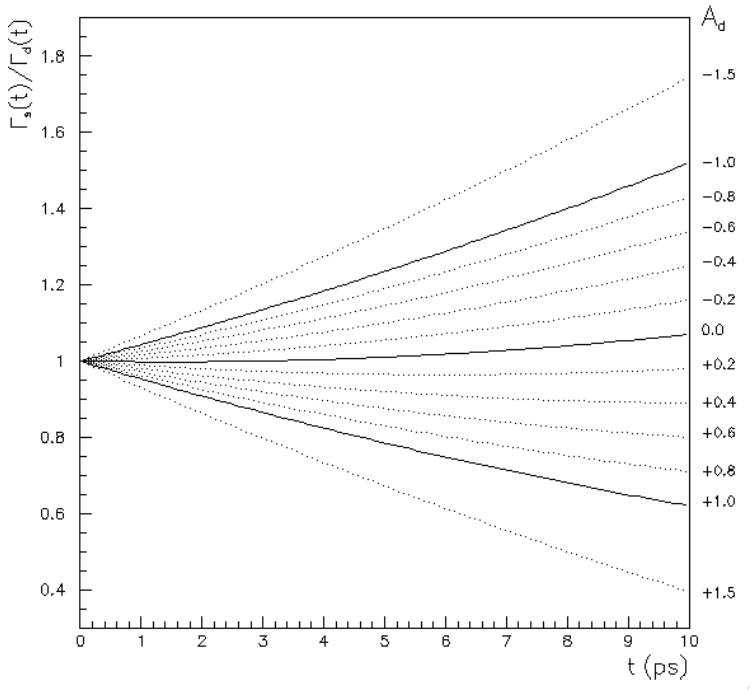

Figure 6.1: Functional form of the ratio of the time-dependent decay rates of $B_s^0 \to \phi\gamma$ over $B^0 \to K^{*0}(892)\gamma$ for several values of $\mathcal{A}^\Delta$ (A_d in the plot).

The PDF used to fit the proper time distribution is based on the physical forms of the decay rate, Eq. (6.2) for $B_s^0 \to \phi\gamma$ and Eq. (6.3) for $B^0 \to K^{*0}(892)\gamma$. Adding the description of detection effects results in a multiplicative time dependent efficiency, called acceptance $\mathcal{A}_B(t)$. Both the decay rate and the acceptance are functions of the physical proper time t, but the observable is actually the reconstructed proper time, t_r, affected by unavoidable detection effects. To represent this, the function is convolved with the proper time resolution that relates both, $\mathcal{R}_B(t, t_r)$. Therefore, the general PDF for the decay time can be built as

$$\Gamma_B(t_r) = [\mathcal{A}_B(t) \times \Gamma_B(t)] \otimes \mathcal{R}_B(t, t_r), \tag{6.4}$$

where $\Gamma_B(t)$ refers to either Eq. (6.2) or (6.3).

6.1 Proper time fit algorithm

In LHCb the reconstruction of the proper time is done through the `PropertimeFitter` tool from the GAUDI analysis package [84, 85]. This tool is explicitly described in Appendix A,whereas this section discusses specific related issues to this analysis.

A discrepancy between data and MC proper time distributions was found and lasted for a long time, which turned out to be originated in the calculation of the proper time. The discrepancy can be seen in Figure 6.2, where both techniques of background subtracted data are compared to the MC signal distribution. For some minority of events (about 3%) in the data the tool erroneously returned the value for $c\tau$ instead of the expected τ. Since it is a large factor and after an exhaustive investigation process, an isolated population of these events was observed far from the expected distribution when plotting the proper time distribution with a wide window. These events appear to belong to the tail of the proper time distribution when the factor is corrected. When left unchecked this caused significant differences in the determination of the higher proper time acceptance parameters, lacking reliability for the use of the MC as a reference. This will be addressed in detail in Section 6.2.

After further investigation, the problem was found to stem from two causes. On the one hand, the rounding of the covariance matrix when saved to lower precision for persistence in the different LHCb data formats (`microDST`,...) provoked in some cases non-positive definite matrices, resulting in failures of the algorithm. On the other hand, with the version of the tool used for this analysis, these types of failures indeed returned a value as if it had succeeded, only not correctly scaled by the c factor. To correct for this, the position-momentum covariance of the B meson has been re-evaluated using the vector meson covariance and the photon-cluster covariance. This reduces the failure rate to 0.15% in data. For consistency, the correction technique is applied both in data and MC.

The mass-constrained proper time option of the algorithm, described in detail in Appendix A, uses the nominal mass of the B meson in the calculation of the proper time instead of its measured value. The former is used in the analysis, as it ensures that the proper time and mass variables are uncorrelated for signal events, a necessary condition for the applicability

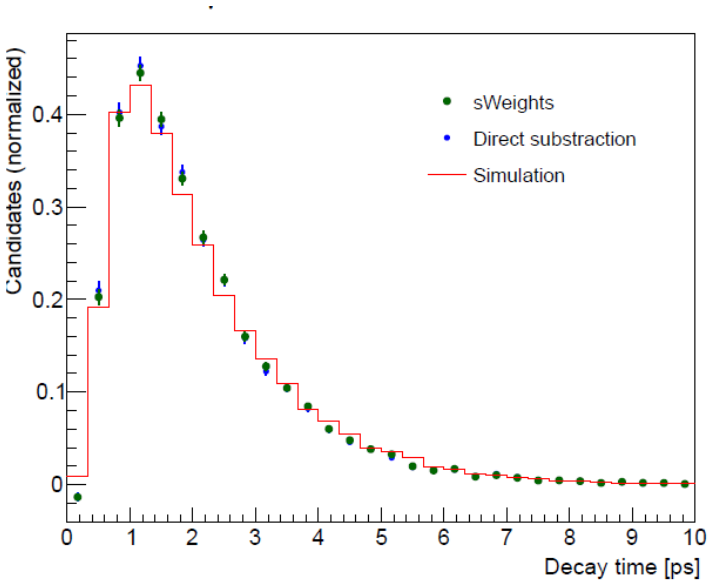

Figure 6.2: Background subtracted data, *sWeighted* data and MC signal proper time distributions.

of the *sPlot* technique, while it improves the proper time resolution.

6.2 Proper time acceptance

The acceptance is an event selection efficiency with a dependence on the proper time. It is a consequence of several unavoidable factors such as the vertexing and track isolation requirements in the selection. These factors produce inefficiencies at different regions of the proper time spectrum, as it can be seen in Figure 6.3.

The chosen parametrization adopted follows the form

$$\mathcal{A}(t; a, t_o, n, \delta\Gamma) = \frac{[a(t-t_0)]^n}{1+[a(t-t_0)]^n} e^{-\delta\Gamma t}, \tag{6.5}$$

where the ratio of polynomials, depending on the parameters a, t_0 and n, dominates the form at low proper times while the exponential part, depending solely on $\delta\Gamma$, describes the shape for the high proper time tail. This shape is derived from exhaustive MC and control data sample studies, as explained in the following sections.

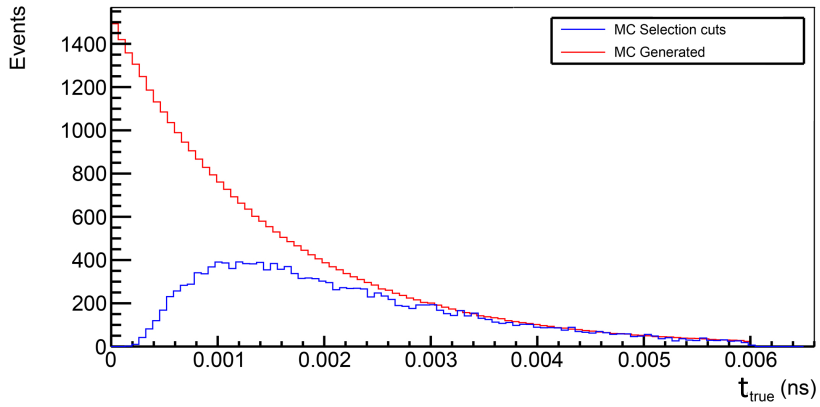

Figure 6.3: Monte Carlo generated proper time (in red) compared to the proper-time distribution after the trigger, stripping and offline selection (in blue), for the $B_s^0 \to \phi\gamma$ decay. The acceptance is defined as the ratio between the two distributions.

6.2.1 Contributions to the common acceptance

Any variable correlated with the B momentum and the vertices' position will play a major role in the shape of the acceptance. Cutting them in the different selection steps as described in Section 4.2 necessarily modifies the shape of the distribution. Since $B_s^0 \to \phi\gamma$ and $B^0 \to K^{*0}(892)\gamma$ have similar kinematical and topological properties, most of these changes are common and affect both acceptances similarly. As the aim is to minimize the differences between them, those variables can be safely used in the selection. Some exceptions were found, where a common selection would produce different parametrizations for the signal and the control channel, which should be avoided. Extensive work was performed in identifying these possible sources of differences, by comparing the effects of all the selection variables on the acceptance.

Two notable cases of variables biasing in a different way the acceptances of the signal and control channels are the DIRA and FD variables, greatly correlated with the proper time determination. The former is the quantity minimized during the proper time fit, while the latter is directly the flight length of the particle in the detector, also used in the fit. Selecting on these variables produces an undesirable difference between the $B_s^0 \to \phi\gamma$ and $B^0 \to K^{*0}(892)\gamma$ acceptances, as shown in the ratio of the two in Figures 6.4 and 6.5. Previous work [111] had already pointed these variables as obsta-

cles in using $B^0 \to K^{*0}(892)\gamma$ as a control channel for $B_s^0 \to \phi\gamma$. This drives the decisions in the offline selection and the stripping version (`S20rXp2`) both tailored specifically for this analysis.

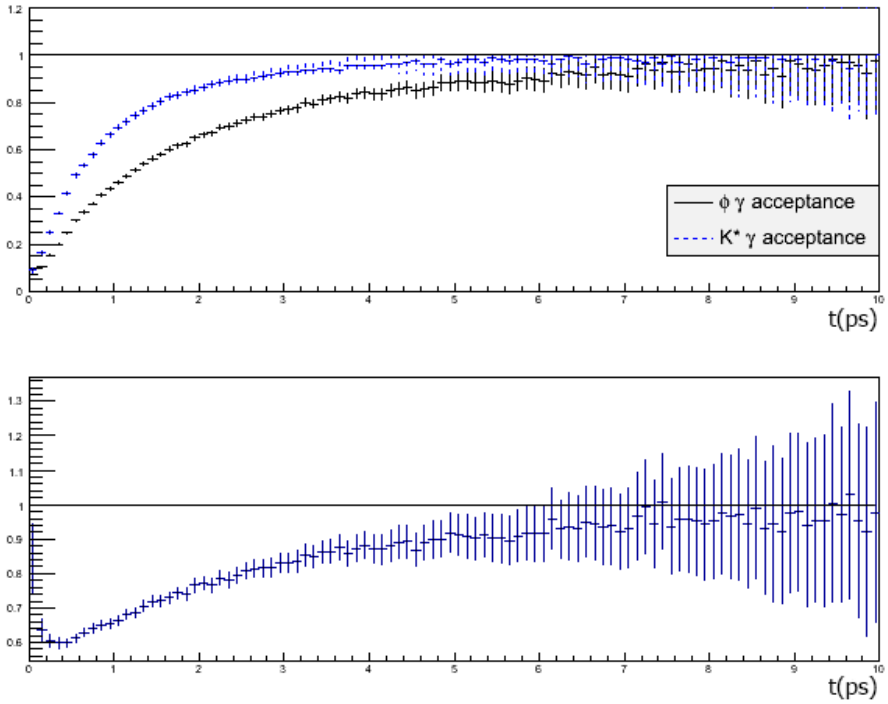

Figure 6.4: The top figure shows the acceptance distributions for the $B_s^0 \to \phi\gamma$ (solid black) and $B^0 \to K^{*0}(892)\gamma$ (dotted blue) decays obtained in MC samples with an unbiased selection and applying the discarded criteria on DIRA (< 20 mrad). The bottom figure shows the ratio of both distributions, where at low proper times an unwanted deviation from unity is observed.

A progression of the effect on the high decay time acceptance parameter $\delta\Gamma$ versus the selection steps, including the changes on the aforementioned variables, is shown in Figure 6.6, with the following tags associated to each reconstruction step:

hasVelo if the tracks (K/π) have VELO hits.

hasVeloAndT if K/π are reconstructible as Long tracks.

isVeloRec if K/π are VELO reconstructed.

isLongRec same as above, but as a Long track.

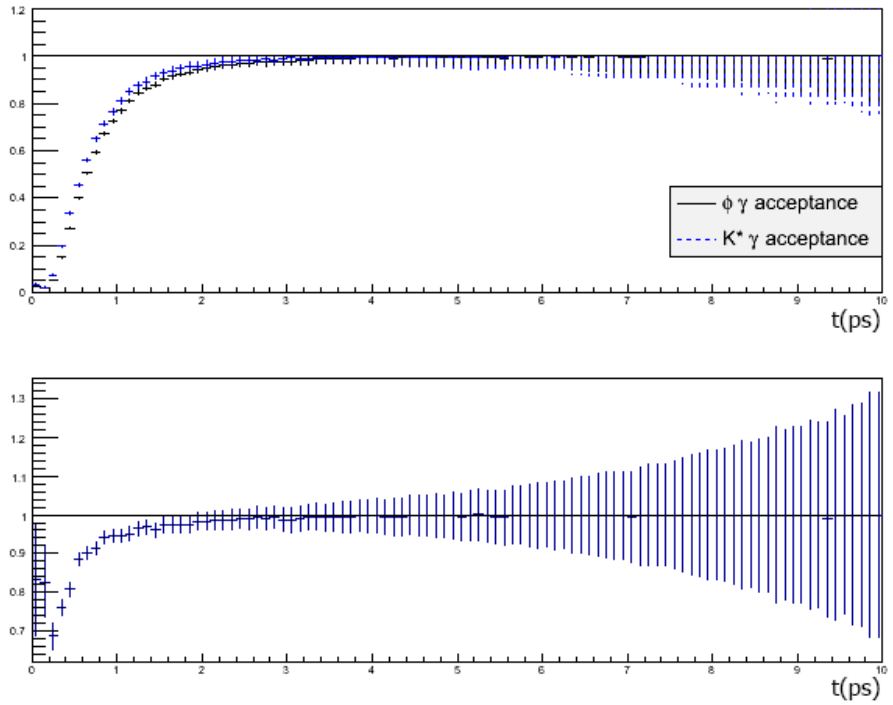

Figure 6.5: The top figure shows the acceptance distributions for the $B_s^0 \to \phi\gamma$ (solid black) and $B^0 \to K^{*0}(892)\gamma$ (dotted blue) decays obtained in MC samples with an unbiased selection and applying the discarded criteria on flight distance (expressed through its χ^2 from the vertex fit, selected at $\chi^2_{\rm FD} > 100$). The bottom figure shows the ratio of both distributions, where at low proper times an unwanted deviation from unity is observed.

iscompleteRec if K/π are reconstructed (associated to a ProtoParticle).

Stripping self-explanatory.

L0 | HLT1 | HLT2TOS the trigger is evaluated only on the signal candidate.

Offline self-explanatory.

6.2.2 Verification of the parametrization

The acceptance parameters of the MC decay time distribution for $B^0 \to K^{*0}(892)\gamma$ are obtained by fitting with a function defined as the

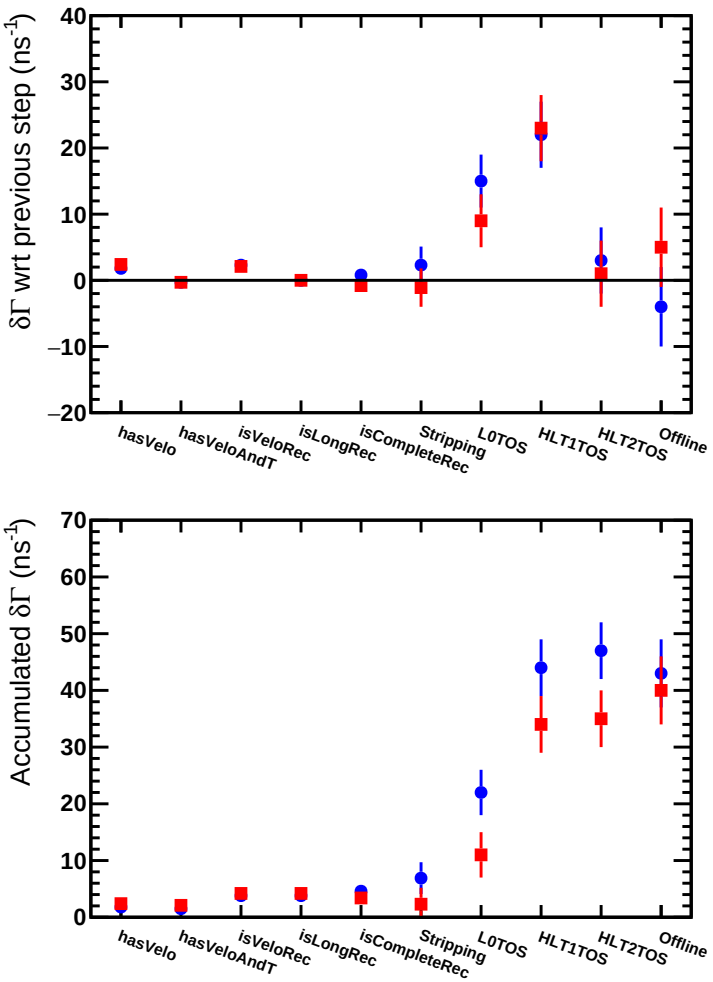

Figure 6.6: High decay time acceptance parameter, $\delta\Gamma$, introduced at each reconstruction or selection step for $B_s^0 \to \phi\gamma$ (blue circles) and $B^0 \to K^{*0}(892)\gamma$ (red squares). The bias introduced with respect to the previous step is shown on top, while the bottom figure corresponds to the total accumulative bias up to a given step. The tags are explained in the text.

product of Eqs. (6.3) and (6.5); fixing its decay width, Γ_d, to the generation value and leaving the acceptance parameters free.

If the MC reproduces the data distributions correctly, by fixing these MC parameters in a fit to the $B^0 \to K^{*0}(892)\gamma$ data distribution with the same function, a value for Γ_d compatible with the world average should be

recovered.

Using the acceptance parametrization from MC in a fit to the data sample, the fitted value of τ_{B^0} was $1.424 \pm 0.012\,\text{ps}$[1]. Being eight standard deviations off when compared to the world average of 1.520 ± 0.004 ps [25], it reveals a clear, hidden problem. After the fix discussed in Section 6.1 the fitted value is 1.524 ± 0.012 ps, compatible with the world average, allowing the analysis to proceed by using the MC parametrization of the acceptance.

The values of the acceptance parameters obtained through the fit to simulated samples of both decay channels are listed in Table 6.1, while the corresponding fit projections are shown in Figure 6.7. It can be observed that both sets of parameters are compatible with each other.

Table 6.1: Acceptance parameters from simulation for the $B_s^0 \to \phi\gamma$ and $B^0 \to K^{*0}(892)\gamma$ decays.

MC acceptance		$B_s^0 \to \phi\gamma$	$B^0 \to K^{*0}(892)\gamma$
$\delta\Gamma$	(ps^{-1})	0.0417 ± 0.0045	0.0457 ± 0.0047
a	(ps^{-1})	1.749 ± 0.068	1.728 ± 0.063
n		2.28 ± 0.17	2.29 ± 0.17
t_0	(ps)	0.143 ± 0.026	0.153 ± 0.026

6.3 Proper time resolution

In Eq. (6.4) a resolution term, $\mathcal{R}_B(t, t_r)$, is included to account for the inaccuracies in the reconstruction of the proper time by the detector. This function relates the reconstructed proper time, t_r, with the physical decay time, t, of the B meson.In this section and for clarity purposes only, the notation t_{true} and t_{reco} will be used for the physical, t, and the reconstructed, t_r, proper times respectively.

To model the resolution a study of the reconstruction is done in simulation by defining the quantity $\delta t = t_{\text{reco}} - t_{\text{true}}$, with t_{reco} being reconstructed as given by Eq. (6.1) using the same `PropertimeFitter` tool as in data, and t_{true} being the simulated physical proper time of the decay. Ideally, the quantity δt should be described by a Dirac δ function as the reconstructed time would correspond exactly to the physical value. In practice this is not the case and it is approximately a Gaussian distribution characterized by

[1] Shown is the statistical uncertainty, only.

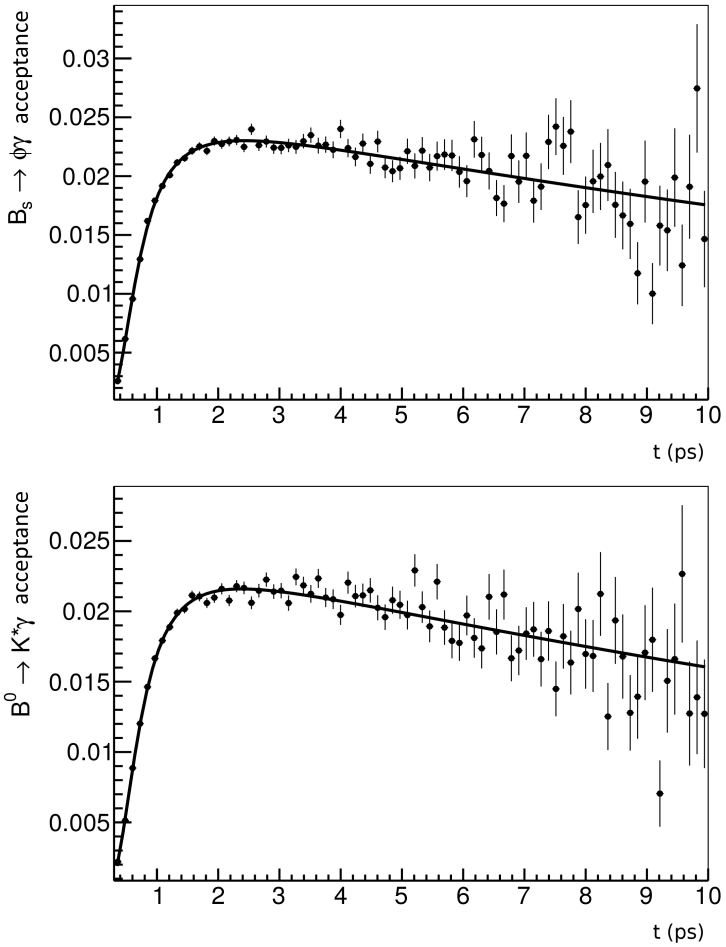

Figure 6.7: Projections of the fit to the acceptance function of selected MC proper time distributions of $B_s^0 \to \phi\gamma$ (top) and $B^0 \to K^{*0}(892)\gamma$ (bottom), using all the available simulation samples, accounting for a total of 9×10^6 events for each channel.

its width and mean. Because of the definition of δt, the mean of the Gaussian is called the resolution bias, t_{bias}. If the measured value of the mass of the B meson is used in the reconstruction of the proper time, the resolution bias has a dependence with it, and mostly disappears when applying a mass constraint, as pictured in Figure 6.8. Since the mass constrained proper time is used in this analysis, no correction is applied.

The resolution is found to vary with proper time linearly, as shown in Figure 6.9. It has been observed that correcting for the widths of the distri-

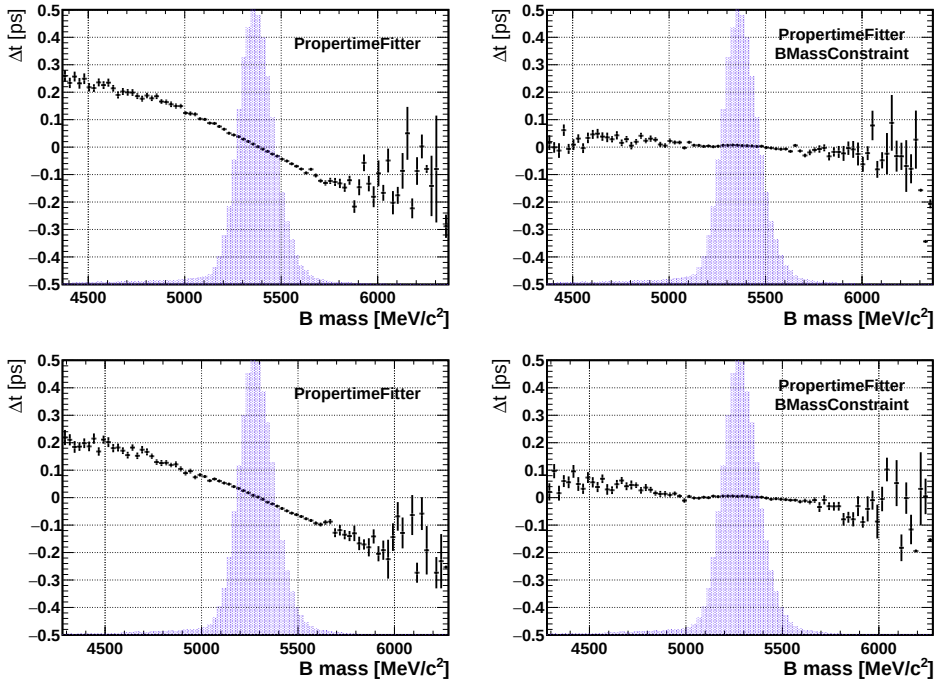

Figure 6.8: Dependence of the resolution bias (Δt in the plots) with the mass for the $B_s^0 \to \phi\gamma$ (top) and $B^0 \to K^{*0}(892)\gamma$ (bottom) decay channels obtained without (with) a mass constraint in the proper-time reconstruction in the left (right) plot. The superimposed blue histograms represent the reconstructed B mass distribution.

butions has no sizeable effect on the results. This is because the resolution width, $\approx$ 60 fs , is significantly smaller than the proper time structure required for the measurement of $\mathcal{A}^{\Delta}$. While the mean induces an event migration across adjacent bins towards higher values, the width distributes them evenly, effectively compensating at the bin edges. To account for this, a time-dependent correction factor only of the resolution bias is applied, event-by-event, to the sample during the fitting procedure.

As shown in Eq. (6.1), the proper time is calculated as a function of the flight distance of the B meson in the detector, measured as the difference between the positions of the secondary and primary vertices. It is also a function of the momentum of the B meson, in turn having a resolution depending on the resolution of its daughter components. The energy resolution in the ECAL provides the major contribution to this resolution. The energy calibration procedure outlined in Section 2.4.2 is applied offline,

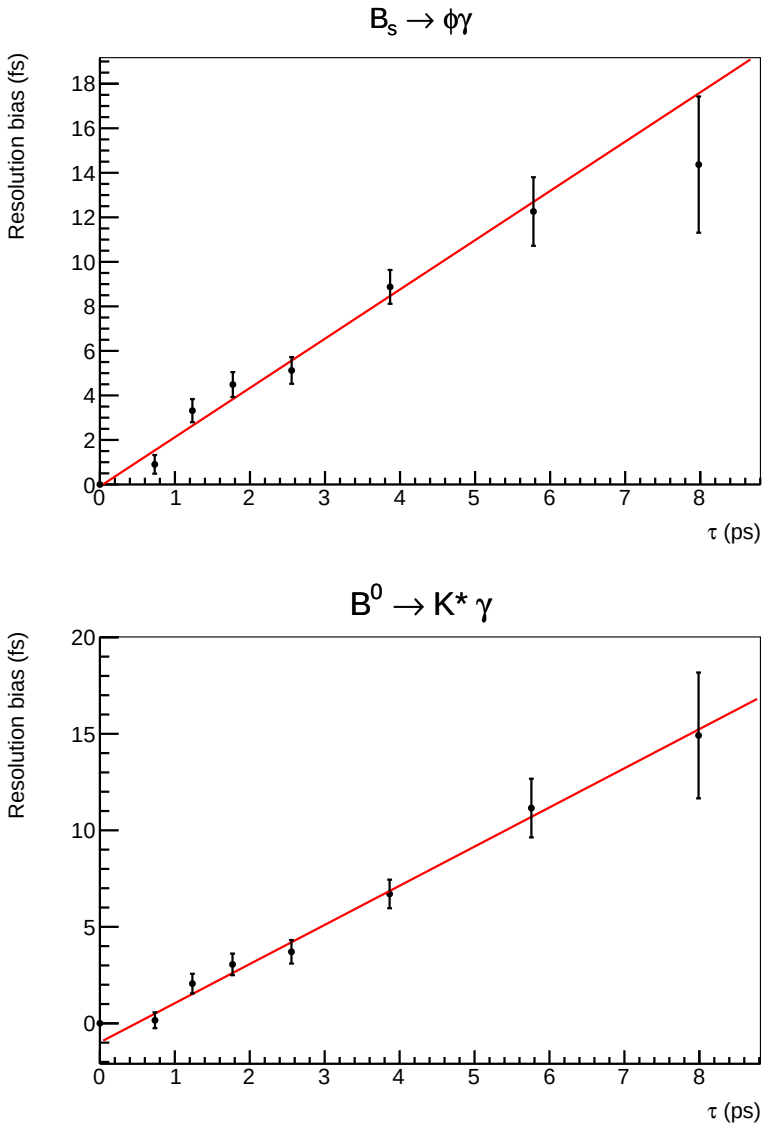

Figure 6.9: Time dependent resolution bias for the $B_s^0 \to \phi\gamma$ (top) and $B^0 \to K^{*0}(892)\gamma$ (bottom) decay channels obtained from simulated events as a function of the reconstructed proper time.

and therefore trigger and stripping requirements on photon quantities are unaffected by this calibration. In the selection for this analysis, most of the resolution bias comes from the photon CL variable, introduced in Section 2.4.4. Therefore, the proper time resolution arises from the accuracy

with which the vertices and the photon momentum are determined.

6.3.1 Resolution control with $B^0 \to J/\psi K^{*0}(892)$ samples

To further evaluate the vertex-related contributions to the resolution, the B^0 proper time in $B^0 \to J/\psi K^{*0}(892)$ samples is reconstructed without the dimuon vertex and only using its momentum, as if the J/ψ was a photon with a well defined momentum. In LHCb the J/ψ momentum resolution is specially high, reaching $\delta p_{J/\psi}/p_{J/\psi} = 0.35\%$, as compared to the photon energy resolution from the ECAL of $\delta E_\gamma / E_\gamma \approx \frac{8.5\%}{\sqrt{E}}$.

Forgoing the track information from the dimuon system the $B^0 \to J/\psi K^{*0}(892)$ proper time can be reconstructed as if the J/ψ was a photon, by only using its momentum. Therefore, an estimator of the effect of missing the location information from the photon in the resolutions of $B_s^0 \to \phi\gamma$ and $B^0 \to K^{*0}(892)\gamma$ can be built by subtracting the reconstructed proper times of the events using the full dimuon vertex from those simulating a photon-like reconstruction in $B^0 \to J/\psi K^{*0}(892)$. Since the momentum resolution for the J/ψ is also very high, only the effect of the vertexing should appear. Such distributions for both the proper time and its mass constrained variant are pictured in Figure 6.10, along with the projection of a fit to a double-tailed crystal ball PDF. The results from the fit are listed in Table 6.2, from where it is deduced that the resolution effect in the radiative channels is dominated by the contributions from the photon energy resolution.

Table 6.2: Contribution of the vertexing to the resolution as obtained from $B^0 \to J/\psi K^{*0}(892)$ data, fitted to a double-tailed crystal ball.

		Proper time	Mass constrained proper time
μ	fs	-0.4 ± 1.2	0.3 ± 1.5
σ	fs	34.9 ± 2.6	37.1 ± 2.9
N_L		11.5 ± 3.8	2.5 ± 0.3
α_L		0.930 ± 0.101	0.81 ± 0.08
N_R		17.6 ± 7.7	1.63 ± 0.17
α_R		0.796 ± 0.083	1.039 ± 0.098

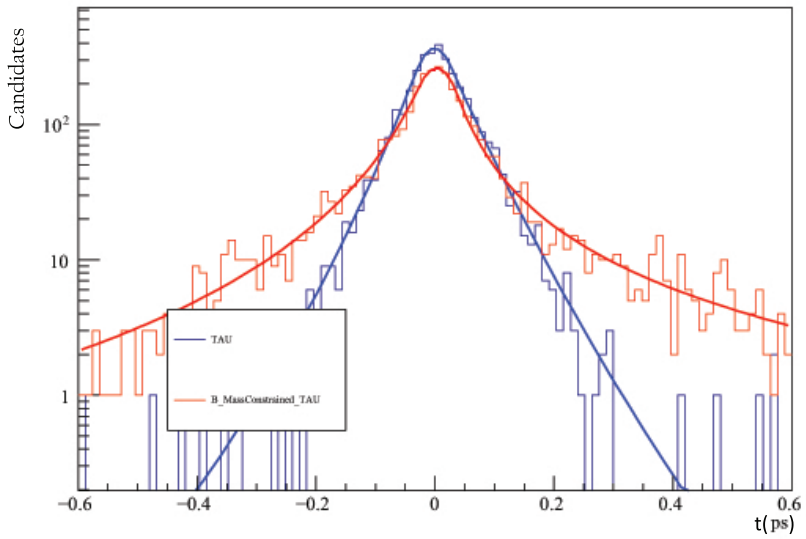

Figure 6.10: Difference between the proper time distributions obtained taking into account the dimuon vertex and ignoring it, in $B^0 \to J/\psi K^{*0}(892)$. The fit projections to double-tailed crystal ball PDFs are overlaid. The red (blue) distributions correspond to the proper time reconstructed with (without) the B mass constraint.

7 | Fit to the normalized proper time distribution

7.1 Fit strategy

The study of the photon polarization in $B_s^0 \to \phi\gamma$ decays is done through a fit to the relative proper time distributions of $B_s^0 \to \phi\gamma$ and $B^0 \to K^{*0}(892)\gamma$ decays, as discussed previously. The advantage of this strategy is expected to lie in the reduction of systematic uncertainties due to the topological and kinematic similarities of both decays, in particular those uncertainties related to the acceptance. While the previous chapter dealt with the description of the proper time distributions, the present is dedicated to the actual fitting procedure, the statistical sensitivity studies and the assignment of systematic uncertainties.

7.1.1 Binning scheme

When applying a ratio of decay widths a binning scheme is mandatory. The shapes of the proper time distributions, while not formally a pure exponential, are dominated by an exponential decay with prolonged tails of decreasing probability. In terms of bins this means a high relative error in the tail bins, as the associated error of a bin is poissonian in nature, the relative error evolving as $1/\sqrt{N}$, with N the events within the given bin. It is easily seen that this relative error diverges when $N \to 0$. Similarly, the low proper time region has low populations due to the acceptance and the effect is similar.

In the ratio of two similar exponential shapes, the statistical fluctuations in the tail bins are enhanced as they are poorly defined owing to the scarcity of events.This affects the fit as the weights of the bins in the tail are small in comparison to those of other more populated bins and are es-

sentially not accounted for in the fit. As a matter of fact, as evidenced in Figure 6.1, the region most sensitive to $\mathcal{A}^{\Delta}$ is at these higher proper time values. To maximize sensitivity, an adaptive binning algorithm has been designed to ensure a similar population in each bin, and thus having all of them participate in the fit with approximately the same proportion. The output of the algorithm provides edges that guarantee a minimum number of events per bin (bin occupancy) for both channels before evaluating the ratio. It is run over a generated toy MC experiment with a shape of the $B_s^0 \to \phi\gamma$ proper time distribution with SM parameters and assuming $\mathcal{A}^{\Delta} = 0$, and the widths obtained are then applied in the binning of both the $B_s^0 \to \phi\gamma$ and $B^0 \to K^{*0}(892)\gamma$ samples.

Setting the range limits for the binning, minimum occupancy[1] and step size, the algorithm works for any given distribution of events with respect to a single variable in the following way:

1. Starts off from one of the two arbitrarily chosen limits for the distribution.

2. Scans the axis in finite steps towards the opposite edge, counting the sum of events between the starting edge and the moving edge until the current value meets either condition:

   (a) If the current sum is equal or above the required occupancy, the moving edge value is saved as a new bin edge and the count reset to zero.

   (b) If the sum is less than the required occupancy and the opposite limit of the distribution has been reached, the last saved bin edge value is replaced by that limit, and the algorithm ends. In other words, the last bin is merged with the penultimate one if found to be underpopulated. This step ensures that the last built bin always surpasses the minimal occupancy condition, even if resulting in a relatively overpopulated bin.

3. If the algorithm hasn't ended due to the condition 2.(b), repeat from step 1, replacing the original scan point with the last saved bin edge value.

The algorithm produces a correct set of bins if the step is smaller than the smallest bin width. If the algorithm produces a bin approximately as wide as the step size, it should be run again with a reduced step size.

[1] Alternatively, one can choose the total number of bins.

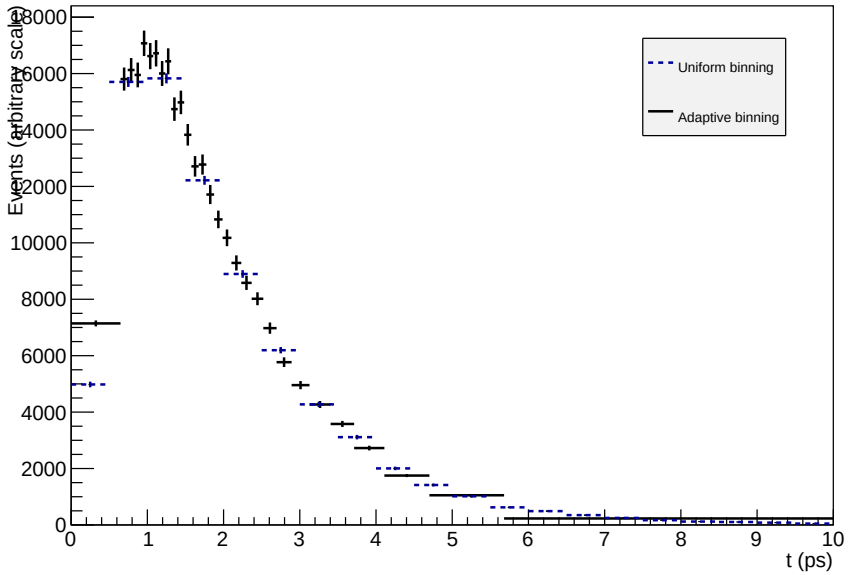

Figure 7.1: An example of adaptive binning of a generated proper time distribution (solid black) line as compared to the uniform binning (dashed red).

Figure 7.1 shows an example of this adaptive binning. The assumptions for the value of $\mathcal{A}^{\Delta}$ when generating the binning have no effect in the measured central value, as it is observed since the fitted value is independent of the binning scheme. Nevertheless, there is an effect on sensitivity as discussed previously, and that's the reason the shape must be as similar as possible to that of the signal so as to avoid incorrect bin fillings. The sensitivity to $\mathcal{A}^{\Delta}$ is observed to have a minimum around 30 bins. A lower number of bins results in larger bins, resulting in the loss of features of the original curve to drive the fit, while a larger number of smaller bins results in larger errors per bin and the scattering in the low population zones appears again. These effects are pictured in Figure 7.2.

7.1.2 Fitting algorithm

Once both the $B_s^0 \to \phi\gamma$ and $B^0 \to K^{*0}(892)\gamma$ proper time distributions are correctly binned, the ratio is calculated by dividing each bin of the former by the corresponding one from the latter. The error of the ratio is calculated using the usual propagation of a ratio with the errors of the original

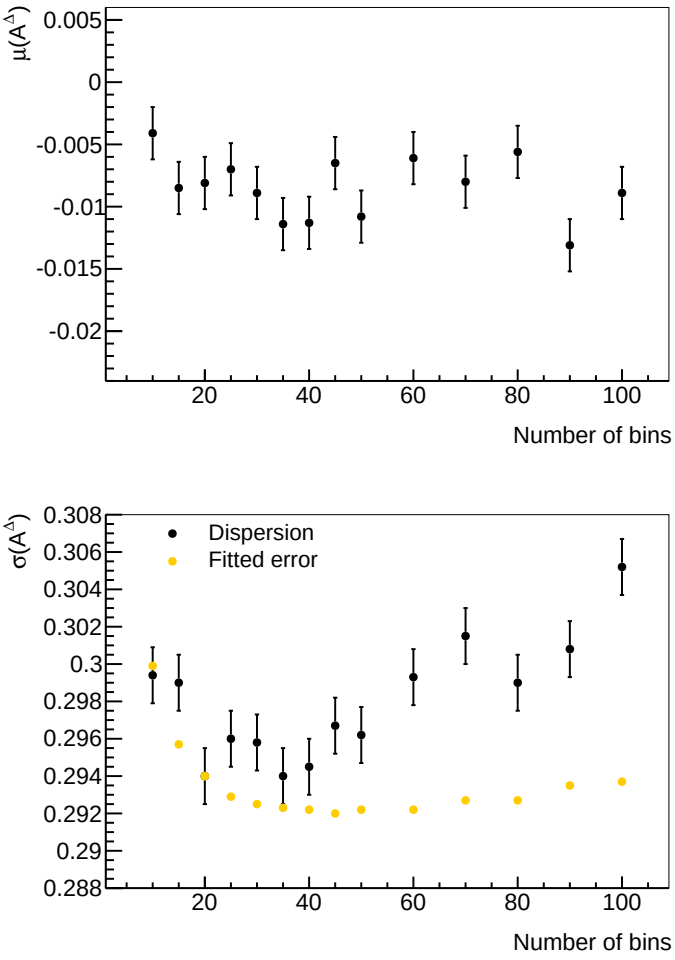

Figure 7.2: Fitted $\mathcal{A}^{\Delta}$ value (top) and sensitivity (bottom) as a function of the number of bins in the adaptive binning scheme, obtained from pseudo-experiments. A maximum bias of -0.01 on $\mathcal{A}^{\Delta}$ is observed, with no dependence on the bin number. On the bottom plot, the sensitivity (yellow) matches the dispersion (black) around 30 bins, which is also close to the minimum.

bins. Since the original bins are *sWeighted* samples, their respective errors are the sum of the *sWeights*.

A χ^2 figure of merit is built by summing the squared distances between

the expected and observed ratio values scaled by the observed uncertainty,

$$\chi^2 = \sum_i^{\mathrm{N}} \left[\frac{R_i^{\mathrm{exp}} - R_i^{\mathrm{obs}}}{\sigma_i^{\mathrm{obs}}} \right]^2 ,$$

where N is the number of bins, R_i the value of ratio in the i-th bin and σ_i its uncertainty. The labels 'exp' and 'obs' refer to the expected and observed values, respectively.

The observed value of the ratio of a given bin, R_i^{obs}, is directly obtained by dividing the binned data distributions as described previously. Somewhat more complicated is the definition of the expected value of the ratio in each bin, R_i^{exp}. It is calculated from the functional forms of the time dependent decay rate for $B_s^0 \to \phi\gamma$ and $B^0 \to K^{*0}(892)\gamma$ described, respectively, in Eqs. (6.2) and (6.3), corrected by their corresponding acceptances as per Eq. (6.5). As discussed in Section 6.3 the resolution is accounted for by shifting the values of the proper time to correct for the small time-dependent bias, as $t \to t - t_{\mathrm{bias}}(t)$.

The default technique of simply choosing the function value in the bin center will bias the ratio value, as the average events generally differ from the function value in the middle point with the discrepancy being proportional to the bin size. Thus, every value of the ratio must be calculated as the ratio of the curve integrals within the bin range,

$$R_i^{\mathrm{exp}} = \frac{\int_{t_i^{\mathrm{low}}}^{t_i^{\mathrm{high}}} \mathcal{A}_{B_s^0 \to \phi\gamma}(t) e^{-t/\tau_{B_s^0}} \left[\cosh \frac{\Delta\Gamma_s}{2} t - \mathcal{A}^{\Delta} \sinh \frac{\Delta\Gamma_s}{2} t \right] \mathrm{d}t}{\int_{t_i^{\mathrm{low}}}^{t_i^{\mathrm{high}}} \mathcal{A}_{B^0 \to K^{*0}(892)\gamma}(t) e^{-t/\tau_{B^0}} \, \mathrm{d}t}, \qquad (7.1)$$

where the usual normalization to the bin width for variable size bins cancels out, as the factor is the same for numerator and denominator.

The χ^2 of the distribution is minimized using the MINUIT package [112] by varying the fit parameter $\mathcal{A}^{\Delta}$ and a normalization parameter that represents the proportion of $B_s^0 \to \phi\gamma$ and $B^0 \to K^{*0}(892)\gamma$ events. Tests have been performed to exclude the possibility of local minima around the best solution and are discussed as part of the systematic uncertainties in Section 7.2.

An example of the fitting algorithm in a pseudo-experiment is shown in Figure 7.3 for illustration purposes only.

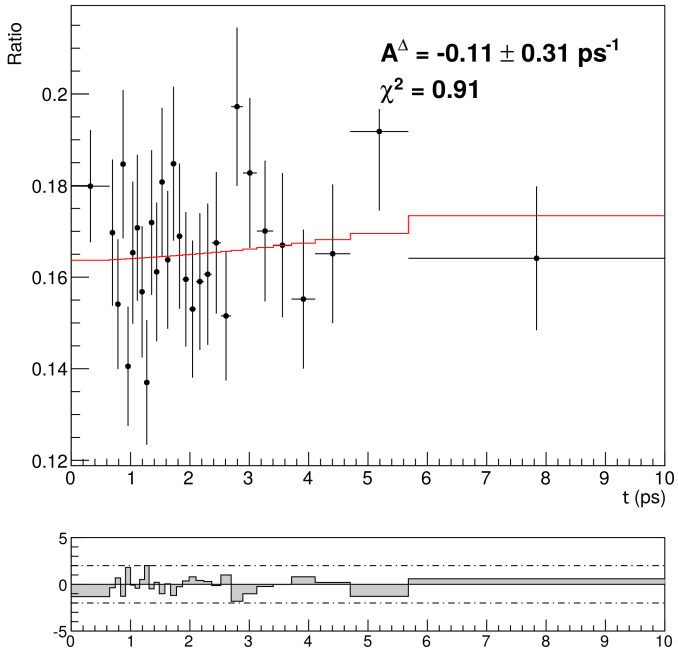

Figure 7.3: An example of the fitted ratio distribution R^{exp} (red line), overlaid on a binned generated proper time distribution R^{obs} (black points), for a Monte Carlo pseudo-experiment. Shown below are the differences between the expected and observed distributions, divided by the observed error.

7.1.3 Statistical sensitivity

The statistical sensitivity arises from the limited sample size. It represents the probability of a measurement differing the sought value following natural random variations in the event pool. By the law of large numbers, individual statistical fluctuations tend to cancel each other with an increasing number of events and the measured value better approximates the expected value. Therefore, the associated uncertainty decreases with the number of events.

The fit procedure has been tested extensively with MC pseudo-experiments also referred to as 'toy experiments' or simply 'toys'. These pseudo-experiments consist in repeating the same fitting procedure over a set of randomly generated samples with the same statistics as the available data samples described by the same functional form. The statistical fluctuations arising from a random generation providing a different proper

time distribution can be studied by observing the cumulative sample of fit results and their respective errors.

A total of 100 000 pure signal samples of each channel are generated, following Eqs. (6.2), (6.3), and (6.4). For each experiment, 4×10^3 $B_s^0 \to \phi\gamma$ and 24×10^3 $B^0 \to K^{*0}(892)\gamma$ events are generated, corresponding to the observed yields in $3\,\text{fb}^{-1}$ of collected luminosity, matching the expected yields after accounting for the diverse production and detection efficiencies. The physical parameters, listed in Table 7.1, are fixed to the 2016 world averages [25]. Several values of the $\mathcal{A}^\Delta$ parameter in the physical range $[-1, +1]$ are generated to study any possible dependence of the statistical sensitivity. The resolution is left out after testing its effect on the results and found to be negligible. The acceptance parameter values are set to those obtained in a fit to the MC samples as described in Section 6.2, and listed in Table 6.1. Examples of the pseudo-experiments are shown in Figure 7.4 for three values of the generated $\mathcal{A}^\Delta$. The variation in uncertainty is pictured in Figure 7.5 and ranges from 0.22 for $\mathcal{A}^\Delta = 1$ to 0.35 for $\mathcal{A}^\Delta = -1$.

Table 7.1: External inputs from [25].

Parameter	**Average**
$\Delta\Gamma_s$	0.083 ± 0.006 ps^{-1}
Γ_s	0.6643 ± 0.0020 ps^{-1}
Γ_d	0.6579 ± 0.0017 ps^{-1}
$\rho(\Gamma_s, \Delta\Gamma_s)$	-0.239
$\tau_{B_s^0}$	1.505 ± 0.004 ps
τ_{B^0}	1.520 ± 0.004 ps

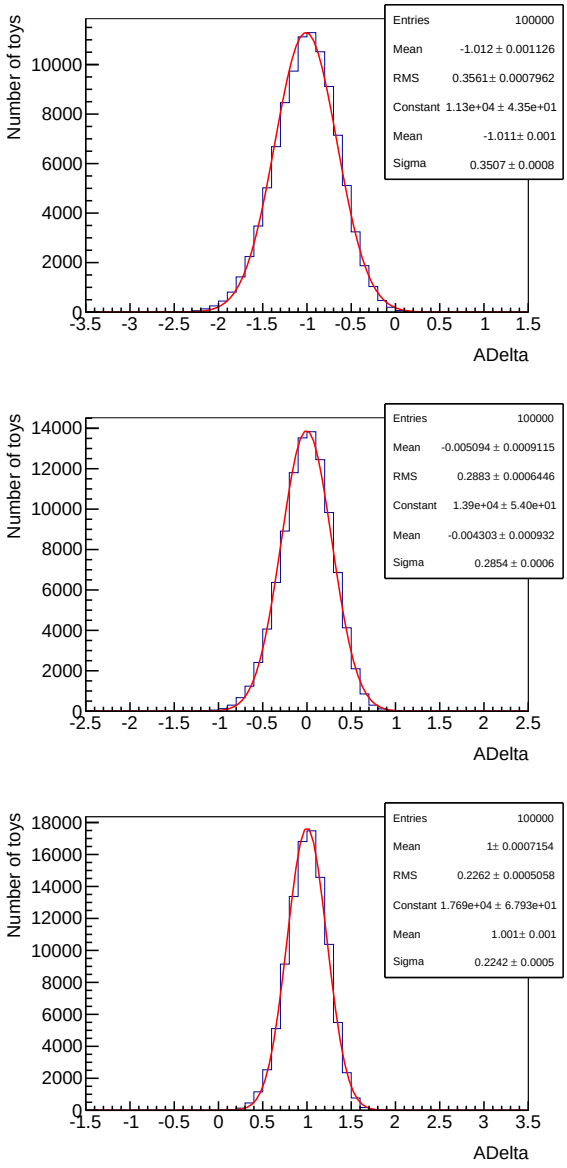

Figure 7.4: Distributions of $\mathcal{A}^{\Delta}$ central values as obtained from fits of pure signal MC pseudo-experiments. Results for three generated $\mathcal{A}^{\Delta}$ values are shown: -1 (top), 0 (middle) and 1 (bottom).

Fixing the value of $\mathcal{A}^{\Delta}$ to its predicted SM value, derived from [26], a study of the dependence of $\sigma_{\mathcal{A}^{\Delta}}$ with the signal yield of $B_s^0 \to \phi\gamma$ was performed. The results fit well to a function evolving as the inverse of the square root of the number of events, as expected, and is plotted in Fig-

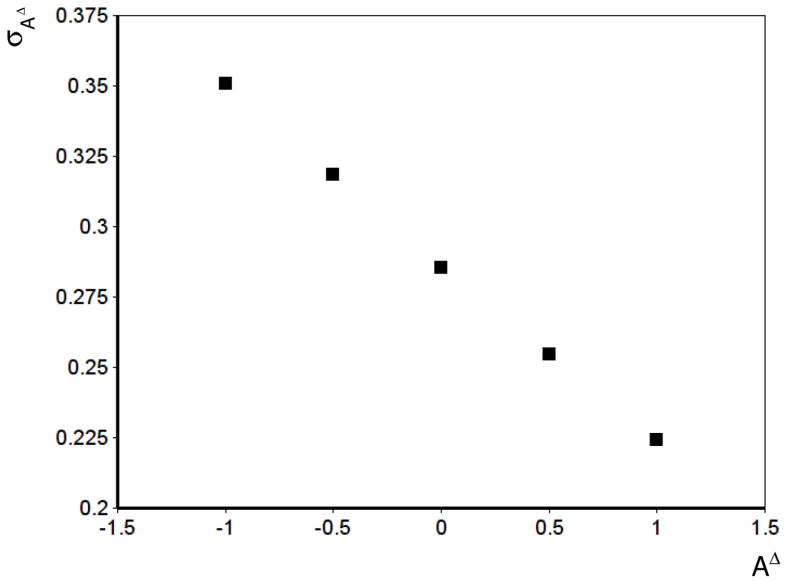

Figure 7.5: Correlation of the sensitivity to $\mathcal{A}^\Delta$ with its value, from simulated pseudo-experiments.

ure 7.6. These tests are made generating only the signal distribution and assuming infinite statistics for the control sample. The statistical uncertainty corresponding to the observed signal yield is ± 0.24. Note this value is for the predicted SM value of $\mathcal{A}^\Delta$ and the statistical sensitivity has a dependence on the actual value, as discussed previously. From pseudo-experiments, using the observed yield of the control sample results in an additional contribution of approximately ± 0.15 to the statistical sensitivity, while simulating the samples with background sources and subtracting them produces a further effect of approximately ± 0.24.

Fitting τ_{B^0} and $\mathcal{A}^\Delta$ from the $B_s^0 \to \phi\gamma$ and $B^0 \to K^{*0}(892)\gamma$ Monte Carlo samples is done as an additional check, with the aim to recover the generation values. The fit projections are shown in Figure 7.7 and the results are

$$\tau_{B^0\mathrm{MC}} = 1.522 \pm 0.005\,\mathrm{ps},$$
$$\mathcal{A}^\Delta_{\mathrm{MC}} = -0.003 \pm 0.072,$$

completely compatible with the generation values $\tau_{B^0\mathrm{gen}} = 1.519\,\mathrm{ps}$ and $\mathcal{A}^\Delta_{\mathrm{gen}} = 0$.

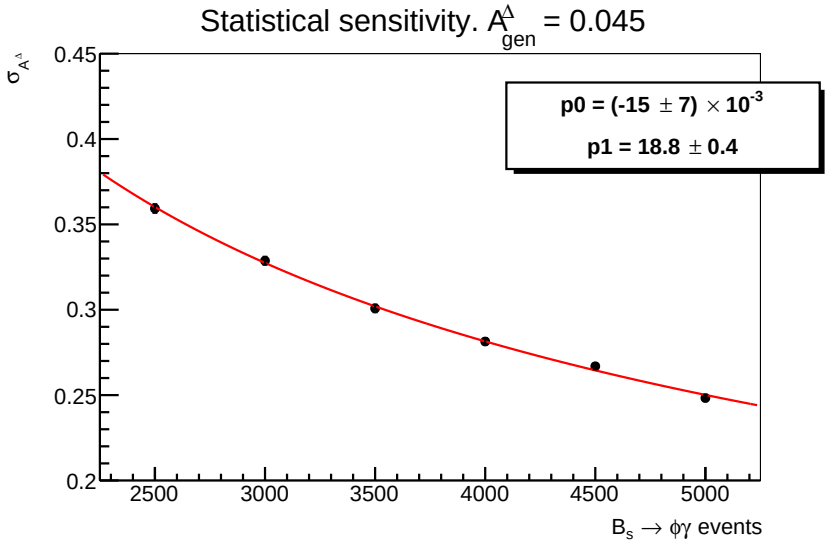

Figure 7.6: Variation of the statistical sensitivity on $\mathcal{A}^{\Delta}$ for different number of $B_s^0 \to \phi\gamma$ signal events, as found from Monte Carlo pseudo-experiments (black points). The fitted curve (red line) follows the form $p_0 + p_1/\sqrt{N}$.

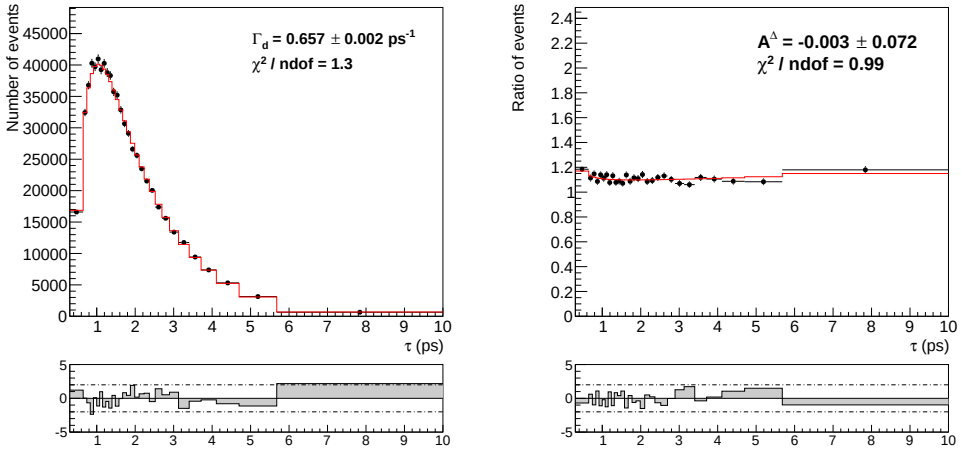

Figure 7.7: Fit projections to recover Γ_d (left) from $B^0 \to K^{*0}(892)\gamma$ and $\mathcal{A}^{\Delta}$ (right) in the ratio framework for the Monte Carlo simulation.

7.2 Systematic uncertainties

The sources of systematic uncertainties on $\mathcal{A}^{\Delta}$ are explained in the following subsections. To avoid experimenter's bias, the result of the analysis

was blinded until all adjustments had been completed [113]. For the sake of simplicity the intermediate blinded steps are omitted in this document, but some references might appear in this section since the evaluations of the uncertainties were performed before unblinding the result. The blinding procedure consisted of adding a random offset to the result before it was printed. While the real value and the offset were unknown to the experimenters, the former can be used internally as input to generate pseudo-experiments for different evaluations without being unblinded to the user.

7.2.1 External parameters

The systematic uncertainties from external inputs entering in the fit (lifetimes of the B_s^0 and B^0 mesons, and the decay width difference of the B_s^0 system) have been obtained using pure signal Monte Carlo pseudo-experiments in which the parameters are varied randomly in the generation, following a Gaussian distribution with σ equal to the experimental uncertainties, and taking into account the correlation $\rho(\Gamma_s, \Delta\Gamma_s)$. The values and errors used for the variation of the external parameters have been extracted from the world averages [25], listed in Table 7.1. The corresponding increase in $\sigma_{\mathcal{A}^\Delta}$ is obtained by subtracting quadratically as

$$\left(\delta\sigma_{\mathcal{A}^\Delta}{}^{\text{Ext.par.}}\right)^2 = \left(\sigma_{\mathcal{A}^\Delta}^{\text{var}}\right)^2 - \left(\sigma_{\mathcal{A}^\Delta}\right)^2,$$

where $\sigma_{\mathcal{A}^\Delta}^{\text{var}}$ and $\sigma_{\mathcal{A}^\Delta}$ are the uncertainties obtained with and without the external parameter variations, respectively. This increase has been considered as the systematic uncertainty, and found to be $^{+0.118}_{-0.127}$. Figure 7.8 (top and middle plots) shows the results of the Monte Carlo pseudo-experiments. The uncertainties are asymmetric because of the dependence of the $\mathcal{A}^\Delta$ sensitivity with its central value. Given this dependence, the Monte Carlo pseudo-experiments are generated with the final $\mathcal{A}^\Delta$ result, blinded to the experimenter externally.

7.2.2 Proper time acceptance

Two effects have been taken into account:

1. **MC statistics.** Analogous to the procedure used to obtain the systematic uncertainties from the external parameters, the fitted parameters from MC of the signal and control channel acceptances have been

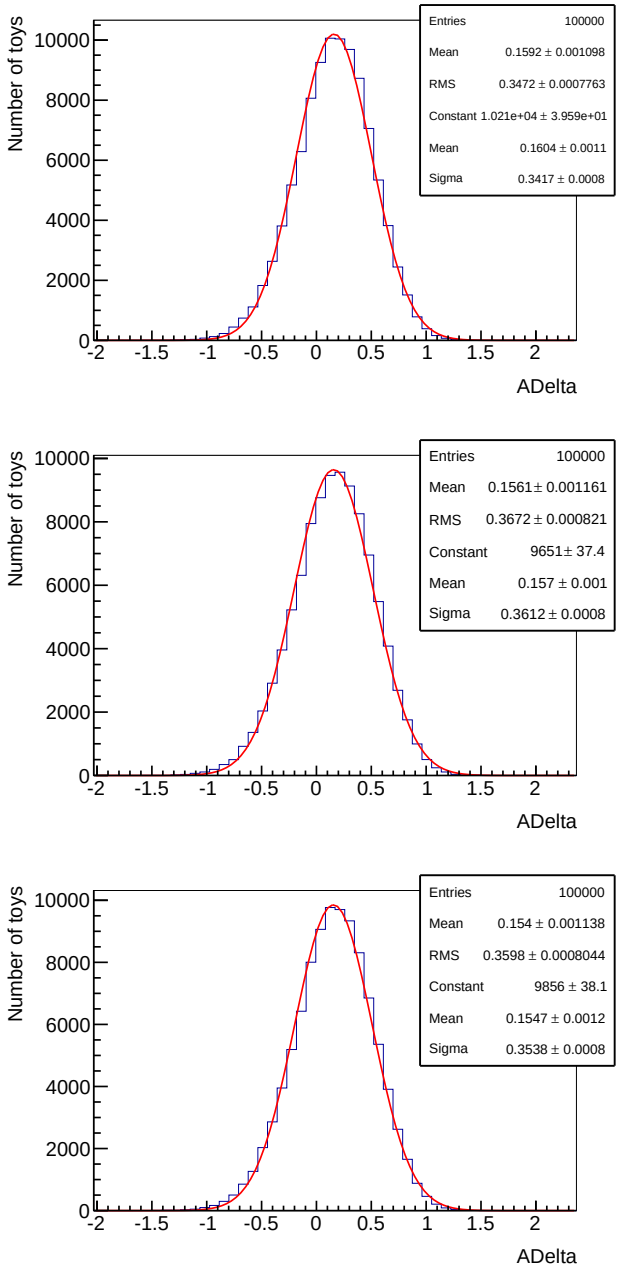

Figure 7.8: MC pseudo-experiments performed to obtain the systematic uncertainties of the external inputs and the acceptance statistics. The reference configuration is shown in the top plot, while the effect on $\mathcal{A}^{\Delta}$ varying the external and acceptance parameters are shown in the middle and bottom plots, respectively. The real $\mathcal{A}^{\Delta}$ data value was used in the pseudo-experiment generation, blinded externally to the experimenter.

varied as Gaussians taking into account the full covariance matrix. The effect induced in $\sigma_{\mathcal{A}^\Delta}$ is taken as systematic uncertainty, evaluated to be $^{+0.095}_{-0.098}$. Figure 7.8 (bottom plot) shows the results of the Monte Carlo pseudo-experiments, using as well internally the unblinded $\mathcal{A}^\Delta$ value from data to generate the pseudo-experiments.

2. **Parametrization.** The integration of the PDF in each bin as per Eq. (7.1) includes a parametrized acceptance in both decays. Since the fit needs to perform the integration of the PDF in each bin, an acceptance function has to be used. An alternative parametrization of the acceptance has been tried, changing the factor $e^{(-\delta\Gamma\, t)}$ of Eq. (6.5) by $1/\cosh(\delta\Gamma\, t)$. The deviation in $\mathcal{A}^\Delta$ is $+0.011$, which has been taken as systematic error.

7.2.3 Resolution

In the reference fit of the ratio, a time dependent correction is applied to take into account the bias of the resolution, as explained in Section 6.3. The difference between omitting the resolution bias and correcting for it amounts to $+0.009$ in $\mathcal{A}^\Delta$. In a conservative approach, a systematic uncertainty of the same amount of the correction has been considered.

Besides, an Apollonios PDF can be used to parametrize the resolution. It is defined as [114],

$$\mathrm{A}(m;\mu,b,\delta,a,n) \propto \begin{cases} e^{-b\sqrt{1+\frac{(m-\mu)^2}{\delta^2}}} & \text{for } \dfrac{m-\mu}{\delta} \geq -a, \\ e^{-b\sqrt{1+a^2}} \left[\dfrac{n\sqrt{1+a^2}}{ba\left(\frac{n\sqrt{1+a^2}}{ba} - a - \frac{m-\mu}{\delta}\right)} \right]^n & \text{for } \dfrac{m-\mu}{\delta} < -a. \end{cases}$$

Several studies have been performed to assess the effect of the resolution function:

1. **Pseudo-experiments generated with resolution.** Using a set of only-signal pseudo-experiments in which a limited resolution parametrized through the Apollonios function has been generated, the observed offset in the central value of the $\mathcal{A}^\Delta$ distribution is -0.014, with respect to pseudo-experiments generated with no resolution, fitting in the two cases without resolution (reference fit). The widths in both cases are compatible. The corresponding pseudo-experiments' results are pictured in Figure 7.9. The source of this

shift is the μ parameter of the resolution function, with σ having no effect.

2. **Constant correction.** The resolution bias depends on the reconstructed decay time, as shown in Figure 6.9. However, using an average constant correction gives the same results in data, changing $\mathcal{A}^{\Delta}$ only by $+0.001$.

3. **Effective acceptance.** Alternatively, one can include the effect of the resolution in the definition of the proper time acceptance. This is done by fitting the acceptance from Monte Carlo using the reconstructed proper time variable with the covariance matrix correction (see Section 6.1), instead of t_{true}. The difference with respect to the reference fit (acceptance function using the true proper time) is $+0.002$.

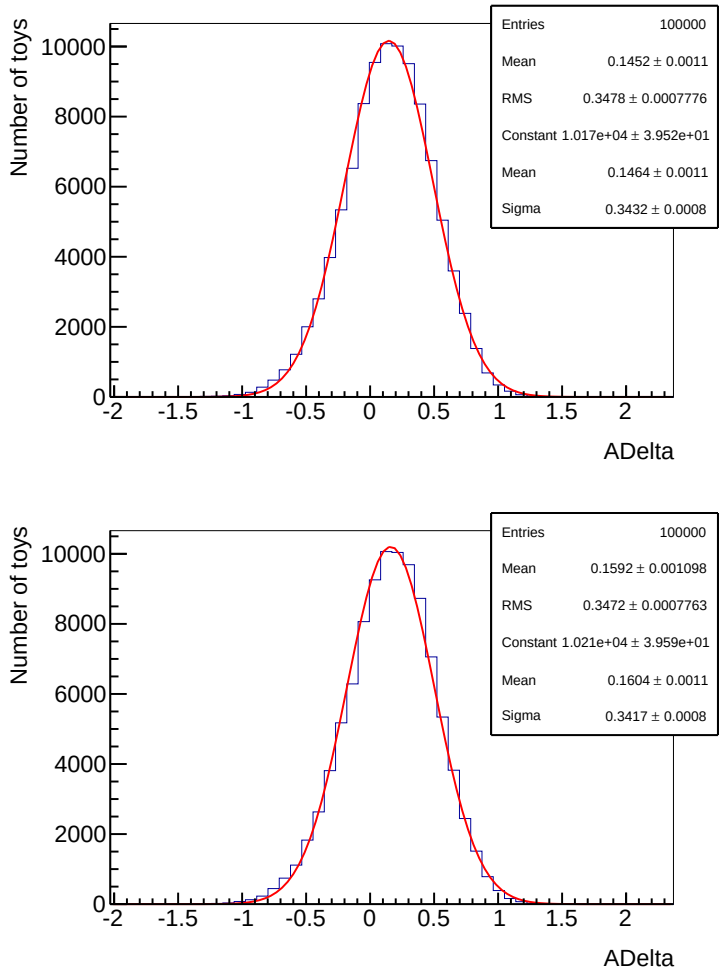

Figure 7.9: From MC pseudo-experiments, effect of generating with the Apollonios resolution (top) compared to no resolution (bottom). Generating with resolution results in a relative displacement of -0.014 in the mean of the $\mathcal{A}^{\Delta}$ distribution, whereas the width remains compatible. The generated $\mathcal{A}^{\Delta}$ value was the real value, unblinded internally.

7.2.4 Signal and background modelling

In order to subtract the different background contributions in data, the *sPlot* technique is used to get the signal *sWeights*, using the B mass as discriminating variable. Peaking backgrounds are included as part of the signal yield.

The contribution of the background modelling to the final result has been checked using different parametrizations in the $B^0 \to K^{*0}(892)\gamma$ mass fit. For the signal shape, a double-sided Crystal-Ball and an asymmetric Apollonios function have been used. For the combinatorial background, a first-order polynomial and an exponential function have been tested.

- Using asymmetric Apollonios (signal): $\Delta\mathcal{A}^{\Delta} = -0.032$.
- Using exponential (combinatorial): $\Delta\mathcal{A}^{\Delta} = +0.050$.
- Using asymmetric Apollonios (signal) and exponential (combinatorial): $\Delta\mathcal{A}^{\Delta} = +0.023$.

The separate effects of alternative modelling of the data and combinatorial background are summed in quadrature for the systematic uncertainty evaluation.

For the partially reconstructed background, alternative shape parametrizations of the most relevant contributions to both channels have been applied on data, with the largest effect being $+0.059$ when changing the partially reconstructed background in $B_s^0 \to \phi\gamma$. Additionally, a set of pseudo-experiments was generated varying the shape parameters of the backgrounds within their uncertainties[2], analogously to the determination of the systematic uncertainty associated to the external parameters' uncertainties. The effect in $\mathcal{A}^{\Delta}$ is below $+0.001$, thus the aforementioned larger value ($+0.059$) is taken as the uncertainty.

The peaking background contribution is estimated from MC pseudo-experiments as pictured in Figure 7.10. Generating without peaking background has an effect of $+0.039 \pm 0.015$ on the mean value. This is also consistent with the effect observed in pseudo-experiments generated increasing the peaking background yield by $3\,\sigma$, where σ is the uncertainty of the yield, and measuring the effect on $\mathcal{A}^{\Delta}$. The effect is divided by 3 to obtain the contribution of the yield uncertainty. The scaling procedure is done to obtain a more pronounced effect in order to isolate the contribution. This is pictured in Figure 7.10 and has a total effect of $+0.033 \pm 0.005$ after scaling back. This value is chosen as the systematic uncertainty.

[2]Due to MC statistics.

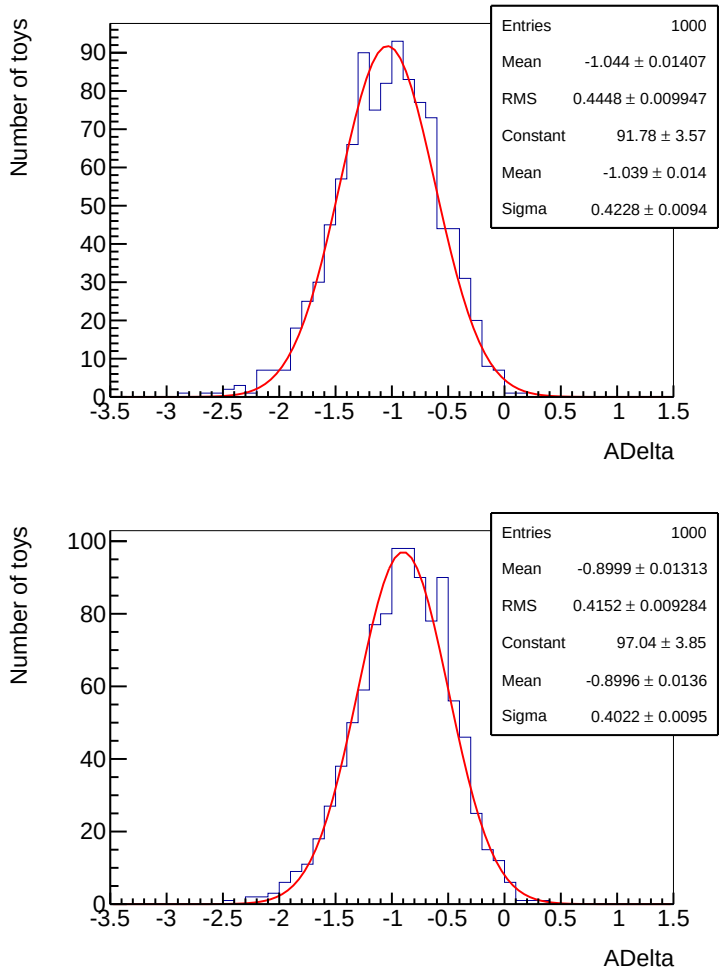

Figure 7.10: Peaking background effect for $\mathcal{A}^{\Delta} = -1$ from Monte Carlo pseudo-experiments, generating with no peaking backgrounds (top) and increasing on $3\,\sigma$ the peaking background contribution (bottom).

7.2.5 Correlation between mass and proper time

Using the reconstructed proper time with mass constraint, no correlation between the mass and proper time variables is observed in data for the signal events, nor the combinatorial background as extracted from the upper-mass sideband. However, the partially reconstructed backgrounds of $B^0 \to K^{*0}(892)\gamma$ extracted from MC indicate potential correlations.

To assess their effects on the $\mathcal{A}^{\Delta}$ measurement, a set

of pseudo-experiments including the correlations of the $B^+ \to K_1(1270)^+(\to K^{*0}(892)\pi^+)\gamma$ and $B^+ \to \phi K^+\gamma$ backgrounds was produced. The impact on $\mathcal{A}^\Delta$ is $+0.116 \pm 0.114$ when generating an initial value of $\mathcal{A}^\Delta_{\text{gen}} = -1$, as pictured in Figure 7.11. The largest value between the effect and its uncertainty is taken as the systematic error.

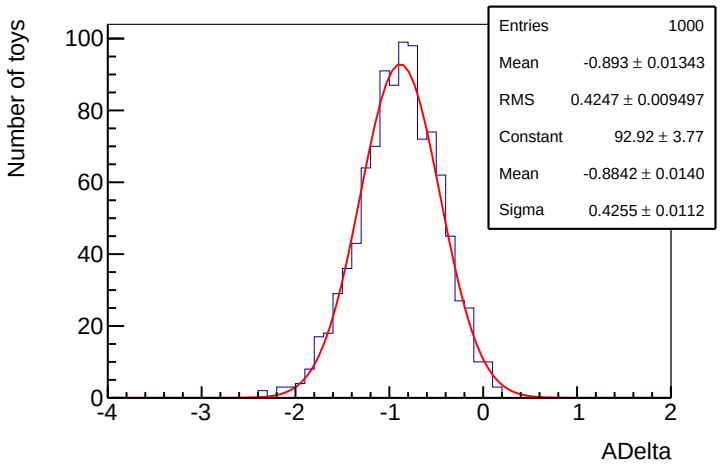

Figure 7.11: Effect of the correlation between the mass and proper time of the partially reconstructed backgrounds on $\mathcal{A}^\Delta$, from pseudo-experiments generated with $\mathcal{A}^\Delta = -1$.

7.2.6 Summary of systematic uncertainties

All the contributions to the systematic uncertainty are listed in Table 7.2. It is dominated by the effect coming from the uncertainties from the external parameters ($^{+0.118}_{-0.127}$), the effect from the mass and proper time correlation in the partially reconstructed backgrounds (0.116) and the limited MC statistics in the acceptance parametrization ($^{+0.095}_{-0.098}$). Studying different parametrizations in the mass fit induces a total systematic error effect of 0.084 and the systematic uncertainty related to the peaking background is 0.033. The contribution to the systematic uncertainty associated to alternative parametrizations of acceptance is 0.011, and the proper-time resolution correction is found to have an effect of 0.009. A quadratic sum of all the contributions gives a total systematic uncertainty of $^{+0.211}_{-0.218}$.

Table 7.2: Systematic uncertainties for $\mathcal{A}^{\Delta}$.

Uncertainty		Variation	$\sigma^{+}_{\mathcal{A}^{\Delta}}$	$\sigma^{-}_{\mathcal{A}^{\Delta}}$
External inputs	Measurement uncertainty	From pseudo-experiments, vary parameters	0.118	0.127
Acceptance	MC statistics	From pseudo-experiments, vary both acceptances	0.095	0.098
	Modelling	Alternative parametrization	0.011	
Resolution	Bias correction	Correction from MC	0.009	
Mass fit modelling	Signal shape	Alternative parametrization	0.032	
	Combinatorial shape	Alternative parametrization	0.050	
	Partially reco. bkg.	Alternative parametrization	0.059	
		Mass-propertime correlation	0.116	
	Peaking	From pseudo-experiments	0.033	
Total			**0.211**	**0.218**

7.3 Results

The projection of the fit to the $B_s^0 \to \phi\gamma$ and $B^0 \to K^{*0}(892)\gamma$ proper time ratio is shown in Fig. 7.12, where the external parameters, listed in Table 7.1, have been fixed to the current world averages [25]. The fitted value of $\mathcal{A}^\Delta$ is $\mathcal{A}^\Delta = -0.847^{+0.407}_{-0.439}$, with the statistical uncertainty, including the signal, control channel and background contributions. The χ^2/ν of the fit is 0.77, indicating a good fit quality. Taking into account the systematic uncertainties, the final result is

$$\mathcal{A}^\Delta = -0.85^{+0.41}_{-0.44}(\text{stat.})^{+0.21}_{-0.22}(\text{syst.}). \tag{7.2}$$

This result is compatible within two standard deviations with the predicted SM value for $\mathcal{A}^\Delta$ of 0.047 ± 0.029 [26]. Even so, the central value lies near the extreme of the physical range.

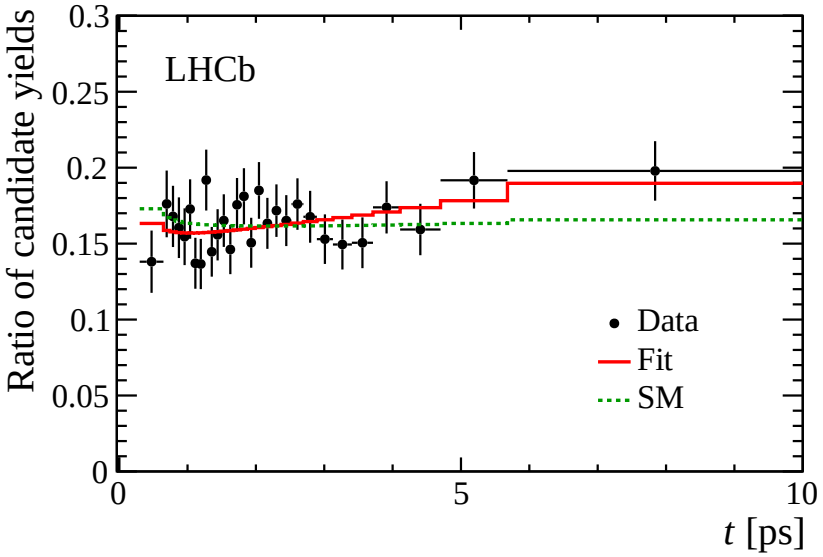

Figure 7.12: Ratio of $B_s^0 \to \phi\gamma$ over $B^0 \to K^{*0}(892)\gamma$ proper time distributions. The data are shown in black points, the fit projection in red solid line and the distribution for the predicted SM value is shown in dashed green line.

7.3.1 Direct fit

A different approach to obtain a measurement of $\mathcal{A}^\Delta$ was developed alongside the analysis presented in this dissertation. This method only differs

from the one deployed in this dissertation in the proper time fitting procedure, which now consists of an unbinned simultaneous maximum likelihood fit of the proper time distributions of $B_s^0 \to \phi\gamma$ and $B^0 \to K^{*0}(892)\gamma$ events. For these two decay modes, the proper-time distributions are obtained identically as described in this dissertation, and the fit is performed simultaneously on both MC and signal data samples. The motivation behind this choice is that the increased statistics of MC can help drive the acceptance parameters in the fit, also profiting from the similarities between the signal and control channels.

The sensitivity of this method is almost identical to that of the ratio strategy, and pseudo-experiments have been generated for several values of $\mathcal{A}^\Delta$ to test the compatibility of the two fitting procedures, with the results shown in Figure 7.13. The difference in the results between both fitters, $\mathcal{A}^\Delta_{\text{Ratio}} - \mathcal{A}^\Delta_{\text{Direct}}$, is compatible with 0 in all cases. The final result in this case is

$$\mathcal{A}^\Delta_{\text{Direct}} = -0.98^{+0.46}_{-0.52}(\text{stat.})^{+0.23}_{-0.20}(\text{syst.}),$$

in agreement with the ratio fit result.

7.3.2 Interpretation of the result

As described in Section 1.4.2, this measurement can provide information about the left- and right-handed electromagnetic penguin Wilson coefficients $\mathcal{C}_{7\gamma}$ and $\mathcal{C}'_{7\gamma}$. Here is presented the new physics contribution $\mathcal{C}^{\text{NP}}_{7\gamma}$ to $\mathcal{C}_{7\gamma}$, as per Eq. (1.105). Updated constraints for these parameters are obtained combining the obtained result with previous knowledge of related observables from other radiative B decays [41], and shown in Figure 7.14. The value for $\mathcal{A}^\Delta$ ($A_{\Delta\Gamma}$ in the legend) is the one obtained in this document, Eq. (7.2). The values for the $S_{K^*\gamma}$ and $\text{BR}(B \to X_s\gamma)$ parameters are the current world averages from [25], the value for $\text{BR}(B_s^0 \to \phi\gamma)$ is derived from [106, 115], and the angular parameters for $B^0 \to K^{*0}(892)\mu^+\mu^-$ and $B^0 \to K^{*0}(892)e^+e^-$ are from [116, 117] and [39], respectively.

The combination is performed using the open source PYTHON package `flavio` [118]. The central value obtained in this analysis corresponds to a non-standard value of $\mathcal{C}'_{7\gamma}$, but it is well in agreement with the SM predictions within the current uncertainty. A comparison with and without $\mathcal{A}^\Delta$

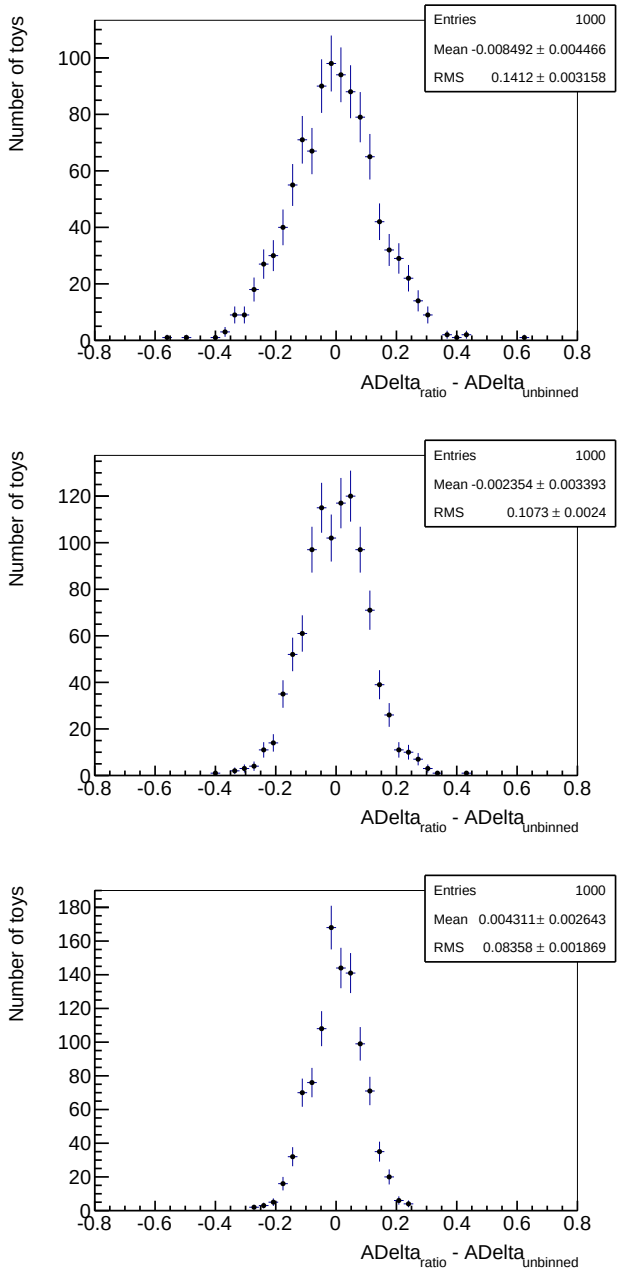

Figure 7.13: One-to-one comparison of the two fitting strategies for $\mathcal{A}^{\Delta} = -1(\text{top}), 0(\text{middle})$, and $1(\text{bottom})$ from pseudo-experiments. The mean values are consistent with zero and the non-zero root mean squares (RMS) are an indication that the methods are not fully correlated, despite the fact that the data samples they use are identical. Results show a difference ganging from 0.09 to 0.14 depending on the value of $\mathcal{A}^{\Delta}$. This is in agreement with the obtained results in data.

in the determination of $\mathrm{Re}(\mathcal{C}_{7\gamma}^{\prime\mathrm{NP}})$ and $\mathrm{Im}(\mathcal{C}_{7\gamma}^{\prime})$ has been done, resulting in

$$\begin{pmatrix} \mathrm{Re}(\mathcal{C}_{7\gamma}^{\prime\mathrm{NP}}) \\ \mathrm{Im}(\mathcal{C}_{7\gamma}^{\prime}) \end{pmatrix} = \begin{pmatrix} 0.019 \pm 0.043 \\ 0.005 \pm 0.034 \end{pmatrix} \qquad \text{without } \mathcal{A}^{\Delta},$$

$$\begin{pmatrix} \mathrm{Re}(\mathcal{C}_{7\gamma}^{\prime\mathrm{NP}}) \\ \mathrm{Im}(\mathcal{C}_{7\gamma}^{\prime}) \end{pmatrix} = \begin{pmatrix} 0.052 \pm 0.039 \\ 0.006 \pm 0.042 \end{pmatrix} \qquad \text{with } \mathcal{A}^{\Delta},$$

where the values are compatible in both cases. The contribution of $\mathcal{A}^{\Delta}$ is most notable in $\mathrm{Re}(\mathcal{C}_{7\gamma}^{\prime\mathrm{NP}})$, as expected from Eq. (1.99).

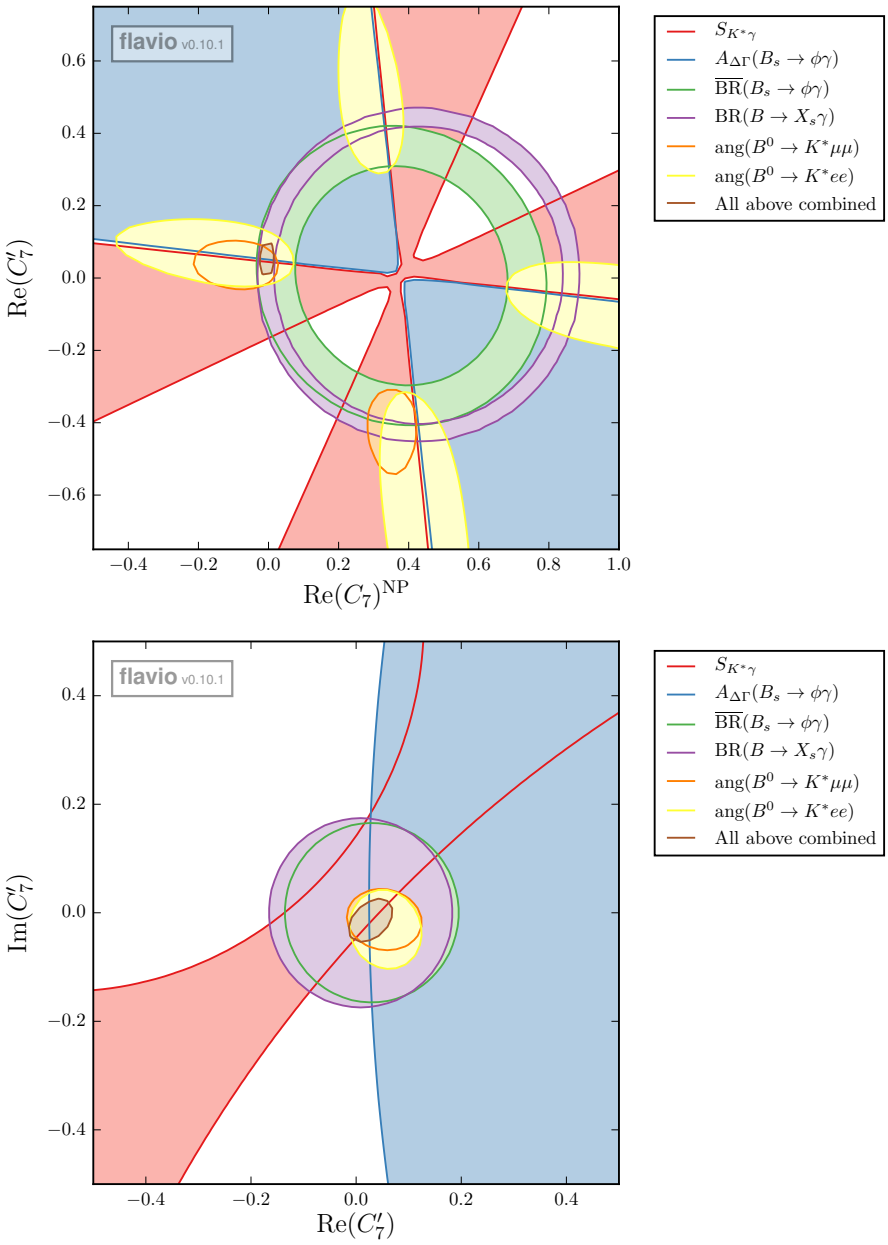

Figure 7.14: Constraints on the electromagnetic penguin Wilson coefficients. The top plot shows the real parts of $\mathcal{C}_{7\gamma}^{\text{NP}}$ and $\mathcal{C}_{7\gamma}^{'}$, while the bottom one shows the real and imaginary parts of $\mathcal{C}_{7\gamma}^{'}$. Contour plots are shown at 1σ for the global and individual constraints.

Conclusions

Precision measurements in particle physics offer a window to study the detailed inner workings of matter. Radiative B decays are an excellent testing bed for certain processes, being examples of flavour-changing neutral currents through penguin loops. The definite and extremal prediction of the SM for the polarization of the photon make $b \to s\gamma$ transitions especially interesting cases to search for models that challenge it, such as the Left-Right Symmetric Model (LRSM) or the unconstrained Minimal SuperSymmetric Model (uMSSM). The structure of neutral meson mixing allows to access the polarization through the study of the untagged lifetime of the $B_s^0 \to \phi\gamma$ decay, characterized by the photon polarization sensitive $\mathcal{A}^\Delta$ parameter.

In the present work this parameter is obtained by studying the ratio of decay time distributions of $B_s^0 \to \phi\gamma$ over $B^0 \to K^{*0}(892)\gamma$. The aim is to reduce systematic contributions by using the kinematically similar $B^0 \to K^{*0}(892)\gamma$ decay, profiting from the null sensitivity to $\mathcal{A}^\Delta$ in the proper time distribution of this channel. The relative sample size of $B^0 \to K^{*0}(892)\gamma$ with respect to $B_s^0 \to \phi\gamma$, around six times larger, is key to reduce the uncertainties in the acceptance parametrizations, which are common. This requires a strict control of the selection to ensure the time dependent acceptances of both channels are as similar as possible. Extensive work has been done to identify the sources of discrepancies in the variables used for the selection. As some of these were applied during the stripping of Run I data, variants of the lines were redesigned and introduced explicitly to reprocess the data for this measurement.

After selection, mass fits are applied to both channels and the background subtracted from their respective proper time distributions using the *sPlot* formalism. The two signal distributions are divided to each other and the proper time fit is performed, obtaining a value of $\mathcal{A}^\Delta$ of

$$\mathcal{A}^\Delta = -0.85^{+0.41}_{-0.44}(\text{stat.})^{+0.21}_{-0.22}(\text{syst.}),$$

This measurement is in agreement with the SM prediction,

$\mathcal{A}^{\Delta}_{\mathrm{SM}} = 0.047 \pm 0.029$ [26], within two standard deviations, and provides additional information for constraining the $\mathcal{C}_{7\gamma}$ and $\mathcal{C}'_{7\gamma}$ Wilson coefficients. In the context of radiative B^0_s decays, this is the first time-dependent measurement and also the first study of photon polarization.

Additional statistics taken during the Run II data taking period and further on will reduce the uncertainty and allow better discrimination between SM and BSM predictions.

A | The `PropertimeFitter` algorithm

For a given particle k, its proper time is obtained in LHCb by an iterative minimization process through the `PropertimeFitter` algorithm. This tool produces a fitted propertime value

$$c\tau = d\frac{m_B}{p_B}, \tag{A.1}$$

where d is the distance of flight of the B meson from its production point to its decay vertex (essentially $\vec{d} \equiv \vec{\mathrm{SV}} - \vec{\mathrm{PV}}$ where the first term is the vector location of the secondary vertex and the second corresponds to the vector location of the primary vertex, both positions being reconstructed in LHCb from the tracks as described in Chapter 2. The inputs to the algorithm are the information of the three-dimensional vector location of the primary vertex, $\vec{\mathrm{PV}}$ and the corresponding 3×3 covariance matrix , as well as the analogous location of the decay vertex of the particle, $\vec{\mathrm{SV}}$, and its four-momentum, q_k, along with the covariance matrices between the particle parameters. These are specifically the 4×4 covariance matrix of the four-momentum components, $cov(q_k)$, the 3×3 covariance matrix of the spatial components of the decay vertex, $cov(\vec{\mathrm{SV}})$ and the 3×4 correlation matrix between the momentum and decay vertex spatial components, $cor(\vec{\mathrm{SV}}, q_k)$. All of these matrices are defined symmetrical.

The details of the algorithm are based on vertex and decay tree (Kalman) fitting techniques, see for example [119, 120]. One can build the seven-dimensional particle vertex s containing all its parameters by simple con-

catenation and the corresponding 7×7 covariance matrix $\mathbf{C}_k$ as

$$\mathbf{s} = \begin{bmatrix} \vec{\mathrm{SV}} & q_k \end{bmatrix}^\top = \begin{bmatrix} x^{\mathrm{SV}} & y^{\mathrm{SV}} & z^{\mathrm{SV}} & p_x & p_y & p_z & E \end{bmatrix}^\top,$$
$$\mathbf{C}_k = \begin{bmatrix} cov(\vec{\mathrm{SV}}) & cor(\vec{\mathrm{SV}}, q_k) \\ cor(\vec{\mathrm{SV}}, q_k)^\top & cov(q_k) \end{bmatrix}.$$

A $\mathbf{C'}_k$ matrix is obtained through the transformation $\mathbf{C'}_k = \mathbf{T}\mathbf{C}_k\mathbf{T}^\top$ with $\mathbf{T}$ a velocity transform matrix, built as

$$\mathbf{T} = \begin{bmatrix} \mathbf{I}_3 & & \mathbf{0}_{3\times 4} & & \\ & 1 & 0 & 0 & 0 \\ & 0 & 1 & 0 & 0 \\ \mathbf{0}_{4\times 3} & 0 & 0 & 1 & 0 \\ & -\frac{p_x}{m} & -\frac{p_y}{m} & -\frac{p_z}{m} & \frac{E}{m} \end{bmatrix},$$

where m is the calculated mass of the particle through the norm of its four-momentum, $m = \sqrt{E^2 - p^2}$. Adding the primary vertex information the complete $dim = 10$ vertex containing all the fit variables, v_0, and the corresponding 10×10 covariance matrix, $\mathbf{C}_0$, can be built. It is assumed that the particle parameters are independent of the estimation of the primary vertex, so the cross covariance matrix between them is a 3×7 null matrix, $\mathbf{0}_{3\times 7}$, therefore,

$$\mathbf{v} = \begin{bmatrix} \vec{\mathrm{PV}} & \vec{\mathrm{SV}} & q_k \end{bmatrix}^\top = \begin{bmatrix} x^{\mathrm{PV}} & y^{\mathrm{PV}} & z^{\mathrm{PV}} & x^{\mathrm{SV}} & y^{\mathrm{SV}} & z^{\mathrm{SV}} & p_x & p_y & p_z & E \end{bmatrix}^\top,$$
$$\mathbf{C} = \begin{bmatrix} cov(\vec{\mathrm{PV}}) & \mathbf{0}_{3\times 7} \\ \mathbf{0}_{7\times 3} & \mathbf{C'}_k \end{bmatrix}.$$

The fit consists of an iterative transformation of these objects until convergence is reached. Convergence is considered when the difference between the calculated χ^2 of the current iteration and the previous is less than a given threshold, by default 0.001. As a safeguard against diverging fits, a maximum number of iterations is imposed, by default 10. $\mathbf{v}_0$ and $\mathbf{C}_0$ represent the initial state of the system, with their values loaded directly from the vertex fit result, while $\mathbf{v}_n$ and $\mathbf{C}_n$ are the transformed values for the n-th iteration. Defining a function vector, $\mathbf{f}_n$ from the components of the previous iteration of the component vector $\mathbf{v}_{n-1}$,

$$\mathbf{f}_n = \begin{bmatrix} (x^{\mathrm{SV}} - x^{\mathrm{PV}})p_z - (z^{\mathrm{SV}} - z^{\mathrm{PV}})p_x \\ (y^{\mathrm{SV}} - y^{\mathrm{PV}})p_z - (z^{\mathrm{SV}} - z^{\mathrm{PV}})p_y \end{bmatrix}_{n-1},$$

and the derivative matrix, $\mathbf{D}_n$, from the same components

$$\mathbf{D}_n = \begin{bmatrix} -p_{z,} & 0 & p_{x,} & p_z & 0 & -p_x & -(z^{\mathrm{SV}} - z^{\mathrm{PV}}) & 0 & (x^{\mathrm{SV}} - x^{\mathrm{PV}}) & 0 \\ 0 & -p_z & p_y & 0 & p_z & -p_y & 0 & -(z^{\mathrm{SV}} - z^{\mathrm{PV}}) & (y^{\mathrm{SV}} - y^{\mathrm{PV}}) & 0 \end{bmatrix}_{n-1}.$$

In both cases the $n-1$ subscript is implied for the internal components of the matrix.

The following objects can be derived:

$$\begin{aligned} \mathbf{d}_n &= \mathbf{f}_{n-1} - \mathbf{D}_n \mathbf{v}_{n-1}, \\ \mathbf{V}_n &= \mathbf{D}_n \mathbf{C}_{n-1} \mathbf{D}_n^\top, \\ \alpha_n &= \mathbf{D}_n \mathbf{v}_0 + \mathbf{d}_n, \\ \lambda_n &= \mathbf{V}_n \alpha_n. \end{aligned}$$

And finally the component vector and its covariance matrix are updated,

$$\begin{aligned} \mathbf{v}_n &= \mathbf{v}_0 - \mathbf{C}_0 \mathbf{D}_{n-1}^\top \lambda_n, \\ \mathbf{H}_n &= \mathbf{D}_{n-1}^\top \mathbf{V}_n \mathbf{D}_{n-1}, \\ \mathbf{C}_n &= \mathbf{C}_0 - \mathbf{C}_0 \mathbf{H}_n \mathbf{C}_0^\top, \end{aligned}$$

and the χ^2 of the iteration is evaluated,

$$\chi_n^2 = \alpha_n \cdot \lambda_n.$$

If $\chi_n^2 - \chi_{n-1}^2 < 0.001$ and $n \leq 10$ the algorithm ends and the proper time is calculated from the latest update to the components, $\mathbf{v}_n$, as

$$c\tau = \frac{(x_n^{\mathrm{SV}} - x_n^{\mathrm{SV}}) m_n}{p_{x,n}}, \tag{A.2}$$

and the proper time covariance matrix, $\mathbf{C}^\tau$, is calculated as

$$\mathbf{C}^\tau = \mathbf{J} \mathbf{C}_n \mathbf{J}^\top, \tag{A.3}$$

where $\mathbf{J}$ is defined as

$$\mathbf{J} = \left[-\frac{m_n}{p_{x,n}} \quad 0 \quad 0 \quad \frac{m_n}{p_{x,n}} \quad 0 \quad 0 \quad -\frac{(x_n^{\mathrm{SV}} - x_n^{\mathrm{PV}}) m_n}{p_{x,n}^2} \quad 0 \quad 0 \quad \frac{x_n^{\mathrm{SV}} - x_n^{\mathrm{PV}}}{p_{x,n}} \right],$$

and the associated uncertainty of the propertime is simply

$$c\sigma_\tau = \sqrt{\mathbf{C}_{1,1}^\tau}. \tag{A.4}$$

After dividing by c, the values τ, σ_τ and the final χ^2 of the fit are returned to the user.

If the user chooses to impose a mass constrain for the proper time fit, the nominal mass for the B meson will be used instead of the default value calculated from the momentum components. In the algorithm this is imposed as an additional transformation after the convergence of the least squares method. After the identification of the B meson its nominal mass is loaded from the database as m_{B} and the following transformations are made:

$$\begin{aligned}
\mathbf{W} &= \begin{bmatrix} 0 & 0 & 0 & 0 & 0 & 0 & 0 & 0 & 0 & 1 \end{bmatrix}, \\
\mathbf{C}_d &= \mathbf{W}\mathbf{C}_n\mathbf{W}^\top, \\
\mathbf{v}'_n &= \mathbf{v}_n - \mathbf{C}_n\mathbf{W}^\top\mathbf{C}_d(\mathbf{W}\mathbf{v}_n - m_{\mathrm{B}}), \\
\mathbf{C}'_n &= \mathbf{C}_n - \mathbf{C}_n(\mathbf{W}^\top\mathbf{C}_d\mathbf{W})\mathbf{C}_n^\top.
\end{aligned}$$

And the mass column is eliminated from the updated covariance matrix,

$$\mathbf{C}'_{9,j(n)} = 0 \,\forall\, j \in [0,9].$$

With these new values, the calculations of the proper time and its covariance and errors follow Eqs. (A.2), (A.3) and (A.4), respectively. As in the non constrained case, the value returned to the user is divided by c.

Glossary

BDT Boosted Decision Tree.

Boosted Decision Tree A machine learning algorithm that, after being explicitly trained on the characteristics of a number of categories, uses several arbitrarily chosen physical variables to classify the likelihood of events to belong in said categories. In LHCb they are generally used to distinguish signal events from background, after being trained with Monte Carlo (MC) samples.

DIRA Acronym for DIRection Angle, the angle subtended between the direction of the reconstructed momentum of a long lived particle and the direction pointing from its associated primary vertex to its seconday vertex.

DLLx Particle Identification (PID) value obtained from linearly adding log-likelihood probabilities obtained from the tracking and PID systems. Represents how likely the mass hypothesis for x is relative to the π hypothesis. See ProbNNx for an improved algorithm..

Downstream Tracks with hits only from the TT and onwards. See Long.

ECAL Electromagnetic Calorimeter.

Electromagnetic Calorimeter Detector that collects the energy of electromagnetic particles such as e^-, γ or π^0.

FD Flight Distance.

Flight Distance The absolute distance between the Secondary Vertex and the Primary Vertex.

gammaCL γ Confidence Level.

γ Confidence Level PID value differentiating a photon from other particles.

GhostProb Ghost Probability.

Ghost Probability Probability that the hits used to fit a track come from diverse random sources and not the passage of a single physical charged particle through a detector.

Hadronic Calorimeter Detector that collects the energy of hadronic particles such as K^+ or π^-.

HCAL Hadronic Calorimeter.

High Level Trigger Divided in HLT1 and HLT2, stages of the trigger run respectively over subsequent partial event reconstruction steps of the online data processing system.

HLT High Level Trigger.

Impact Parameter The distance between the particle and a given point, generally a vertex.

Inner Tracker Silicon microstrip track detectors conforming the inner regions of the Tracking Stations . Described in detail in Section 2.3.3. See also Outer Tracker (OT).

IP Impact Parameter.

IT Inner Tracker.

L0 Level 0 Trigger.

Long Tracks with hits in all of the tracking subsystems. See Downstream.

MC Monte Carlo.

Monte Carlo Random sampling method used in computer simulation. In the context of LHCb it generally refers to the simulation of physical processes within the detector, along with the reconstruction and processing, resulting in realistic models of the decays.

OT Outer Tracker.

Outer Tracker Drift-straw track detector conforming the outer regions of the Tracking Stations. Described in detail in Section 2.3.4. See also Inner Tracker (IT).

Particle Identification Classification of any given track into a particular mass hypothesis (K,p,π,...) based on the information from the different detector subsystems. See ProbNNx and DLLx for variables that evaluate this concept.

PDF Probability Density Function.

PID Particle Identification.

pitch The distance between two sensitive areas in a detector module.

Preshower detector Scintillation detector placed before the Electromagnetic Calorimeter (ECAL) after a lead conversion plate. Its purpose is the discrimination of electrons from charged pions.

Primary Vertex The vertex associated with the production of particles in an event, found by fitting reconstructed tracks that best point to the interaction point of the detector.

ProbNNx PID value obtained from a neural network multivariate algorithm that uses information from the tracking and PID systems along with their correlations. Represents the probability of a particle being x. Improvement over DLLx.

PS Preshower Detector.

PV Primary Vertex.

RICH Ring Imaging Cherenkov detector.

Ring Imaging Cherenkov Detector that identifies the velocities of particles from the angle of Cherenkov radiation. Together with the momentum, the mass can be calculated and therefore the PID of the particle determined.

Scintillator Pad Detector Scintillation detector placed in the foremost end of the calorimeter system. Its purpose is the discrimination of electrons from photons and between converted and non converted photons.

Secondary Vertex The vertex associated with the decay of long-lived particles, found by fitting the reconstructed tracks that within the desired particle's selection criteria form a good vertex.

SM Standard Model.

SPD Scintillator Pad Detector.

Standard Model The theory that describes the elementary particles and its interactions.

SV Secondary Vertex.

TIS Trigger Independent of Signal.

TOB Trigger On Both.

TOS Trigger On Signal.

Tracker Turicensis Silicon microstrip track detector located just upstream of the LHCb magnet, covering the full acceptance. Described in detail in Section 2.3.3.

Trigger Independent of Signal Events which generate a positive trigger decision even when removing the signal candidate components from the event. Complementary category to Trigger On Signal (TOS) and Trigger On Both (TOB).

Trigger On Both Events for which neither the presence of the signal alone nor the rest of the event alone are sufficient to generate a positive trigger decision, but rather both are necessary. Complementary category to TOS and Trigger Independent of Signal (TIS).

Trigger On Signal Events for which the presence of the signal is sufficient to generate a positive trigger decision. Complementary category to TIS and TOB.

TT Tracker Turicensis.

VELO VErtex LOcator.

Vertex Locator Silicon microstrip track detector located nearest to the interaction point in LHCb. Described in detail in Section 2.3.2.

Bibliography

[1] LHCb, R. Aaij *et al.*, *First experimental study of photon polarization in radiative B_s^0 decays*, arXiv:1609.02032.

[2] A. Pich, *The Standard model of electroweak interactions*, in *High-energy physics. Proceedings, European School, Aronsborg, Sweden, June 18-July 1, 2006*, 2007. arXiv:0705.4264.

[3] E. D. Commins and P. H. Bucksbaum, *Weak interactions of leptons and quarks*, Cambridge University Press, Cambridge, 1983.

[4] Particle Data Group, K. A. Olive *et al.*, *Review of Particle Physics*, Chin. Phys. **C38** (2014) 090001.

[5] S. Hannestad, A. Mirizzi, G. G. Raffelt, and Y. Y. Y. Wong, *Neutrino and axion hot dark matter bounds after WMAP-7*, JCAP **1008** (2010) 001, arXiv:1004.0695.

[6] LHCb, R. Aaij *et al.*, *Observation of $J/\psi\phi$ structures consistent with exotic states from amplitude analysis of $B^+ \to J/\psi\phi K^+$ decays*, arXiv:1606.07895.

[7] LHCb, R. Aaij *et al.*, *Amplitude analysis of $B^+ \to J/\psi\phi K^+$ decays*, arXiv:1606.07898.

[8] P. W. Higgs, *Broken symmetries and the masses of gauge bosons*, Phys. Rev. Lett. **13** (1964) 508.

[9] F. Englert and R. Brout, *Broken symmetry and the mass of gauge vector mesons*, Phys. Rev. Lett. **13** (1964) 321.

[10] G. S. Guralnik, C. R. Hagen, and T. W. B. Kibble, *Global conservation laws and massless particles*, Phys. Rev. Lett. **13** (1964) 585.

[11] M. Kobayashi and T. Maskawa, *CP Violation in the Renormalizable Theory of Weak Interaction*, Prog. Theor. Phys. **49** (1973) 652.

[12] L.-L. Chau and W.-Y. Keung, *Comments on the parametrization of the kobayashi-maskawa matrix*, Phys. Rev. Lett. **53** (1984) 1802.

[13] L. Wolfenstein, *Parametrization of the kobayashi-maskawa matrix*, Phys. Rev. Lett. **51** (1983) 1945.

[14] J. Charles *et al.*, *Current status of the Standard Model CKM fit and constraints on $\Delta F = 2$ New Physics*, Phys. Rev. **D91** (2015), no. 7 073007, arXiv:1501.05013.

[15] E. Noether, *Invariant Variation Problems*, Gott. Nachr. **1918** (1918) 235, arXiv:physics/0503066, [Transp. Theory Statist. Phys.1,186(1971)].

[16] J. S. Schwinger, *The Theory of quantized fields. 1.*, Phys. Rev. **82** (1951) 914.

[17] G. Luders, *On the Equivalence of Invariance under Time Reversal and under Particle-Antiparticle Conjugation for Relativistic Field Theories*, Kong. Dan. Vid. Sel. Mat. Fys. Med. **28N5** (1954) 1.

[18] T. D. Lee and C.-N. Yang, *Question of Parity Conservation in Weak Interactions*, Phys. Rev. **104** (1956) 254.

[19] C. S. Wu *et al.*, *Experimental Test of Parity Conservation in Beta Decay*, Phys. Rev. **105** (1957) 1413.

[20] R. L. Garwin, L. M. Lederman, and M. Weinrich, *Observations of the Failure of Conservation of Parity and Charge Conjugation in Meson Decays: The Magnetic Moment of the Free Muon*, Phys. Rev. **105** (1957) 1415.

[21] L. D. Landau, *On the conservation laws for weak interactions*, Nucl. Phys. **3** (1957) 127.

[22] J. H. Christenson, J. W. Cronin, V. L. Fitch, and R. Turlay, *Evidence for the 2 pi Decay of the k(2)0 Meson*, Phys. Rev. Lett. **13** (1964) 138.

[23] BaBar, J. P. Lees *et al.*, *Observation of Time Reversal Violation in the B^0 Meson System*, Phys. Rev. Lett. **109** (2012) 211801, arXiv:1207.5832.

[24] A. Bettini, *Introduction to elementary particle physics*, 2008.

[25] Heavy Flavor Averaging Group (HFAG), Y. Amhis *et al.*, *Averages of b-hadron, c-hadron, and τ-lepton properties as of summer 2014*, arXiv:1412.7515, Update with results up to Spring 2016 at http://www.slac.stanford.edu/xorg/hfag/rare/index.html Accessed: 2016-08-30.

[26] F. Muheim, Y. Xie, and R. Zwicky, *Exploiting the width difference in $B_s \to \phi\gamma$*, Phys. Lett. **B664** (2008) 174, arXiv:0802.0876.

[27] D. Atwood, M. Gronau, and A. Soni, *Mixing induced CP asymmetries in radiative B decays in and beyond the standard model*, Phys. Rev. Lett. **79** (1997) 185, arXiv:hep-ph/9704272.

[28] BaBar, B. Aubert *et al.*, *Limits on the decay rate difference of neutral $-B$ mesons and on CP, T, and CPT violation in $B^0\overline{B}^0$ oscillations*, Phys. Rev. **D70** (2004) 012007, arXiv:hep-ex/0403002.

[29] LHCb, R. Aaij *et al.*, *Opposite-side flavour tagging of B mesons at the LHCb experiment*, Eur. Phys. J. **C72** (2012) 2022, arXiv:1202.4979.

[30] LHCb, R. Aaij *et al.*, *B flavour tagging using charm decays at the LHCb experiment*, JINST **10** (2015), no. 10 P10005, arXiv:1507.07892.

[31] LHCb, R. Aaij *et al.*, *A new algorithm for identifying the flavour of B_s^0 mesons at LHCb*, JINST **11** (2016), no. 05 P05010, arXiv:1602.07252.

[32] R. Fleischer, *CP violation and the role of electroweak penguins in nonleptonic B decays*, Int. J. Mod. Phys. **A12** (1997) 2459, arXiv:hep-ph/9612446.

[33] K. G. Wilson, *Nonlagrangian models of current algebra*, Phys. Rev. **179** (1969) 1499.

[34] G. Buchalla, A. J. Buras, and M. E. Lautenbacher, *Weak decays beyond leading logarithms*, Rev. Mod. Phys. **68** (1996) 1125, arXiv:hep-ph/9512380.

[35] B. Grinstein, Y. Grossman, Z. Ligeti, and D. Pirjol, *The Photon polarization in $B \to X\gamma$ in the standard model*, Phys. Rev. **D71** (2005) 011504, arXiv:hep-ph/0412019.

[36] LHCb, R. Aaij *et al.*, *Observation of Photon Polarization in the $b \to s\gamma$ Transition*, Phys. Rev. Lett. **112** (2014) 161801, arXiv:1402.6852.

[37] M. Gronau, Y. Grossman, D. Pirjol, and A. Ryd, *Measuring the photon polarization in B —> K pi pi gamma*, Phys. Rev. Lett. **88** (2002) 051802, arXiv:hep-ph/0107254.

[38] M. Gronau and D. Pirjol, *Photon polarization in radiative B decays*, Phys. Rev. **D66** (2002) 054008, arXiv:hep-ph/0205065.

[39] LHCb, R. Aaij *et al.*, *Angular analysis of the $B^0 \to K^{*0}e^+e$ decay in the low-q^2 region*, JHEP **04** (2015) 064, arXiv:1501.03038.

[40] L. L. Everett *et al.*, *Alternative approach to b —> s gamma in the uMSSM*, JHEP **01** (2002) 022, arXiv:hep-ph/0112126.

[41] A. Paul and D. M. Straub, *Constraints on new physics from radiative B decays*, arXiv:1608.02556.

[42] E. Kou, C.-D. Lü, and F.-S. Yu, *Photon Polarization in the $b \to s\gamma$ processes in the Left-Right Symmetric Model*, JHEP **12** (2013) 102, arXiv:1305.3173.

[43] H. Dijkstra, H. J. Hilke, T. Nakada, and T. Ypsilantis, *LHCb Letter of Intent, LHCb Collaboration*, .

[44] A. D. Sakharov, *Violation of CP Invariance, c Asymmetry, and Baryon Asymmetry of the Universe*, Pisma Zh. Eksp. Teor. Fiz. **5** (1967) 32, [Usp. Fiz. Nauk161,61(1991)].

[45] CMS, S. Chatrchyan *et al.*, *Observation of a new boson at a mass of 125 GeV with the CMS experiment at the LHC*, Phys. Lett. **B716** (2012) 30, arXiv:1207.7235.

[46] ATLAS, G. Aad *et al.*, *Observation of a new particle in the search for the Standard Model Higgs boson with the ATLAS detector at the LHC*, Phys. Lett. **B716** (2012) 1, arXiv:1207.7214.

[47] LHCb, R. Aaij *et al.*, *First Evidence for the Decay $B_s^0 \to \mu^+\mu^-$*, Phys. Rev. Lett. **110** (2013), no. 2 021801, arXiv:1211.2674.

[48] Y. K. Hsiao, P. Y. Lin, L. W. Luo, and C. Q. Geng, *Fragmentation fractions of two-body b-baryon decays*, Phys. Lett. **B751** (2015) 127, arXiv:1510.01808.

[49] LHCb, A. A. Alves, Jr. *et al.*, *The LHCb Detector at the LHC*, JINST **3** (2008) S08005.

[50] *LHCb: Technical Proposal*, Tech. Proposal, CERN, Geneva, 1998.

[51] LHCb, R. Aaij *et al.*, *LHCb Detector Performance*, Int. J. Mod. Phys. **A30** (2015), no. 07 1530022, arXiv:1412.6352.

[52] LHCb, *LHCb magnet: Technical design report*, CERN-LHCC-2000-007.

[53] J. André *et al.*, *Status of the LHCb magnet system*, IEEE Trans. Appl. Supercond. **12** (2002) 366.

[54] J. André *et al.*, *Status of the LHCb dipole magnet*, IEEE Trans. Appl. Supercond. **14** (2004), no. 2 509.

[55] A. Hicheur and G. Conti, *Parameterization of the LHCb magnetic field map*, in *Proceedings, 2007 IEEE Nuclear Science Symposium and Medical Imaging Conference (NSS/MIC 2007): Honolulu, Hawaii, October 28-November 3, 2007*, pp. 2439–2443, 2007. doi: 10.1109/NSSMIC.2007.4436650.

[56] LHCb, *LHCb VELO TDR: Vertex locator. Technical design report*, CERN-LHCC-2001-011.

[57] M. G. Van Beuzekom, W. Vink, L. W. Wiggers, and M. Zupan, *Pile-up veto L0 trigger system for LHCb using large FPGA's*, 2002. http://cds.cern.ch/record/599532.

[58] J. Gassner, M. Needham, and O. Steinkamp, *Layout and Expected Performance of the LHCb TT Station*, 2004. LHCb-2003-140, CERN-LHCb-2003-140.

[59] LHCb, *LHCb: Inner tracker technical design report*, CERN-LHCC-2002-029.

[60] *LHCb: Outer tracker technical design report*, CERN-LHCC-2001-024.

[61] G. Veale *et al.*, *Drift-tube detectors for current and future high energy facilities*, JINST **115** (1987) 978.

[62] LHCb, R. Aaij *et al.*, *Measurement of the track reconstruction efficiency at LHCb*, JINST **10** (2015), no. 02 P02007, arXiv:1408.1251.

[63] LHCb, *LHCb: RICH technical design report*, CERN-LHCC-2000-037.

[64] LHCb, *LHCb calorimeters: Technical design report*, CERN-LHCC-2000-036.

[65] S. Barsuk, *The Shashlik electro-magnetic calorimeter for the LHCb experiment*, in *Calorimetry in particle physics. Proceedings, 11th International Conference, CALOR 2004, Perugia, Italy, March 29-April 2, 2004*, pp. 61–67, 2004.

[66] G. Avoni *et al.*, *The electromagnetic calorimeter of the HERA-B experiment*, Nucl. Instrum. Meth. **A580** (2007) 1209.

[67] G. David *et al.*, *Performance of the PHENIX EM calorimeter*, IEEE Trans. Nucl. Sci. **43** (1996) 1491.

[68] M. Angelone *et al.*, *Properties of para-Terphenyl as Detector for α, β and γ radiation*, IEEE Trans. Nucl. Sci. **61** (2014), no. 3 1483, arXiv:1305.0442.

[69] G. I. Britvich *et al.*, *Search for new scintillators for high-energy resolution electromagnetic calorimeters*, Nucl. Instrum. Meth. **A426** (1999) 453.

[70] A. F. Adadurov, P. N. Zhmurin, V. N. Lebedev, and V. D. Titskaya, *Optimizing concentration of shifter additive for plastic scintillators of different size*, Nucl. Instrum. Meth. **A599** (2009) 167.

[71] A. Arefev *et al.*, *Beam test results of the LHCb electromagnetic calorimeter*, CERN-LHCB-2007-149.

[72] LHCb, *LHCb muon system technical design report*, CERN-LHCC-2001-010.

[73] LHCb, *LHCb: Addendum to the muon system technical design report*, CERN-LHCC-2003-002.

[74] LHCb, *LHCb: Second addendum to the muon system technical design report*, CERN-LHCC-2005-012.

[75] LHCb, P. R. Barbosa-Marinho *et al.*, *LHCb online system technical design report: Data acquisition and experiment control*, CERN-LHCC-2001-040.

[76] LHCb, *Addendum to the LHCb online system technical design report*, CERN-LHCC-2005-039, CERN-LHCC-2001-040-ADD-1.

[77] G. Haefeli *et al.*, *The LHCb DAQ interface board TELL1*, Nucl. Instrum. Meth. **A560** (2006) 494.

[78] LHCb, *LHCb trigger system technical design report*, CERN-LHCC-2003-031.

[79] J. Albrecht, C. Fitzpatrick, V. Gligorov, and G. Raven, *The upgrade of the LHCb trigger system*, JINST **9** (2014), no. 10 C10026, arXiv:1410.5012.

[80] R. Aaij and J. Albrecht, *Muon triggers in the High Level Trigger of LHCb*, LHCb-PUB-2011-017, CERN-LHCb-PUB-2011-017, 2011.

[81] V. V. Gligorov, *A single track HLT1 trigger*, Tech. Rep. LHCb-PUB-2011-003. CERN-LHCb-PUB-2011-003. LHCb-INT-2010-053, CERN, Geneva, Jan, 2011.

[82] R. Aaij *et al.*, *Tesla : an application for real-time data analysis in High Energy Physics*, Comput. Phys. Commun. (2016) , arXiv:1604.05596.

[83] LHCb, *LHCb TDR computing technical design report*, CERN-LHCC-2005-019.

[84] P. Mato, *GAUDI-Architecture design document*, LHCb-98-064, CERN-LHCb-98-064.

[85] G. Barrand *et al.*, *GAUDI - A software architecture and framework for building HEP data processing applications*, Comput. Phys. Commun. **140** (2001) 45.

[86] R. Brun and F. Rademakers, *ROOT: An object oriented data analysis framework*, Nucl. Instrum. Meth. **A389** (1997) 81.

[87] *The* ROOT *project*, https://root.cern.ch/. Accessed: 2016-08-30.

[88] I. Belyaev *et al.*, *Simulation application for the LHCb experiment*, eConf **C0303241** (2003) TUMT003, arXiv:physics/0306035.

[89] LHCb, I. Belyaev *et al.*, *Handling of the generation of primary events in Gauss, the LHCb simulation framework*, in *Proceedings, 2010 IEEE Nuclear Science Symposium and Medical Imaging Conference (NSS/MIC 2010)*, pp. 1155–1161, 2010. doi: 10.1109/NSSMIC.2010.5873949.

[90] LHCb, M. Clemencic *et al.*, *The LHCb simulation application, Gauss: Design, evolution and experience*, J. Phys. Conf. Ser. **331** (2011) 032023.

[91] LHCb, *The* GAUSS *project*, http://lhcb-release-area.web.cern.ch/LHCb-release-area/DOC/gauss/. Accessed: 2016-08-30.

[92] T. Sjostrand, S. Mrenna, and P. Z. Skands, *PYTHIA 6.4 Physics and Manual*, JHEP **05** (2006) 026, arXiv:hep-ph/0603175.

[93] T. Sjostrand, S. Mrenna, and P. Z. Skands, *A Brief Introduction to PYTHIA 8.1*, Comput. Phys. Commun. **178** (2008) 852, arXiv:0710.3820.

[94] *The* PYTHIA *project*, http://home.thep.lu.se/~torbjorn/Pythia.html. Accessed: 2016-08-30.

[95] D. J. Lange, *The EvtGen particle decay simulation package*, Nucl. Instrum. Meth. **A462** (2001) 152.

[96] E. Barberio, B. van Eijk, and Z. Was, *PHOTOS: A Universal Monte Carlo for QED radiative corrections in decays*, Comput. Phys. Commun. **66** (1991) 115.

[97] E. Barberio and Z. Was, *PHOTOS: A Universal Monte Carlo for QED radiative corrections. Version 2.0*, Comput. Phys. Commun. **79** (1994) 291.

[98] GEANT4, S. Agostinelli *et al.*, *GEANT4: A Simulation toolkit*, Nucl. Instrum. Meth. **A506** (2003) 250.

[99] LHCb, *The* BOOLE *project*, http://lhcb-release-area.web.cern.ch/LHCb-release-area/DOC/boole/. Accessed: 2016-08-30.

[100] LHCb, *The* MOORE *project*, http://lhcb-release-area.web.cern.ch/LHCb-release-area/DOC/moore/. Accessed: 2016-08-30.

[101] LHCb, *The* BRUNEL *project*, http://lhcb-release-area.web.cern.ch/LHCb-release-area/DOC/brunel/. Accessed: 2016-08-30.

[102] LHCb, *The* DAVINCI *project*, http://lhcb-release-area.web.cern.ch/LHCb-release-area/DOC/davinci/. Accessed: 2016-08-30.

[103] LHCb, *The stripping project*, http://lhcb-release-area.web.cern.ch/LHCb-release-area/DOC/stripping/. Accessed: 2016-08-30.

[104] *LHCb particle table*, http://www.physik.uzh.ch/~nchiapol/lhcb/particles.txt. Accessed: 2016-08-30.

[105] LHCb, R. Aaij *et al.*, *Measurement of the ratio of branching fractions* $\mathcal{B}(B^0 \to K^{*0}\gamma)/\mathcal{B}(B_s^0 \to \phi\gamma)$, Phys. Rev. **D85** (2012) 112013, arXiv:1202.6267.

[106] LHCb, R. Aaij *et al.*, *Measurement of the ratio of branching fractions* $BR(B^0 \to K^{*0}(892)\gamma)/BR(B_s^0 \to \phi\gamma)$ *and the direct CP asymmetry in* $B^0 \to K^{*0}(892)\gamma$, Nucl. Phys. **B867** (2013) 1, arXiv:1209.0313.

[107] O. Deschamps and A. Puig Navarro, *Measurement of the ratio of branching fractions* $B(B^0 \to K^{*0}\gamma)/B(B_s^0 \to \phi\gamma)$ *and direct CP violation in* $B^0 \to K^{*0}\gamma$, , LHCb-CONF-2012-004.

[108] ARGUS, H. Albrecht *et al.*, *Search for Hadronic* $b \to u$ *Decays*, Phys. Lett. **B241** (1990) 278.

[109] M. Pivk and F. R. Le Diberder, *SPlot: A Statistical tool to unfold data distributions*, Nucl. Instrum. Meth. **A555** (2005) 356, arXiv:physics/0402083.

[110] M. Pivk, *sPLOT: A Quick introduction*, in *Statistical Problems in Particle Physics, Astrophysics and Cosmology (PHYSTAT 05): Proceedings, Oxford, UK, September 12-15, 2005*, pp. 173–177, 2006. arXiv:physics/0602023.

[111] F. Soomro, *Radiative decays of B mesons at LHCb*, PhD thesis, Imperial Coll., London, 2011.

[112] F. James and M. Roos, *Minuit: A System for Function Minimization and Analysis of the Parameter Errors and Correlations*, Comput. Phys. Commun. **10** (1975) 343.

[113] A. Roodman, *Blind analysis in particle physics*, eConf **C030908** (2003) TUIT001, arXiv:physics/0312102, [,166(2003)].

[114] D. Martínez Santos and F. Dupertuis, *Mass distributions marginalized over per-event errors*, Nucl. Instrum. Meth. **A764** (2014) 150, arXiv:1312.5000.

[115] Belle, D. Dutta *et al.*, *Search for $B_s^0 \to \gamma\gamma$ and a measurement of the branching fraction for $B_s^0 \to \phi\gamma$*, Phys. Rev. **D91** (2015), no. 1 011101, arXiv:1411.7771.

[116] LHCb, R. Aaij *et al.*, *Angular analysis of the $B^0 \to K^{*0}\mu^+\mu^-$ decay using 3 fb^{-1} of integrated luminosity*, JHEP **02** (2016) 104, arXiv:1512.04442.

[117] CMS, V. Khachatryan *et al.*, *Angular analysis of the decay $B^0 \to K^{*0}\mu^+\mu^-$ from pp collisions at $\sqrt{s} = 8$ TeV*, Phys. Lett. **B753** (2016) 424, arXiv:1507.08126.

[118] D. Straub, *flavio v0.11*, Aug., 2016. doi: 10.5281/zenodo.59840.

[119] W. D. Hulsbergen, *Decay chain fitting with a Kalman filter*, Nucl. Instrum. Meth. **A552** (2005) 566, arXiv:physics/0503191.

[120] R. Frühwirth *et al.*, *Data Analysis Techniques for High-Energy Physics, Second Edition*, Cambridge Monographs on Particle Physics, Nuclear Physics and Cosmology, Cambridge University Press, 2000.